Distributed Energy Program

FY04 Annual Reports

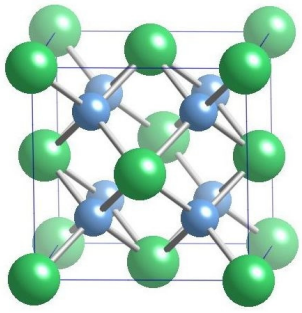

Materials for Distributed Energy

OAK RIDGE NATIONAL LABORATORY

MANAGED BY UT-BATTELLE FOR THE DEPARTMENT OF ENERGY

FY 2004

Progress Report for Distributed Energy Materials

Energy Efficiency and Renewable Energy
Distributed Energy Research

Debbie Haught
Technology Development Manager

D. P. Stinton
Oak Ridge National Laboratory Technical Advisor

May 2005

CONTENTS

Recuperator Alloys—Composition Optimization for Corrosion Resistance

Bruce A. Pint
Metals and Ceramics Division
Oak Ridge National Laboratory
Oak Ridge, TN 37831-6156
(865) 576-2897, E-mail: pintba@ornl.gov

DOE Technology Development Manager: Debbie Haught
(202) 586-2211; (202) 586-7114 (fax); e-mail: debbie.haught@ee.doe.gov
ORNL Technical Advisor: Karren More
(865) 574-7788; fax (865) 576-5413; e-mail: morekl1@ornl.gov

Objective

- Determine minimum Cr and Ni contents needed for corrosion resistance in exhaust gas to assist in the development of a cost-effective replacement for type 347 stainless steel in microturbine recuperators operating at 650–700°C.
- Develop an improved understanding of the role of water vapor on the accelerated corrosion of stainless steels including mechanistic and mathematical lifetime models.

Approach

- Study the corrosion behavior of model and commercial alloys in foil and sheet form in laboratory tests designed to simulate the water content in microturbine exhaust gas
- Characterize the growth of reaction products and loss of Cr from the substrate to quantify the rate of degradation.

Accomplishments

- Commercial and model alloy specimens reached 10,000 h of laboratory testing at 650°, 700° and 800°C in humid air.
- Initial characterization of the post-test commercial foil specimens revealed that near-surface grain boundary Cr depletion at 650°C can lead to localized accelerated attack in highly alloyed stainless steels due to the slow diffusion of Cr in the substrate at this temperature.
- Results from model alloy testing continue to confirm that both Ni and Cr additions are critical to corrosion resistance in humid air environments and that minor Mn and Si additions also increase corrosion resistance.

Future Direction

- Continue testing of commercial, laboratory-scale model alloys in order to better understand their likely long-term performance in recuperator applications.
- Complete testing program of laboratory-scale, creep-resistant Fe-20 Cr-20 Ni-base compositions for possible scale-up to commercial fabrication.
- Quantify degradation of materials by measuring residual Cr contents as a function of time and temperature and gain a better understanding of factors controlling Cr consumption and depletion in this system.

Introduction

In order to boost the efficiency of current microturbines, higher engine temperatures are needed. However, increasing the recuperator or heat exchanger temperature from <600°C to 650–700°C results in a drastic loss in durability for the type 347 stainless steel thin section (75–125 µm) components. The problem is due to accelerated corrosion attack due to the presence of water vapor in the exhaust gas.[1] Figure 1 shows examples of this behavior on

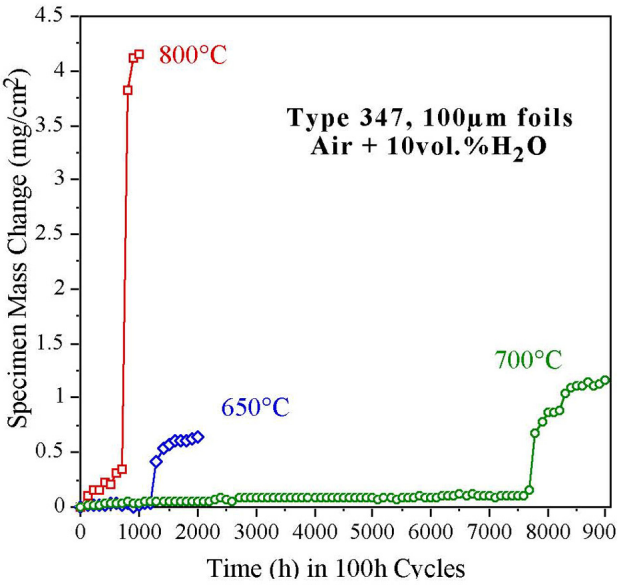

Figure 1. Specimen mass gain for type 347 stainless steel foil specimens exposed for 100 h cycles in air + 10 vol. % H_2O at various temperatures.

commercial 347 100-µm foil specimens with low mass changes in humid air until the onset of accelerated attack (AA). Note the large variation in the incubation period prior to the onset of accelerated attack as a function of temperature. The change in temperature is due to the competing temperature-dependent processes of scale growth, Cr diffusion in the alloy, and evaporation Without the addition of water vapor, specimens of type 347 foil formed a protective scale with slow parabolic kinetics during 50,000-h tests (Figure 2). A thin Cr- and Mn-rich oxide scale formed in laboratory air, while large Fe-rich oxide nodules formed in the presence of water vapor at 650°C (Figure 3). These nodules grow wider and deeper with time, consuming a large fraction of the foil thickness in relatively short times. Therefore, new steels are needed for recuperators to

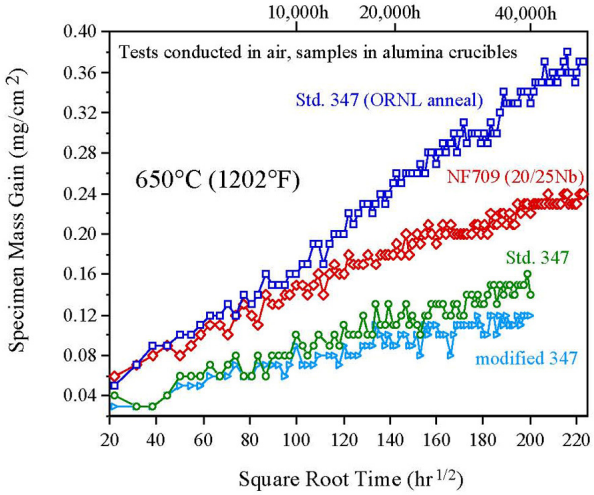

Figure 2. Specimen mass gain of various stainless steels plotted versus square root time to show the parabolic relationship during 500h cycles in laboratory air at 650°C.

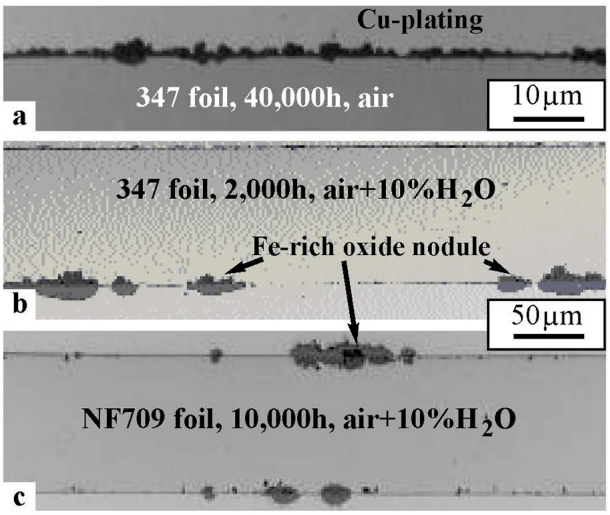

Figure 3. Light microscopy of polished cross-sections of stainless steel foils oxidized at 650°C: (a) type 347, 40,000h in air (b) 347, 2,000h in humid air and (c) NF709, 10,000h in humid air.

operate at 650–700°C in the next generation of microturbines. Both commercial and laboratory-scale materials are being tested in order to better understand the corrosion phenomenon in this environment and assist with the development of economical replacement options. Model alloys also are being tested in order to provide a clear, fundamental understanding of alloying effects on corrosion resistance.

Approach

Commercial foil specimens were obtained from alloy and engine manufacturers or rolled to foil from thicker starting materials. Model alloys were vacuum induction melted and cast in a water-chilled copper mold, followed by hot forging and rolling to 2.5 mm. The sheets were then cold rolled to 1.25 mm and annealed under Ar + 4%H_2 for 2 min at 1000°C. Sheet specimens (12 × 17 × 1.2 mm) were polished to a 600 grit SiC finish. Chemical compositions were measured by combustion and plasma analysis after casting. The oxidation tests were done in air + 10 ± 1 vol. % water vapor with 100-h cycles at 650–800°C. After oxidation, selected specimens were Cu-plated and sectioned for metallographic analysis and electron probe microanalysis (EPMA) to determine Cr depletion profiles.

Results

Oxidation Testing

Testing at 650°C to 10,000 h has been completed on a number of foil materials (Figure 4). Commercial-type 347 foil showed AA between 1000 and 2000 h under these conditions. Four modifications of type 347 foil[2,3] also were tested and showed superior performance. The third modification began to show AA at 8000 h, but the other three compositions did not show AA after 10,000 h.

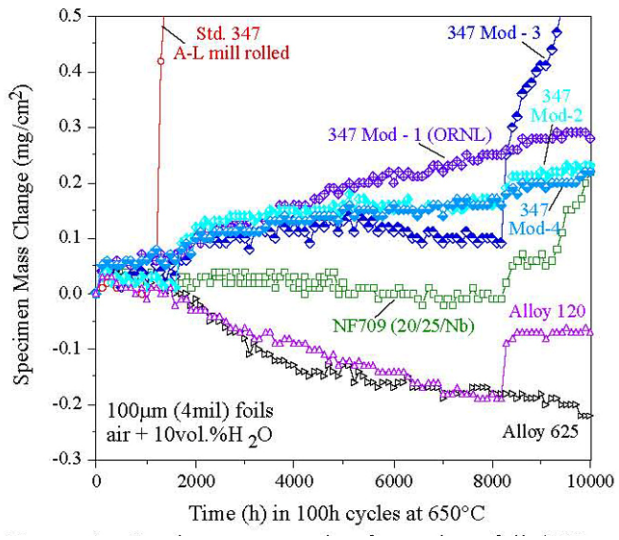

Figure 4. Specimen mass gains for various foil (100 µm thick) materials during 100-h cycles in humid air at 650°C.

Higher alloyed commercial alloys also were tested (Figure 4). These alloys showed low mass gains or mass losses likely due to volatilization of $CrO_2(OH)_2$. However, the specimen of Fe-20 Cr-25 Ni + Nb (rolled from NF709 tube) showed increased mass gain (the onset of AA) during the last 2000 h of testing (Figure 3c). The specimen of alloy 120 (Fe-25 Cr-35 Ni) also showed an increase at one point but did not continue to gain afterward. Specimens of Ni-base alloy 625 also showed fairly continuous mass losses during the test.

Figure 5 shows specimen mass gain results for foils tested at 700°C for up to 10,000 h. Low mass gains and/or mass losses reflect a slow oxidation rate and some evaporation. A mass increase was noted for 20/25/Nb foil after ≈8500 h. For both mill-rolled and ORNL-rolled alloy 120 foils, a continuous mass loss was observed. Also shown in Figure 5 are results for two specimens of an ORNL-rolled Fe-20 Cr-20 Ni-4 Mn foil. This composition is the first attempt to develop a cost-effective creep- and corrosion-resistant stainless steel. The higher mass gain for this foil compared with some of the other compositions is not attributed to AA but instead to its higher Mn content (compared with 1–2% in the other alloys). The high Mn content leads to excessive incorporation of Mn in the scale and a faster oxidation rate (but without Fe-rich oxide nodule formation). As mentioned in prior quarterly reports, Mn can be beneficial in preventing AA, but in a thin

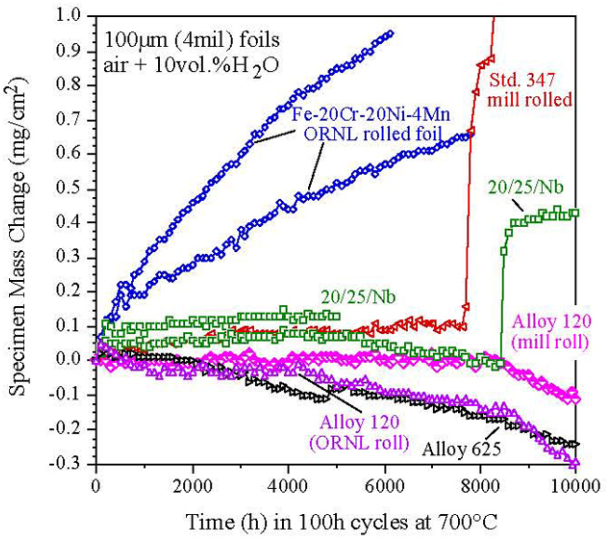

Figure 5. Specimen mass gains for various foil (100 µm thick) materials during 100-h cycles in humid air at 700°C.

foil, increasing the metal consumption rate can be detrimental to its lifetime.

Figure 6 shows the results for foils tested at 800°C in air + 10 % H_2O. Only the foil specimen of alloy 120 ran to 10,000 h. This specimen showed a larger mass gain for the last 2000 h of the test with some nodule formation indicating the onset of AA. However, it was a more gradual onset than the other materials. The foil specimen of alloy 625 was stopped at 6000 h for characterization and did not show any signs of AA. The specimens of Fe-20 Cr-25 Ni + Nb were stopped at 5000 for characterization, and after 6000 and 7000 h due to AA. Foil specimens of Fe-20 Cr-20 Ni-4 Mn were stopped after 2000 h due to excessive mass gain. These specimens outlasted commercial 347 foil, which showed AA after less than 1000 h at 800°C (Figure 1). In general, the failure times for the various foils show the benefit of increasing Cr and Ni content. The Fe-20 Cr-25 Ni + Nb foil specimens showed AA between 5000 and 7000 h, while alloy 120 showed only a modest increase in mass after 8,000 h. The performance of the Fe-20 Cr-20 Ni-4 Mn likely reflects the previously mentioned problem with the high Mn content. New laboratory-scale heats with compositions based on Fe-20 Cr-20 Ni have been fabricated in an attempt to achieve better corrosion resistance.

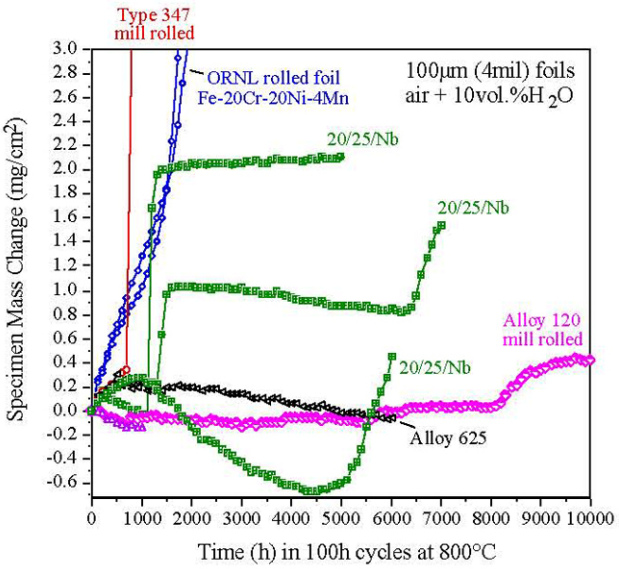

Figure 6. Specimen mass gains for various foil (100 µm thick) materials during 100-h cycles in humid air at 800°C.

To clarify the role of composition, a series of model alloys was produced to further understand the role of Cr and Ni content in oxidation resistance and particularly lifetime.[4] The alloys contain H1.7% Mn and 0.25% Si additions but no strengthening elements, and they were rolled to 1.2-mm sheet to annealed to achieve an H20 µm grain size. Figure 7 shows that for compositions with 20% Cr, increasing the Ni content leads to a longer time until the onset of AA during 100-h cycles in humid air at 800°C. The alloy with the most Cr and Ni, Fe-20 Cr-25 Ni, has yet to undergo AA.

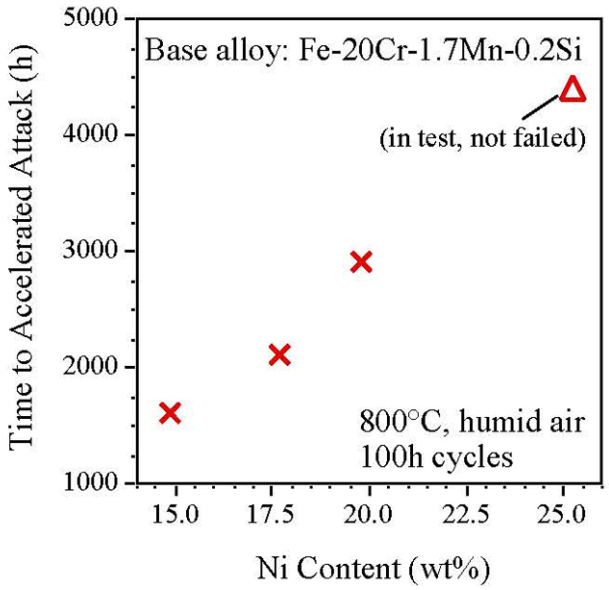

Figure 7. Time to accelerated attack in 100h cycles in air plus 10% H_2O at 800°C for various Ni additions in model alloys with a base Fe-20 Cr-1.7 Mn-0.2 Si composition. The specimen with the highest Ni content has yet to reach AA.

In general, the specimen mass gains presented in this section are a combination of several factors, including growth, evaporation, and spallation of the reaction product:

$$\Delta M_{specimen} = \Delta M_{oxide\ growth} - \Delta M_{evap.} - \Delta M_{spall}$$

Thus while mass gain can be used to differentiate the onset of AA, it is not very useful in quantifying the extent of attack because of the competing factors. Thus additional characterization is necessary.

Characterization of Cr depletion

In order to quantify the extent of attack, composition maps and profiles were measured across polished foil specimen cross-sections exposed for 10,000 h using EPMA. The work is still in progress, but the initial results were somewhat surprising. It was assumed that alloys with high Cr and Ni content—such as HR120, alloy 803,and even NF709—would be virtually immune to AA. However, the mass gain data for HR120 and NF709 at 650°C (Figure 4) showed some indication of AA before 10,000 h and cross-sections confirmed it (Figure 3c). Figure 8 shows that the Cr depletion in HR120 was

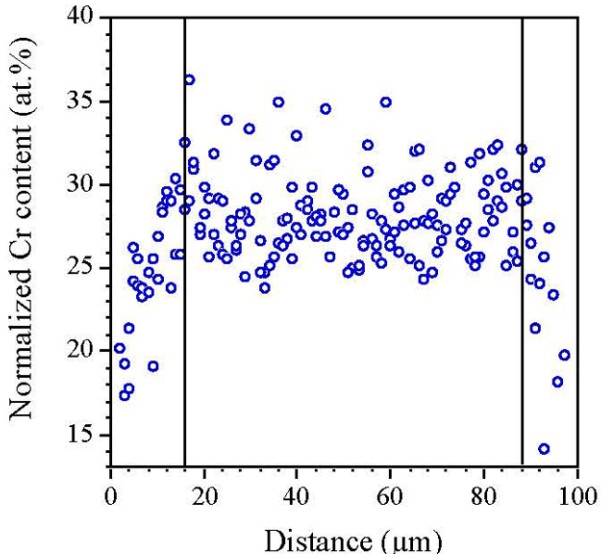

Figure 8. EPMA Cr profiles from three scans across the cross-section of HR120 foil after 10,000 h at 650°C in humid air. The Cr depletion appears to be only 12–15 μm from the surface.

localized to only 12–15 μm into the metal, with the underlying material being virtually unaffected. (The variations in Cr within the center of the material are due to Cr-rich intermetallic phase formation.) Maps of the Cr content illustrate the situation even better (Figure 9). Not only is the Cr depletion concentrated near the surface, but also the alloy grain boundaries have been selectively depleted. Whenever the depletion reached a significantly high level, AA was observed. Bright areas mark Cr-rich phases in the metal and the Cr-rich oxide at the specimen surface. Chromium also is enriched in the oxide that forms beneath the Fe-rich oxide nodules (arrows in Figure 9). Thus both NF709 and HR120 were susceptible to AA after 10,000 h at 650°C (Figures 9a and 9c). However, NF709 formed nodules after 10,000 h at 700°C as a result of Cr depletion on the alloy grain boundaries near the surface (Figure 9b). With its higher Cr and Ni contents, HR120 did not appear to show significant depletion or AA after 10,000 h at 700°C (Figure 9d). This is likely due to faster Cr diffusion at 700°C, which allowed some Cr from the center of the specimen to diffuse to the surface and reduce the extent of the depletion.

Conclusions

Work has continued on studying the effect of water vapor on the corrosion of commercial, laboratory-scale, and model stainless steels at 650–800°C. Results on model alloys have shown the benefit of higher Cr and/or Ni contents in resisting AA caused by the presence of water vapor. However, characterization of commercial alloy foils after 10,000-h exposures has shown that even highly alloyed steels are not immune to AA, because Cr diffusion in the alloy is sufficiently slow at 650° and 700°C that the near-surface alloy grain boundary regions become depleted in Cr; and all Fe-base alloys become susceptible to the detrimental effect of water vapor. These observations will need to be taken into account for development of a lifetime model.

References

1. B. A. Pint and J. M. Rakowski , NACE Paper 00-259, Houston, TX, presented at NACE Corrosion 2000, Orlando, FL, March 2000.
2. P. J. Maziasz, R. W. Swindeman, J. P. Montague, M. Fitzpatrick, P. F. Browning, J. F. Grubb, and R. C. Klug, *Mater. High Temp.*, **16**, 207 (1999).
3. P. J. Maziasz, R. W. Swindeman, J. P. Shingledecker, K. L. More, B. A. Pint, E. Lara-Curzio, and N. D. Evans, in *Parsons 2003, Engineering Issues in Turbine Machinery, Power Plant and Renewables*, A. Strang, et al. eds., Maney, London, pp.1057–73, 2003.
4. B. A. Pint, R. Peraldi, and P. J. Maziasz, *Mater. Sci. Forum*, **461–464**, 815–822 (2004).

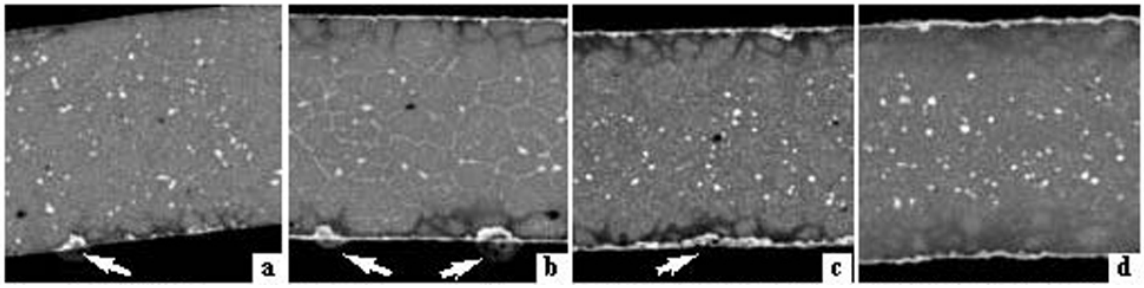

Figure 9. EPMA Cr maps after 10,000 h exposures in humid air of (a) NF709 at 650°C, (b) NF709 at 700°C, (c) HR120 at 650°C, and (d) HR120 at 700°C. The foils are all 100 μm in thickness and arrows mark nodule formation.

Awards/Patents

B. A Pint was named to the International Advisory Board of the journal *Oxidation of Metals*.

Publications/Presentations

B. A. Pint, "The Long-Term Performance of Model Austenitic Alloys in Humid Air," NACE Paper 04-530, Houston, TX, presented at NACE Corrosion 2004, New Orleans, March 2004.

B. A. Pint and K. L. More, "Stainless Steels with Improved Oxidation Resistance for Recuperators," ASME Paper #GT2004-53627, presented at the International Gas Turbine Institute Turbo Expo, Vienna, Austria, June 2004 (by More).

B. A. Pint, R. Peraldi, and P. J. Maziasz, "The Use of Model Alloys to Develop Corrosion-Resistant Stainless Steels," *Mater. Sci. Forum*, **461–464,** 815–822 (2004); poster presented at the 6th International Conference on High Temperature Coatings and Protection of Materials, Les Embiez, France, May 2004.

R. Peraldi and B. A. Pint, "Effect of Cr and Ni Contents on the Oxidation Behavior of Ferritic and Austenitic Model Alloys in Air With Water Vapor," *Oxid. Met.*, **61,** 463–83 (2004).

Recuperator Materials Testing and Evaluation

Edgar Lara-Curzio
Metals and Ceramics Division
Oak Ridge National Laboratory
Oak Ridge, TN 37831-6069
(865) 574-1749; fax (865) 574-6098; e-mail: laracurzioe@ornl.gov

DOE Technology Development Manager: Debbie Haught
(202) 586-2211; (202) 586-7114 (fax); e-mail: debbie.haught@ee.doe.gov
ORNL Technical Advisor: Karren More
(865) 574-7788; fax (865) 576-5413; e-mail: morekl1@ornl.gov

Objective

- Screen and evaluate candidate materials for microturbine recuperators and identify the mechanisms responsible for their degradation on exposure to microturbine exhaust gases.
- Evaluate the evolution of mechanical and physical properties of microturbine recuperator materials as a function of service history.

Approach

- Acquire a commercially available microturbine and modify it, in collaboration with its manufacturer, to operate at recuperator inlet temperatures as high as 850°C. Determine the durability of candidate recuperator materials by placing test specimens at a location upstream of the recuperator and then characterizing the evolution of the material's physical and mechanical properties as a function of time of exposure.
- During exposure tests inside the microturbine, subject test specimens to various levels of mechanical stress to simulate the stresses associated with the flow of compressed air in one direction and the flow of exhaust gases in the other.
- Evaluate microturbine recuperators decommissioned after field operation to characterize their microstructures and determine their residual mechanical and physical properties.

Accomplishments

- Determined the effect of time of exposure on the mechanical properties, corrosion resistance, and microstructure of 347 stainless steel, stainless steels modified at Oak Ridge National Laboratory (ORNL), and alloys 625LCF, HR120®, and HR230®.
- Determined the residual properties of five decommissioned microturbine recuperators.

Future Direction

- Complete evaluation of HR-120 alloy foils in ORNL's microturbine recuperator test facility for exposures of up to 3000 h and compare results with those obtained in long-term cyclic testing performed in the laboratory.
- Evaluate 20-25Nb foils received from Allegheny Ludlum in ORNL's microturbine recuperator test facility to compare and contrast their performance with that of HR-120.

Introduction

The challenging performance targets for the next generation of microturbines include fuel-to-electricity efficiency of 40%, capital costs of less than $500/kW, nitrogen oxides (NO_x) emissions reduced to single parts per million, several years of operation between overhauls, a life of 40,000 hours, and fuel flexibility.[1] Significant increases in microturbine efficiency can be achieved through higher engine operating temperatures, which can be realized through the use of advanced metallic alloys and ceramics for high-temperature components.

One of the critical components of low-compression-ratio microturbines is the recuperator, which is responsible for a significant fraction of the overall efficiency of the microturbine.[2] Conventional recuperators are thin-sheet metallic heat exchangers that recover some of the waste heat from the exhaust stream and transfer it to the incoming air stream. The preheated incoming air is then used for combustion, because less fuel is required to raise its temperature to the required level at the turbine inlet. Most of today's compact recuperators are manufactured using 300 series (e.g., 347) stainless steels, which are used at exhaust-gas temperatures of <600°C.[3] At higher temperatures, these materials are susceptible to creep deformation and oxidation, which lead to structural deterioration and leaks that reduce the effectiveness and life of the recuperator. The temperature requirements for the next generation of microturbines have prompted efforts to screen and evaluate candidate materials with the required creep and corrosion resistance. Furthermore, developmental efforts will be needed to adapt current recuperator manufacturing processes to advanced alloys, reduce costs, and enable long-term reliable operation at higher temperatures.

As part of a program sponsored by DOE to support microturbine manufacturers in developing the next generation of microturbines, a recuperator test facility was established at ORNL. The objective of this test facility is to screen and evaluate candidate materials for microturbine recuperators inside a microturbine at turbine exit temperatures (TETs) as high as 850°C. Furthermore, the preparation of samples for these experiments, which requires welding test specimens to a sample holder, provides the means for identifying potential manufacturability barriers associated with a particular material.

Approach

In 2001, ORNL acquired a 60-kW Capstone microturbine. In collaboration with Capstone Turbine Corporation, the microturbine was modified to achieve higher TET values. The system was also to allow the placement of test specimens through six port bosses at the entrance of the recuperator. Figure 1 shows a photograph of ORNL's microturbine recuperator testing facility and a schematic of the modified microturbine indicating the location of the port bosses with respect to the location of the radial recuperator. Further details of ORNL's microturbine recuperator testing facility can be found elsewhere.[4,5]

The diameter of the sample holder onto which the foils under evaluation are laser-welded was 23.1 mm. Prior to welding the foils, type-K thermocouples were placed in each one of the four holes in the sample holder. During exposure tests, the sample holders were subjected to a constant pressure of 60 psi (0.41 MPa) to reproduce the state of stress that recuperator cells experience during normal microturbine operation. This pressure corresponds to the difference between the pressure of compressed air on one side of the cell and the pressure of the exhaust gases on the other. The pressure inside the sample holder is controlled using a computerized system for the duration of the test. This system also provides the means for determining whether an increase in volume in the sample holder has occurred, which would be associated with creep deformation or rupture of the foils.

During exposure tests, the samples along the length of the sample holder are subjected to a temperature gradient. For a nominal TET value of 800°C, temperature variation along the length of the sample holder spans between 650°C and 760°C. The temperature gradient, which results from the configuration of the microturbine, turned out to be a nice feature because it allows for the evaluation of materials over a wide range of temperatures during the same test.

The baseline mechanical properties of the materials investigated in this study were determined at ambient temperature. Miniature dog-bone-shaped tensile specimens were obtained by electron discharge machining from foils 20.3 cm wide. Test specimens were obtained with their main axis either parallel or perpendicular to the rolling direction. The

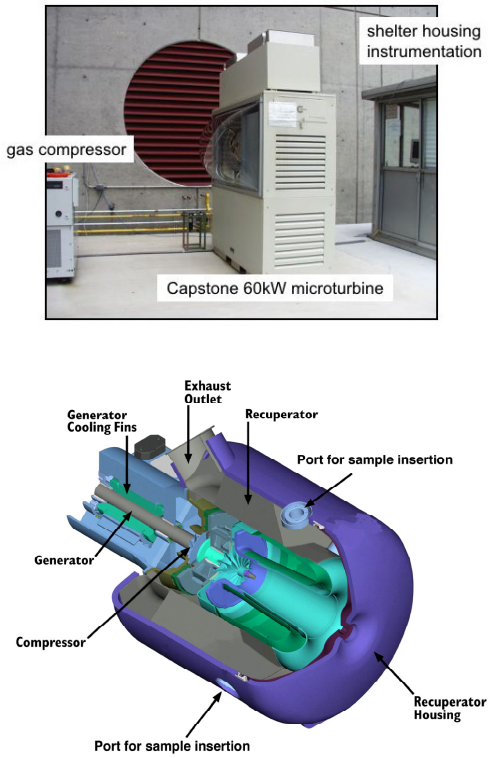

Figure 1. ORNL's microturbine recuperator testing facility (top). Schematic of modified 60-kW Capstone microturbine (middle). Sample holders with and without foils (bottom).

dimensions of the dog-bone-shaped miniature tensile specimens were 10 mm long, with a gauge section 1.27-mm wide and 3.8-mm long. Figure 2 depicts one of those test specimens.

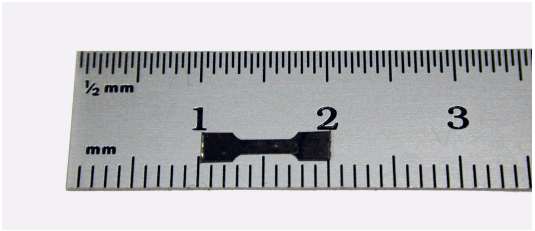

Figure 2. Miniature test specimen for evaluation of mechanical properties of metallic foils. Test specimens are obtained by electron-discharge machining.

The tensile stress-strain behavior of the miniature test specimens was determined under a constant crosshead displacement rate of 0.01 mm/min using an electromechanical testing machine. A special set of grips and alignment fixture were used to transfer the load to the test specimens and to ensure alignment to eliminate spurious bending strains. Values for the 0.2% yield stress, ultimate tensile strength and strain failure were obtained from each stress-strain curve. These results are listed in Table 1.

At the end of 500-h test exposures, the sample holders were retrieved from the microturbine and the foils were removed from the sample holder. Miniature tensile test specimens were obtained from the foils by electron discharge machining. Other pieces of the foil were used for microstructural characterization using scanning electron microscopy (SEM) and chemical analysis using an electron probe micro-analyzer (EPMA). Although special precautions were taken to preserve the integrity of the scale formed on the surface of the foils evaluated, it was not possible to know if any material had spalled off before the sample holders were removed from the microturbine.

Results

During the reporting period, the materials investigated included alloys HR-120® and 230® alloy. These are chromia-forming austenitic nickel-based alloys developed by Haynes International. Figure 3 depicts a backscattered scanning electron micrograph of the cross-sections of an 89-µm-thick foil of alloy 230. The presence of tungsten carbide particles the alloy is evident in the micrograph (brightly imaging particles). It can also be observed that these carbide particles tend to be aligned along certain planes parallel to the rolling direction.

Table 1. Summary of tensile results for as-received materials.

230® alloy	0.2% yield strength (MPa)	Ultimate tensile strength (MPa)	Failure strain (%)
0.089-mm thick			
⊥ to rolling direction	452± 24	780 ± 18	36 ± 4
‖ to rolling direction	422 ± 12	770 ± 11	34 ± 2
0.102-mm thick			
⊥ to rolling direction	466 ± 23	817 ± 12	40 ± 4
‖ to rolling direction	489 ± 45	818 ± 27	36 ± 3
HR-120® alloy			
0.089-mm thick			
‖ to rolling direction	373 ± 31	697 ± 4	37 ± 5

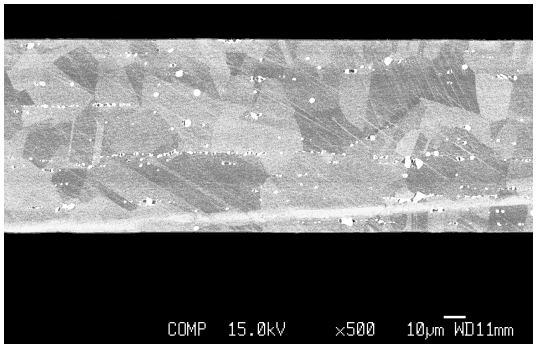

Figure 3. Backscattered scanning electron micrograph of 89-µm-thick foil of 230 alloy.

Alloy 230®

Figure 4 depicts a sample holder with alloy 230 foils at the end of the 500-h exposure test. At the end of the 500-h exposure of alloy 230, the foils had a dull appearance and grew darker with exposure temperature along the length of the sample holder. There was no evidence of creep deformation, in contrast to the ballooning experienced by foils of 347 stainless steel exposed to similar conditions.[5]

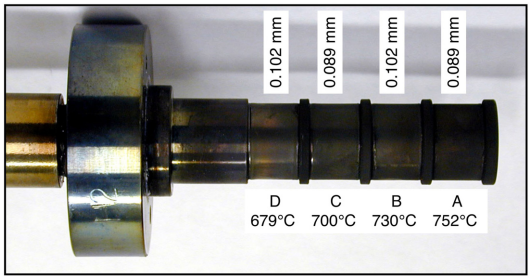

Figure 4. Sample holder with 230 alloy foils after 500-h exposure in ORNL's microturbine recuperator testing facility at TET of 800°C.

Scanning electron micrographs of the foil cross sections after exposure for 500 hours revealed the existence of a scale of chromium oxide on the surface that was exposed to the microturbine exhaust gases. A series of intergranular cracks had developed on both sides of the foils. However, these cracks were several micrometers long and had spanned more than one grain near the surface that had been exposed to the microturbine exhaust gases. Elemental maps obtained from foils exposed to 752°C, which are depicted in Figure 5, revealed that the surfaces of those cracks were rich in oxygen but deficient in chromium. The depletion of chromium from the grain boundaries of the base metal near the surfaces evident in the elemental maps. At this time, the mechanisms that lead to the formation of cracks on the surface have not been identified.

Figure 6 presents stress versus strain curves obtained from the evaluation of test specimens obtained from the foil at location 1 of the sample holder. Also included in Figure 6 are stress-strain curves for the as-received material. It was found that the ultimate tensile strength and ductility of 230 alloy decreased by 30% and 60%, respectively, after 500 h exposure at 752°C. At the lowest exposure temperature of 679°C, the ultimate tensile strength and ductility decreased by 10% and 25%, respectively.

Table 2 summarizes the tensile results. The loss of ductility of 230 alloy after exposure to microturbine exhaust gases is most likely the result of carbide precipitation at the grain boundaries. Storey et al. reported that the precipitation of large M6C carbides and smaller grain boundary M23C6 precipitates was responsible for the 30% decrease in

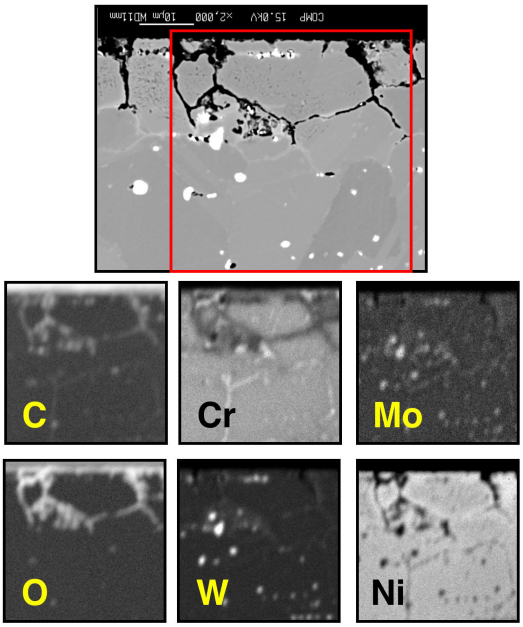

Figure 5. Elemental maps obtained from a foil of 230® alloy after 500-h-long exposure. The surface at the bottom of the micrographs was exposed to the microturbine exhaust gases.

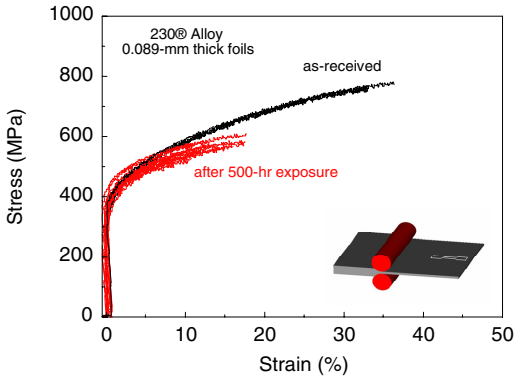

Figure 6. Tensile stress–strain results from the evaluation of 89-µm-thick foils of 230® alloy before and after 500-h exposure at 752°C.

Table 2. Summary of tensile results for 230® alloy.

Foil	Thickness (mm)	T (°C)	0.2% σ_y (MPa)	UTS (MPa)	Failure strain (%)
1	0.089	752	415 ± 12	561 ± 28	13.0 ± 3.0
2	0.102	736	457 ± 15	660 ± 34	19.0 ± 3.4
3	0.089	700	418 ± 41	644 ± 24	19.0 ± 2.9
4	0.102	679	481 ± 7.1	728 ± 22	27.0 ± 6.3

UTS = ultimate tensile strength

ductility in alloy 230 after 1500-h-long exposures at 760°C.[6] These authors also reported that heat treatment at 1177°C for 3 h was sufficient to redissolve the embrittling phases without grain growth and to restore as-processed ductility values.

Equation 1 was found to provide a good representation of the ultimate tensile strength of alloy 230 foils as a function of 500-h exposure temperature in ORNL's microturbine.

$$\frac{\sigma}{\sigma_o} = 1 - \left(\frac{T}{900}\right)^{7.5}, \qquad (1)$$

where T is the exposure temperature in degrees Centigrade and σ_o is the tensile strength at 20°C.

Alloy HR-120®

Figure 7 depicts the sample holder with HR-120® alloy foils at the end of the 500-h exposure in ORNL's microturbine. Under regular lighting conditions, the appearance of the foils in locations 2, 3, and 4 of the sample holder was shiny and brassy. The foil that had been exposed to the highest temperature had a dark, dull appearance.

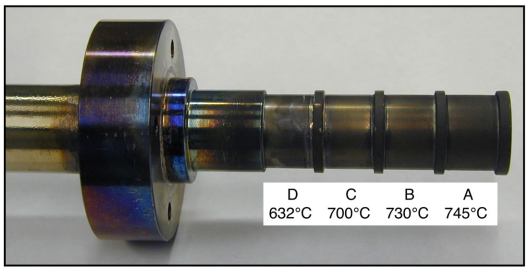

Figure 7. Sample holder with HR120® alloy foils after 500-h exposure in ORNL's microturbine recuperator testing facility at TET = 800°C.

Scanning electron micrographs of cross-sectional areas obtained from HR-120® alloy foils after 500-h microturbine exposure revealed that only a very thin multilayered oxide scale, consisting of mixed oxides of nickel, silicon, chromium, and iron had formed on the surface exposed to the exhaust gases. An elemental chemical analysis (Figure 8) revealed that the grain boundaries closest to the surface exposed to the exhaust gases had been depleted of chromium but were rich in nickel.

Gleeson and Harper reported a silicon-rich oxide in the scale formed on HR-120 alloy after cycling oxidation for 720 days in air at 982°C.[7] They also reported the depletion of chromium in the base metal near the surface and the formation of scales

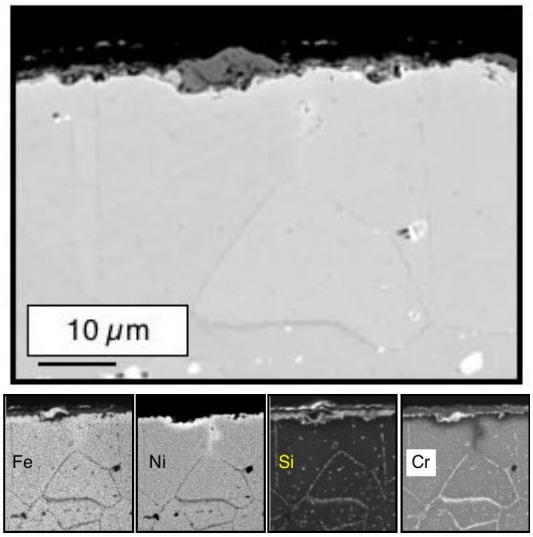

Figure 8. Scanning electron micrograph of cross-sectional area of HR-120® alloy foil after 500-hr exposure at 745°C. The upper surface in the micrograph was exposed to the microturbine exhaust gases.

containing Cr_2O_3+$NiCr_2O_4$ and NiO after thermal cycling at temperatures above 1093°C. At temperatures above 1200°C, they reported the presence of a fast-growing Fe_3O_4 oxide. This is consistent with these results, considering the accelerated oxidation of the material in water vapor at lower temperatures

Figure 9 presents stress versus strain curves obtained from the tensile evaluation of HR-120 alloy foils before and after 500-h-long exposure in ORNL's microturbine recuperator testing facility. It was found that the ultimate tensile strength and

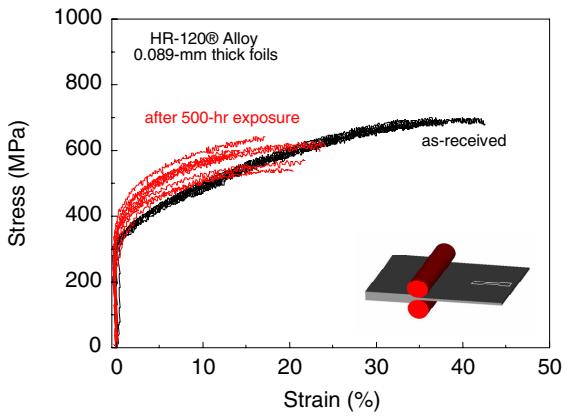

Figure 9. Tensile stress-strain results from the evaluation of 89-μm-thick foils of HR-120® alloy before and after 500-h exposure at 745°C.

ductility of the HR-120 alloy decreased by 15% and 50%, respectively, after exposure at 745°C. At the lowest exposure temperature of 632°C, the ultimate tensile strength and ductility decreased by 10% and 23%, respectively. Table 3 summarizes the tensile results.

Table 3. Summary of tensile results for HR-120®

Foil	T (°C)	0.2% σ_y (MPa)	UTS (MPa)	Failure strain (%)
1	745	388 ± 35	594 ± 32	18.0 ± 4.4
2	730	421 ± 37	615 ± 30	21.0 ± 4.4
3	700	408 ± 39	582 ± 48	23.0 ± 4.7
4	632	407 ± 27	631 ± 53	29.0 ± 4.7

UTS = ultimate tensile strength

The temperature dependence of the ultimate tensile strength for the HR-120 alloy after 500-h exposure in ORNL's microturbine was found to be well described by Eq. (2):

$$\frac{\sigma}{\sigma_o} = 1 - \left(\frac{T}{1000}\right)^6 \qquad (2)$$

where T is the exposure temperature in degrees Centigrade and σ_o is the tensile strength at 20°C.

Figure 10 compares the effect of exposure temperature in ORNL's microturbine recuperator testing facility on the tensile strength of 347 stainless steel and alloys 230 and HR-120. It was found that among the three alloys, HR-120 exhibited the best retention of tensile strength, followed by alloy 230 and finally by 347 stainless steel. Equation (3) was found to describe well the dependence of the ultimate tensile strength of 347 stainless steel with temperature after a 500-h-long exposure.

While there are no fundamental bases behind the form of the correlations in Eqs. (1–3), it is interesting to observe that larger "normalizing temperature" and smaller exponent are associated with increasing resistance to exposure to microturbine exhaust gases. A detailed analysis of the effect of exposure to microturbine exhaust gases on the properties and microstructure of 347 stainless steel can be found elsewhere.[5]

$$\frac{\sigma}{\sigma_o} = 1 - \left(\frac{T}{825}\right)^{9.4} \qquad (3)$$

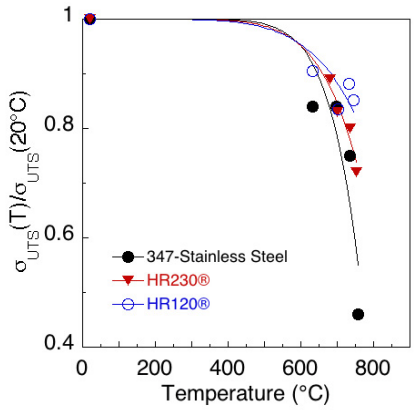

Figure 10. Effect of temperature on the ultimate tensile strength of 347 stainless steel and alloys 230® and HR-120® after 500-h exposure in ORNL's microturbine recuperator testing facility.

Summary

A test facility for screening and evaluating candidate materials for the next generation of microturbine recuperators has been designed and is operational at ORNL. The core of the test facility is a 60-kW Capstone microturbine, which was modified to operate at higher turbine exit temperatures and to allow the placement of test specimens at the entrance of its radial recuperator. Sample holders have been designed and instrumented to allow for continuous recording of the temperature of the thin metallic foil test specimens and to subject these to mechanical stresses through the internal pressurization of the sample holder. Materials under evaluation are welded to the sample holder using laser or e-beam techniques. The testing allows for the identification of potential manufacturability "showstoppers."

Results have been presented from the evaluation of 89-µm-thick and 102-µm-thick foils of alloys 230 and HR-120. It was found that the ultimate tensile strength and ductility of alloy 230 decreased by 30% and 60%, respectively, after 500 h exposure at 752°C. At the lowest exposure temperature of 679°C, the ultimate tensile strength and ductility decreased by 10% and 25%, respectively. Alloy 230 experienced cracking on the surface exposed to the microturbine exhaust gases, and the length of those cracks grew with temperature of exposure. The surface cracks were found to be rich in oxygen, but the grain boundaries in the metal near the surface were found to be depleted of chromium. However, the concentration of chromium, in the form of chromium carbide, was higher in the bulk grain boundaries. It is believed that the precipitation of these carbides is responsible for the decrease in tensile strength of the material with temperature of exposure.

The ultimate tensile strength and ductility of HR-120 alloy decreased by 15% and 50%, respectively, after 500 h exposure at 745°C. At the lowest exposure temperature of 632°C, the ultimate tensile strength and ductility decreased by 10% and 23%, respectively. A layered scale comprising oxides of nickel, chromium, iron, and silicon was found to have formed on the surface of HR-120 alloy foils that were exposed to the microturbine exhaust gases. While silicon was found to be present both inside grains and at grain boundaries, it was found that grain boundaries near the interface between the base metal and the oxide scale had been depleted of chromium. Alloy HR-120 was found to exhibit the greatest resistance to exposure to microturbine exhaust gases, followed by alloy 230 and 347 stainless steel.

References

1. *Advanced Microturbine Systems Program, Plan for Fiscal Years 2000 Through 2006*, U.S. Department of Energy, Office of Energy Efficiency and Renewable Energy, Office of Power Technologies, March 2000.
2. C. F. McDonald, "Heat Recovery Exchanger Technology for Very Small Gas Turbines," *Intl. Journal of Turbo and Jet Engines*," **13,** 239–261 (1966).
3. O. O. Omatete, P. J. Maziasz, B. A. Pint, and D. P. Stinton, *Assessment of Recuperator Materials for Microturbines*, ORNL/TM-2000-304, Oak Ridge National Laboratory, 2003.
4. E. Lara-Curzio, P. J. Maziasz, B. A. Pint, M. Stewart, D. Hamrin, N. Lipovich, and D. DeMore, "Test Facility for Screening and Evaluating Candidate Materials for Advanced Microturbine Recuperators," ASME paper 2002-GT-30581, presented at the International Gas Turbine and Aeroengine Congress and Exhibition, Amsterdam, Netherlands, June 3–6, 2002.
5. E. Lara-Curzio, R. M. Trejo, K. L. More, P. J. Maziasz, and B. A. Pint, "Screening and Evaluation of Materials for Advanced Microturbine

Recuperators," in *Proceedings of ASME Turbo Expo 2004*, paper GT-2004-54255,Vienna, Austria, June 14–17, 2004.
6. J. Storey, D. L. Klarstrom, G. L. Hoback, V. R. Ishwar and J. I. Qureshi, "The Metallurgical Background to Rejuvenation Heat Treatments and Weld Reparability Procedures for Gas Turbine Sheet Metal Components," *Materials at High Temperatures* **18** (4) 241–247 (2001).
7. B. Gleeson and M. A. Harper, "The Long-Term, Cyclic-Oxidation Behavior of Selected Chromia-Forming Alloys," *Oxidation of Metals*, **49**(314) 373–399 (1998).

Publications/Presentations

E. Lara-Curzio, R. M. Trejo, K. L. More, P. J. Maziasz, and B. A. Pint, "Screening and Evaluation of Materials for Advanced Microturbine Recuperators," in *Proceedings of ASME Turbo Expo 2004*, paper GT-2004-54255, Vienna, Austria, June 14–17, 2004.

E. Lara-Curzio, R. M. Trejo, K. L. More, P. J. Maziasz, and B. A. Pint, "Screening and Evaluation of Materials for Advanced Microturbine Recuperators," presented at ASME Turbo Expo 2004, Vienna, Austria, June 16, 2004.

Advanced Alloys for High-Temperature Recuperators

P. J. Maziasz
Metals and Ceramics Division
Oak Ridge National Laboratory
P.O. Box 2008, MS-6115
Oak Ridge, TN 37831-6115
(865) 574-5082; fax: (865) 754-7659; e-mail: maziaszpj@ornl.gov

DOE Technology Development Manager: Debbie Haught
(202) 586-2211; fax: (202) 586-7114; e-mail: debbie.haught@ee.doe.gov
ORNL Technical Advisor: Karren More
(865) 574-7788; fax: (865) 576-5413; e-mail: morekl@ornl.gov

Objectives

- Continue creep and oxidation testing and microstructural evaluation of commercial high-temperature recuperator alloys
- Complete Phase I scale-up commercial processing of sheets and foils of new AL20-25+Nb with Allegheny-Ludlum (AL); deliver foils and sheets to microturbine recuperator manufacturers to make and test air cells.
- Complete Phase II to optimize commercial processing of sheets and foils of AL20-25+Nb
- Characterize recuperator air cells made from advanced alloys.

Approach

- Creep- and oxidation-test and characterize microstructure of advanced recuperator alloys supplied by recuperator original equipment manufacturer (OEMs) or sheet/foil makers to determine improvements relative to standard 347 stainless steel.
- Work in a joint program with AL to facilitate the final stages of its commercialization of AL20-25+Nb to meet the needs of recuperator OEMs.
- Work with recuperator OEMs on manufacturing-specific issues for primary-surface (PS) and brazed-plate-and-fin (BPF) recuperator air cells related to the implementation of advance alloys.

Accomplishments

- Defined and initiated a joint project with AL to produce commercial sheets and foils of AL20-25+Nb to meet the recuperator manufacturing needs of Ingersoll-Rand Energy Systems and Capstone Turbines. Sheets and foils were produced and ORNL testing began at the end of FY 2004 (completed milestone for Subtask 1.5).
- Provided characterization assistance and recommendations on BPF recuperator air cell failures, including a change in braze alloy and then replacement of a portion of 347 steel air cell components with a more corrosion- and heat-resistant alloy. The first ORNL recommendation has been implemented on the current production of Ingersoll Rand PowerWorks 250-kW units.

Future Direction

- Complete sheet/foil commercialization effort on AL20-25+Nb.
- Support characterization of all commercial advanced alloys in Oak Ridge National Laboratory (ORNL) Recuperator Test Facility.
- Complete characterization of fresh and engine-tested recuperator air cells made from commercial advanced alloys.

Introduction

Microturbines are ultraclean, relatively quiet, and fuel-flexible and are attractive for distributed generation (DG), combined heat and power (CHP), and possibly combined-cycle (microturbine–fuel cell) applications. DG can immediately remedy some of the power transmission grid problems and deficiencies that were magnified by the Blackout of 2003 in the Midwestern and the Northeastern United States.[1] Microturbines can also play an important role in various homeland security strategies in the United States by removing critical facilities—like hospitals, water treatment plants, and infrastructure—from dependence on the electric grid.[1,2] Recuperators are compact heat exchangers necessary for high-efficiency, advanced microturbines. They are a costly and challenging component of such systems, limiting maximum operating temperature and lifetime.[3–5] Recuperators for industrial turbines and microturbines have traditionally been made from 347 stainless steel, but problems with performance and durability are becoming evident for such steels as temperatures approach or exceed 650–700°C, particularly in moist air. Economic and efficiency advantages have pushed microturbine engine sizes up from 30–70 kW to 200–250 kW for both stand-alone power generation and CHP applications. If microturbines are used to generate power during peak demand, then cycling will further challenge the recuperator with thermal shock during rapid heat-up. Durable, reliable recuperators (and packaging and ducting) are critical components for attractive microturbine systems.

Recuperator Development over the Last Decade

Today, there are two main types of recuperators used on commercial microturbines in the United States. Both are compact, counterflow recuperators with high effectiveness, and both are designed for high-quality mass manufacturing at a reasonable cost.[4] One type is the PS recuperator (PSR), designed by Solar Turbines and Caterpillar; it consists of welded air cells made from folded foils, and is used in several different kinds of final geometries.[3–6] Rectangular PSR air cell stacks positioned horizontally above the engine have been employed by various Solar Turbines industrial gas turbines, by Honeywell 75-kW microturbines, and most recently, by the new Mercury 50 4.6-MW gas turbine engine.[7] The Capstone Turbines commercial 30- and 60-kW and new 200-kW, microturbines have all used specially designed annular assemblies of PSR air cells, which surround the turbine.[8] The other type is the BPF recuperator (BPFR), which includes the completely brazed vertical stack, developed by Toyo,[5] and uniquely designed air cells of folded foils brazed to sheet-plates and stacked vertically, developed by Ingersoll Rand for its commercial PowerWorks 70-kW and new 250-kW microturbines.[9] The Ingersoll Rand BPFR made from alloy 625 is also employed on the Rolls Royce WR21 advanced-cycle gas turbine designed for naval marine applications.[10] Another type of PSR is the spirally wrapped recuperator, manufactured by continuously spooling foils or sheets[5] with different designs and sizes, being developed by Rolls Royce[11] and Acte, S.A.[12]

Development of durable and reliable recuperator technology has paralleled and been pushed by the introduction of commercial microturbines in 1996–1997, in conjunction with the initial and continuing phases of a collaboration by Southern California Edison, the U.S. Department of Energy (DOE), and others to study the installation, operation, and maintenance of microturbines to promote distributed power generation.[13,14] Another driver for the development of better recuperators came from the DOE Advanced Microturbine Program in 2000,[15] with the ambitious goal to design and build microturbines with efficiencies of 40% or more. Before 2000, nearly all recuperators were made using 347 stainless steel (Figure 1)[5,16] and generally performed well at temperatures below 1200°F.

More recent research has highlighted the problems that can limit the performance of 347 stainless steel at 1250–1300°F and above, particularly the accelerated attack (AA) caused by moisture-enhanced oxidation at these conditions.[17,18] Generally, larger microturbines with higher efficiency will also increase the operating temperatures and pressures in the recuperator. Focused research on the DOE Advanced Microturbines Program over the last several years has defined and addressed the needs for better metal foils and sheets that can withstand prolonged use at higher temperatures, but which also still remain affordable for recuperator applications.

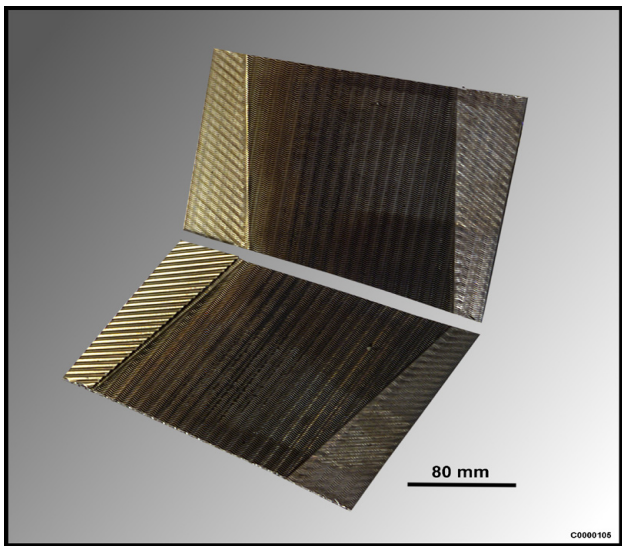

Figure 1. Two PSR air cells from Honeywell recuperator of 347 stainless steel foil, after relatively short-term microturbine exposure. Darker portion (right) has seen maximum temperature and oxidation; lighter side (left), lower temperature and slight heat tint. This indicates temperature gradient across air cell that such components typically have because of counterflows of cool air and hot exhaust. Component showed no evidence of AA.

Approach

Summary of Challenges to Metal Sheet/Foil Recuperators

The first challenge is, of course, manufacturing the desired components, but by far the greatest challenge is long-term operation at elevated temperatures without failure. While the minimum need for recuperators is to survive until scheduled maintenance intervals (5,000 to 10,000 h), the desired lifetime is the same of that of the overall microturbine system, which can range from 40,000 to 80,000 h.[13,15] Both PSR and BPFR air cells are made with high-quality automated and/or continuous manufacturing processes that produce consistent results, and each air cell is pressure checked at room temperature to ensure there is no leakage.[8,9]

In service, several metallurgical effects of high-temperature exposure can degrade recuperator performance prior to the cracking that causes leakage of pressurized air into the exhaust, or the severe deformation that reduces effectiveness. These effects include oxidation, creep, fatigue, and aging-induced precipitation in the matrix and along grain boundaries of the alloy. For 347 stainless steel, such effects are not significant at 1100–1200°F, become concerns at 1200–1250°F, and can be severe at 1300°F and above. Creep can close the exhaust gas passages of a PSR to restrict gas flow, and the heavy ferrous oxide deposits on the surfaces of foils associated with severe AA can reduce thermal conductivity and heat transfer. Oxidation resistance is more an inherent function of alloy composition (Cr and Ni content),[19] while creep and aging behavior can also be affected by metallurgical processing parameters [i.e. grain size, solution annealing (SA) temperature, dispersion, and abundance of various precipitate phases].

The significant differences in manufacturing processes between PSR and BPFR air cells may also affect how each behaves, particularly for service above 1300°F. The PSR air cells are made from folded foils of 347 stainless steel that are 0.003 to 0.005 in. thick and are welded to a similar steel wire or bar (321 or 347 steel) to form the seal at the end. Folding produces from 5–15% cold strain in the foil, depending on the location along the fold. However, the ends of the foil near the weld are crushed flat prior to welding, so they may be cold-worked 30% or more. Relative to SA material (which is usually tested to produce properties data), 20–25% cold-working can enhance the formation of deleterious intermetallic phases (σ, Laves) during aging; 5–15% cold work can cause either accelerated or retarded creep-rates; and 20–50% cold-work would certainly cause recrystallization of the original grain structure into a new fine-grained microstructure, with details that are very sensitive to minor or impurity alloying elements in austenitic stainless steels.[20–22] By contrast, BPFR air cells are welded to seal the ends and then brazed, which removes all prior cold deformation and restores all the materials in the air cell to an SA condition. However, the braze joint and its effects on the bonded stainless steel sheets and foils are an additional and unique factor that needs to be considered for this recuperator. To date, there are no systematic studies or data to address all of these concerns, but data should be accumulated as ongoing studies of turbine-exposed or failed air cells continue, particularly the studies from the ORNL Recuperator Test Facility.[23]

Results

Selection and Evaluation of Advanced Alloys for Recuperators with Higher-Temperature Capability

1. Creep-rupture testing of commercial heat-resistant alloys

Results for recent commercial sheets and foils obtained from commercial materials producers or recuperator manufacturers and creep-rupture tested at 750°C and 100 MPa are shown in Figure 2. Planess PM2000 (an ODS Fe-Cr alloy with aluminum) sheet shows virtually no creep (even at 120 MPa), and alloy 625 (Ni-22Cr-9Mo-3.5Nb) shows very little after 7000–8000 h (both tests are ongoing). Previous work on alloy 625 foil with lab-scale processing at ORNL ruptured after about 4500 h at the same creep conditions, so the commercial sheet is much stronger. Both alloy 625 and PM2000 would have advantages for recuperators in which strain limits, rather than rupture, define lifetime. Alloy 625 is being used for the PSR for the Solar Turbines Mercury 50 industrial turbine engine[7] and for the Ingersoll-Rand BPFR used with the Rolls-Royce WR-21 marine turbine engine.[10] Given the combination of cost and creep resistance, alloy 625 is clearly the most cost-effective at about 3.5–4 times the cost of 347 steel.[9,16] Foils of HR120 (Fe-25Cr-35Ni – Mo,Nb,N) and HR230 (Ni-22Cr-14W-5Co-3Fe-2Mo) (0.003-0.004 in. thick) show much less creep resistance than alloy 625 but are still about ten times better than 347 steel. The effects of grain size/processing on creep resistance at these conditions are shown for HR230 in Figure 3 and HR120 in Figure 4. Thicker products like boiler tubing of HR230 show much more creep resistance than foils,[24] indicating that these foils are below the critical grain size for creep resistance in this alloy (typically 10–20 μm grain size). Processing and microstructural behavior during aging determine such creep behavior, with foils usually seeing somewhat lower processing temperatures and much shorter processing times than plate or tubing products. Given the tubing behavior, it is unlikely that sheet of HR230 would perform as well as alloy 625, and at 8–9 times the cost of 347 steel, HR230 is not a cost-effective choice. By contrast, the creep-rupture resistance of HR120 is similar for foil and bar products (Figure 4), indicating much less

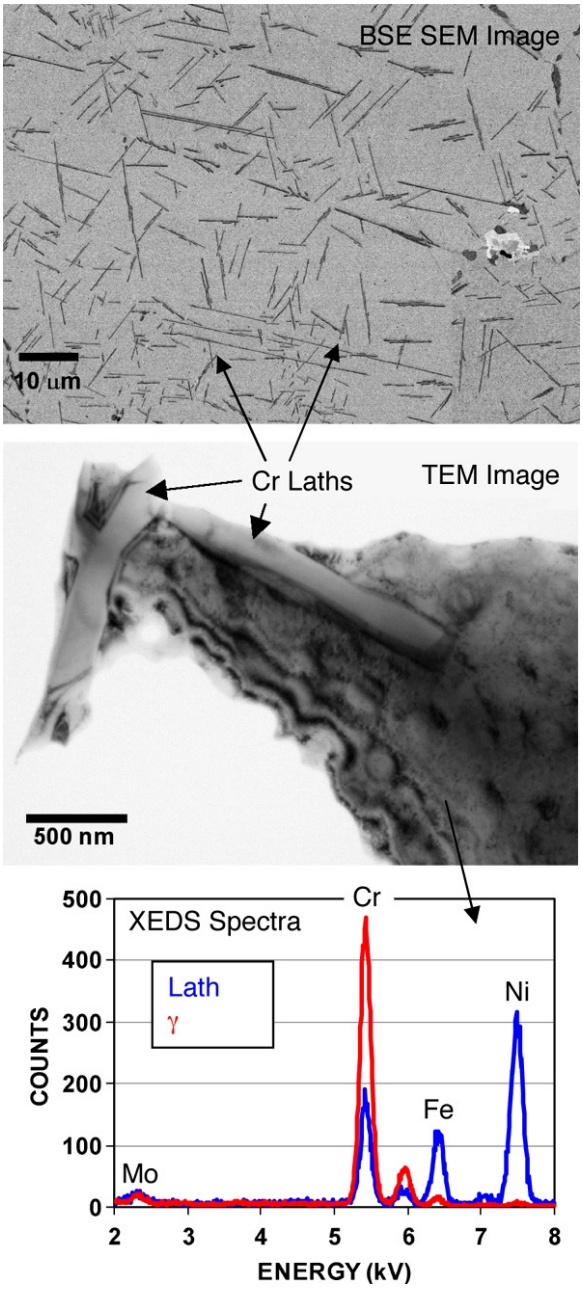

Figure 2. Creep data on commercial sheets and foils tested at 750°C and 100 MPa (except for the PM2000 ODS alloy, tested at 120 MPa) in air at ORNL.

sensitivity to grain size/processing than HR230. However, previous ORNL data on a similar foil showed 2–3 times better creep resistance for the same test conditions,[25,26] so there is clearly a need for more data to better define the typical creep resistance of such foils and their microstructural characteristics. It is likely that HR120 sheet would have similar creep resistance to foil; at about 3.5 times

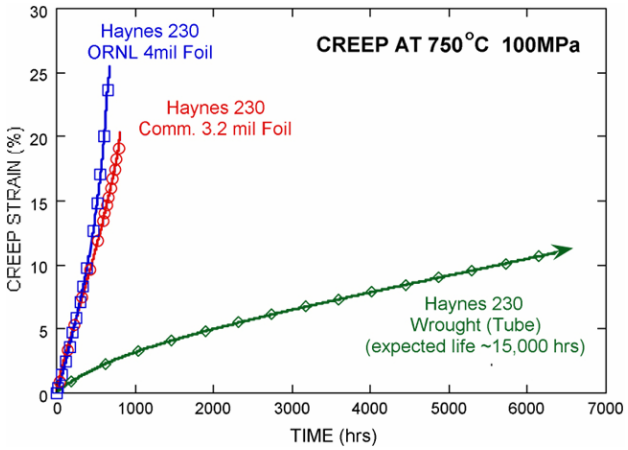

Figure 3. Creep tests of fine-grained foils and coarser-grained tubing of HR230 illustrate fine-grain size effect, which dramatically reduces or eliminates the secondary creep regime, if that grain size is below the critical grain size for creep resistance.

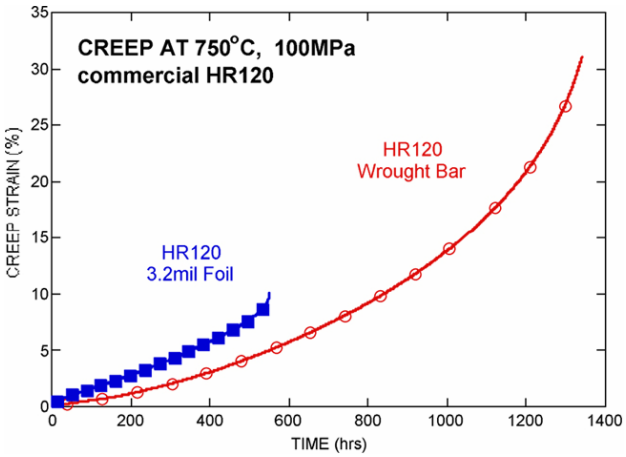

Figure 4. Creep testing of foil and bar of alloy HR 120 shows roughly parallel creep curves, despite significant differences in processing and grain size between these specimens.

the cost of 347 steel, it represents a cost-effective performance upgrade, particularly considering its excellent oxidation resistance.

Creep-rupture testing on this group of alloys was also done at 704°C (1300°F) and 150 MPa because most near-term microturbine recuperators would benefit from reliable materials that can be used at or slightly above this temperature; data are shown in Figure 5. Alloy 625 sheet is very creep-resistant (test is ongoing), while 347 steel foil is very weak. The two foils if HR 120 behaved differently; one was only slightly weaker at 704°C, and the other was several times weaker. [25,27]

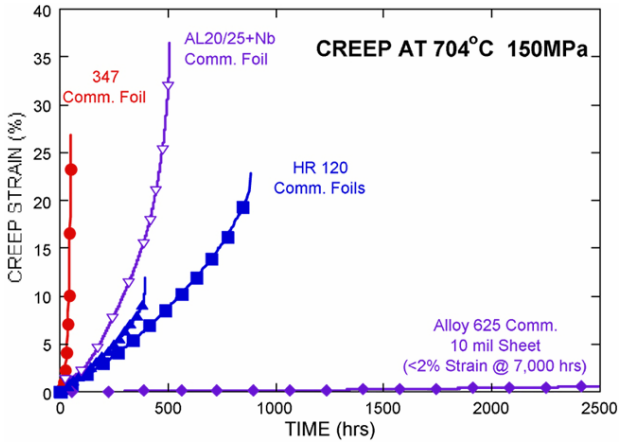

Figure 5. Creep data on commercial sheets and foils tested at 704°C and 150 MPa in air at ORNL. Two different foils of HR120 show similar creep curves, but differences in rupture elongation that directly determine the differences in rupture lifetime.

2. Testing and characterization of new AL20-25+Nb sheets and foils

In 2003-2004, AL introduced a new high-temperature alloy, AL20-25+Nb (Fe-20Cr-25Ni – Mo,Nb,N), which was developed together with Solar Turbines earlier for foil recuperator applications.[6] This alloy is another in a group of improved alloys based on the austenitic stainless alloy composition of Fe-20Cr-25Ni, which includes Nippon Steel's NF709 and Sandvik's 12R72HV for fossil energy boiler tubing with more corrosion resistance and creep strength than 17-14CuMo and 347H stainless steels.[28, 29–31] ORNL had made lab-scale foils, rolled from slit and flattened NF709 boiler tubing, and had done creep and oxidation testing in 2001–2003.[25,27,32] Based on these preliminary results, interest from the microturbine recuperator manufacturers, and potential for pricing between the cost of 347 steel and of alloy 625, ORNL and AL defined a joint project in 2004 to expand commercial foil development for microturbine recuperator manufactures.

Phase I of this project has produced 10- and 15-mil sheets and 4-, 5-, and 8-mil foils in commercial quantities suitable for manufacturing trials of PSR and BPFR recuperator air cells. ORNL is currently performing creep-testing and microstructural analysis on these new foils and sheets. Creep rupture

data for a new foil of AL20-25+Nb creep-rupture tested at 704°C is also shown in Figure 5. The creep resistance of AL20-25+Nb is only slightly less than that of the similar commercial HR120 foil (particularly below 5% strain) and is several times better than that of standard 347 steel, with excellent rupture ductility. Based on these initial data, ORNL and AL will define processing changes that can optimize the creep resistance (similar to the previous joint project on 347 steel) [25,27,33] and then produce limited quantities of selected sheets and foils in a Phase II effort of commercial processing. Coils of foils and sheets of the Phase I material needed for recuperator air cell manufacturing were shipped this year to Ingersoll Rand. Coils of foil needed for recuperator air cell manufacturing by Capstone Turbines will be supplied from Phase II material early next year. ORNL will complete creep testing and microcharacterization of Phase I and II materials next year. Foils of materials from both phases will also be tested in the ORNL Recuperator Test Facility next year.

3. Microstructural analysis of creep-tested foils

Microstructural analysis has been conducted on the gage portions of selected creep-ruptured foil specimens tested at 704 or 750°C, including scanning and analytical electron microscopy (SEM and AEM), to characterize microstructural changes and identify precipitate phase forming during creep. Creep data on these alloys, including 347 steel and alloys HR120, NF709 and 625, have been published previously.[25,27] Figure 6a shows the rapid formation of Fe-Cr σ-phase at grain boundary triple points in standard 347 steel (with a fine 2–5 μm grain size) after only 51.4 h creep at 704°C. Coarser-grained (>20 μm) alloy 625 creep-tested at 750°C for 4510 h has a stable dispersion of Si-Mo-Cr-Ni M_6C particles along the grain boundaries and dense lath/subgrain boundary structure within each grain (Figure 6b). The grains in alloy 625 show no dislocation networks or fine γ' precipitation. Apparently, the fine laths and intergranular precipitation help provide the creep strength observed in alloy 625.

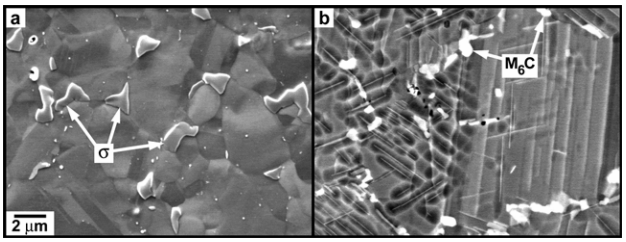

Figure 6. SEM shows (a) rapid formation of Fe-Cr σ-phase at grain boundaries during creep at 704°C and 152 MPa; (b) relatively stable dispersion of Si-Mo-Cr-Ni.

NF709 and HR120 austenitic stainless alloys develop similar grain boundary structures during creep, but they have somewhat different intragranular precipitate structures, as shown in Figure 7. NF709 has a finer grain structure (10–15 μm), a uniform dispersion of mainly Si-Mo-Cr-Ni M_6C, some Cr-rich $M_{23}C_6$ particles along the grain boundaries, and little or no coarse intragranular precipitation after 5015 h of creep. In comparison, the HR120 has a coarser grain structure (30–40 μm) and copious precipitation of $M_{23}C_6$ along the grain boundaries and inside the grains.

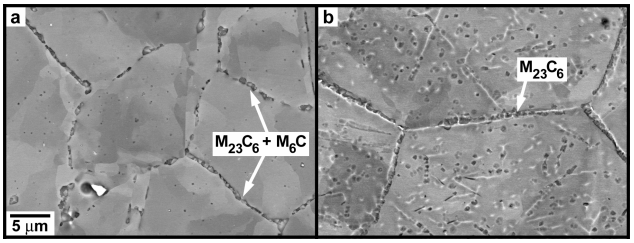

Figure 7. SEM micrographs show precipitation along grain boundaries in foils of (a) alloy NF709 and (b) alloy HR120 (rupture after 3319h), both creep-tested at 750°C and 100 MPa.

Higher-magnification AEM shows both NF709 and HR120 have fine dispersions of NbC precipitates within the grains that formed during creep and in the dislocation networks (Figure 8). The stable carbide strengthening of grain boundaries and matrix provides the creep resistance for both of these alloys.

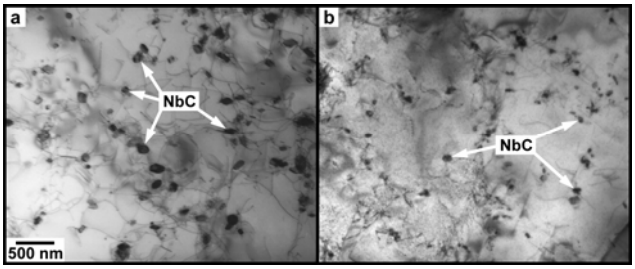

Figure 8. TEM micrographs show fine NbC precipitation within the grains in foils of (a) alloy NF709 (rupture after 5015 h) and (b) alloy HR120 (rupture after 3319 h), both creep-tested at 750°C and 100 MPa.

Conclusions

Alloys 625 and HR120 are commercially available sheet and foil materials that have significantly better oxidation and creep-resistance than standard commercial 347 steel at 650–750°C. Such property differences should directly enhance the performance and temperature capability of recuperators at about 3.5-4 times the cost of 347 steel. The new AL20-25+Nb alloy being commercialized has the potential to offer similar improvements in performance at a lower cost. DOE-sponsored work at ORNL is focused on providing the critical data that enable recuperator manufacturers to take advantage of cost-effective advanced alloys as soon as possible.

References

1. P. L. Lemar and E. A. Kime, eds., "Blackout Creates Local Water Supply Concerns," *DG Monitor*, **3**(5), Resource Dynamics Corp., Vienna, VA, (September/October 2003.)
2. R. R. Judkins, I. Wright, and J. Stringer, eds., "Microturbines are Generating Interest," *Materials and Components in Fossil Energy Applications*, Newsletter No. 143, U.S. Department of Energy and the Electric Power Research Institute, published by Oak Ridge National Laboratory, Oak Ridge, TN (December 1, 1999).
3. M. E. Ward, "Primary Surface Recuperator Durability and Applications," report no. TTS006/395, Solar Turbines, Inc., San Diego, CA, 1995.
4. C. F. McDonald, "Heat Recovery Exchanger Technology for Very Small Gas Turbines," *International Journal of Turbo and Jet Engines*, **13**, 239–261, (1996).
5. C. F. McDonald, "Recuperator Considerations for Future Higher Efficiency Microturbines," *Applied Thermal Engineering*, **23**, 1463–1487 (2003).
6. J. M. Rakowski, C. P. Stinner, M. Lipschutz, and J. P. Montague, "The Use and Performance of Oxidation and Creep-Resistant Stainless Steels in an Exhaust Gas Primary Surface Recuperator Application," ASME paper GT2004-53917, American Society of Mechanical Engineers, New York, 2004.
7. I. Stambler, "Mercury 50 Rated at 4600 kW and 38.5% Efficiency With 5 ppm NO_x," *Gas Turbine World*, 12–16 (February–March 2004).
8. B. Treece, P. Vessa, and R. McKeirnan, "Microturbine Recuperator Manufacturing and Operating Experience," ASME paper GT-2002-30404, American Society of Mechanical Engineers, New York, 2002.
9. J. Kesseli, T. Wolf, J. Nash, and S. Freedman, 2003, "Micro, Industrial, and Advanced Gas Turbines Employing Recuperators," ASME paper GT2003-38938, American Society of Mechanical Engineers, New York, 2003.
10. D. Branch, "The WR-21—From Concept to Reality," pp. 1039–1055 in *Parsons 2003: Engineering Issues in Turbine Machinery, Power Plants and Renewables*, The Institute of Materials, Minerals and Mining, Maney Publishing, London, UK, 2003.
11. J. I. Oswald, D. A. Dawson, and L. A. Clawley, "A New Durable Gas Turbine Recuperator," ASME paper 99-GT-369, American Society of Mechanical Engineers, New York, 1999.
12. H. Antoine and L. Prieels, "The ACTE Spiral Recuperator for Gas Turbine Engines," ASME paper GT2002-30405, American Society of Mechanical Engineers, New York, 2002.
13. S. L. Hamilton, *The Handbook of Microturbine Generators*, PennWell Corp., Tulsa, OK, 2003.
14. V. D. Agular and S. L. Hamilton, "The Best Applications for Microturbines," *Cogeneration and On-Site Power Production*, **5(**4) 101–106 (July–August 2004).
15. *Advanced Microturbine Systems—Program Plan for Fiscal Years 2000–2006*, Office of Power Technologies, Office of Energy Efficiency and Renewable Energy, U.S. Department of Energy, Washington, D.C., March 2000.

16. P. J. Maziasz and R. W. Swindeman, “Selecting and Developing Advanced Alloys for Creep-Resistance for Microturbine Recuperator Applications,” *Journal of Engineering for Gas Turbines and Power*, **125**, 310–315, American Society of Mechanical Engineers (2003).
17. B. A. Pint and J. M. Rakowski, “Effects of Water Vapor on the Oxidation Resistance of Stainless Steels,” paper 00259, presented at Corrosion 2000, NACE-International, Houston, TX, 2000.
18. B. A. Pint, K. L. More, and P. F. Tortorelli, “The Effect of Water Vapor on Oxidation Performance of Alloys Used in Recuperators,” ASME paper GT-2002-30543, American Society of Mechanical Engineers, New York, 2002.
19. B. A. Pint and R. Peraldi, “Factors Affecting Corrosion Resistance of Recuperator Alloys,” ASME paper GT2003-38692, American Society of Mechanical Engineers, New York, 2003.
20. P. J. Maziasz, “Microstructural Stability and Control for Improved Irradiation Resistance and for High-Temperature Strength of Austenitic Stainless Steels,” pp. 116–161 in *MiCon 86: Optimization of Processing, Properties and Service Performance Through Microstructural Control*,” ASTM-STP-979, American Society for Testing and Materials, Philadelphia, 1986.
21. P. J. Maziasz and R. W. Swindeman, “Modified 14Cr-16Ni Stainless Steels With Improved Creep Resistance at 700°C Due to Tailored Precipitate Microstructure,” pp. 283–290 in *Advances in Materials Technology for Fossil Power Plants*, ASM-International, Materials Park, OH, 1987.
22. P. J. Maziasz, et al., “Improved Creep-Resistance of Austenitic Stainless Steel for Compact Gas Turbine Recuperators,” *Materials at High Temperatures*, **16**(4), 207–212 (1999).
23. E. Lara-Curzio, R. Trejo, K. L. More, P. J. Maziasz, and B. A. Pint, “Screening and Evaluation of Materials for Microturbine Recuperators,” ASME paper GT2004-54254, American Society of Mechanical Engineers, New York, 2004.
24. J. P. Shingledecker, R. W. Swindeman, R. L. Klueh, and P. J. Maziasz, “Mechanical Properties and Analysis of Ultra-Supercritical Steam Boiler Materials,” *Proc. 29th International Technical Conference on Coal Utilization & Fuel Systems*, National Energy Technology Laboratory, Morgantown, WV, 2004.
25. P. J. Maziasz, R. W. Swindeman, J. P. Shingledecker, K. L. More, B. A. Pint, E. Lara-Curzio, and N. D. Evans, “Improving High Temperature Performance of Austenitic Stainless Steels for Advanced Microturbine Recuperators,” pp. 1057–1073 in *Parsons 2003: Engineering Issues in Turbine Machinery, Power Plants and Renewables*, The Institute of Materials, Minerals and Mining, Maney Publishing, London, UK, 2003..
26. P. J. Maziasz, B. A. Pint, R. W. Swindeman, K. L. More, and E. Lara-Curzio, “Selection, Development and Testing of Stainless Steels and Alloys for High-Temperature Recuperator Applications,” ASME paper GT-2003-38762, American Society of Mechanical Engineers, New York, 2003.
27. P. J. Maziasz, B. A. Pint, J. P. Shingledecker, K. L. More, D. E. Evans, and E. Lara-Curzio, “Austenitic Stainless Steels and Alloys With Improved High-Temperature Performance for Advanced Microturbine Applications,” ASME paper GT2004-54239, American Society of Mechanical Engineers, New York, 2004.
28. M. Staubli et al., “Materials for Advanced Steam Power Plants: The European COST522 Action,” pp. 305–324 in *Parsons 2003: Engineering Issues in Turbine Machinery, Power Plants and Renewables*, The Institute of Materials, Minerals and Mining, Maney Publishing, London, U K, 2003.
29. M. Kikuchi, M. Sakakibara, Y. Otoguro, H. Mimura, S. Araki, and T. Fujita, “An Austenitic Heat Resisting Steel Tube Developed For Advanced Fossil-Fired Steam Plants,” pp. 267–276 in *High Temperature Alloys, Their Exploitable Potential*, Elsevier Science Publishing, New York, 1987.
30. T. Takahashi et al., “Development of High-Strength 20Cr-25Ni (NF709) Steel for USC Boiler Tubes,” Nippon Steel Technical Report no. 38, Nippon Steel Corp., Tokyo, Japan, July 1988.
31. *Quality and Properties of NF709 Austenitic Stainless Steel for Boiler Turbing Applications*, 1996, Nippon Steel Corp., Revision 1.1, Tokyo, Japan.

32. B. A. Pint and K. L. More, “Stainless Steels with Improved Oxidation Resistance for Recuperators,” ASME paper GT2004-53627, American Society of Mechanical Engineers, New York, 2004.
33. C. Stinner, “Processing to Improve Creep and Stress Rupture Properties of Alloy T347 Foil,” Allegheny-Ludlum Technical Center internal report, Brackenridge, PA, 2003 (available upon request).

Honors and Awards

Phil Maziasz was appointed vice-chair of the ASM Technical Programming Board and vice-chair for the ASM 2004 Materials Solutions Conference and Exposition.

Phil Maziasz served as chair of the ASM and TMS Joint Commission on *Metallurgical and Materials Transactions Journal*.

Phil Maziasz was appointed to the ASM William Hunt Eisenman Award Committee, serves as chair of the Honor and Awards Committee, and is a member of the executive committee of the ASM Oak Ridge Chapter.

Publications/Presentations

P. J. Maziasz, B. A. Pint, J. P. Shingledecker, K. L. More, D. E. Evans, and E. Lara-Curzio, “Austenitic Stainless Steels and Alloys With Improved High-Temperature Performance for Advanced Microturbine Applications,” ASME paper GT2004-54239, American Society of Mechanical Engineers, New York, NY, 2004.

P. J. Maziasz, “Improving High-Temperature Performance of Austenitic Stainless Steels for Advanced Microturbine Recuperators, invited talk at Fuel Cell Energy, Inc., Danbury, CT, November 11, 2003.

P. J. Maziasz, “Highlights of ORNL Efforts to Improve High Temperature Performance of Austenitic Stainless Steels,” invited talk at General Electric Power Systems, Schenectady, NY, March 18, 2004.

P. J. Maziasz, “Austenitic Stainless Steels with Improved High-Temperature Performance for Advanced Microturbine Recuperators,” talk given at ASME Turbo Expo 2004, Vienna, Austria, June 14–17, 2004.

Reliability Evaluation of Microturbine Components

H. T. Lin
Metals and Ceramics Division
Oak Ridge National Laboratory
P.O. Box 2008, MS-6068
Oak Ridge, TN 37831-6068
(865) 576-8857; fax: (865) 475-6098; e-mail: linh@ornl.gov

DOE Technology Program Manager: Debbie Haught
(202) 586-2211; fax: (202) 586-7114; e-mail: Debbie.haught@ee.doe.gov
ORNL Technical Advisor: David Stinton
(865) 574-4556; fax: (865) 241-0411; e-mail: stintondp@ornl.gov

Objectives

- Facilitate the successful implementation of ceramic components in advanced microturbines to increase efficiency and reduce NO_x emissions
- Provide critical insight into how microturbine environments influence the microstructure and the chemistry, and thus the mechanical reliability, of materials

Approach

- Evaluate and document the mechanical properties of very small specimens machined from complex-shaped ceramic components for verification of probabilistic component design and life prediction
- Characterize the evolution and changes in the microstructure and chemistry of silicon nitride grains and secondary phase after exposure to engine environments

Accomplishments

- Characterization of the biaxial mechanical properties of a Norton NT154 Si_3N_4 microturbine rotor showed that the as-processed airfoil samples exhibited 20–40% lower strength than those machined from the hub region.
- Characterization of the biaxial mechanical properties of the United Technologies Research Center (UTRC) Kyocera SN282 Si_3N_4 vane ring showed ~13% lower strength than those tested with a machined surface.
- Evaluation of long-term steam jet tests for Japan AIST environmental barrier coating (EBC) systems showed that Lu-silicates exhibited slower recession rates than other RE-silicates.
- The mechanical property database for the Norton NT154 and the Kennametal SiAlON manufactured under the Task II program has been transferred to UTRC, GE, and Capstone for component design and the life prediction effort.

Future Direction

- Generate a mechanical property database for the Norton NT154 Si_3N_4 for probabilistic microturbine component design and life prediction
- Generate a mechanical property database for NT154 Si_3N_4 microturbine rotors manufactured under optimized processing conditions for component design verification
- Conduct long-term steam jet testing on EBC systems developed by AIST, Japan, under the U.S.-Japan Joint Project to provide insight into the recession mechanisms and the design database for new EBC systems

Introduction

The mechanical properties and reliability of complex-shaped ceramic components (especially thin airfoil sections) play a key role in determining the long-term performance of advanced microturbines. The processing steps in production lines and/or the chemical compositions employed sometimes need to be modified in order to achieve consistent mechanical properties for components. In addition, thin airfoils are often used with as-processed surfaces, which can exhibit microstructures and chemistries different from those in the bulk material and test coupons. These differences influence the long-term mechanical reliability and chemical stability of the materials. There is a critical need to generate a database for complex-shaped ceramic components designed and manufactured for advanced microturbines. The mechanical properties of very small specimens machined from ceramic components (e.g., blades, nozzles, vanes, and rotors) as processed and after engine testing will be evaluated under various controlled environments. This work will allow microturbine companies to verify the mechanical properties of components and apply the database that is generated in advanced probabilistic component design and lifetime prediction methodologies. The work also provides a critical insight into how microturbine environments influence the microstructure and the chemistry, and thus the mechanical performance, of materials.

Approach

Two silicon nitride microturbine components—a rotor and a vane ring, as shown in Figure 1—were acquired from material suppliers and/or end users in as-fabricated condition in order to characterize their mechanical properties and microstructure. Biaxial discs were machined from both the airfoil and hub surfaces by first diamond-core-drilling small cylinders with nominal diameters of 6.0 mm. Each cylinder was then machined only on the back face until the thickness was 0.4–0.5 mm. With this procedure, one face of each specimen always consisted of the as-processed surface of the airfoil.

During testing, the as-processed airfoil surface was loaded in tension, while discs from the hub region were tested such that the 600-grit machined surfaces were in tension. The biaxial flexure strength was measured using a ball-on-ring arrangement.[1,2]

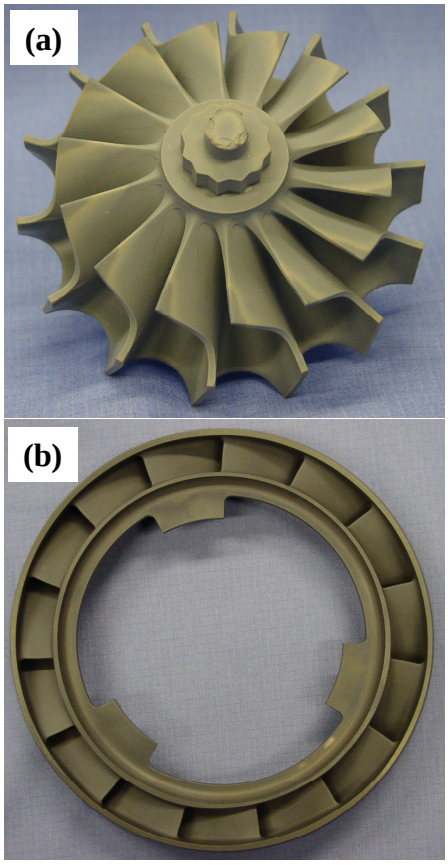

Figure 1. Photos of silicon nitride microturbine components. (a) NT154 silicon nitride rotor, and (b) SN282 silicon nitride integrated vane ring.

The specimen was loaded to failure at a displacement rate of 0.05 mm/s. Both optical and scanning electron microscopy (SEM) techniques were carried out to determine the strength-limiting flaws in the selected biaxial flexure disks sectioned from the airfoil and hub regions.

Dynamic fatigue studies were also conducted to establish a database for candidate silicon nitride ceramics (e.g., Saint-Gobain NT1514 and Kennametal SiAlON) for use by microturbine manufacturing companies in probabilistic component design and life prediction tasks. All test bend bars were longitudinally machined according to the ASTM C1161-2002 standard with 600-grit surface finish, and were tested at temperatures up to 1204°C in air and under stressing rates of 0.003 MPa/s and 30 MPa/s per the ASTM C1368 standard.[3,4] The accumulated strength data were then further analyzed. The strengths for each test set were fit to a two-parameter Weibull

distribution using the program CERAMIC, which uses maximum likelihood estimation as advocated in ASTM C1239.[5–7] Reported results are uncensored because fractography analysis was conducted only to identify strength-limiting flaws for a limited number of samples via optical and scanning electron microscopy.

Results

Microturbine Components

The results for uncensored Weibull strength distribution obtained for samples machined from the airfoil and hub regions of the Norton NT154 silicon nitride microturbine rotor, which is similar to the Ingersoll-Rand SN237 silicon nitride rotor, are shown in Table 1. Note that the airfoil and hub samples were tested with the as-processed and machined surfaces in tension. Some of the hub discs were also tested with the as-processed surface to compare results with those of the finished surface. Mechanical results show that as-processed discs from airfoils exhibited characteristic strengths ~25% lower than the strengths of discs obtained from the hub region, but with similarly low Weibull moduli (i.e., 5.1 and 7.6). The low Weibull moduli could arise from surface defects introduced during the green machining process or during the encapsulated hot-isostatic-pressing. Also, the as-processed discs from airfoils and hub regions exhibited 45% and 26% lower characteristic strength, respectively, than those of as-machined discs obtained from the hub. Note that the machined hub discs exhibited high Weibull moduli similar to those of machined bend bars from production billets (Table 1). The conversion of biaxial strength to flexure strength using the results of machined hub biaxial discs yielded a flexure strength of 744 MPa, which is approximately 10% lower than the characteristic strength (833 MPa) obtained for the machined standard test bend bars from the billets (as shown in Table 1). Previous studies of alumina ceramics have shown that biaxial strength can reliably predict flexure strength, which is consistent with the actual values measured for bend bars machined from the same billets. Thus, bend bars will be machined from the same NT154 hub region to verify the results.

The mechanical results for airfoil samples machined from a UTRC SN282 silicon nitride integral vane ring is shown in Figure 2. Results show that the characteristic strength of as-processed SN282 airfoil samples is ~23% higher that that obtained for the NT154 airfoil samples, but with similar low Weibull moduli. The difference in characteristic strength could arise from differences in the airfoil surface finish and the silicon nitride microstructure. On the other hand, the measured characteristic strength of as-processed biaxial discs is comparable to that obtained from bend bars with as-processed surfaces. Note that the characteristic strength of bend bars with as-processed surfaces is about 13% lower than values obtained from standard test bend bars machined from the same test billets, similar to the results obtained from all of the commercially available silicon nitride ceramics. The lower strength of samples with as-processed surfaces can be attributed to the presence of surface flaws from processing as well as differences in the microstructure and the chemistry of the subsurface region.

Mechanical Database Generation

Figure 3 compares flexure strength as a function of test temperature for NT154 silicon nitride manufactured under the Task II program. In general, the machined NT154 samples, which were processed with and without (baseline) organic binder, exhibited mechanical properties comparable to the NT154 samples developed in the 1990s. The materials processed with organic binder exhibited 10% higher strength than those baseline materials (but with a similar Weibull modulus). However, the NT154 samples with an as-processed surface exhibited a strength degradation of 55–68% plus low Weibull moduli due to the presence of a large surface reaction layer. A proprietary diffusion barrier coating (DBC) has been developed and employed for the sintering of NT154 to prevent the development of a surface reaction layer and thus retain the mechanical strength. A mechanical database for NT154 bend bars sintered with DBC will be generated in FY 2005.

Mechanical properties screening studies for Kennametal SiAlON materials processed with ten different sintering additives were completed in FY 2004. These SiAlON materials were evaluated at room temperature and 1204°C in air under dynamic fatigue conditions. Mechanical results showed that the values of the inert characteristic strength of

Table 1. Summary of uncensored Weibull and strength distributions for biaxial discs machined from Norton NT154 microturbine rotor

Material ID	No. of spmns. tested	Disp. rate (mm/s)	Temp. (°C)	Uncens. Weibull modulus	±95% uncens. Weibull modulus	Uncens. chrctistic strength (MPa)	±95% uncens. chrctstic strength (MPa)
NT154-20B AP-Airfoil	14	0.1	20	5.13	3.40 7.09	527	469 590
NT154-20B AP-Hub	15	0.1	20	7.62	4.99 10.75	706	652 761
NT154-20B AM-Hub	14	0.1	20	24.37	15.50 35.30	960	936 983
NT154 AM-Billet	15	30 MPa/s	20	13.99	8.96 20.23	833	798 867

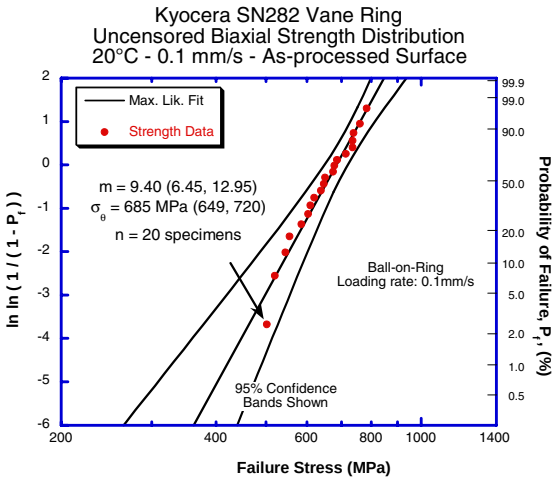

Figure 2. Weibull strength distribution of biaxial strength for discs machined from airfoil of Kyocera SN282 vane ring.

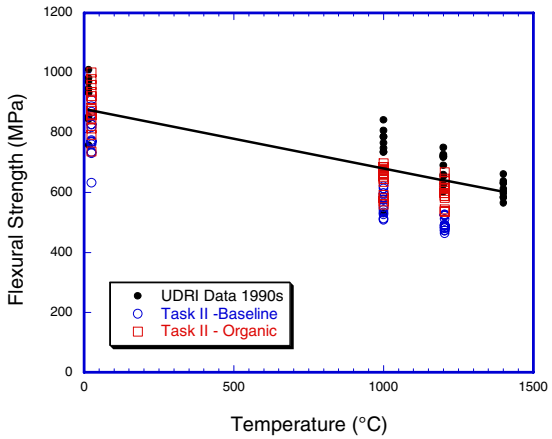

Figure 3. Comparison of flexural strength versus test temperature between NT154 silicon nitride manufactured in microturbine Task II and in 1990s.

SiAlON strongly depend on the size and content of elongated β-SiAlON grains. For instance, the material containing fine α-SiAlON matrix plus a relatively high content of β-SiAlON grains exhibited higher characteristic strengths than materials with more equiaxed microstructure. The effect of β-SiAlON elongated grain size and content on the measured mechanical strength is consistent with results previously reported for silicon nitride ceramics. Two SiAlON materials, ab831 and ab531, have been selected for further processing refinement and more complete mechanical properties database generation. The database generation effort is currently in progress and will be continued in FY 2005.

Conclusions

Biaxial mechanical results show that the samples from the as-processed airfoil region exhibit a characteristic strength that is significantly lower (20–40%) than that obtained for samples from the machined hub. Also, the strength of the machined biaxial discs is greatly inferior to the values obtained from standard test bend bars due to the large differences in surface-to-volume ratio. A key lesson learned in this study is that the actual mechanical properties of complex-shaped ceramic components are often quite different from those determined from standardized simple-shaped test specimens. The application of component characterization can address this limitation by providing a mechanical database

directly from the ceramic components in question for probabilistic component design and life prediction.

References

1. R. Thiruvengadaswamy and R. O. Scattergood, "Biaxial Flexure Testing of Brittle Materials," *Scripta Metall. et Mater.*, **25,** 2529–32 (1991).
2. D. K. Shetty, A. R. Rosenfield, P. McGuire, B. K. Bansal, and W. H. Duckworth, "Biaxial Flexure Tests for Ceramics," *Ceram. Bull.*, **59**(12), 1193–97 (1980).
3. "Standard Test Method for Flexural Strength of Advanced Ceramics at Ambient Temperatures," ASTM C1161, Annual Book of ASTM Standards, Vol. 15.01, American Society for Testing and Materials, West Conshohocken, PA, 2002.
4. "Standard Test Method for Determination of Slow Crack Growth Parameters of Advanced Ceramics by Constant Stress-Rate Flexural Testing at Room Temperatures," ASTM C1368, Annual Book of ASTM Standards, Vol. 15.01, American Society for Testing and Materials, West Conshohocken, PA, 1999.
5. "Life Prediction Methodology for Ceramic Components of Advanced Heat Engines, Phase 1," ORNL/Sub/89-SC674/1-2, Prepared by AlliedSignal Engines, Phoenix, AZ, DOE Office of Transportation Technologies, 1995.
6. "Practice for Reporting Uniaxial Strength Data and Estimating Weibull Distribution Parameters for Advanced Ceramics," ASTM C1239, Annual Book of ASTM Standards, Vol. 15.01, American Society for Testing and Materials, West Conshohocken, PA, 1999.
7. R. L. Barnett, C. L. Connors, P. C. Hermann, and J. R. Wingfield, "Fracture of Brittle Materials under Transient Mechanical and Thermal Loading," AFFDL-TR-66-220, U.S. Air Force Flight Dynamics Laboratory, March 1967.

Honors

H. T. Lin, Chair of Editorial Board, *International Journal of Applied Ceramic Technology*, The American Ceramic Society, 2004–2006.

Publications/Presentations

M. K. Ferber and H. T. Lin, "Characterization of Ceramic Components Exposed in Industrial Gas Turbines," 237–251 in *Ceramic Transactions,* Vol. 142, *Silicon-Based Structural Ceramics for New Millennium* (2003).

P. F. Becher, G. S. Painter, H. T. Lin, and M. K. Ferber, "Tailoring the Composition of Self-Reinforced Silicon Nitride Ceramics to Enhance Mechanical Behavior," in *Fracture Mechanics of Ceramics* (in press).

H. T. Lin and M. K. Ferber, "Characterization of Mechanical Reliability of Silicon Nitride Microturbine Rotors," in *Proceedings of International Symposium on New Frontier of Advanced Si-Based Ceramics and Composites*, June 20–23, 2004, Gyeongju, Korea (in press).

S. M. Zemskova, H. T. Lin, M. K. Feber, and A. J. Haynes, "CVD Mullite Coatings Performance Under High-Temperature High-Load Conditions," same as above (in press).

M. K. Ferber and H. T. Lin, "Mechanical Characterization of Monolithic Ceramics for Gas Turbine Applications," same as above (in press).

S. Ueno**,** D. D. Jayaseelan, N. Kondo, T. Ohji, S. Kanzaki and H.-T. Lin, "Development of EBC for Silicon Nitride," same as above (in press).

H. T. Lin, M. K. Ferber, A. A. Wereszczak, and T. P. Kirkland, "Evaluation Methodology for Mechanical Properties of Complex-Shaped Ceramic Components," presented at 28th International Cocoa Beach Conference and Expo on Advanced Ceramics and Composites, January 25–30, 2004, Cocoa Beach, FL.

H. T. Lin and M. K. Ferber, "Characterization of Mechanical reliability of Silicon Nitride Microturbine Rotors," presented at the International Symposium on New Frontier of Advanced Si-Based Ceramics and Composites, June 20–23, 2004, Gyeongju, Korea.

Development and Characterization of Advanced Materials for Microturbine Applications

M. K. Ferber
Metals and Ceramics Division
Oak Ridge National Laboratory
P.O. Box 2008, MS-6068
Oak Ridge, TN 37831-6068
(865) 576-0818; fax: (865) 574-6098, e-mail: ferbermk@ornl.gov

DOE Technology Development Manager: Debbie Haught
(202) 586-2211; fax: (202) 586-7114; e-mail: debbie.haught@ee.doe.gov
ORNL Technical Advisor: Terry Tiegs
(865) 574-5173; fax: (865) 574-4357; e-mail: tiegstn@ornl.gov

Objectives

- Evaluate the long-term mechanical and chemical stability of advanced materials of interest to the DE Program. This includes (1) structural ceramics, which are being considered for use as hot-section components in microturbines, and (2) thick thermal barrier coatings (TTBCs) being developed for thermal management in combustor liners used in industrial gas turbines.
- Develop and characterize toughened silicon nitrides (TSNs), which utilize beta seeds as the primary toughening mechanism

Approach

- The structural ceramics effort focuses on the development and utilization of test facilities for evaluating the influence of high-pressure and high-temperature water vapor upon the long-term mechanical behavior of monolithic ceramics with environmental barrier coatings.
- The primary focus of the effort on TTBCs is on the evaluation of changes in microstructure and thermal properties arising from long-term aging tests.

Accomplishments

- A unique steam injection system was used to evaluate the effectiveness of new environmental barrier coatings. This system is capable of simulating the surface recession and oxidation found in ceramic components exposed in turbine engine field tests.
- A comprehensive database of the mechanical properties of a number of commercial silicon carbides and silicon nitrides was incorporated into a newly developed software package for implementing reliability analysis. The Integrated Reliability Assessment software allows users to rapidly implement reliability estimates comparing a number of candidate materials.

Future Direction

- Initiate a property assessment of current TSNs. The resulting data will be incorporated into the Integrated Reliability Assessment software.
- Establish and optimize the processing baseline for the first generation of TSNs with high strength and increased toughness combined with controlled thermal expansion.

Introduction

A major metric of the Distributed Energy Program is to develop a portfolio of technologies that show an average 25% increase in efficiency and decrease NO_x emissions less than 0.15 lb/MWhr by 2008. Efficiency increases require either the development of materials with improved high-temperature capability (structural ceramics and ceramic composites) or use of thermal management (protection) strategies (thermal barrier coatings) that allow existing materials to operate at higher temperatures.

The primary objective of this project is to evaluate the long-term mechanical and chemical stability of advanced materials of interest to the DE Program. Currently the project is evaluating structural ceramics being considered for use as hot-section components in microturbines, and TTBCs being developed for thermal management in combustor liners used in industrial gas turbines. The structural ceramics effort focuses on the development and utilization of test facilities for evaluating the influence of high-pressure and high-temperature water vapor upon the long-term mechanical behavior of monolithic ceramics having environmental barrier coatings. In the case of TTBCs, the primary focus is on the evaluation of changes in microstructure and thermal properties arising from long-term aging tests.

A secondary objective of the program is to develop and characterize toughened silicon nitrides (TSN) ceramics with the following attributes:

- fracture toughness 10 $MPa \cdot m^{1/2}$ with fracture strengths >1 GPa;
- high mechanical reliability at low and intermediate temperatures coupled with creep resistance at the desired operating temperatures;
- enhanced resistance to elevated-temperature environmental damage; and
- thermal expansion coefficients tailored to enhance the effectiveness of environmental barrier coating (EBC) systems.

Approach

Structural Ceramics

Over the last 30 years, a number of programs in Russia, Europe, Japan, and the United States have sought to introduce monolithic ceramic components into gas turbines with the goals of increasing efficiency and lowering emissions. High-performance silicon nitride and silicon carbide ceramics typically have been leading candidates for use in these applications. Recent field tests involving silicon nitride vanes and blades have shown that these materials can experience significant recession due to the loss of the normally protective silica scale.

A major issue with these environmental effects is that they are not easily reproduced in the laboratory. Although it is possible to conduct mechanical tests under conditions of high-pressure and high-temperature water vapor, representative gas turbine velocities cannot be readily obtained over the entire gage section. Burner rigs are capable of generating both high pressure and high velocities, but they generally do not have provisions for applying controlled mechanical stresses. Moreover, the high hourly costs for such tests can place limits on the total exposure time that can be achieved.

During this fiscal year, an extensive effort was undertaken to develop and validate a cost-effective method for simulating the effects of recession by incorporating a steam injection system into existing hardware for the testing of standard button-head tensile specimens (see Figure 1).

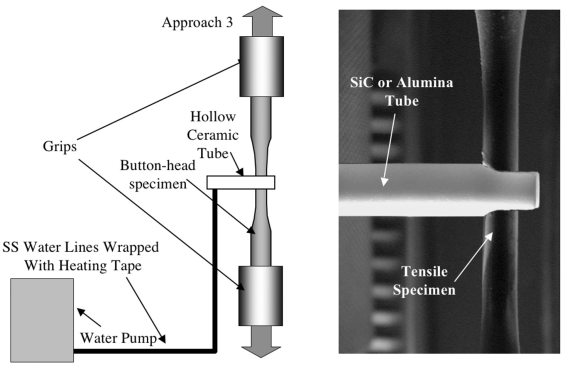

Figure 1. Overview of steam injection system.

Thermal Barrier Coatings

The effort to characterize free-standing TTBCs was conducted in support of Solar Turbines Advanced Industrial Materials Program. These specimens, which were in the form of disks, nominally 10 mm in diameter and 1.17 mm thick, were aged for 100, 500, 1000, 2000 and 5000 h at temperatures of 1800, 1900, 2000, 2100, 2150, 2200, 2250, and 2300°F (982, 1038, 1093, 1149, 1177, 1204, 1232, and 1260°C). Hardness, thermal diffusivity, and

strength were measured for the samples aged for 2000 and 5000 h. The microstructures of selected samples were also evaluated using scanning electron microscopy. The density was measured for all of the aged specimens.

Results

Structural Ceramics

The system shown in Figure 1 was extremely effective in simulating recession and enhanced oxidation. For example, Figure 2 illustrates a SiC specimen after 500 h of exposure in a water-vapor-saturated environment at 1 atm total pressure and 1200°C. The loss of material in the vicinity of the injection tube is indicated by the dotted line. The gage section was subsequently sectioned by cutting along a plane passing through the center of the alumina tube contact point and parallel to the longitudinal axis of the tensile specimen. No oxidation scale was found along the recessed surface of the SiC in the region of direct steam injection. This behavior is quite similar to that observed in engine tests, where the primary effect of the high-pressure, high-velocity water vapor is to cause continued recession of the surface with minimal or no silica scale formation. On the other hand, a thick, highly cracked silica scale was observed along those SiC surfaces located just outside of the injection area. This would be expected, given the lower velocity of steam in this region. Similar thick, nonprotective scales have been observed on the back surfaces of SiC-SiC combustors liners, where the velocity is also quite low.[1]

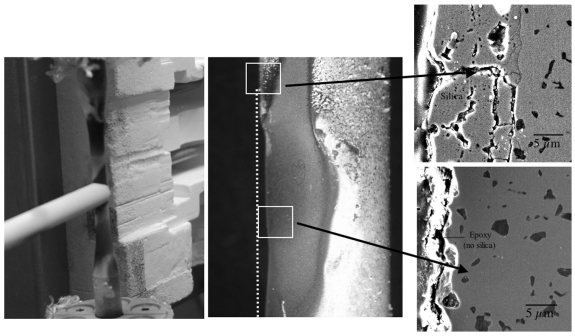

Figure 2. Sintered alpha SiC tensile specimen after 500 h exposure to a saturated-water-vapor environment at 1200°C. The white dotted line on the right shows the position of the original surface prior to testing.

In addition to using the steam injection system for recession measurements, specialized software for reliability analysis of ceramic components was also developed. The assessment of component reliability is a result of the combining of three critical inputs:

- Mechanical properties including strength, slow crack growth, fatigue, and creep for the candidate ceramic are collected.
- Numerical analyses are used to predict the temperature and stress distributions for the component in question.
- Life prediction software is used to combine the experimental mechanical property data with the stress and temperature maps to estimate the probability of survival.

If the resulting value is too low, either the component geometry must be modified to lower the maximum stress, or a better (stronger, more fatigue-resistant) material must be selected.

The implementation of the reliability assessment process faces a number of challenges. The first involves the difficulty of collecting all of the required input data, which are generally scattered among a variety of sources (e.g., the materials suppliers, research laboratories, and universities). A second challenge is that most software reliability algorithms do not have a user-friendly process for varying properties so that reliability can be maximized.

The Integrated Reliability Assessment software (Figure 3) addresses these challenges by first providing an integrated database for a number of commercial silicon carbides and silicon nitrides. As a

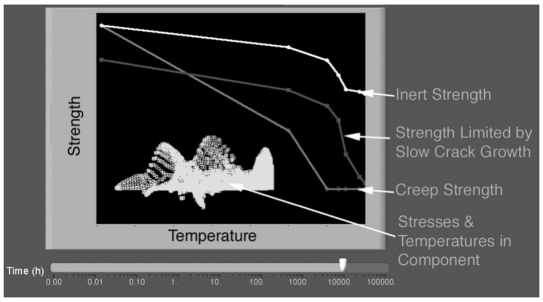

Figure 3. Overview of main screen of the Integrated Reliability Assessment software.

result, the user is able to rapidly implement reliability estimates comparing a number of candidate materials. The results of each analysis are displayed graphically by generating strength/stress vs temperature plots to compare finite element results for a specific component with the strength-temperature data for a number of commercial ceramics from the database. The strength is adjusted to account for both slow crack growth and creep. At the same time, the effect of recession that would occur during turbine operation is simulated by increasing the finite element stresses as the material is lost. The program also allows the user to vary the key properties for a specific material so that component reliability can be maximized. The modified or target properties then become critical input to process optimization studies implemented by the materials suppliers in order meet the lifetime requirements for a given component.

Thermal Barrier Coatings

The normalized thermal conductivity measured at 900°C is plotted as a function of aging time and temperature in Figure 4. At the lowest temperature of 982°C (1800°F), the thermal conductivity was relatively independent of aging time. At 1150ºC (2100°F), the thermal conductivity increased steadily with aging time and was 1.7 times greater than the as-sprayed value after 5000 h. At the highest aging temperature of 1260ºC (2300°F), the thermal conductivity after 500 h was 2.7 times that of the as-sprayed specimen. For times exceeding 500 h, the thermal conductivity did not change appreciably. As shown in Figure 5, the apparent density also increased with aging time and temperature. Subsequent SEM showed that sintering was the primary cause of these density variations. It is also likely that sintering of the TTBC was a major cause of the increase in thermal conductivity.

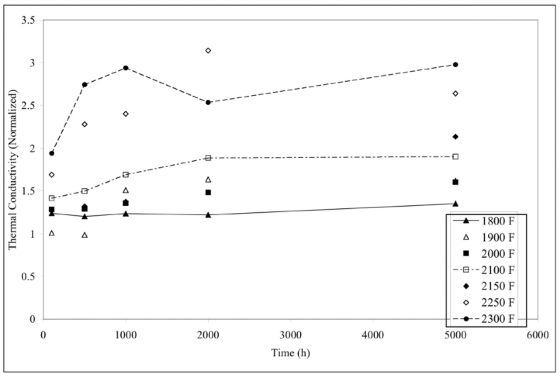

Figure 4. Thermal conductivity (measured at 900°C) as a function of aging temperature and time. The thermal conductivity was normalized by dividing the experimental data by the value measured for the as-sprayed samples.

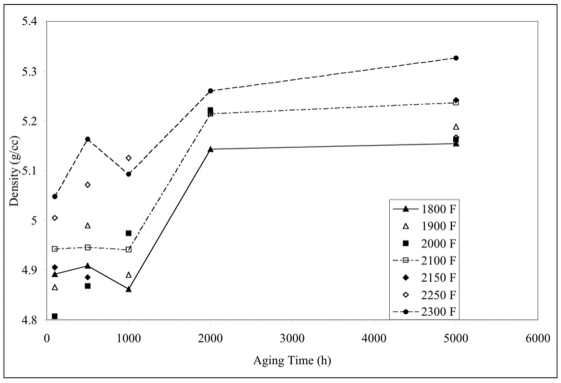

Figure 5. Apparent density as a function of aging temperature and time.

Subsequent dilatometry studies were used to evaluate the extent of sintering occurring during aging. Specifically, thin rectangular freestanding TTBC specimens with a nominal length of 25 mm were aged at 1310°C in commercial dual-rod system (Theta Industries, Inc., 26 Valley Road, Port Washington, NY 11050). The dilation of each specimen was measured relative to that of a single crystal sapphire reference specimen. The resulting data were used to calculate the percentage of relative shrinkage, or $\Delta L/L_o$ (%), as a function of time and temperature. The density of the specimen was also calculated as a function of time by assuming that the shrinkage was isotropic (Figure 6). After each individual run, the monoclinic phase content was determined using Raman spectroscopy.[2] Sintering of the TTBC occurred throughout the total exposure time of 400 h. After about 100 h, the monoclinic phase was detected at room temperature. It is likely that the cubic phase transformed to the tetragonal phase at the test temperature, and upon cooling, the tetragonal transformed to the monoclinic. The large volume change accompanying this latter transformation would be expected to be detrimental to the

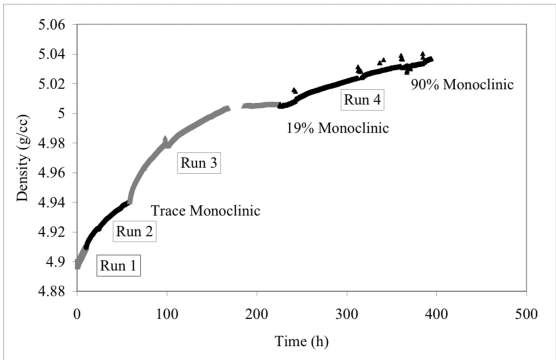

Figure 6. Density as calculated from dilatometry data as a function of aging time at 1310°C. The phase content was determined from piezospectroscopy measurements.

adherence of the TTBC if it were deposited on a metallic substrate.

Conclusions

The use of direct steam injection onto the gage section of a button-head tensile specimen was found to be a cost-effective method of simulating the oxidation and recession behaviors of non-oxide ceramics observed in actual field tests. For example, in the region of direct steam impingement, the substrate surfaces experience significant recession consistent with the relatively high velocity. Furthermore the microstructures of the recessed surfaces were identical to those observed in ceramic vanes used in actual field tests. Outside of the impingement region, the lower steam velocity resulted in the formation of a thick, nonprotective scale.

In the case of the thermal barrier coatings, dilatometry measurements showed that sintering was active at 1310°C. For times exceeding 100 h, zirconia underwent a phase transformation that led to the formation of the monoclinic phase at room temperature.

References

1. M. K. Ferber, H. T. Lin, and J. Keiser, "Oxidation Behavior of Non-Oxide Ceramics in a High-Pressure, High-Temperature Steam Environment," in *Mechanical, Thermal and Environmental Testing and Performance of Ceramic Composites and Components*, *ASTM STP 1392*, ed. M. G. Jenkins, E. Lara-Curzio and S. T. Gonczy, American Society for Testing and Materials, West Conshohocken, PA, 2000.
2. M. J. Lance, J. A. Haynes, M. K. Ferber, and W. R. Cannon, "Monoclinic Zirconia Distributions in Plasma Sprayed Thermal Barrier Coatings," *J. Therm. Spray Technol.* **9(**1), 68–72 (2000).

Honors/Awards/Patents

M. K. Ferber served on the International Advisory Committee of the International Symposium on New Frontiers on Advanced Si-Based Ceramics and Composites.

Publications/Presentations

M. K. Ferber and H. T. Lin, "Mechanical Characterization of Monolithic Ceramics for Gas Turbine Applications," accepted for publication in *Proceedings of the International Symposium on New Frontiers on Advanced Si-Based Ceramics and Composites,* Trans Tech Publications Ltd., 2004 (Invited).

G. Ojard, M. Ferber, and K. Johnson, "Characterization of Si_3N_4 Bars Extracted from Various Regions of a Billet by Resonance and Flex Testing," to be published in the *Proceedings of the 28th International Cocoa Beach Conference and Exposition on Advanced Ceramics and Composites*, 2004.

Reliability Analysis of Microturbine Components

Stephen F. Duffy and Eric H. Baker
Connecticut Reserve Technologies, LLC
Stow, Ohio 44224
(330) 678-7328; e-mail:sduffy@crtechnologies.com, baker@crtechnologies.com

DOE Technology Development Manager: Debbie Haught
(202) 586-2211; fax: (202) 586-7114; e-mail: debbie.haught@ee.doe.gov
ORNL Technical Advisor: Matt Ferber
(865) 576-0818; fax: (865) 574-6098; e-mail: ferbermk@ornl.gov

Objectives

- Develop characteristic strength Weibull modulus "maps" for both surface- and volume-distributed flaws that limit strength in ASTM C1161B and ASTM C1161C bend bars and ASTM C1273 button-head tensile specimen geometries
- Update CARES and WeibPar algorithms and provide to participants of the DE Program

Approach

- Create a capability within the CARES algorithm that allows an end user to output (unitless) area or volume (or both) loading factors (k_A and k_V, respectively) as a function of Weibull modulus
- Create a capability within the CARES algorithm to estimate "allowable" effective stress in a component when a specific failure probability is known
- Update the CARES algorithm so that it interfaces with ANSYS 8.0 and implement an edge failure mode

Accomplishments

- CRT has developed the ability to compute effective area, effective volumes, and confidence bounds on reliability prediction using the CARES algorithm and the WeibPar software for arbitrary component geometries.
- CRT is continuing to develop and enhance methods to determine Weibull distribution metrics for complex-shaped microturbine rotors.

Future Direction

- Create a capability to pool censored data and to determine confidence bounds about pooled censored data
- Create a capability to determine confidence bounds about the predicted reliability of a component

Introduction

Conceptually, distributed power generators in the form of microturbines provide more fuel-flexible systems near the point of energy consumption. Localized distributed generation will avoid transmission and distribution power losses. Barriers to distributed energy resources are being addressed by the Distributed Energy (DE) Program of the U.S. Department of Energy (DOE). Advanced structural ceramics, such as silicon nitride, are required to enable microturbines to operate at higher temperatures that translate into fuel savings and emissions reductions.

Ceramics exhibit significant scatter in tensile strength; thus, probabilistic design approaches must be utilized. Two software algorithms have been developed as design aids for the engineer designing components fabricated from ceramics: the CARES algorithm (originally developed at the NASA Glenn Research Center) and CRT's WeibPar algorithm. These algorithms were upgraded under the DE Program to reverse-engineer material requirements using a turbine blade analysis developed for the Ingersoll-Rand (IR) microturbine.

The strength of silicon nitrides is limited by the presence of flaws that result from processing. Various surfaces of a component may see different treatments—e.g., as processed surfaces in comparison to polished surfaces. Accounting for the different surface treatments and the statistical strength distributions associated with each treated surface will lead to more accurate predictions of expected component life, expressed as component reliability as a function of time.

Approach

Material Characterization Maps

The approach has been to define and implement a method that establishes Weibull distribution metrics for silicon nitride vendors based on a relevant component. Service stress states from the various treated surfaces of a rotor blade are combined with stipulated component reliability in order to develop material performance curves. These curves are then scaled to standard ceramic test coupons (e.g., bend bar specimens), making component requirements transparent to material vendors.

Through the use of ANSYS Parametric Design Language (APDL), surfaces of a rotor component with a specified finish (as-fired, ground, etc.) are identified. Using APDL the ANSYS results file is queried and stresses are mapped to the relevant element surfaces. With the surface information (geometry and stress state) the WeibPar algorithm runs CARES to compute the Weibull parameters that correspond to the component reliability stipulated a priori.

This design approach allows changes and improvements in system requirements to take place in parallel with enhancements in material properties. In the past this was typically a serial process where system engineering would follow improvements in ceramic materials. Material characterization maps can be generated for a given component under specified operating conditions. This information can now influence the goals of a ceramic materials development program.

Reliability Software Enhancements

CRT has also developed the ability to compute effective area and effective volumes using the CARES algorithm and the WeibPar software for arbitrary component geometries. With this ability WeibPar is able to generate confidence bounds on component probability of failure (or reliability) using bootstrap methods. Bootstrap methods characterize uncertainty in estimates that arise from random sampling error, i.e., errors due to testing a finite number of test specimens that represent an assumed infinite sample population. As the term "bootstrap" implies, this type of method is a resampling technique. The original data set used to estimate Weibull parameters is resampled using numerical simulation and reevaluated many times over. Each simulated data set is generated such that the number of sample points matches the original finite number of test specimens.

In the parametric bootstrap technique implemented here, an assumed distribution is utilized—in this case, the two-parameter Weibull distribution. In addition, maximum likelihood estimators are employed, since this method has been shown to be the most efficient. When combined with the component's effective volume or effective area, the method is capable of characterizing confidence bounds as well as bias associated with estimates of the maxi-

mum strength of a component and the component probability of failure. We focus on the latter in this effort. Thus, a step-by-step methodology was developed that provides confidence bounds on component reliability through bootstrap techniques.

Results

Material Characterization Maps

The finite element model of the complex-shaped rotor consists of a 1/16 slice of the turbine blades and is modeled with 672 SOLID45 elements and 22,695 SOLID95 elements. Figure 1 depicts the principal stress solution at 38 seconds into the load history.

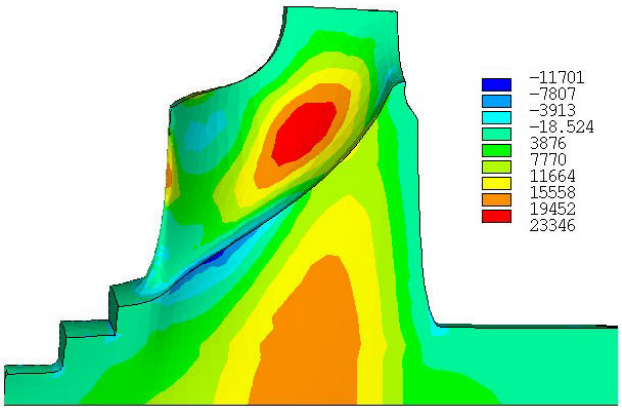

Figure 1. Principal stress plot.

The CARES program treats all the volume elements as one group of 23,367 elements because both groups were assigned the same material properties in the finite element model. The volume reliability results are not detailed in this report, since the primary focus is surface reliability.

In order to calculate surface reliability the volume elements with free surfaces are identified by a revised CARES surface macro. This macro was extensively modified for this particular model because the nodes and elements were decoupled from the solid geometry. The surfaces of interest in this model are the as-fired surfaces and the surfaces that have been ground or polished. The relative locations of these surfaces are depicted in Figure 2.

The types and number of elements associated with each surface can be found in Table 1. Figure 3 highlights the as-fired surface with blue elements and the ground surface as the red and green elements. Although the red and green elements are both ground surfaces, they have been differentiated here because they are generated from different underlying volume elements.

Table 2 indicates the relative surface area of each element group as well as the maximum stress within that group. The blue surface (MatID 103) has the largest surface as well as the highest stress. As a result, this surface dominates the component design.

WeibPar and CARES were utilized to back-calculate Weibull material strength parameters given a particular failure rate. Figure 4 depicts the material characterization maps for the rotor.

The material strength parameters are then converted to specimen-specific characteristic strength parameters. The Mil-handbook B bend specimen was utilized for this case study. Figure 5 depicts the specimen-specific characteristic strength parameters for the various failure rates.

Reliability Software Enhancements

As indicated above, CRT has developed an ability to compute bounds on component reliability using bootstrap techniques. In an upcoming report CRT will provide figures similar to those depicted in Figures 6 and 7 relative to the IR rotor. In Figure 6 a relationship has been established between the effective area of a component and the Weibull modulus of the material used to fabricate the component.

Figure 7 depicts the bounds on component reliability based on the size of the data set used to generate the Weibull parameters and the information in Figure 3. The blue diamond is the component probability of failure given the biased maximum likelihood Weibull parameters. The extreme two data points (red circles) are the 5% and 95% confidence bounds. One can be 90% certain that the actual component reliability falls between these two points. The open blue circle is the mean probability of failure. This point is the unbiased probability of failure.

Conclusions

A method of generating material-specific and specimen-specific strength characterization maps was developed and applied to the case study of the Ingersoll-Rand gas turbine rotor. The WeibPar and CARES algorithms were updated to automate the generation of these characterization maps. Additionally, component reliability confidence bounds via

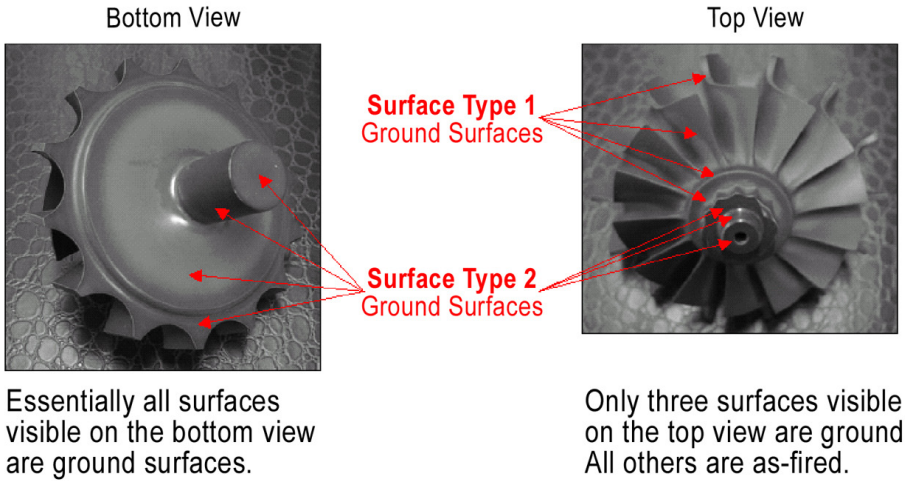

Figure 2. Ground and as-fired surfaces on the rotor.

Table 1. Identified surfaces for CARES

MatID	Color in Fig. 3	Surface type	No. of surface elements	Volume element type
101	Green	Ground	84	SOLID 45
102	Red	Ground	790	SOLID 95
103	Blue	As-fired	3,374	SOLID 95

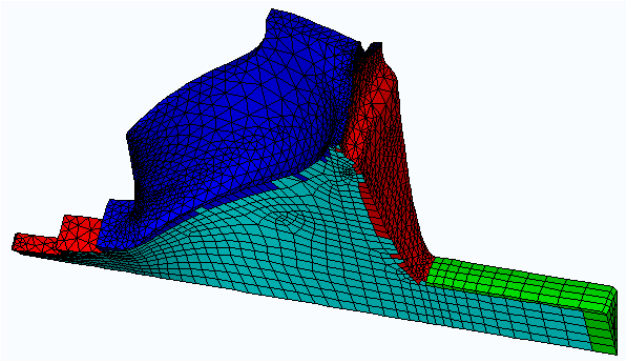

Figure 3. Identified surfaces for CARES.

Table 2. Surface principal stress results

MatID	Area	Max stress	Element no.
101	0.2256	357	143
102	0.7241	1,519	18983
103	2.3253	22,925	10765

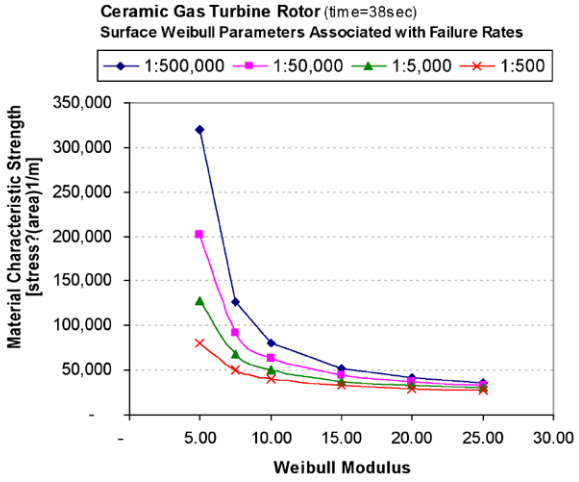

Figure 4. Weibull material strength parameters for various failure rates.

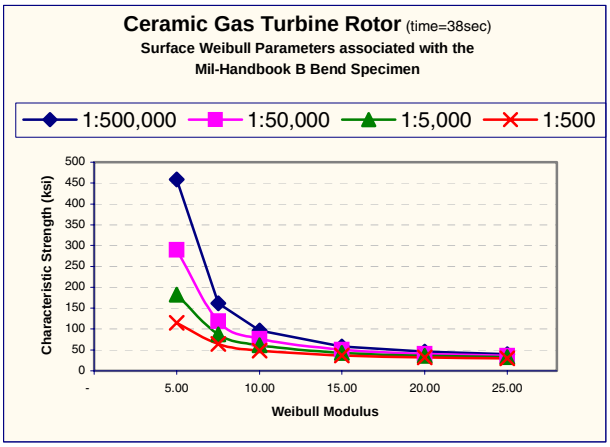

Figure 5. Weibull characteristic parameters for a four-point flexure specimen.

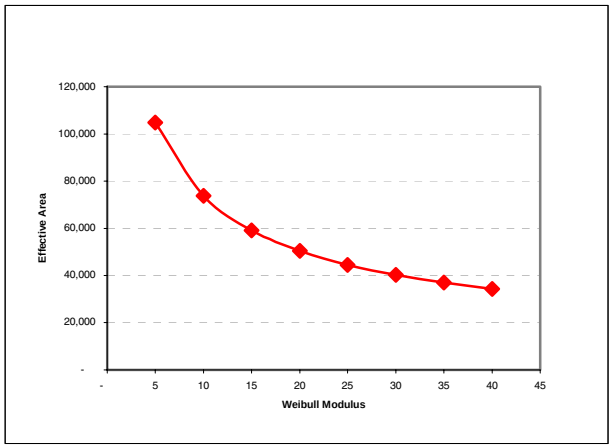

Figure 6. Component effective area as a function of Weibull modulus.

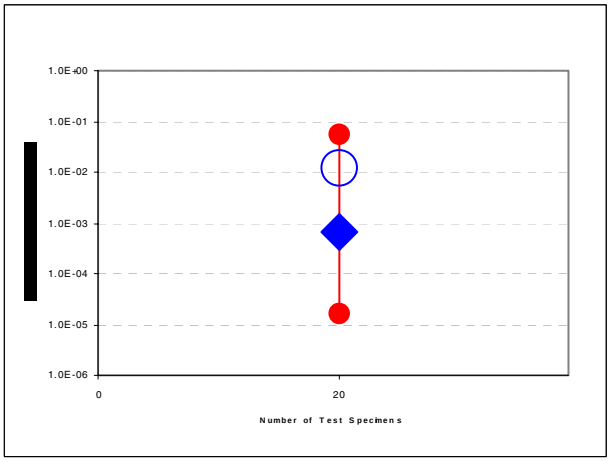

Figure 7. Confidence bounds on component reliability.

the bootstrap technique were added to WeibPar and CARES.

Presentations

S. F. Duffy, E. Baker, J. Kesseli, A. Wereszczak, and C. Johnson, "Weibull Strength Parameter Requirements for Si_3N_4 Turbine Rotor Reliability," presented at the Environmental Barriers Coatings Workshop, Nashville, TN, November 18–19, 2003.

S. F. Duffy, L. A. Janosik, A. A. Wereszczak, B. Schenk, A. Suzuki, J. Lamon, and D. J. Thomas, "Life Prediction of Structural Components," presented at the 28th Annual Cocoa Beach Conference and Exposition on Advanced Ceramics and Composites Ceramics and Components in Energy Conversion Systems, Cocoa Beach, FL, January 28, 2004.

NDE Technology Development for Microturbines

William A. Ellingson
Energy Technology Division
Argonne National Laboratory
Argonne, IL 60439-4838
(630) 252-5068, e-mail: ellingson@anl.gov

DOE Technology Development Manager: Debbie Haught
(202) 586-2211 ;fax: (202) 586-7114 ; e-mal : debbie.haught@ee.doe.gov
ORNL Technical Advisor: D. P. Stinton
(865) 574-4556; fax: (865) 241-0411; e-mail:stintondp@ornl.gov

Objective

- Develop low-cost, high-speed nondestructive characterization (NDC) technologies for rejecting defective monolithic ceramic components during processing to improve yields and reduce component cost.
- Develop reliable NDC methods to evaluate the condition of environmental barrier coatings (EBCs) for monolithic ceramics or composites.

Approach

- Work directly with industrial suppliers of monolithic ceramics and EBCs to establish defect types of primary concern and develop appropriate NDC methods for them.
- Work with end users of advanced materials, namely the gas turbine industry, to identify barriers related to implementing the technologies.

Accomplishments

- Using data from NDC of EBCs on ceramic composites, revealed that NDC data corresponded exactly to spallation patterns observed in field tests of engine components.
- Used data from application of NDC to reject ceramic composite components prior to insertion in engines, thereby mitigating damage to the engine if the composites had failed in service.
- Used data from NDC to assess condition of gas turbine components coated with EBCs.
- Demonstrated laser-based NDC to detect various as-machined surface conditions on monolithic ceramics.

Future Direction

- Quantify the assessment of as-machined surfaces of monolithic ceramic components with an emphasis on relating these data to strength of the materials.
- Transfer NDC technologies to industry.
- Complete development of an automated feature software package for 3-dimensional (3D) X-ray computed tomographic image data sets.

Introduction

The use of advanced ceramic materials in microturbines and industrial gas turbines enables higher operating temperatures and thus greater efficiency. These materials include low-cost monolithic ceramics for hot-section components of microturbines or industrial gas turbines and EBCs for monolithic ceramics or ceramic matrix composites. Given the increased reliance on ceramic components and coatings, it is necessary to have a method for nondestructively evaluating the condition of the component to avoid costly, sometimes catastrophic failures. Critical defects that must be detected include internal voids and cracks in monolithic ceramic components; surface and near-subsurface features such as cracks and creep damage in monolithics; and prespall, impact damage, and overall degradation of EBCs. Several nondestructive evaluation techniques are being investigated for inspection of monolithic ceramic components and EBC coatings on both monolithic and ceramic matrix composite substrates. The ceramic materials used thus far are optically translucent. Thus proper application of an optical method—such as elastic optical scattering, developed at Argonne National Laboratory (ANL), or OCT—is a useful tool for investigating the surface and near- subsurface condition of monolithic components and EBCs. A specific issue of concern is as-produced surface finish. Elastic optical scattering can assess this condition. For detection of internal cracks and voids, volumetric X-ray computed tomography (CT) is used. These techniques can be automated by using automated feature recognition software.

Approach

High-Resolution X-ray CT

For monolithic ceramics, development of nondestructive evaluation technology is a collaborative effort with materials suppliers to produce low-cost ceramic components for advanced microturbines and industrial gas turbines. NDE technologies under development include high-speed, high-definition 3D X-ray CT for detection of internal voids or cracks within full-sized monolithic ceramic components. A schematic diagram of the ANL X-ray CT system is shown in Figure 1. The system uses advanced CMOS and amorphous silicon detector technology in the form of linear or area detectors.

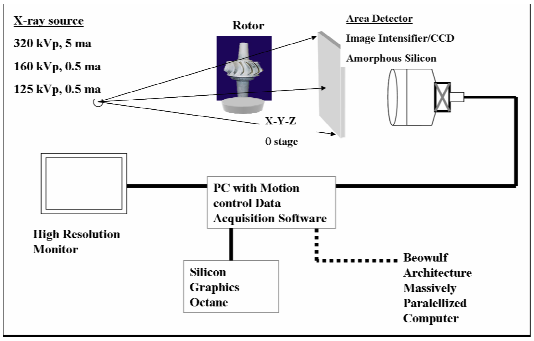

Figure 1. Schematic of ANL X-ray CT system.

Three detectors can be used interchangeably—a 40× 40 cm flat-panel area detector with 400-µm square pixels, a 40×40-cm flat-panel area detector with 200-µm square pixels, or a 45-cm linear detector with 80-µm square pixels. Multiple X-ray sources are also used interchangeably. The most powerful source operates at 420 kV, which is approximately 3–4 times the energy of a medical CT system. The combination of source and detector is chosen so as to optimize the resolution of the system, data acquisition time, and attenuation of the system for a particular material.

Data acquired from the X-ray CT system must be reconstructed using a complex, computation-intensive, mathematical algorithm to produce cross-sectional images or 3D volume renderings of the object under investigation. The time required to complete this reconstruction has been a limiting drawback to the widespread application of X-ray CT as a production evaluation tool. Recent efforts have drastically reduced the reconstruction time. A 50-node Beowulf cluster has been implemented to perform the reconstruction calculation. The cluster consists of 50 2.8-GHz Intel Pentium 4 processors connected in a local area network (LAN) via Ethernet. Special libraries called the Message Passing Interface (MPI) were developed by a consortium of academic and industrial research partners led by ANL. The MPI allows data and instructions to be communicated among the 50 nodes, thus creating a massively parallelized computing system with the capabilities of a supercomputer at a fraction of the cost. Software is under development that will allow automated

detection of defects and features that could cause components to fail.

Elastic Optical Scattering

Elastic optical scattering uses polarized laser light to probe the surface and near-surface of monolithic ceramic components and EBCs. The optical translucency of the ceramic materials used allows the laser to penetrate the surface of the component and scatter from subsurface defects or the EBC/substrate interface. A portion of the light transmitted at the air/ceramic interface changes polarization state, while light reflected from that interface does not change polarization states. This allows light reflected from the surface to be separated from light that penetrates the surface and is backscattered by subsurface features. A change in the distribution of the backscattered light also occurs when a subsurface defect is present. These two principles, illustrated in Figure 2 and discussed in more detail in refs. 1–4, provide the capability to monitor surface condition, detect near-subsurface defects, and monitor the evolution of the EBC/ceramic or EBC/ceramic matrix composite interface to detect defects such as prespall, subsurface cracks, and coating degradation. A system developed at ANL (Figure 3) uses polarized optics and two optical detectors to take advantage of the principles illustrated in Figure 2.

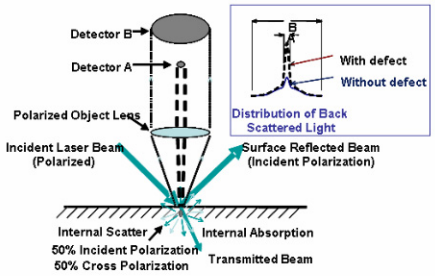

Figure 2. Illustration of physics involved in elastic optical scattering inspection of ceramic components and coatings.

Optical Coherence Tomography

A second optical technique useful for investigating ceramic components and coatings, OCT, is based on a Michelson interferometer.[5] A basic block diagram of the ANL OCT system is shown in Figure 4.

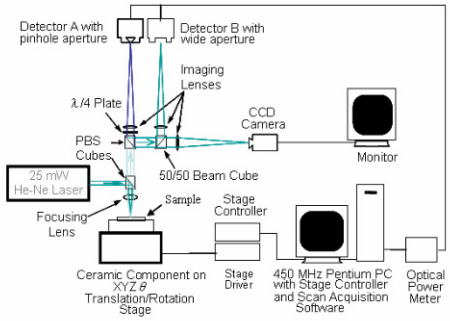

Figure 3. Schematic diagram of elastic optical scattering system.

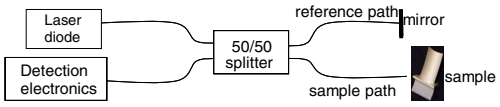

Figure 4. Block diagram of basic elements in OCT system.

Light emitted from a 10-mW superluminecent light emitting diode at a wavelength of 1310 nm is split into two fiber optic cables—a reference path and a sample path. Light in the reference path is reflected from a fixed-plane mirror, while light from the sample path is reflected from the surface and subsurface features of the ceramic sample. The reflected light from the sample path travels a distance that closely matches the distance traveled by the light in the reference path; this constraint incorporates depth resolution into the technique. Thus data can be obtained from a cross-sectional plane perpendicular or parallel to the surface of the sample.

Results

High-Resolution X-ray CT

A typical 2D cross-section of a ceramic rotor blank with an internal crack is shown in Figure 5. This image was obtained from a 112-mm-diameter unbladed gelcast Si3N4 AS800 rotor (Figure 6). Images such as Figure 5 were reconstructed using the Beowulf cluster described in the previous section. A plot of the reconstruction time for N nodes (up to 18) is shown in Figure 7. The dashed line on the plot indicates the reconstruction time required for the same data set using a single PC workstation.

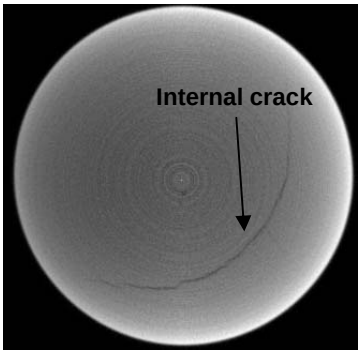

Figure 5. Typical X-ray CT 2D cross-section. X-ray CT investigation reveals an internal crack.

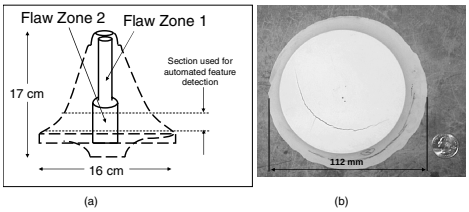

Figure 6. Description of a typical sample investigated with X-ray CT system.

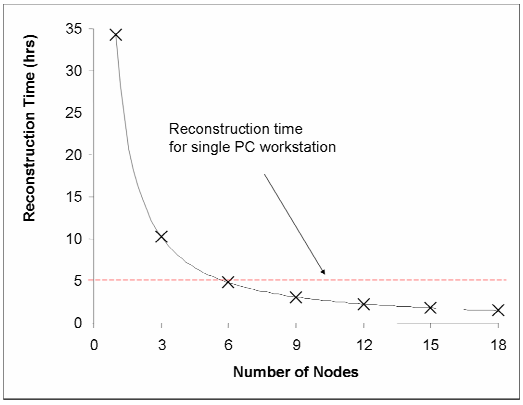

Figure 7. Effect of number of nodes in Beowulf cluster on reconstruction time.

Thus using almost a third of the cluster reduces reconstruction times by a factor of approximately 5. Use of more nodes provides incremental improvement in the reconstruction time.

Advanced digital image processing techniques can then be applied to the reconstructed data for feature extraction and automated processing of the images. Edge detection routines were applied to the image shown in Figure 5. The resulting processed image from the Canny edge detector is shown in Figure 8. The method could not completely resolve the defect from the image; thus additional efforts are focusing on additional processing methods that can be applied to increase the robustness of detection.

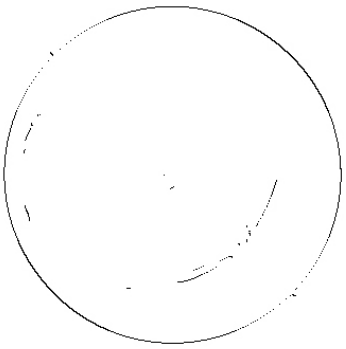

Figure 8. Example of automated feature detection—the edges of the X-ray CT reconstruction image in Figure 5 determined by the Canny method.

Elastic Optical Scattering

The elastic optical scattering technique has been used to investigate EBC coatings on monolithic and composite ceramic substrates. A BSAS EBC on an SiC/SiC substrate (Figure 9) was investigated using the elastic optical scattering technique. This sample had previously been exposed to high temperatures, and a portion of the EBC coating had spalled. The approximate area that was investigated is also shown in Figure 9.

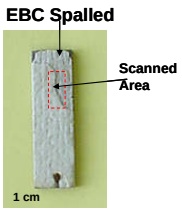

Figure 9. Photograph of BSAS EBC on SiC/SiC sample with EBC partially spalled.

The resulting laser backscatter data, acquired with 10-μm resolution at a wavelength of 633 nm, are shown in Figure 10. The large image was obtained using the ratio of the measurement of detector B to the measurement of detector A. A portion of this image (see inset) was enhanced to increase the contrast, revealing subsurface cracks present in

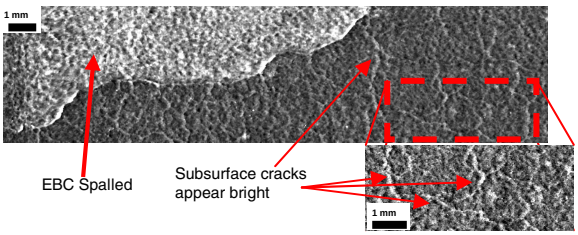

Figure 10. Elastic optical scattering data from BSAS EBC on SiC/SiC substrate with EBC partially spalled.

the intact EBC coating. These cracks appear brighter than the surrounding regions without any defects present.

The laser backscatter technique was also used to investigate EBCs on monolithic ceramic substrates. A series of four Si_3N_4 vanes with tantalum oxide EBC is shown in Figure 11. As indicated in the figure, each of these vanes has been exposed to a number of hours at high temperature.

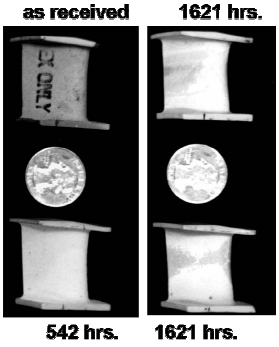

Figure 11. Photographs of Si3N4 vanes with tantalum oxide EBC investigated by elastic optical scattering.

One of the vanes that was exposed to temperature for 1621 hours was sectioned and polished to obtain a cross-sectional micrograph. The suction side of the vane was scanned with the elastic optical scattering technique. A 1D plot of the normalized gray-scale values in this image was compared with the cross-sectional micrograph. This comparison is shown in Figure 12.

The correlation shown in Figure 12 indicates changes in EBC thickness are reflected in the elastic optical scattering data. Also, the extreme roughness of the area between approximately 11 and 16 mm from the top platform is reflected in the elastic optical scattering data.

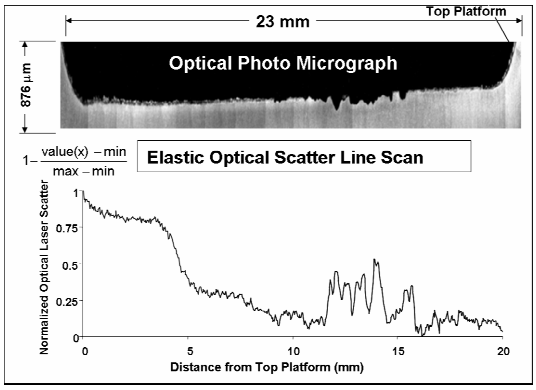

Figure 12. Correlation of EBC thickness to elastic optical scattering data.

Optical Coherence Tomography

The main advantage of OCT compared with elastic optical scattering is that it is capable of resolving not only the spatial size of a defect but also the depth of the defect to within the resolution limits of the system. (For the ANL OCT system this is approximately 20 µm). The same BSAS EBC sample described above and investigated with the laser backscatter technique was investigated by OCT. The initial investigation of this sample produced the image shown in Figure 13. The image shows the region in which the EBC is spalled; however, it does not reveal any information about the subsurface condition of the coating.

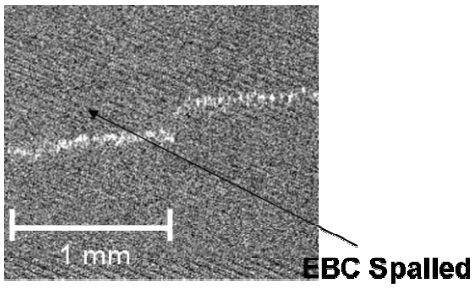

Figure 13. Original OCT vertical cross-section image from a BSAS EBC on SiC/SiC sample.

Since it is imperative that the technique provide information about the subsurface condition of the coating, several enhancements were made to the OCT system. They included improving the signal-to-noise ratio by upgrading the detector and detection amplifier gain, adding mechanical stability and increased alignment accuracy, and increasing the optical input power to 10 mW. The same

sample was again investigated. The vertical cross-section image from this sample after the system upgrades is shown in Figure 14.

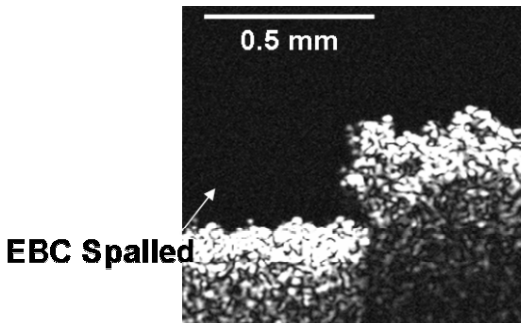

Figure 14. OCT vertical cross-section image from a BSAS EBC on SiC/SiC sample after the OCT system was upgraded as described above.

The new OCT vertical cross-section was compared with a cross-sectional micrograph. The thickness of the EBC coating was measured for each. The measured thickness from the micrograph was 0.29 mm (± 10 µm), and the measured thickness from the OCT vertical cross section was 0.30-mm (± 10 µm).

Additional vertical and horizontal cross-sectional images were obtained from this BSAS EBC sample. Figure 15 shows another vertical cross-section acquired approximately 100-µm away from the location of the scan in Figure 14. This image shows the area in which the EBC has spalled, however, it also reveals a probable subsurface crack as a dark line. Compared with the elastic optical scattering data, which revealed the presence of the cracks, this image also reveals the extent of the crack in terms of depth location.

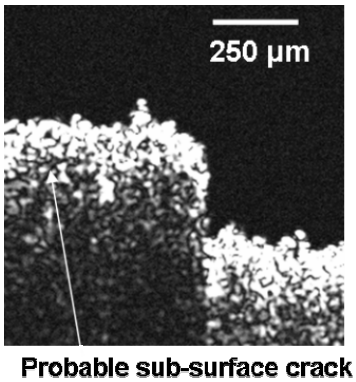

Figure 15. OCT vertical cross-section image from a BSAS EBC on SiC/SiC sample showing a probable subsurface crack.

The OCT system can also acquire horizontal cross-section images (i.e., images from a plane parallel to the surface of the sample). Two horizontal cross-section images from the BSAS EBC sample are shown in Figure 16. These images were obtained from a region in which part of the EBC was intact and the other area was spalled (see the "scanned area" in Figure 9). These images were acquired from depths of 200-µm and 250-µm below the surface of the EBC, respectively. The bright region in the upper left corner of each image is the SiC/SiC substrate, as these images were acquired from depths close to the EBC/CMC interface. Again, probable subsurface cracks can be seen in each of these images. The evolution of the crack as it approaches the EBC/CMC interface can also be tracked with a series of scans at varying depths.

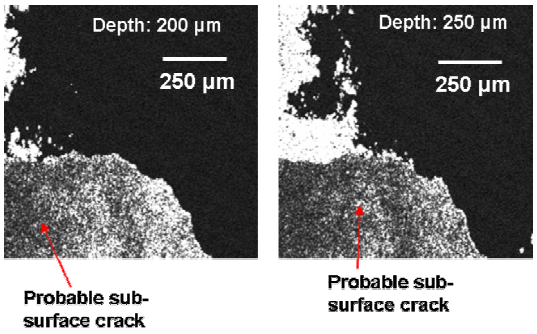

Figure 16. OCT horizontal cross-section of BSAS EBC on SiC/SiC substrate with the EBC partially spalled: (left) cross-section 200 µm below the EBC surface; (right) cross-section 250-µm below the EBC surface.

The depth resolution of OCT can be used to aid in the classification of a flaw as critical or non-critical, since the depth of the flaw an be a key parameter in that determination. However, at this time, the data acquisition process required to obtain the resolution and contrast of the images shown here is extremely slow. Thus additional efforts are being carried out to improve the robustness of the system as well as the signal-to-noise ratio in order to reduce the data acquisition time.

Conclusions

High-resolution, 3D X-ray CT, elastic optical scattering, and OCT are all beneficial tools for monitoring the condition of monolithic ceramic components and EBC-coated ceramic matrix composites. The use of massively parallelized computing and automated feature recognition will enable advanced defect detection techniques for internal flaws within monolithic ceramic components. Additional efforts to improve these methods, as well as efforts to further reduce reconstruction time, are under way.

Elastic optical scattering has been shown to be a method useful for detecting several types of defects critical to the health of EBCs. The detection of prespall and coating thickness is critical to the practical use of EBCs, as these defects can cause critical failures if undetected.

The advancements made in the OCT system at ANL have enabled it to emerge as the newest useful tool in evaluation of EBCs. The ability to resolve the presence and location of defects with the near subsurface of a sample provides additional information that elastic optical scattering is not yet capable of detecting. Efforts continue on elastic optical scattering and OCT to improve signal-to-noise and develop theoretical models to correlate with the experimental data and models of the material system to work toward remaining useful life assessment and failure prediction.

References

1. W. A. Ellingson and M. P Brada, “Optical Method and Apparatus for Detection of Surface and Near-Surface Defects in Dense Ceramics,” U.S. Patent 5,426,506, June 30, 1995.
2. W. A. Ellingson, J. A. Todd, and J. Sun, “Optical Method and Apparatus for Detection of Defects and Microstructural Changes in Ceramics and Ceramic Coatings,” U.S. Patent 6,285,449, September 4, 2001.
3. W. A. Ellingson and J. Sun, J., “ Automated Real-Time Detection of Defects during Machining of Ceramics,” U.S. Patent 5, 689,332, November 18, 1997.
4. R. J. Visher, W. A. Ellingson, M. D. Shields, and A. Feuerstein, “Laser-based Inspection of Thermal Barrier Coatings,” To be published in *Proceedings of the ASM International Surface Engineering Conference*, Orlando, FL, August 2–4, 2004.
5. B. E. Bouma and G. J. Tearney, *Handbook of Optical Coherence Tomography*, Marcel Dekker, New York, 2002.

Oxidation/Corrosion Characterization of Microturbine Materials

Karren L. More and P. F. Tortorelli
Metals and Ceramics Division
Oak Ridge National Laboratory
Oak Ridge, TN 37831-6064
(865) 574-7788; fax: 865-576-5413; e-mail: morekl1@ornl.gov

DOE Technology Development Manager: Debbie Haught
(202) 586-2211; fax: (202) 586-7114; e-mail: debbie.haught@ee.doe.gov
ORNL Technical Advisor: Terry Tiegs
(865) 574-5173; fax: (865) 574-4357; e-mail: tiegstn@ornl.gov

Objectives

- Characterize and conduct corrosion analyses of ceramic materials provided to Oak Ridge National Laboratory (ORNL) as part of the Microturbine Materials Program.
- Expose candidate ceramic materials to high water-vapor pressures (in Keiser rigs) to simulate high-temperature, high-pressure environmental effects associated with microturbines.
- Evaluate the reliability of environmental barrier coatings (EBCs) on Si_3N_4 (in Keiser rigs) for selected microturbine applications.

Approach

- Conduct short- and long-term Keiser rig exposures of candidate ceramic materials at elevated temperatures (1135–1315°C) and H_2O pressures (0.3–2.0 atm) to evaluate oxidation performance.
- Perform extensive post-exposure microstructural analyses to elucidate oxidation (degradation) mechanisms and kinetics at elevated H_2O pressures.
- Provide performance data to individual material manufacturers for process optimization.

Accomplishments

- Long-term Keiser rig exposures of several Saint Gobain Si_3N_4 materials at 1200°C showed that its oxidation resistance is comparable to that of materials made by Honeywell and Kyocera.
- Keiser rig exposures of ATK-COI Ceramics A/N 720 oxide/oxide composite showed that the material retained nearly 100% of its ultimate tensile strength (UTS) at 1135°C and up to 80% of its UTS at 1200°C.
- Keiser rig exposures of two different Kennametal Sialon compositions at 1200°C showed that their oxidation resistance is not as good as that of Si_3N_4.

Future Direction

- Continue collaboration with Saint Gobain Ceramics to expose new Si_3N_4 materials in Keiser rigs and optimize oxidation resistance of NT-154 Si_3N_4 for microturbine applications.
- Continue collaboration with ATK-COI Ceramics to evaluate oxide/oxide composite material and EBCs at 1250°C in H_2O.
- Continue collaboration with external EBC producers/processors to evaluate new/improved EBC compositions for Si_3N_4 in the Keiser rigs.

Introduction

Si_3N_4 is considered a primary candidate ceramic material for several hot-section components in microturbines. However, exposure of unprotected Si-based materials to the high temperature and high water-vapor pressures typical of gas turbine combustion environments results in rapid oxidation and surface loss/recession due to SiO_2 volatilization.[1–3] Thus it has become imperative to fully understand the oxidation behavior of Si_3N_4 materials exposed to microturbine combustor conditions. To this end, ORNL Keiser rigs continue to be used to evaluate the microstructural and compositional stability of different Si_3N_4 formulations as a function of temperature and water-vapor pressure. Si_3N_4 recession rates can be measured and degradation mechanisms elucidated following exposure of the material to simulated microturbine operating conditions in the Keiser rigs. In FY 2004, several new Si_3N_4 and Sialon materials, produced by Saint Gobain Ceramics and Kennametal, respectively, were exposed for ~1500 h at 1200°C and two water vapor pressures, 0.3 and 2.0 atm. Microstructural evaluation and data analysis after Keiser rig exposure showed that at least two of the Si_3N_4/Sialons had recession rates comparable to those measured previously for AS800 (Honeywell Ceramic Components) and SN282 (Kyocera) Si_3N_4, and the other formulations were inferior in terms of corrosion resistance. Based on these initial data, ORNL has received additional new compositions of Si_3N_4 and Sialon materials from both manufacturers and will expose them under similar conditions starting in FY 2004 and continuing into FY 2005.

Approach

Keiser Rig exposures and post-exposure characterization (oxidation analyses) of three different microturbine materials have been the primary focus of the work conducted in FY 2004:

- Saint Gobain's new NT-154 Si_3N_4 was exposed for up to 1500 h at 1200°C, 10 atm total pressure, and 0.3 and 2.0 atm H_2O. Similar NT-154 compositions were processed using three different processing routes.
- Kennametal's Sialon materials (two different compositions) were exposed for up to 1500 h at 1200°C, 10 atm total pressure, and 0.3 and 2.0 atm H_2O.
- ATK-COI Ceramics' A/N720 oxide/oxide composite material was exposed for 3000 h at two different temperatures, 1135 and 1200°C, 10 atm total pressure, and 1.0 atm H_2O.

Coupons for each material were exposed in separate furnace runs in 500 h increments. After each 500-h run, specimens were removed from the Keiser rigs, weighed, measured, and sectioned to microstructurally evaluate the progression of oxidation.

Results

Coupons of three different Saint Gobain NT-154 Si_3N_4 (similar NT-154 compositions produced via different processing routes) were exposed in the Keiser rig using the conditions described earlier. Differences in oxidation performance were observed between the three NT-154 Si_3N_4 materials following the exposures. The oxidation performance for the NT-154 Si_3N_4 materials is compared in Figure 1. For this graph, the thickness of the silica scale that forms on the NT-154 specimen surface is plotted versus the square root of the specimen exposure time at 1200°C. These data quantify the oxidation rates for the different NT-154 Si_3N_4 materials, which were exposed under similar conditions in the Keiser rig.

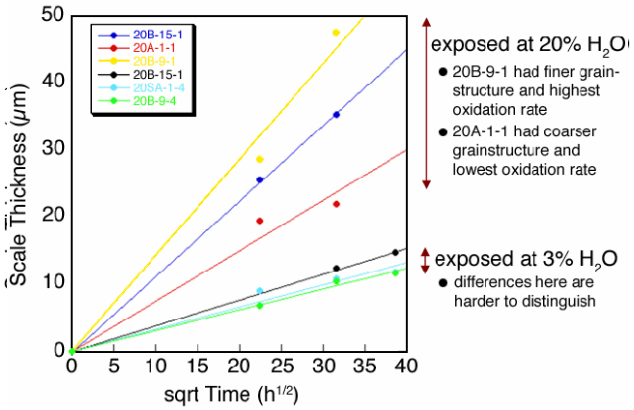

Figure 1. Oxide scale thickness vs. exposure time and H_2O pressure for three different Saint Gobain NT-154 Si_3N_4 materials. Exposure was for 1000 h.

As Figure 1 shows, clear differences in oxidation rates were measured for the specimens exposed to 20% H_2O, whereas the differences in rates between the specimens exposed to 3% H_2O were not nearly as distinct. The reason for the difference in oxidation rate observed for exposure to 20% H_2O depends on the starting Si_3N_4 microstructure, which

is produced as a result of the Si_3N_4 processing (all three Si_3N_4 materials contained the same amount of additives). The Si_3N_4 microstructure and surface oxide scale formed on the three NT-154 Si_3N_4 specimens are shown in Figure 2(a–c). (These Si_3N_4 specimens are the same ones used to generate the data plotted in Figure 1, after only 500 h exposure at 1200°C and 20% H_2O.) Note that the NT-154 specimen that had the highest oxidation rate (designated as 20B-9-1, Figure 2c) had the smallest overall Si_3N_4 grain size and a finer secondary phase size (finer-scale distribution), and the NT-154 specimen that had the lowest oxidation rate (designated 20A-1-1, Figure 2a) had the largest overall Si_3N_4 grain size and a much wider/larger dispersion/distribution of the secondary phase.

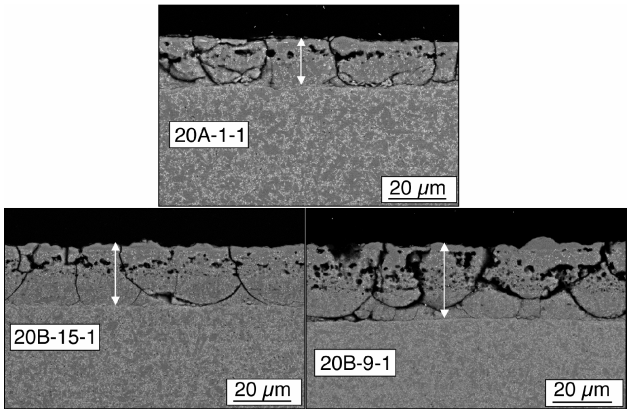

Figure 2. Scanning electron microscope images of NT-154 Si_3N_4 cross-sections showing surface microstructure for three different NT-154 specimens exposed in the Keiser rig for 500 h at 1200°C and 2.0 atm H_2O.

Coupons of two different Kennametal Sialon compositions (designated ab532-2308A and ab832-2308E, both with a relatively high rare earth content) were exposed in the Keiser rig for a total of 2000 h (in 500-h increments) using conditions given earlier. Significant differences in oxidation behavior were observed between the two different Sialon materials at both water-vapor pressures used during the exposures. As shown in Figure 3, Sialon composition ab532-2308A exhibited a significantly greater thickness loss (recession) at both 0.3 and 2.0 atm H_2O than Sialon composition ab832-2308E. In fact, composition ab532-2308A had a total coupon thickness loss of ~55% after 2000 h at an H_2O pressure of

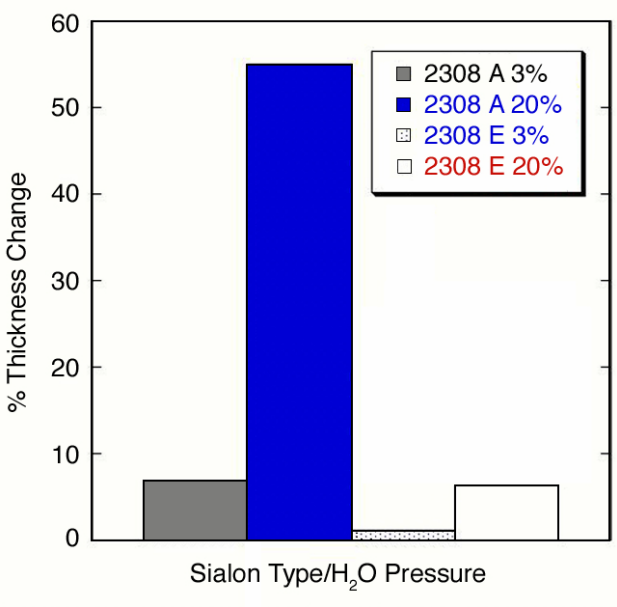

Figure 3. Percentage change in specimen thickness vs. Sialon composition and H_2O pressure for two different Kennametal Sialon materials.

2.0 atm, which corresponded to ~1–2 μm/h thickness loss during exposure. This rate of recession (material loss) was approximately an order of magnitude greater than that previously determined/measured for either Si_3N_4 or SiC. Sialon composition ab832-2308E was more stable during exposure to high water-vapor pressures and exhibited only ~5–6% total thickness loss during exposure for 2000 h at 2.0 atm H_2O.

ATK-COI Ceramic's A/N720 oxide/oxide composite material (originally being considered by Capstone for combustor liners in its C60 microturbines) was subjected to long-term exposures (0–3000 h) in a simulated microturbine environment in the Keiser rig at 1135 and 1200°C, 10 atm total system pressure, and an N_2-10%O_2-10%H_2O-6%CO_2 gas mixture. For this study, 36 1×7 in. bars (to be used for post-exposure tensile tests) and 36 1×2 in. coupons (to be used for post-exposure microstructural characterization and shear tests) were exposed in the first 1000-h exposure. The as-processed A/N720 was fully characterized. [4] In addition, smaller samples were cut from the 1×2 in. coupons for thermogravimetric analysis in both air and air+10% H_2O in the microbalance.

While microstructural information after long-term Keiser rig exposures is still being compiled,

results from the A/N720 post-exposure (both 1135 and 1200°C) mechanical testing in tension are compared in Figure 4. These data compare all the UTS data measured from coupons of as-processed A/N720 and A/N720 exposed for 1000, 2000, and 3000 h at 1135°C and A/N720 exposed for 1000, 2000, and 3000 h at 1200°C. As can be seen from Figure 4, no statistical differences were observed for the tensile strength of the composite material exposed at 1135°C for times up to 3000 h, whereas the material exposed at 1200°C exhibited a strength decrease with increased exposure time.

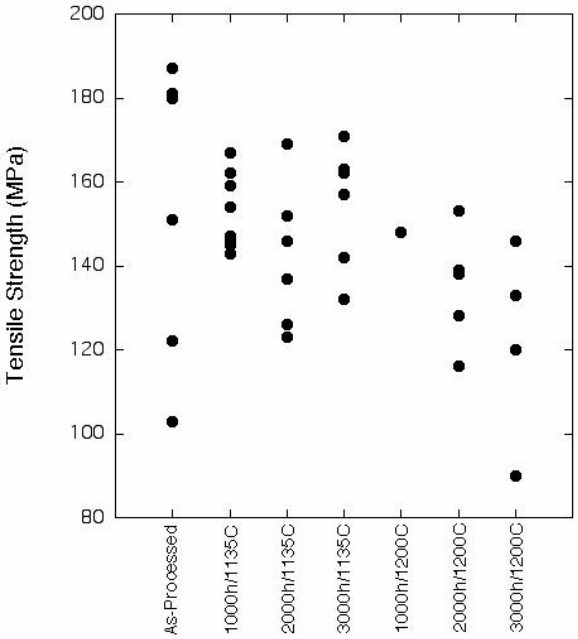

Figure 4. UTS results for A/N720 oxide/oxide composite material comparing as-processed to material exposed for up to 3000 h at 1135°C and 1200°C.

Conclusions

During FY 2004, ORNL's Keiser rig was used to expose numerous candidate microturbine materials (Si_3N_4, Sialon, and A/N720) to simulated microturbine engine combustion environments in order to evaluate and compare the oxidation performance of the different materials under high H_2O-vapor exposure conditions. Long-term Keiser rig exposures have shown that the new NT-154 Si_3N_4 material produced by Saint Gobain is comparable (in terms of oxidation resistance) to both Honeywell's AS800 and Kyocera's SN282 Si_3N_4, whereas the Sialon material produced by Kennametal does not exhibit good oxidation resistance compared with Si_3N_4. The A/N720 oxide/oxide composite exposures have shown that this material can retain up 100% of its UTS after 3000 h at 1135°C and up to 80% of its UTS after 3000 h exposure at 1200°C. The Keiser rig exposures of the NT-154 and A/N720 will continue in FY 2005.

References

1. E. J. Opila, and R. E. Hann, "Paralinear Oxidation of CVD SiC in Water Vapor," *Journal of The American Ceramic Society*, **80**(1), 197–205 (1997).
2. R. C. Robinson and J. L. Smialek, "SiC Recession Caused by SiO2 Scale Volatility Under Combustion Conditions: I, Experimental Results and Empirical Model," *Journal of The American Ceramic Society*, **82**(7), 1817–25 (1999).
3. E. J. Opila, J. L. Smialek, R. C. Robinson, D. S. Fox, and N. S. Jacobsen, "SiC Recession Caused by SiO2 Scale Volatility Under Combustion Conditions," *Journal of The American Ceramic Society*, **82**(7), 1826–34 (1999).
4. *Distributed Energy Research Quarterly Report January 1–March 31, 2003*, Office of Energy Efficiency and Renewable Energy, U. S. Department of Energy, Washington, D.C.

Publications/Presentations

K. L. More and P. F. Tortorelli, "Evaluation of EBCs in the Keiser Rigs," presented at the Environmental Barrier Coatings Workshop, Nashville, TN, November 18–19, 2003.

K. L. More, E. Lara-Curzio, P. F. Tortorelli, A. Szweda, D. Carruthers, and M. Stewart, "Evaluating the High-Temperature Stability of an Oxide/Oxide Composite Material at High-Water-Vapor Pressures," presented at the 28th International Conference and Exposition on Advanced Ceramics and Composites, Cocoa Beach, FL, January 25–30, 2004.

K. L. More, P. F. Tortorelli, T. Bhatia, and G. D. Linsey, "Evaluating the Stability of BSAS-Based EBCs in High Water-Vapor Pressure Environments," presented at the Turbo Expo 2004, Vienna, Austria, June 6–10, 2004, and published as ASME Paper #GT2004-53863, American Society of Mechanical Engineers, New York.

Mechanical Characterization of Monolithic Silicon Nitride Si_3N_4

Roger R. Wills
Advanced Ceramics Group
University of Dayton Research Institute
Dayton, Ohio 45469-0162
(937) 229 4341, e-mail: roger.wills@udri.udayton.edu

DOE Technology Development Manager: Debbie Haught
(202) 586 2211; (202) 586-7114(fax); e-mail: debbie.haught@ee.doe.gov
ORNL Technical Advisor: Mattison K. Ferber
(865) 576 0818; fax (865) 574 6098; e-mail: ferbermk@cosmail1.ctd.ornl.gov

Objective

- Determine the high-temperature properties of Kyocera SN281 silicon nitride to assess its suitability as a material for hot-section microturbine components.
- Search for and screen candidate high-temperature materials known as environmental barrier coatings (EBCs) that show excellent resistance to oxidation by water vapor under turbine operating conditions.
- Upgrade a Web-based database containing the properties of structural ceramics.

Approach

- Ascertain the effect of water vapor on the dynamic fatigue characteristics of Kyocera SN281 silicon nitride at 1400 to 1500°C.
- Study the oxidation behaviour of aluminum silicon carbide, a potential EBC, in air and air/water vapor environments to quantify its corrosion rate and susceptibility to erosion by water vapor.

Accomplishments

- Found a new mechanism of slow crack growth in this form of silicon nitride, with no slow crack growth observed below 1400°C and slow crack growth rates lower in water vapor than in air.
- Prepared aluminum silicon carbide by hot-pressing a combination of aluminum carbide and silicon carbide powders at 1825°C.
- Determined the oxidation kinetics of aluminum silicon carbide, showing parabolic kinetics with no deleterious effect of water vapor compared with air, in contrast to what is seen for silicon nitride or silicon carbide ceramics. This is due to the formation of a surface dual oxide layer containing an outer alumina layer.
- Constructed Excel input files for the CARES^{TM} ceramic component design program and added them to the Web-based database at the University of Dayton. Use of the database enables users to design ceramic components.

Future Direction

- Evaluate the corrosion of aluminum silicon carbide after exposure to high-pressure steam in the Keiser rig at Oak Ridge National Laboratory (ORNL).
- Assess the oxidation resistance in high-temperature water vapor of candidate ceramics such as refractory silicates, mixed oxides, and silicon aluminum oxynitrides.
- Determine the thermal properties of these candidate ceramics if no such data exist.

Introduction

Microturbine efficiency increases with increasing turbine inlet temperature, so that the hotter the turbine can be run, the greater the power generated and the economic payback to the user. For high-temperature operation, the materials of construction in the hot section need to be made from reliable ceramic materials. Kyocera's silicon nitride is a promising candidate hot-section material; some of its high-temperature properties are analyzed in this report.

For microturbines designed to operate above about 1150°C, water vapor in the turbine's atmosphere slowly causes erosion of silicon nitride or carbide components in the hot section, as shown in Figure 1. Coatings known as oxidation barriers or EBCs are needed to protect the underlying silicon-based structural ceramic from this water vapor attack. This report discusses research on one potential ceramic for use in oxidation barriers, aluminum silicon carbide.

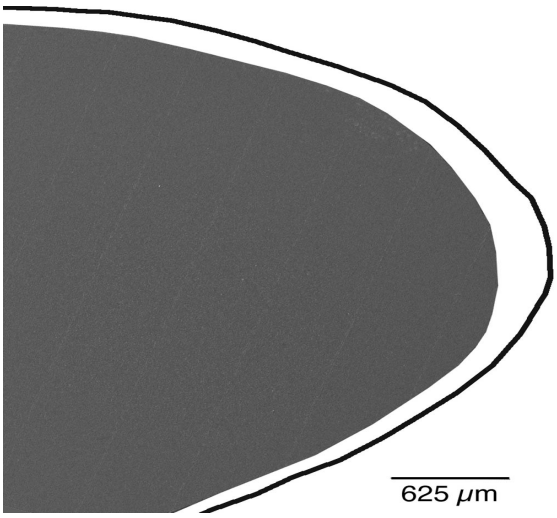

Figure 1. Erosion of the mid-span region of a SN282 silicon nitride vane after 625 hours in an engine test. The dark line is the profile of the original vane.

Approach

Evaluation of Kyocera SN281

Dynamic fatigue tests of this grade of silicon nitride were conducted at 1400 and 1500°C in both air and water-vapor-saturated air to ascertain its resistance to slow crack growth under load. Size B four-point-bend bars were machined from billets of the material and held in a silicon carbide four-point-bend fixture while being subjected to stresses applied at different crosshead speeds at the test conditions. Two stressing rates of 30 MPa/sec and 0.003 MPa/sec were applied.

Oxidation of Aluminum Silicon Carbide

The Al-Si-C-N system[1] contains several ternary compounds, including Al_4SiC_4, $Al_4Si_2C_5$, $Al_4Si_4C_7$, $Al_4Si_3C_6$, Al_8SiC_7, and Al_5C_4SiN. The compound Al_4SiC_4 appears to be the most promising ternary compound because of its high melting point (~2037°C).[2] In early work on this ceramic, Shoennahl[3] showed that at 1400°C it formed alpha alumina. It was thus thought worthy of further investigation as a potential oxidation barrier material.

Silicon carbide powder (2-micron particle size, Alfa Aesar) and aluminum carbide powder (–325 mesh, Alfa Aesar) were mixed in *n* hexane for 24 hours, dried, and stored under vacuum. Powder compacts were prepared by dry pressing. Hot pressing was conducted at 1750, 1825, and 1980°C for 1 hour in argon at 5000 psi pressure. Microstructural analysis of hot-pressed samples was performed using X-ray diffraction (XRD) and scanning electron microscopy (SEM) coupled with an energy dispersive analysis system (EDAX). Sample densities were determined using the Archimedes method, by weighing in both air and water. The thermal expansion of the Al_4SiC_4 was measured using a dilatometer, the thermal diffusivity by the laser flash technique, and the specific heat using differential scanning calorimetry. The thermal conductivity of Al_4SiC_4 was then calculated from knowledge of the density, thermal diffusivity, and specific heat.

Oxidation of the Al_4SiC_4 was performed in both air and water-vapor-saturated air atmospheres at 1400 and 1500°C using thin rectangular ground samples. The kinetics were determined by weighing samples after known exposure times. Small plate samples for oxidation studies were cut from the hot-pressed Al_4SiC_4 billet and generally had a surface area of greater than 400 mm^2 in accordance with the ASTM G54-77 standard for oxidation samples. Materials and oxide layers were characterized using XRD and SEM/EDAX techniques.

Results

Dynamic Fatigue Testing of Kyocera SN281

Dynamic fatigue testing at 1400 and 1500°C was conducted using stressing rates of 0.003 and 30 MPa/s. While fracture origins are frequently difficult to discern in this grade of silicon nitride, it appeared that fracture occurred at surface flaws, based upon optical microscopy and SEM. Figures 2 and 3 compare the slow crack growth behaviour at 1400 and 1500°C in both ambient air and the air/water vapor atmosphere. All the graphs were calculated using regression analysis. The exponent *n* shown in both figures is a measure of the crack growth rate, with higher values of *n* indicating slower rates of crack growth.

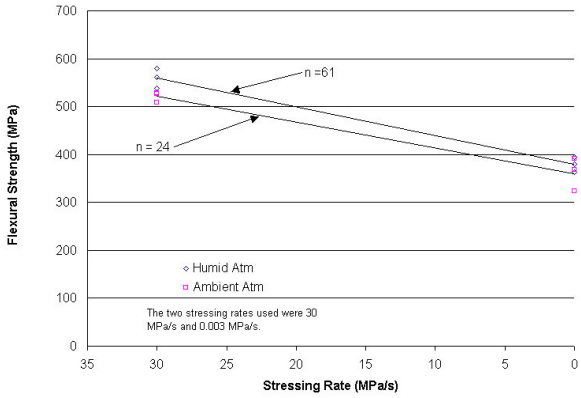

Figure 2. Dynamic fatigue of SN281 in air and air/water vapor atmospheres at 1400°C.

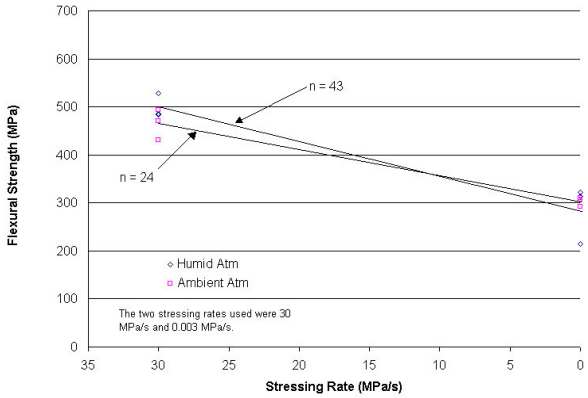

Figure 3. Dynamic fatigue of SN281 in air and air/water vapor atmospheres at 1500°C.

While the crack growth rates in air are identical (N=24), the addition of water vapor to the atmosphere reduces crack growth rates. This is consistent with a crack blunting mechanism due to oxidation of the silicon nitride during dynamic fatigue. Higher oxidation rates at the higher temperature in the air/water vapor atmosphere would also be expected to increase the crack growth exponent, but this is not what is observed. Rather the exponent dropped from 61 at 1400°C to 43 at 1500°C. In a water-vapor-saturated environment, the two principal chemical reactions occurring at the crack tip are oxidation of the silicon nitride to silica and volatilization of tetrahydroxysilane. One possible explanation for the change in the slow crack growth exponent is that volatilization of material in front of the crack tip is occurring and is a more influential factor than oxide growth in governing crack tip velocity. Removal of local material in and around the crack tip would certainly enhance crack velocity.

Most silicon nitrides exhibit crack growth exponents in air that decrease with increasing temperature. For example, Saint Gobain's NT164 has *n* values of 159, 35, and 18 at 1038, 1150 and 1350°C. In contrast, SN281 has a constant *n* of 24 in air at both 1400 and 1500°C.

The classic explanation of slow crack growth invokes crack formation ahead of the main crack as a result of grain boundary sliding facilitated by a viscous grain boundary phase. Since the viscosity of the grain boundary phase decreases with increasing temperature, the value of *n* decreases. This mechanism does not appear to be operating in the SN281 silicon nitride. Rather, there appears to be some threshold-based mechanism, since an increase in temperature does not cause enhanced slow crack growth. Damping studies by Pezzotti et al.[4] show that the lutetium silicate phases entrapped at multiple grain junctions lock grain motion and retard grain boundary sliding in this temperature regime. Grain boundary sliding and diffusional flow do not occur until >1621°C.

The most likely model to explain these data would be one that assumes that a crack propagates along the grain boundary by a process of surface and grain boundary diffusion in which adjoining grains behave elastically. Chang[5] developed such a model and showed good agreement between theory and

experiment with a set of creep crack growth data on several Si-Al-O-N samples.[6] In this model,

$$K/K_{min} = 1/2[(v/v_{min})^{1/2} + (v/v_{min})^{-1/2}] \ , \qquad (1)$$

where K is the stress intensity factor, $K_{min} = 1.69$, K_{ic} is the minimum K below which no crack growth is predicted, K_{ic} is the critical stress intensity factor, v is the crack tip velocity, and v_{min} is the minimum crack velocity for $K = K_{min}$. It seems likely that slow crack growth in SN281 follows this model, but crack growth data as a function of K is needed to confirm this.

Oxidation of Aluminum Silicon Carbide

The results of the hot pressing experiments (see Table 1) showed that single phase Al_4SiC_4 was obtained by hot pressing at 1825°C. Below this temperature, the reaction was incomplete, with a small amount of Al_4C_3 being detected by XRD. At 1900°C, some decomposition of the Al_4SiC_4 is evident from the detection of free carbon and aluminum. The single-phase Al_4SiC_4 sample was close to theoretical density (99.73%), using 3.028 g/cm^3 as the density of Al_4SiC_4.2

Table 1. Hot pressing of Al_4SiC_4

Processing conditions	Sample density (g/cm^3)	Phase analysis (XRD)
1900°C, 5 ksi for 1 h	2.79	Al_4SiC_4, Al and C
1825°C, 5 ksi for 1 h	3.02	Al_4SiC_4
1750°C, 5 ksi for 1 h	2.96	Al_4SiC_4, Al_4C_3

Oxidation data were analyzed for linear, parabolic, and logarithmic kinetics using least mean squares analysis. Figure 4 is a typical plot showing a good fit of the data (R2 =0.9942) to parabolic kinetics. This type of oxidation kinetics, which was found at all temperatures and in both atmospheres, is exhibited by many ceramics and implies that diffusion of oxygen through the oxide layer is the rate-determining step controlling the reaction rate. The surface of the white oxide (see Figure 5) was uneven and consisted of 2- to 5-micron particles bonded together in clusters frequently separated by microporosity so that oxygen might be able to access the interior of the growing oxide layer. The oxide layer

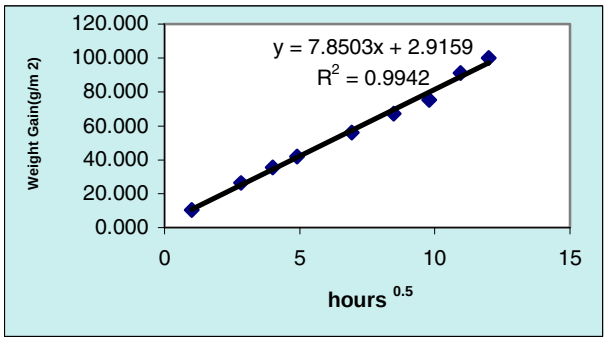

Figure 4. Parabolic oxidation of Al_4SiC_4 in air at 1500°C.

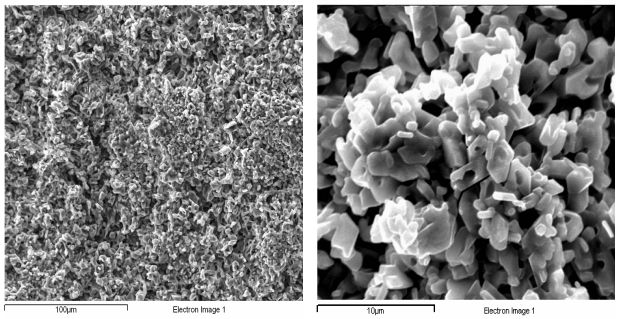

a **b**

Figure 5. Surface of oxide layer showing (a) rough surface of oxide layer and (b) layer consisting of clusters of approximately 3-micron crystallites and some porous regions.

itself (see fracture surface in Figure 6) is dense, so that the reaction rate is probably controlled by diffusion through the oxide itself, not by channels of microporosity permeating the oxide scale. If microporosity did control the oxidation rate, linear kinetics would be expected.

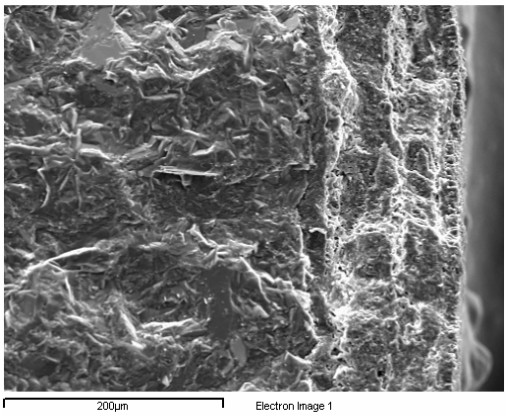

Figure 6. Fracture surface through the oxide layer and underlying Al4SiC4.

The reaction product was a dual oxide layer (see Figure 7) consisting of an inner mullite layer and an outer alumina layer. After 144 hours at 1400°C, the oxide thickness was 68 microns; whereas after the same period at 1500°C, the thickness was 100 microns. The mullite and alumina layers are approximately the same thickness.

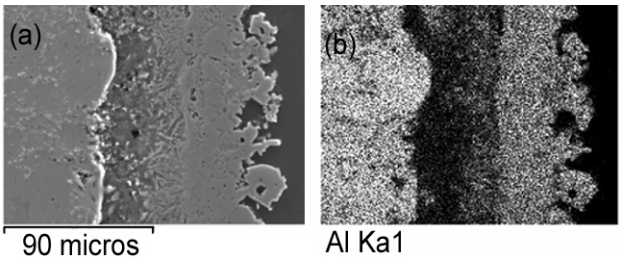

Figure 7. Dual layer oxide(a) formed on Al_4SiC_4 after oxidation in air at 1500°C for144 hours in air with (b) differing aluminum contents in the oxide layers.

The reaction products and weight gain can be explained by Eq. (2):

$$2Al_4SiC_4 + 12O_2 = 8CO + 3Al_2O_3.2SiO_2 + Al_2O_3 \quad (2)$$

The formation of two layers implies a two-step process occurs in which silica and alumina are first formed by the following reaction:

$$Al_4SiC_4 + 6O_2 = SiO_2 + 2Al_2O_3 + 4CO \quad (3)$$

The XRD studies of Yamamoto, et al.[7] support this suggestion, since they found the initial reaction resulted in the formation of amorphous silica and γ alumina.

Subsequent reaction between the silica and alumina then gives rise to mullite and the additional alumina remains:

$$SiO_2 + 2Al_2O_3 = 0.5\ (3Al_2O_3.2SiO_2) + 0.5Al_2O_3 \quad (4)$$

The addition of water vapor to the atmosphere had no effect on the oxidation of Al_4SiC_4, as shown in Figure 8. The same dual oxide layer was formed, and no change in oxide thickness was found. Thus the addition of water vapor had no effect on the oxidation kinetics. This is in agreement with studies on the oxidation of other materials, such as NiAl, that result in alumina formation.[8] In contrast, silicon-based ceramics, which form a silica oxidation layer,

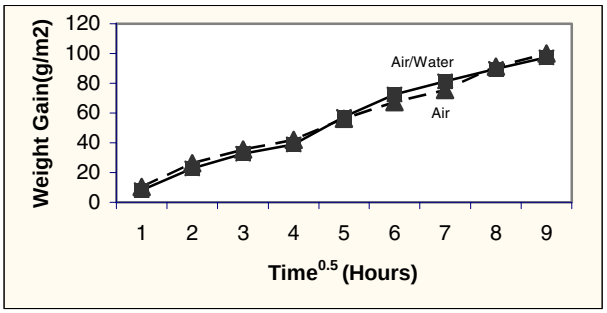

Figure 8. Comparison of the oxidation of Al4SiC4 in air and air/saturated water vapor at 1500°C.

show increased reaction rates in water vapor containing atmospheres due to volatilization of $Si(OH)_4$.

The activation energy for oxidation in water vapor saturated air was calculated at 179 kJ/mole from the parabolic rate constants at 1400 and 1500°C. The question is to what process this corresponds. Since there are two oxide layers formed, it may represent diffusion through either layer, an interface reaction, or possibly diffusion through a thin amorphous layer. The present value is significantly lower than the values of 293 kJ/mole and 322 kJ/mole reported for the dry oxidation of NiAl and AlN,[8,9] both of which form Al_2O_3. This would suggest that diffusion through the alumina layer is not the rate-determining step. The activation energy for oxygen diffusion through amorphous silica is 126 kJ/mole,[10] and similar values have been found in the oxidation of silicon nitride,[11] silicon carbide,[12] and silicon oxynitride.[11] These values are closer to the value for Al_4SiC_4; but if an amorphous silica phase is present, it does not reach the surface of the alumina layer. Otherwise the reaction kinetics would show a dependency upon the presence of water vapor, and this is not observed. Furthermore, an amorphous phase would likely be in the form of an aluminosilicate glass rather than pure silica, and data by Mackenzie et al.[13] show that the activation energy for oxidation through a predominantly aluminosilicate phase formed on a silicon oxynitride sialon is 454 kJ/mole.

Thus diffusion through an aluminosilicate layer seems improbable, as the rate-determining process in the overall oxidation process. Diffusion through the mullite layer is also an unlikely explanation since oxygen diffusivity measurements by Fileitz et al.[14] using an oxygen isotope technique together with secondary ion mass spectrometry gave an activation energy of 363 kJ/mole. Since there is no evi-

dence to support diffusion through either the alumina or mullite layers formed during wet oxidation, it seems more likely that the measured activation energy corresponds to an interface or rearrangement mechanism associated with the formation of the two separate layers.

The thermal conductivity of Al_4SiC_4 was determined to be 8 watts/mk at room temperature. In contrast the thermal conductivity of hexalloy SA, a sintered silicon carbide manufactured by Saint Gobain Ceramics, is 125 watts/mk. The thermal expansion of Al_4SiC_4, measured using a dilatometer, was found to be $6.9x10^{-6}$ °C over the temperature range room temperature to 1300°C. As shown in Table 2, the thermal properties of Al_4SiC_4 are closer to those of mullite than alumina or silicon carbide. Since it has a lower thermal expansion than alumina or zirconia and the rare earth oxides and is not as susceptible to erosion by water vapor like silicon nitride and silicon carbide ceramics it is a material worth considering in designing high temperature structures.

Table 2. Comparison of the thermal properties of Al_4SiC_4

Material	Thermal expansion ($\times10^{-6}$°C)	Thermal conductivity (Watts/mk)
Al_4SiC_4	6.9	8
Mullite*	5.22	6
Alumina*	9.0	14
SiC*	5.0	125

*Engineering Property Data Handbooks, Metals and Ceramics Information Center, Battelle Columbus Laboratories, 505 King Avenue, Columbus, Ohio.

Conclusions

Dynamic fatigue testing of Kyocera's SN281 grade of silicon nitride shows that it has the best resistance to slow crack growth of any additive-based silicon nitride ever tested. This appears to be due to the presence of a refractory grain boundary phase that locks grain motion and grain boundary sliding.

The oxidation of Al_4SiC_4 in the temperature range 1400 to 1500°C in both air and water-vapor-saturated air follows parabolic kinetics with an activation energy of 179 kJ/mole. Unlike silicon nitride and silicon carbide structural ceramics, Al_4SiC_4 exhibited no change in oxidation rate with the addition of water vapor. Based upon these laboratory screening tests, Al_4SiC_4 is worthy of further evaluation as a potential oxidation barrier material, and a sample has been sent to ORNL for testing in its high-pressure steam rig. Oxidation causes the formation of a dual oxide layer on the surface of the Al_4SiC_4 with the inner layer of mullite and an outer layer of alumina. It is this alumina layer that prevents the oxidation rate from increasing in the presence of water vapor. The overall reaction can be explained in terms of a two-step reaction with the reaction rate controlled by a rearrangement or interface process rather than diffusion through either the mullite or alumina layers.

References

1. L. L. Oden and R. A. McCune," Contribution to the Phase Diagram Al4C3-AlN-SiC," *J. Amer. Ceram. Soc*., **73**(6), 1529 (1990).
2. H. Yokokawa, M .Fujita, S. Ujiie, and M. Dokiya, "Phase Relations Associated with the Aluminum Blast Furnace: Aluminum Oxycarbide Melts and Al-C-X(X=Fe, Si) Liquid Alloy," *Metall. Trans B*, **18B**, 433–444 (1987).
3. J. Schoennahl, B. Miller, and M. Daire, "Preparation and Properties of Sintered Materials in the Systems Si-Al-C and Si-Ti-C," p. 338 in *Materials Science Monographs 4: Sintering—New Developments*, Elsevier Science Publishing, Amsterdam, 1979.
4. G. Pezzotti, K. Ota, Y. Yamamoto, and Hua-Tay Lin, "Elementary Mechanisms Behind the High Temperature Deformation Behaviour of Lutetium Doped Silicon Nitride," *J. Amer. Ceram. Soc*., **86**(3), 471 (2003).
5. T. Chang, "A Diffusive Crack Growth Model for Creep Fracture," *J. Amer. Ceram. Soc*., **65**(2), 93 (1982).
6. M. H. Lewis and B. S. B. Karunaratne, "Determination of High Temperature K_1–V Data for Si-Al-O-N Ceramics," pp. 13–32 in *Fracture Mechanics Methods for Ceramics, Rocks and Concrete*, ed. S.W. Freiman and E.R. Fuller, Jr., ASTM STP 745, American Society for Testing and Materials, 1981.
7. O. Yamamoto, M. Ohtani, and T. Sasamoto, "Preparation and Oxidation of Al4SiC4," *J. Mater. Res*., **17**, 774 (2002).
8. E. Opila, N. Jacobsen, D. Humphrey, T. Yoshio, and K. Oda, "The Oxidation of AlN in Dry and

Wet Oxygen," *Electrochemical Proceedings 98-9*, 430–37 (1998).
9. F. S. Petit, *Trans. Met. Soc.* AIME, **239**, 1296 (1967).
10. B. E. Deal and A. S. Grove, "General Relationship for the Thermal Oxidation of Silicon," *J. Appl. Phys.*, **36**, 3770–78 (1965).
11. P. Goursat, P. Lortholary, D. Tetard, and M. Billy, "Silicon Nitride and Oxynitride Stability in Oxygen Atmospheres at High Temperatures," pp. 315–326 in *Proceedings of the 7th International Symposium on the Reactivity of Solids*, Bristol, UK, Chapman and Hall, London, UK, 1972.
12. J. A. Costello and R. E. Tressler, "Oxidation Kinetics of Silicon Carbide Crystals and Ceramics: I In Dry Oxygen," *J. Amer. Ceram. Soc.*, **69**(9), 674–81 (1986).
13. K. J. D. MacKenzie, C. M. Sheppard, G. C. Barris, A. M. Mills, S. Shimada, and H. Kiyono, "Kinetics and Mechanism of Thermal Oxidation of Sialon Ceramic Powders," *Thermochimica Acta*, **318**, 91–100 (1998).
14. P. Fielitz, G. Borchardt, M. Schmucker, and H. Schneide, "How to Measure Volume Diffusivities and Grain Boundary Diffusivities of Oxygen in Polycrystalline Oxides," *Solid State Ionics*, **160**, 75–83 (2003).

Publications/Presentations

R. R. Will and S. Goodrich, "Oxidation of Al_4SiC_4," presented at the American Ceramic Meeting in Cocoa Beach, FL, in January 2005.

Microstructural Characterization of CFCCs and Protective Coatings

Karren L. More and P.F. Tortorelli
Metals and Ceramics Division
Oak Ridge National Laboratory
Oak Ridge, TN 37831-6064
(865) 574-7788, E-mail: morekl1@ornl.gov

DOE Technology Development Manager: Debbie Haught
(202) 586-2211; fax: (202) 586-7114; E-mail: Debbie.haughty@ee.doe.gov
ORNL Technical Advisor: Terry Tiegs
(865) 574-5173; fax: (865) 574-4357; E-mail: tiegstn@ornl.gov

Objectives

- Use low-cost methods to characterize continuous fiber ceramic composite (CFCC) materials and CFCC combustor liners after exposure to simulated (in a Keiser rig) and actual (Solar Turbines engine test) combustion environments.
- Expose candidate environmental barrier coatings (EBCs) to high water-vapor pressures (in the Keiser rig) to determine thermal stability and protective capability.
- Work with CFCC and coating suppliers/manufacturers to evaluate new/improved ceramic fibers, protective coatings, and composite materials.

Approach

- Conduct short- and long-term Keiser rig exposures of candidate EBC compositions at elevated H_2O pressures to evaluate the coatings' H_2O permeation-resistance, volatility-resistance, and thermal stability at temperatures greater than 1100°C.
- Work with Solar Turbines to evaluate long-term engine-tested EBC/CFCC combustor liners (microstructurally and mechanically).

Accomplishments

- Modified an Oak Ridge National Laboratory (ORNL) Keiser rig to show proof-of-principle of operating a Keiser rig at very high water-vapor pressures (20 atm total system pressure and 18 atm H_2O at 1250°C) to induce volatilization of BSAS-based EBC compositions.
- Exposed ~28 new EBC compositions in a Keiser rig for several collaborators, including Ceramatec, SMaHT Ceramics, Inc., UTRC, the University of Colorado, and Northwestern University.
- Evaluated SAS-based EBC/CFCC combustor liners from two separate engine tests at Solar Turbines engine test sites in Bakersfield, CA, and Lawrence, MA.

Future Direction

- Continue collaboration with Solar Turbines to evaluate field-exposed EBC/CFCC liners, including oxide/oxide liners currently running in a Centaur 50S engine at the Bakersfield test site and GE pre-preg liners that will be run in FY 2005.
- Conduct extensive study of volatilization results from ORNL's Keiser rig so that volatilization mechanisms are understood and different EBC compositions are compared.
- Continue collaboration with external EBC producers/processors to evaluate new/improved EBC compositional stabilities at elevated H_2O pressures in ORNL's Keiser rig.

Introduction

Structural, Si-based ceramic materials (SiC, SiC/SiC composites, Si_3N_4) are being developed for use as hot-section components in gas turbines and microturbine engines as a result of their excellent high-temperature stability and property retention compared with their metallic counterparts. However, exposing unprotected Si-based materials to the high temperatures and high water-vapor pressures typical of gas turbine combustion environments results in rapid oxidation[1,2] and surface loss/recession due to SiO_2 volatilization.[3,4] There has been a significant amount of research during the past several years in EBC development for the protection of Si-based composites and monolithics.[5,6] Protective surface coatings (specifically EBCs) are absolutely required to prevent degradation of oxidation- and volatilization-susceptible Si-based ceramic substrates during their use in high-H_2O-pressure environments typical of combustion turbines. ORNL has played a critical role in the evaluation of EBC stability during the past several years by

- developing long-term (>1000-h) exposure protocols at high H_2O pressure in ORNL Keiser rigs (to date, >700,000 specimen exposure hours have been accumulated) to evaluate EBC and substrate stability
- providing a mechanistic understanding of EBC/CFCC degradation and failure mechanisms at high H_2O pressures
- establishing collaborations with external partners to evaluate new and promising EBC compositions by exposing samples in the Keiser rigs
- continuing the relationship with Solar Turbines to evaluate field-exposed EBC/CFCC combustor liners

EBCs based on the barium-strontium-aluminosilicate (BSAS) and mullite system are currently the system of choice for engine hot-section components.[7,8] SiC/SiC CFCC liners with BSAS-based EBCs ran in the two engine tests for 13,937 and 15,144 h. The application of EBCs to the gas-path surfaces significantly increased the combustor liner engine life compared with unprotected SiC/SiC liners; however, several life-limiting factors were identified following the long-term engine tests, the most significant of which was volatilization of the BSAS top coat. The significant volatilization of the BSAS phase during engine testing demonstrated the critical need for an inexpensive laboratory exposure test to screen candidate EBC compositions for volatility before testing in an actual engine. The Keiser rigs have been used to screen EBCs at relatively high standard H_2O pressures (0.3–2.0 atm) in terms of (1) thermal stability of the coating and interfacial region at elevated temperatures (1100–1350°C) and (2) permeation resistance to oxidizing species (primarily steam).[9] Because of the low gas-flow velocities in the Keiser rig ($5–33 \times 10^{-4}$ m/s), volatilization could not be fully assessed using the standard exposure conditions. In FY 2004, the potential use of the Keiser rig to evaluate the volatility of candidate EBCs has been explored. Calculations based on generalized volatility reactions and mass flux of volatilized species have shown that high H_2O pressures can be used to compensate for the low gas-flow velocities used in the Keiser rig. Substantial fluxes of volatile species can be obtained by increasing the H_2O pressure from 1.5 atm (typical value corresponding to water-vapor pressure in a gas turbine combustor) to 20 atm.

Approach

Previous high-temperature, high-pressure exposures of EBC/CFCC materials in the Keiser rig were conducted to evaluate the thermal stability and protective capability of different EBC formulations using exposure conditions that best simulated the temperature, pressure, and principal reactive gas species (H_2O) of combustor environments.[9] For example, to evaluate materials for use in a Solar Turbines Centaur 50S engine, all Keiser rig exposures of EBC/SiC-SiC ceramic matrix composites were conducted at ~1200°C (2200°F), 1.5 atm H_2O (balance air), and 10 atm total system pressure. In the present study, an extremely high H_2O pressure (~18 atm) and elevated temperature (1250°C) are being used to (1) validate that very high water-vapor pressures can be used to induce volatility in the Keiser rig (i.e., high H_2O pressures to compensate for low gas-flow velocities in the Keiser rig) and (2) to measure (rank) the volatility of candidate EBCs.

Several "proof-of-principle" specimens were included in the initial high water-vapor-pressure exposures to demonstrate and measure volatilization in the Keiser rig. High-purity SiC (produced by chemical vapor deposition) and quartz have been well

characterized after exposure to high water-vapor pressures[1,2] and were included as standards in the initial high-pressure Keiser rig runs. Also, since the primary purpose of these experiments was to measure the volatilization rates of currently-used, state-of-the-art EBCs, specimens of hot-pressed BSAS, barium aluminosilicate (BAS), and strontium aluminosilicate (SAS) materials were exposed simultaneously with the standards. All of the samples to be exposed in the ORNL furnace had their surfaces mechanically ground flat and parallel, and each sample was weighed and measured. The BSAS, BAS, and SAS coupons were also microstructurally characterized in the as-processed condition for comparison with the same material after exposure in the Keiser rig. Pre- and post-exposure cross-section specimens were imaged in a scanning electron microscope (SEM) equipped with a backscatter detector and compositionally analyzed using an electron probe microanalyzer (EPMA). In this way, reaction products (or the lack thereof) that formed during exposure, as well as any other microstructural changes, were identified, characterized with respect to their spatial dimensions, and compared with the as-processed microstructures.

Results

Evaluating Volatility at High H_2O Pressures in the Keiser Rig

Volatilization of Si-based ceramics can be the life-limiting factor for the use of these materials in combustion environments, where high temperatures, elevated oxidizing potentials, and significant gas-flow velocities exacerbate the volatilization process. This degradation mechanism has been shown to be of specific relevance for SiC and Si_3N_4, where SiO_2 forms by oxidation and then readily reacts with environmental H_2O to form volatile species.[3,4] Of the various volatilization reactions, the one forming $Si(OH)_4$,

$$SiO_2 + 2H_2O = Si(OH)_4 \ , \qquad (1)$$

has been shown to be predominant in combustion environments.[10] It is therefore of interest to examine the various factors involved in volatilization under oxidizing conditions as part of studies that are aimed at developing and characterizing materials that are stable at the high water-vapor pressures associated with various combustion conditions.

For the present work, it is assumed that the release of a volatile species is controlled by diffusion through a gaseous boundary layer adjacent to the solid oxide surface under laminar-flow conditions. These assumptions have been shown to be appropriate for combustion associated with moderate gas-flow velocities (~40 m/s) and should also apply to the slow-flow, large-diameter, flat-specimen conditions of the Keiser rig. The mass flux associated with volatilization, J, can be described as[10]

$$J \propto (\rho' vL/\eta)^{1/2}(\eta/\rho' D)^{1/3}(D\rho/L) \ , \qquad (2)$$

where v is the linear gas velocity, η is the gas viscosity, D is the interdiffusion coefficient of the volatile species in the major gas component, ρ is the concentration of the volatile species at the solid-gas interface, ρ' is the concentration of the major gas component, and L is the characteristic specimen length parallel to the flow direction and over which the volatility is averaged.

For the conditions associated with the Keiser rig, Eq. (2) reduces to

$$J \propto (v^{1/2} \bullet \Sigma p_{vol})/(p_{tot})^{1/2} \ , \qquad (3)$$

where p_{vol} is the partial pressure of a volatile species and p_{tot} is the total system pressure.

For the present case, in which the primary interest is in volatilization of oxides in the presence of water vapor, the formation of a volatile hydroxide product, $A_xO_{y+z}H_{2z}$, can be generally represented as

$$A_xO_y\,(s) + zH_2O\,(g) = A_xO_{y+z}H_{2z}\,(g) \qquad 4)$$

The equilibrium constant for this reaction, *K4*, can be expressed in terms of the activity of the oxide, $a(A_xO_y)$, and partial pressures as

$$K4 = p(A_xO_{y+z}H_{2z})/(p^z H_2O \bullet a(A_xO_y)) \qquad (5)$$

and is also related to the free energy of formation of $A_xO_{y+z}H_{2z}$, $\Delta G(A_xO_{y+z}H_{2z})$:

$$K4 = \exp(-\Delta G(A_xO_{y+z}H_{2z})/RT) \qquad (6)$$

where T is the absolute temperature and R is the universal gas constant. Combining Eqs. (5) and (6) yields

$$p(A_xO_{y+z}H_{2z}) = \exp(-\Delta G(A_xO_{y+z}H_{2z})/RT) \bullet p^z H_2O \bullet a(A_xO_y) \quad (7)$$

Assuming the reaction shown in Eq. (4) generates the only volatile species, and using Eq. (3), the mass flux of volatile species can be described as

$$J \propto n^{1/2} \bullet \exp(-\Delta G(A_xO_{y+z}H_{2z})/RT) \bullet p^z H_2O \bullet a(A_xO_y/(p_{tot})^{1/2} \quad (8)$$

A flux equation of the form shown in Eq. (8) has been shown to describe measurements of SiC and Si_3N_4 recession controlled by volatilization of SiO_2 quite well.[4] However, at low gas-flow velocities and modest pressures, as employed in many laboratory experiments, specimen mass losses due to volatilization are small [Eq. (8)] and thus difficult to measure, particularly because of large mass gains due to accelerated solid-state oxidation at elevated $p(H_2O)$.[1,2] This was the case for experiments previously conducted in the Keiser rig, which focused on the effects of elevated H_2O pressures (typically 0.3–0.0 atm) on oxidation of Si-based ceramics and environmental barrier coatings.[1,2,8] However, as shown by Eq. (8), mass fluxes for a given ν can be increased substantially by using higher H_2O pressures, particularly if z 1.

An example of how higher H_2O pressures can be used to generate more readily measurable mass fluxes can be determined for that of SiO_2 {Eq. (1), where, from Eqs. (4) and (8)

$$J \propto \nu^{1/2} \bullet \exp(-\Delta G(Si(OH)_4)/RT) \bullet p^2 H_2O \bullet a(SiO_2)/(p_{tot})^{1/2} \quad (9)$$

and $a(SiO_2) = 1$. Relatively high fluxes of $Si(OH)_4$ can be achieved by increasing $p(H_2O)$ since J is proportional to the square of the water-vapor pressure. Therefore, if there is no change in mechanism, low gas-flow velocities can be offset by higher $p(H_2O)$. This is illustrated in Figure 1, which plots J/J_o versus $p(H_2O)$ for the case represented by Eq. (9), where J_o is the $Si(OH)_4$ flux for typical combustor liner conditions [ν = 35 m/s, $p(H_2O)$ = 1.5 atm, T = 1200°C] and J is for the same temperature with $\nu = 6\times10^{-4}$ m/s (typical gas-flow velocity in the Keiser rig). Note from Figure 1 that the normalized flux can be increased by approximately two orders of magnitude by increasing $p(H_2O)$ from 1.5 atm (pressure typically used) to 18 atm.

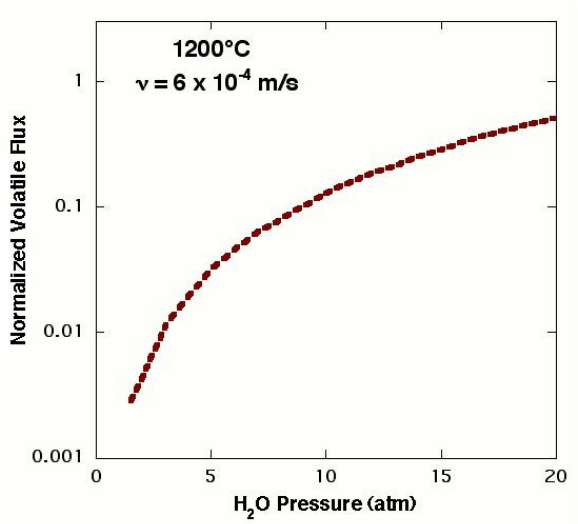

Figure 1. Plot of flux of $Si(OH)_4$ due to volatilization of SiO_2 in an H_2O-containing environment at 1200°C, a total pressure of 20 atm, and a gas velocity of $6X10^{-4}$ m/s as a function of the partial pressure of H_2O.

The results shown in Figure 1 show that the high-temperature, high-pressure capability offered by a Keiser rig (or similar exposure facility) can be used to yield relatively high volatility fluxes by conducting experiments at substantially higher water-vapor pressures. Therefore, this approach can be used to screen and rank the volatility resistance of candidate ceramics for use in combustion environments as bulk materials or protective surface coatings (such as those needed for EBCs). However, such use is predicated on no change in the rate-controlling volatilization mechanism as the water-vapor pressure is increased. Given the nature of the process described above (diffusion of volatile product across a laminar gas-boundary region), it is not expected that changes in pressures over the range indicted in Figure 1 would result in a change in mechanism.

Referring to Eq. (8), it is important to note that the ability to use higher water-vapor pressures to

screen the volatilization resistance of candidate materials in systems using low gas-flow velocities depends critically on *z*, the number of moles of H_2O needed to form one mole of volatile product [see Eq. (4)]. A low *z* value would make it more difficult to achieve easily measurable volatile fluxes by increasing the water-vapor pressure over a reasonable range. As an example, the difference in the normalized flux between $z = 1$ and $z = 2$ is shown in Figure 2 for $\nu = 6 \times 10^{-4}$ m/s and 1200°C. While there is about an order of magnitude increase in the volatile flux when $p(H_2O)$ is increased from 1.5 to 20 atm for $z = 1$, this enhancement is still about 10× less than for $z = 2$. Thus it is important to understand the nature of the predominant volatility reaction [Eq. (4)] to determine if $p(H_2O)$ elevation will yield the desired measurements and to effectively compare relative results for *J* for different oxides.

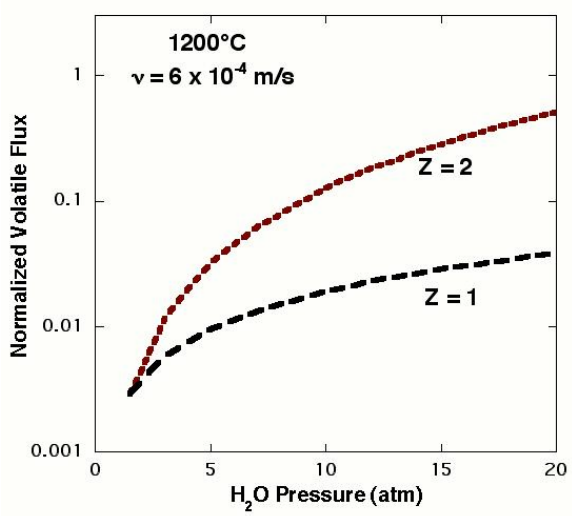

Figure 2. Plot of normalized volatile flux of a volatile species in an H_2O-containing environment at 1200°C, a total pressure of 20 atm, and a gas flow velocity of 6×10^{-4} m/s as a function of H_2O pressure illustrating difference between z = 1 and z = 2.

Proof-of-Principle—Initial Material Exposures in Keiser Rig at High H_2O Pressure

The gravimetric data from the first set of exposures at 1250°C, 20 atm total system pressure, and 18 atm H_2O are shown in Figure 3. All three aluminosilicates (BSAS, BAS, SAS) exhibited similar kinetic behavior and had lower total mass losses and rates of volatilization than the standard materials

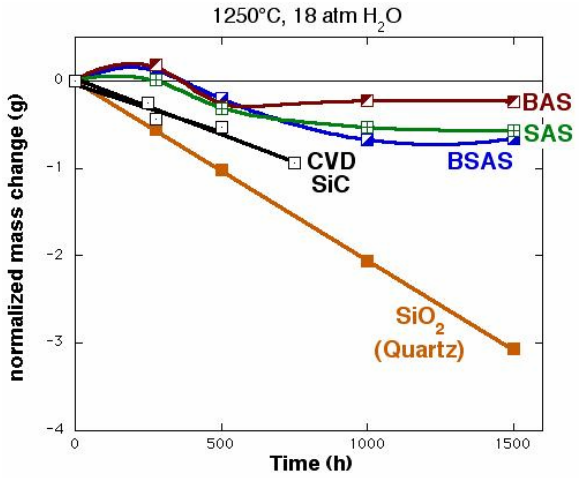

Figure 3. Initial gravimetric data for BSAS, BAS, SAS, CVD SiC, and SiO_2 exposed at 1250°C and18 atm H_2O for 1500 h.

included, SiO_2 and SiC. At times greater than 500 h, the volatilization rate of SiO_2 was approximately an order of magnitude greater than that for the aluminosilicates. This difference is about what would be expected based on results from combustor liner exposures.[7]

Quantitative estimates of the material recession rates will require more detailed tracking of specimen dimensions and accompanying microstructural analyses. These controlled exposures will be conducted starting in FY 2005. However, the volatilization trends are clear from the results in Figure 3. Therefore, these findings provide the proof-of-principle of this approach of using simple high-pressure, low-gas-velocity exposures for qualitative differentiation of the volatilization resistance among different candidate materials being developed for EBC applications. An added benefit of doing these experiments at high H_2O pressures (versus standard lower pressures but high gas velocities) is that permeation resistance can also be evaluated.

Conclusions

During FY 2004, ORNL's Keiser rig was modified to accommodate very high H_2O pressures of ~20 atm. Keiser rig exposures have previously been used to accurately assess an EBC's ability to effectively protect Si-based ceramics. In the present work, an analysis based on volatility reactions and mass flux of volatilized species has shown that operation at very high H_2O pressures can be used to

compensate for the low gas velocities (~6×10^{-4} m/s) in the Keiser rig. Operating at much higher H_2O pressures can expand the use of the Keiser rig to evaluate the volatility of candidate EBCs in addition to addressing EBC thermal stability and protective capability issues. An initial set of exposures of Ba- and Sr-based EBCs and chemically vapor-deposited SiC and quartz at an H_2O pressure of ~18 atm and 1250°C for 1500 h validated the principles discussed. Controlled experiments using the same exposure conditions on a variety of additional materials will be conducted during FY 2005.

References

1. K. L. More, P. F. Tortorelli, M. K. Ferber, and J. R. Keiser, "Observations of Accelerated SiC Recession by Oxidation at High Water-Vapor Pressures," *Journal of The American Ceramic Society*, **83**(1), 211–13 (2000).
2. K. L. More, P. F. Tortorelli, M. K. Ferber, J. R. Keiser, N. Miriyala, W. D. Brentnall, and J. R. Price, "Exposure of Ceramics and Ceramic Matrix Composites in Simulated and Actual Combustor Environments," *Journal of Engineering for Gas Turbines and Power*, **122**, 212–18 (2000).
3. E. J. Opila, and R. E. Hann, "Paralinear Oxidation of CVD SiC in Water Vapor," *Journal of The American Ceramic Society*, **80**(1), 197–205 (1997).
4. R. C. Robinson and J. L. Smialek, "SiC Recession Caused by SiO_2 Scale Volatility Under Combustion Conditions: I: Experimental Results and Empirical Model," *Journal of The American Ceramic Society*, **82**(7), 1817–25 (1999).
5. H. E. Eaton, G. D. Linsey, K. L. More, J. B. Kimmel, J. R. Price, and N. Miriyala,"EBC Protection of SiC/SiC Composites in a Gas Turbine," ASME Paper 2000-GT-631 (2000).
6. K. N. Lee, "Current Status of EBCs for Si-Based Ceramics," *Surface Coatings and Technology*, **133–134**, 1–7 (2000).
7. K. L. More, P. F. Tortorelli, L. R. Walker, J. B. Kimmel, N. Miriyala, J. R. Price, H. E. Eaton, E. Y. Sun, and G. D. Linsey, "Evaluating EBCs on Ceramic Matrix Composites After Engine and Laboratory Exposures," ASME Paper GT-2002-30630 (2002).
8. J. B. Kimmel, J. R. Price, K. L. More, P. F. Tortorelli, E. Y. Sun, and G. D. Linsey, "The Evaluation of CFCC Liners After Field Testing in a Gas Turbine–IV," ASME Paper GT-2003-38920 (2003).
9. K. L. More, P. F. Tortorelli, and L. R. Walker, "Verification of an EBC's Protective Capability by First Stage Evaluation in a High-Temperature, High-Pressure Furnace," ASME Paper GT-2003-38923 (2003).
10. E. J. Opila, J. L. Smialek, R. C. Robinson, D. S. Fox, and N. S. Jacobsen, "SiC Recession Caused by SiO2 Scale Volatility Under Combustion Conditions," *Journal of The American Ceramic Society*, **82**(7), 1826–34 (1999).

Awards/Patents

Karren More and Peter Tortorelli of ORNL received the National Aeronautics and Space Administration's (NASA's) "Turning Goals Into Reality" award in 2004. The award acknowledges outstanding contributions and exceptional progress toward achieving one of the program goals and objectives of the Office of Aeronautics. More and Tortorelli were part of a partnership receiving the award for collaborative work on coated ceramic matrix composite components for gas turbine applications. Other team members were NASA Glenn, U.S. Army Research Laboratory, DOE, GE Aircraft Engines, Pratt & Whitney, United Technologies Research Center, Solar Turbines, GE Power systems Composites, COI Ceramics, Goodrich Corp., Ohio Aerospace Institute, the University of Toledo, Cleveland State University, and QSS Group.

Publications/Presentations

K. L. More, P. F. Tortorelli, T. Bhatia, and G. D. Linsey, "Evaluating the Stability of BSAS-Based EBCs in High Water-Vapor Pressure Environments," presented at Turbo Expo 2004, Vienna, Austria, June 6–10, 2004, and published as ASME Paper #GT2004-53863.

D. W. Coffey, K. L. More, and T. Brummett, "TEM Evaluation of Thin Interfacial Coatings on Continuous Fibers Using the Focused Ion Beam Technique," presented at the Microscopy Society of America Annual Meeting, Savannah, GA, August 1–5, 2004, and published in *Microscopy and Microanalysis*, **10**(2) (2004).

Saint-Gobain Hot-Section Materials Development

Vimal K. Pujari, Robert H. Licht, Ara M. Vartabedian, William T. Collins, and James M. Garrett
Saint-Gobain Ceramics & Plastics, Inc.
Northboro Research & Development Center
9 Goddard Road, Northboro, MA 01532
(508) 351-7929; e-mail: vimal.k.pujari@saint-gobain.com

DOE Technology Development Manager: Debbie Haught
(202) 586-2211; fax: (202) 586-7114; e-mail: debbie.haught@ee.doe.gov
ORNL Technical Advisor: Terry Tiegs
(865) 574-5173; fax: (865) 574-4357; e-mail: tiegstn@ornl.gov

Objectives

- Develop and improve a cost-effective, reliable monolithic silicon nitride material for hot-section components in distributed energy advanced microturbine systems
- Through surface engineering, demonstrate sufficient environmental stability for component operation without an environmental barrier coating (EBC), or with a compatible EBC

Approach

- Characterize and improve the material properties of NT154 silicon nitride, including machined and as-processed (AP) surfaces
- Fully characterize green-machined NT154 specimens and components, and continue to optimize green-machining process
- Evaluate candidate surface modification of NT154 materials in recession-resistance tests and develop surface modification procedures for these candidate materials

Accomplishments

- Through the use of a new hot isostatic pressing (HIP) process, achieved AP strengths of up to 717 MPa for NT154 silicon nitride, demonstrating a 46% improvement
- Manufactured several complex-shaped microturbine rotors using the new HIP process, achieving an excellent part-to-part variation of 0.006 in., a concentricity of 0.003 in., and an average surface roughness of 30 µin. Biaxial flexure AP strengths of samples taken from the blade and hub region were measured to be 596 and 706 MPa, respectively. Fully machined biaxial flexure discs cut from a shaft section had strength and Weibull modulus values of 960 MPa and 24.4, respectively.

Future Direction

- Continue development of recession-resistant solutions both internally and through outside collaborations and evaluate the candidate materials in rig tests
- Continue with material improvements to NT154 silicon nitride
- Continue with improvements to net shape forming capabilities and supply components for contractor testing

Introduction

Silicon nitride offers excellent thermomechanical properties such as high strength and creep resistance at elevated temperatures, a low coefficient of thermal expansion, and high thermal shock resistance. This makes it a suitable candidate material for high-temperature gas turbine components such as integrally bladed rotors (IBRs), vanes, and combustor liners. During the early 1990s extensive effort at Saint-Gobain was directed towards the development of a high-temperature silicon nitride–based ceramic material (NT154), net shape forming processes, and prototype component field evaluations.[1] For example, under the U.S. Department of Energy's Ceramic Technology Project, a highly reliable closed-loop processing (CLP) methodology[2] was developed and led to significant improvements in the properties of NT154 silicon nitride.

The goal of this program is to resume development of NT154 and the related processes as they relate to high-temperature (1100–1300°C) microturbine applications for the distributed generation of power (approximately 25–500 kW). The successful use of ceramics as an enabling material for achieving higher-temperature microturbine operation will result in improved efficiency, reduced fuel use, and lower emissions.

The technical effort involved a three-pronged approach: (a) NT154 material development and improvement; (b) net shape forming development of rotors and vanes; and (c) development of recession-resistant solutions for silicon nitride in a high-temperature (1100–1300°C), high-gas-velocity (20–50 m/s), humid (10% H_2O) gas turbine environment. The progress towards each of these three areas is highlighted.

Approach

As noted above, Saint-Gobain is following a three-pronged approach in the development of silicon nitride components for the gas turbine markets: material development, net shape forming, and recession control. It is believed that all areas are crucial in the commercialization of ceramic components. During Phase I of the contract, the focus was on resuming development of NT154 silicon nitride. NT154 silicon nitride is a glass-encapsulated composition formed through HIP and containing 4 wt % Y_2O_3. Work on the composition of NT154, which was originally developed in the late 1980s, had been dormant since the mid-1990s. This goal of resuming NT154 production with comparable or improved properties was achieved in 2003.

Continued improvement of NT154 has been ongoing. A major effort has gone into optimizing the AP strength of NT154. There has also been an effort to improve high-temperature strength and to understand the phenomenon of slow crack growth.

A new focus in the area of materials development is recession control. Material recession, caused by volatilization in humid gas turbine environments, is an issue for silicon nitride and has been reported in the literature. Methodologies for improving the recession resistance of NT154 are being investigated as part of Phase II of the contract, which began in early 2004.

Net shape forming has been a major focus area. Initially, both green-machining and casting methods have been explored, with the main focus on green machining. The current green-machining procedure was developed and optimized during 2002 and 2003. Net shape components made by green machining were densified and analyzed during 2004.

Results

Material Development and Improvement

After development of NT154 resumed in 2003, the first set of tiles was delivered to ORNL. The fast fracture strength of this set of NT154 tiles agreed with historical values for the material (Figure 1). The second set of tiles delivered to ORNL for

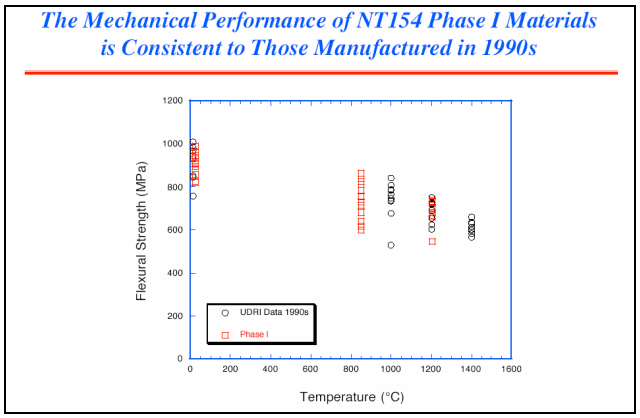

Figure 1. Fracture strength of NT154, 1990s development phase and 2003 measurements. (Courtesy of H. T. Lin, ORNL)

mechanical property evaluation was used to examine the effect of the binder system being used for green machining.

The room-temperature results from that testing are shown in Figure 2. The results are very similar to those measured for the first set of tiles, which had minimal binder content. In essence, the green-machining binder system seems to have had minimal impact on properties at room temperature. These results have been confirmed internally. In fact, internal testing indicated that high-temperature fast-fracture strength actually increases with the addition of the binder system. The strength increase was as much as 21% at 1200°C, with a high of 766 MPa.

The main area identified for improvement continued to be AP strength, which has historically been a concern for silicon nitride. The glass-encapsulated HIP process used to densify NT154 creates a reaction layer in the silicon nitride due to its interaction with the glass encapsulant. In addition to the decreased toughness present in the reaction layer, the glass–silicon nitride interaction can also create surface defects. Combined, these two factors lead to an AP strength that is less than the strength of the bulk-machined NT154 specimen. Therefore, the objective was to minimize the glass–silicon nitride interaction. This objective was accomplished using a new proprietary HIP process. The process was developed in a laboratory-scale HIP during 2003 and optimized for production in 2004. When optimized, the new HIP process results in a near-surface toughness that is comparable to the toughness of the bulk material and a surface roughness similar to the roughness of the sample in the green state.

The AP flexural strength of NT154 samples from various HIP runs is shown in Figure 3. It can clearly be seen that the new process always results in improved AP strength. The average improvement has been 46%, with a maximum AP strength of 717 MPa.

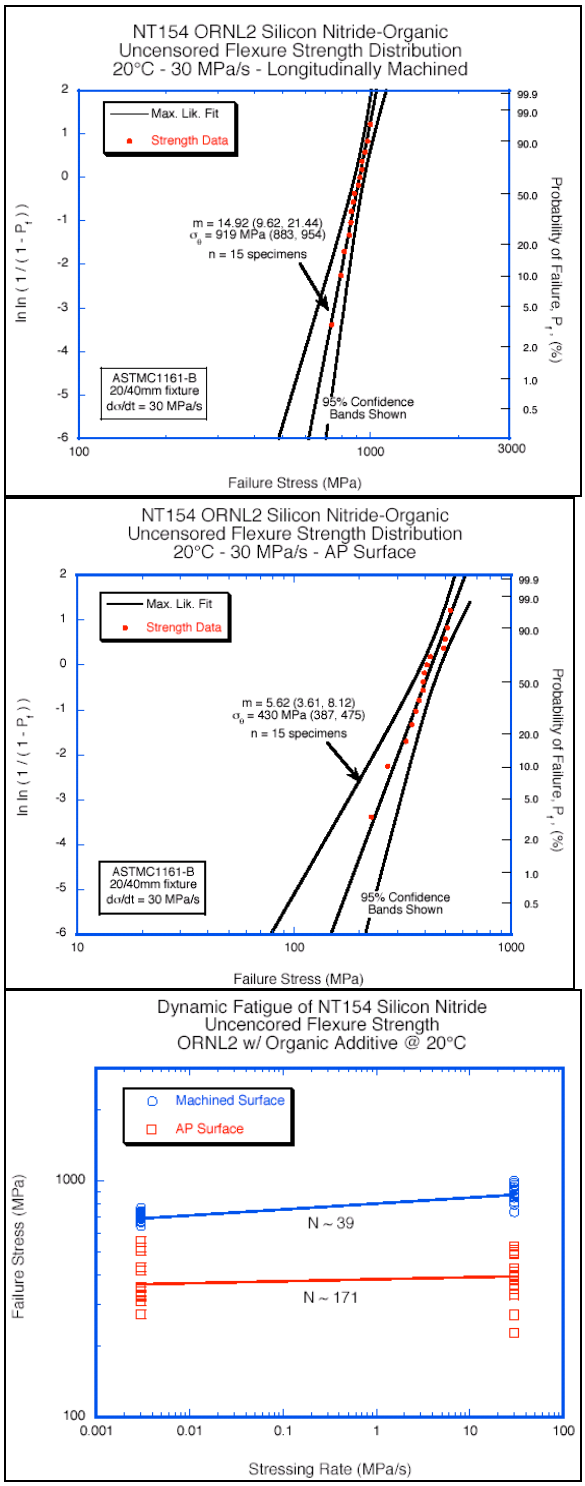

Figure 2. Mechanical property data for the green machining composition of NT154. (Courtesy of H. T. Lin, ORNL)

Net Shape Forming

Four radial rotors of an experimental complex-shaped microturbine rotor design were green-machined using procedures developed during 2002 and 2003. The average surface roughness of the green rotors is ~30 µin (~0.8 µm Ra). Coordinate

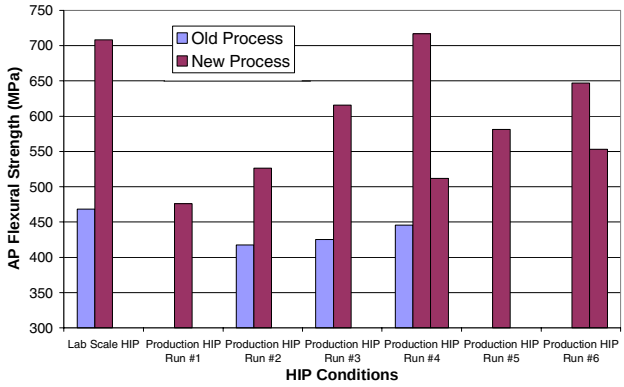

Figure 3. AP strength of old and new HIP processes.

measuring machine (CMM) measurements on the green rotors confirmed that all measurements were within 0.004 in. of the nominal, which is an indication of the consistency and accuracy of the green forming process.

Two of the green-machined rotors (Figure 4) have been densified with the proprietary new HIP process. The two rotors have an excellent average surface roughness of 30–33 μin on the AP surfaces. Based on the CMM measurements taken, the two rotors exhibited a maximum part-to-part variation of 0.006 in., which is an indication of the consistency of the process. A measured concentricity within 0.003 in. for the two rotors is an indication of the uniform shrinkage seen with this process.

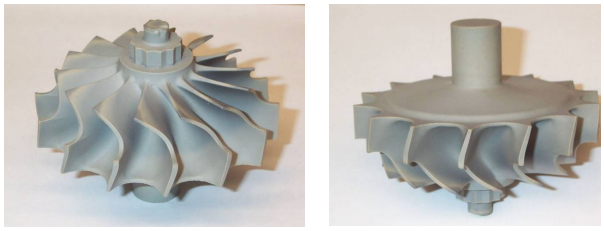

Figure 4. Dense NT154 microturbine rotor.

The two rotors were delivered to ORNL for evaluations of mechanical properties. Disks core-drilled from the blade and hub regions are being tested in biaxial flexure to establish the AP and bulk strength of actual components. The test data for the first rotor and the blade AP data for the second rotor have been completed. For the first rotor, the biaxial flexure AP strengths for the blade and the hub region were measured to be 527 and 706 MPa, respectively (Figure 5a). Slight adjustments to the green-machining process resulted in an ~10% surface finish improvement for the second rotor. As a result, the blade AP strength for the second rotor increased to 596 MPa, a 13% improvement. Machined biaxial flexure discs cut from the hub section of the first rotor were also tested (Figure 5b). A characteristic strength of 960 MPa and a Weibull modulus of 24.4 were measured. These AP and machined biaxial strength values from the rotors compare well with the data generated using modulus of rupture bars machined from tiles. This series of tests suggest that the mechanical property data generated from test bars have been reproduced in large net shaped components.

The additional two rotors will be densified in the near future. After appropriate analyses and measurements, spin testing is planned for these rotors.

Recession Control

Recession, which is due to volatilization in high-temperature, humid gas turbine environments, is an issue for silicon nitride and silicon carbide, and has been reported in the literature.[3] Recession-resistant solutions for NT154 are being investigated as part of Phase II of this contract.

Baseline (uncoated) NT154 tiles were supplied to ORNL for Keiser rig testing to evaluate the environmental stability in the microturbine environment. Silica-scale-thickness data for 1000 h of testing are shown in Figure 6. Micrographs showing the silica scale after 500 h of testing seem to indicate that microstructural differences between the samples appear to impact the silica scale thickness, with the coarser microstructure resulting in a decreased silica scale thickness. In general, the fact that the measured thickness of the silica scale formed on the NT154 tiles is very similar to the measured thickness on other silicon nitride samples verifies the need for an environmental barrier coating (EBC) or a suitable surface modification.

The development of a recession-resistant solution for NT154 consists of three key steps: (a) identification of candidate materials, (b) application of recession-resistant materials on NT154, and (c) densification of recession-resistant material.

Candidate materials have been chosen on the basis of literature data, thermodynamic calculations, and available coefficient of thermal expansion (CTE) data. A close CTE match to NT154 (3.3×10^{-6}/°C for 20–1370°C) is critical to crack-free coatings or surface layers.

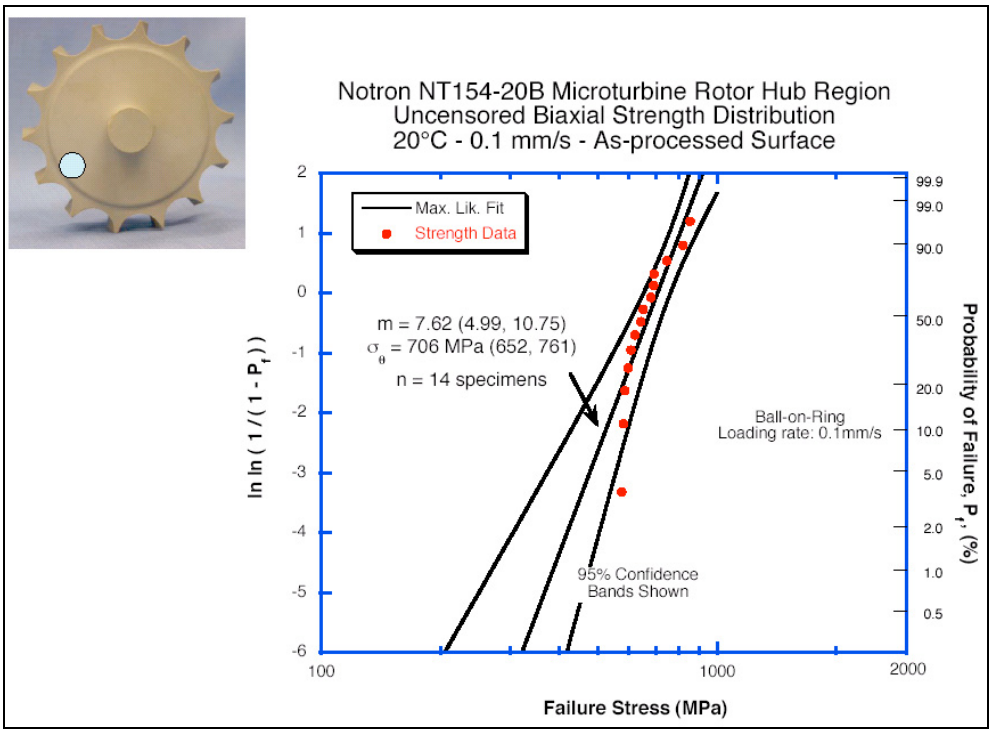

(a)

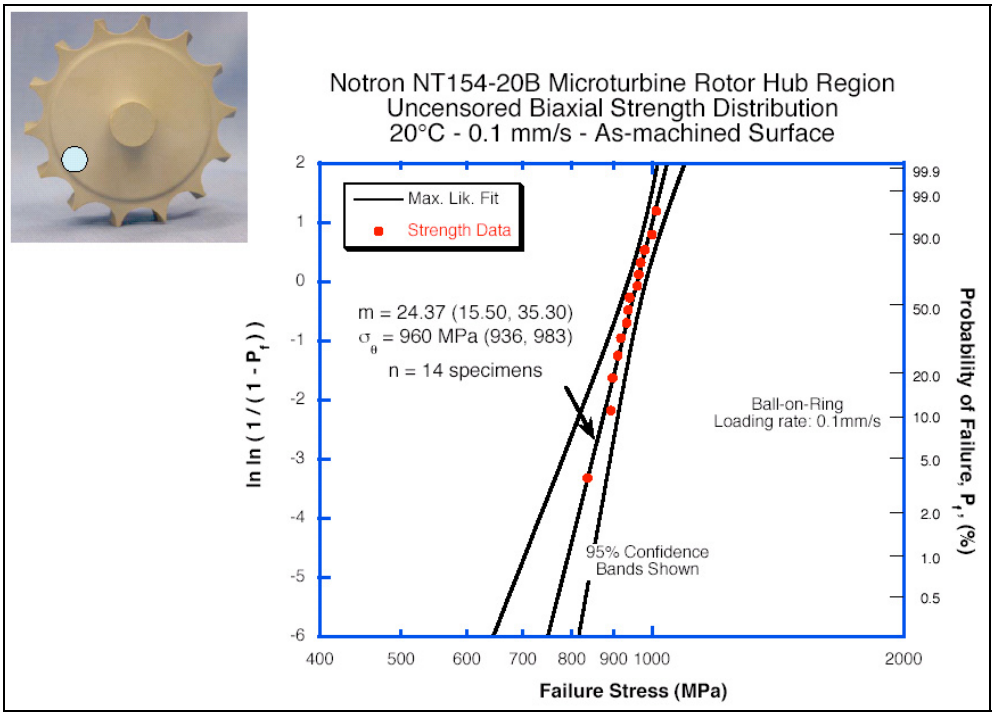

(b)

Figure 5. AP (a) and machined (b) biaxial flexure strength of hub region of NT154 rotor. (Courtesy of H. T. Lin, ORNL)

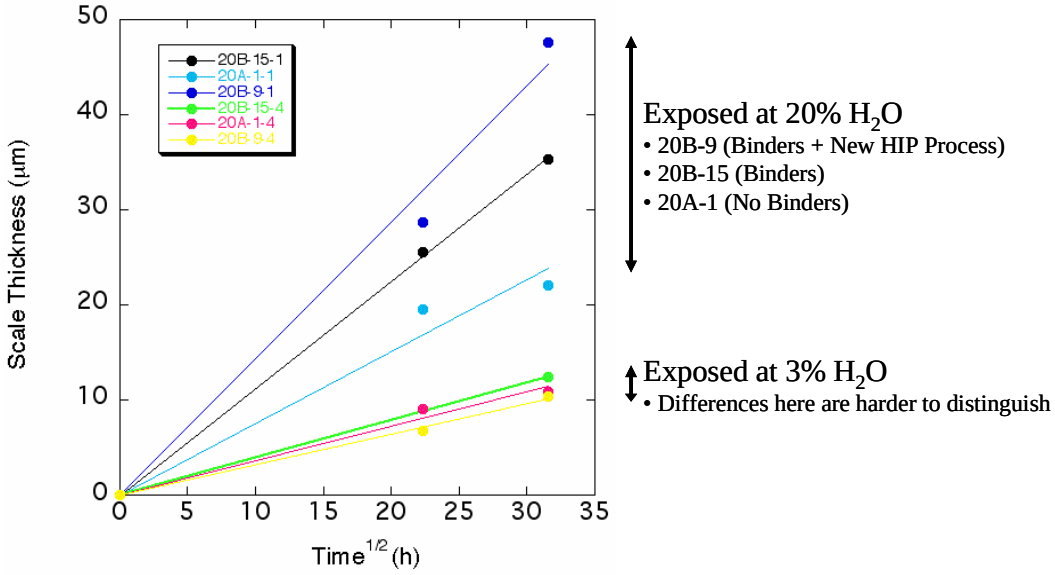

Figure 6. Keiser rig data for NT154. (Courtesy of K. More, ORNL)

Two application and densification approaches were evaluated internally during 2004: pack cementation and HIP Engineered Environmental Protection Surface (HEEPS).

The pack cementation approach consists of embedding dense NT154 in a reactive powder bed and firing it at a specified temperature in a specified environment. The intent is to completely transform the surface of the silicon nitride into a candidate recession-resistant material.

The internal pack cementation work concentrated on oxide powder beds. Most of the work was done in air at 1500–1600°C. The intent was to form continuous layers of rare earth silicates and/or disilicates, which have been shown to have low volatility in the turbine environment. In general, for the conditions used, only minor modifications to the silicon nitride surface were seen. The issues include incomplete transformation of the surface, low reaction depths (typically <10 μm), near-surface cracking, and creep deformation of the silicon nitride during 1600°C pack cementation runs. As a result, the samples showed only a modest improvement over baseline NT154 in an internal recession test. SEM images of a representative collection of pack cementation samples are shown in Figure 7.

HIP Engineered Environmental Protection Surface, or HEEPS, is a patented approach to co-densify an EBC coating and NT154 during the typical NT154 HIP process (high-temperature HEEPS).

Therefore, the EBC coating is applied to green NT154 prior to the HIP step. Various rare earth oxide and silicate coatings were explored with limited success.

It appears that for the coatings applied, there is an issue with coatings diffusing into the silicon nitride and possibly also into the HIP glass encapsulant. Microprobe scans of cross sections indicate that the coating penetrates as much as 5 mm into the sample. Also, there is no evidence of a coating in the samples examined. To date, the HEEPS samples tested in the internal recession rig have shown no improvement over baseline NT154. The solution involves either choosing a coating composition that is more stable at the higher NT154 densification HIP temperature, or applying a suitable composition onto densified NT154 and performing a second HIP run at a lower temperature suitable for the coating material. The latter approach (low-temperature HEEPS) is currently being examined.

An internal recession test rig was developed to help screen candidate materials and coatings. The test has been very useful in screening out the poor samples and helping to identify the samples that are worth subjecting to further, more extreme testing. The internal rig is set up in a high-purity alumina tube furnace. Air is flowed through heated deionized water into one end of the tube and past the samples (which are placed on alumina shelves inside the tube); then the water is condensed out and collected

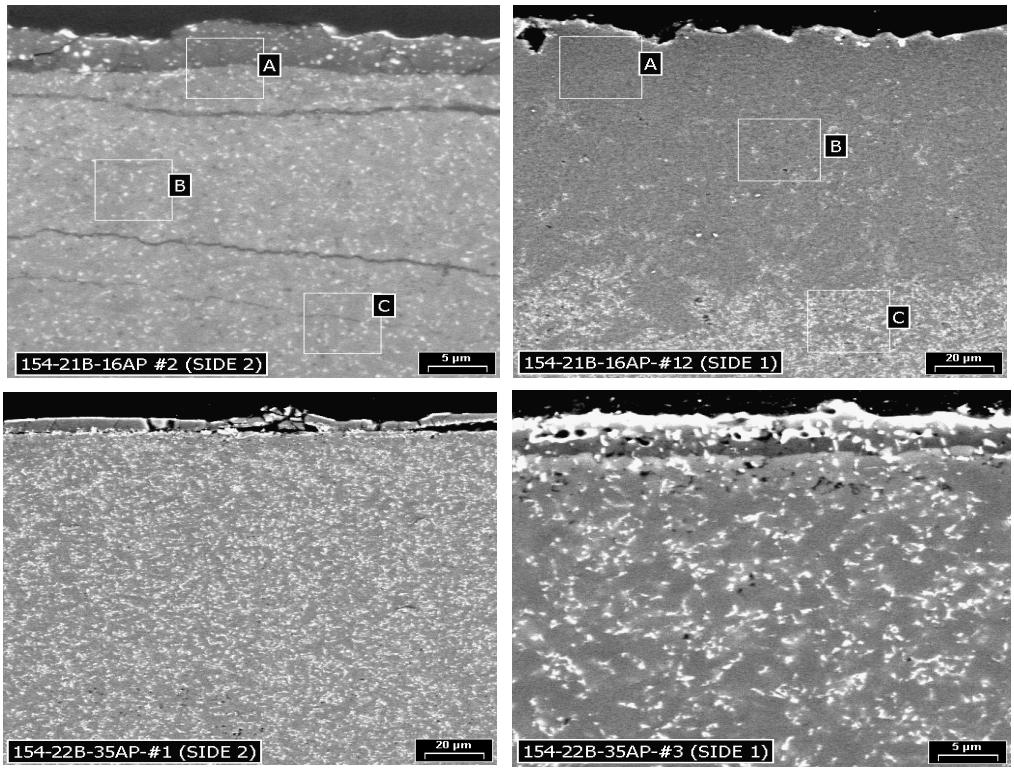

Figure 7. SEM images of cross sections of pack cementation NT154 samples.

on the other end of the tube. A pump keeps the water level, and therefore the water temperature, constant throughout the run. The percentage of water and the flow rate of the air can be controlled.

A typical recession test in the internal test rig is run at 1200°C, ~50% H_2O, and ~0.2 m/s air flow rate through the tube for a total of ~72 h. The samples are weighed before and after the test, and the mass change is normalized to exposed surface area and time. The results from one of the runs, listed in order from best to worst, are shown in Table 1.

In addition to its ongoing internal development of recession resistance, Saint-Gobain is collaborating with several outside organizations. These collaborations range from supplying NT154 for experimentation (to United Technologies Research Center and ORNL) to a two-way development program set up with Ceramatec.

Conclusions

Saint-Gobain has reintroduced and reestablished NT154 high-temperature silicon nitride for use in turbine applications. Further improvements to the HIP process resulted in a 46% improvement in AP strength.

Net shape forming by green machining has been developed and demonstrated on several rotors. Excellent dimensional control and surface finish have been shown. Test specimens machined from rotors were tested in biaxial flexure at ORNL. Machined strengths up to 960 MPa and AP strengths up to 706 MPa have been measured. The series of tests suggest that the mechanical property data generated from test bars have been reproduced in large net shaped components.

Work is ongoing in the development of recession resistance for NT154. The development of a recession-resistant solution for NT154 consists of identifying candidate materials, applying recession-resistant materials onto NT154, and densifying recession-resistant material. Internal research on pack cementation and HEEPS was reviewed.

Environmental Protection Systems for Ceramics in Microturbines and Industrial Gas Turbine Applications—Part A: Conversion Coatings

Stephen D. Nunn
Metals and Ceramics Division
Oak Ridge National Laboratory, P.O. Box 2008, M/S 6087
Oak Ridge, TN 37831
(865) 576-1668; fax: (865) 574-4357; email: nunnsd@ornl.gov

DOE Technology Development Manager: Debbie Haught
(202) 586-2211; fax: (202) 586-7114; e-mail: debbie.haught@ee.doe.gov
ORNL Technical Advisor: Terry Tiegs
(865) 574-5173; fax: (865) 574-4357; e-mail:tiegstn@ornl.gov

Objective

- Develop low-cost protective coatings for silicon-based ceramics that may be used in microturbines and industrial gas turbines to enable increasing the engine operating temperature and improve the overall turbine efficiency.

Approach

- Investigate the low-cost pack cementation process for producing selected conversion coating layers on ceramic substrates.
- Evaluate properties of coated substrates, including resistance to oxidation/corrosion at elevated temperatures in the presence of water vapor.

Accomplishments

- Produced ytterbium-based coating compositions on commercial silicon nitride material substrates that appear to be stable in high-temperature, humid environments.
- Produced ytterbium-based coatings on a silicon carbide fiber/silicon carbide matrix composite fabricated by an industrial collaborator.
- Mechanical property testing of coated silicon nitride materials indicate a decrease in strength of 20 to 35% compared with uncoated materials .

Future Direction

- Refine the pack cementation coating process and demonstrate the ability to produce uniform coatings on complex-shaped ceramic substrates.
- Continue to evaluate promising coating compositions for resistance to degradation in the gas turbine engine environment.

Introduction

The use of advanced structural ceramics, such as silicon nitride (Si_3N_4), in gas turbine engines can allow operation at higher temperatures, thus improving engine efficiency. Silicon nitride normally forms a protective silica layer when exposed to air at high temperatures. However, in the combustion engine environment, the presence of water vapor results in the volatilization of the silica layer, leading to erosion and degradation of the component. An environmental barrier coating (EBC) for silicon nitride that resists the effects of the engine environment is needed to enable use of these advanced materials in microturbines and industrial gas turbine engines.

A coating process called pack cementation has been used for many years to coat turbine engine components made from metallic superalloys. This process is being adapted to produce coatings on ceramic materials. When a ceramic substrate is heated while embedded in a reactive powder pack, a surface conversion coating can be formed at the surface of the part. The composition of the resulting coating will depend on the composition of the pack, the temperature, the furnace atmosphere, and the composition of the substrate.

Approach

Three commercial silicon nitrides were evaluated in coating tests: Honeywell AS800, Kyocera SN282, and Saint-Gobain NT154. In addition, a melt-infiltrated silicon carbide/silicon carbide (SiC/SiC) composite from an industrial collaborator was examined. The ceramic substrates were processed in powder packs that were formulated to produce strontium (Sr) -based and ytterbium (Yb) -based coatings. Previous work has indicated coatings of these general compositions had superior corrosion resistance.

Processing temperatures varied from 1200 to 1600°C, and furnace atmospheres of either air or argon (Ar) were used. In most cases, multiple heating steps were employed to produce the final coating composition.

After the pack cementation process, samples were evaluated by X-ray diffraction analysis to identify the composition of the coating that was formed. Samples were cross-sectioned and polished to examine the morphology of the coating by optical microscopy and scanning electron microscopy (SEM). Coating surfaces were also examined by SEM. Selected samples were tested by 4-point bending to determine the flexure strength of both coated and uncoated materials. The protective characteristics of the coatings were evaluated by exposing samples at 1200 to 1400°C in flowing air containing 20% water vapor.

Results

Pack Cementation Coating

Coatings of Sr- and/or Yb-based compounds were produced on Si_3N_4 and SiC/SiC composite substrates. Powder pack compositions of $Sr(NO_3)_2$ + Al_2O_3, Yb_2O_3 + Al_2O_3, and Yb_2O_3 alone were used to form the coatings. A listing of the coating compositions that were formed on the different substrate materials is shown in Table 1.

Table 1. Coating phases formed by pack cementation processing.

Substrate	Coating compositions
AS800	$SrSiO_3$ + unknown phase
	$SrAl_2Si_2O_8$ + $LaAl_{11}O_{18}$ + glass
	$Yb_2Si_2O_7$ + SiO_2
SN281/282	$SrAl_2Si_2O_8$ + $Lu_3Al_5O_{12}$
	$(Lu,Yb)_2Si_2O_7$ + $(Lu,Yb)_2SiO_5$
NT154	$SrSiO_3$ + unknown phase
	$Yb_3Al_5O_{12}$
	$Yb_2Si_2O_7$ + SiO_2
	Yb_2SiO_5 + SiO_2
SiC/SiC	$Yb_2Si_2O_7$ + Yb_2SiO_5

All of these compounds are refractory and, individually, are stable in air. The predominantly $SrSiO_3$ coatings that were formed on AS800 and NT154 at 1200°C in Ar were found to form a low-melting-temperature compound when exposed to air above 1200°C. $SrSiO_3$ has a melting temperature of 1580°C, but the mixed composition of the coating and the chemical elements present in the substrates (Si_3N_4) + sintering aids) combined to form a low-melting-point compound under oxidizing conditions. Similarly, $SrAl_2Si_2O_8$, which could be formed in a mixed-phase coating on AS800 and SN282 at 1400°C in Ar, was unstable when heated in air.

The Yb coating compounds were found to be more stable than the Sr compounds. The rare earth garnet phase, $Yb_3Al_5O_{12}$, was formed on NT154 when processed at 1400°C in Ar. This coating layer

is shown in the optical micrograph in Figure 1a. This compound was stable at 1200°C in air, but converted to $Yb_2Si_2O_7$ + SiO_2 + mullite ($Al_6Si_2O_{13}$) when heated to 1400°C in air. A $Yb_2Si_2O_7$ + SiO_2 coating could be formed directly on NT154 and was found to be stable at temperatures exceeding 1500°C in air.

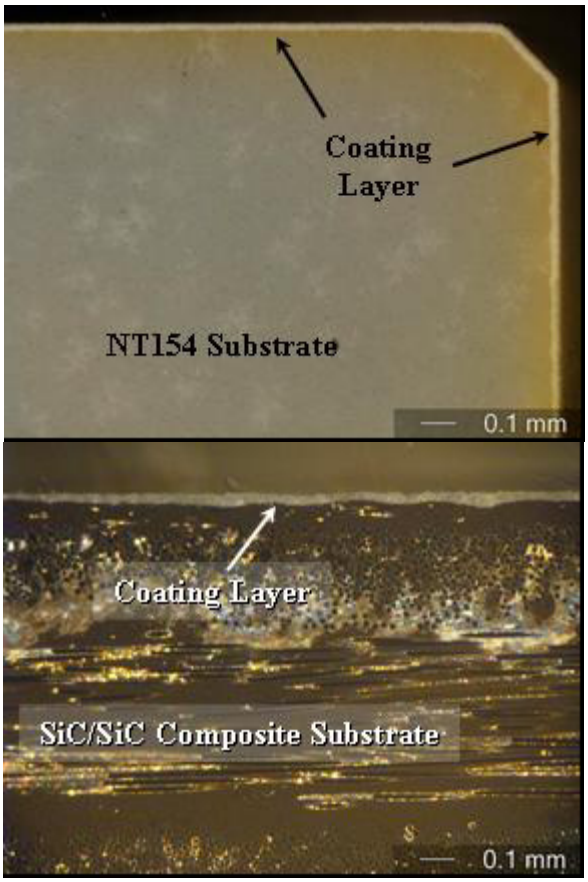

Figure 1. Photomicrographs of the polished cross-section of (above) NT154 silicon nitride coated with $Yb_3Al_5O_{12}$ and (below) SiC/SiC composite coated with $Yb_2Si_2O_7$ + Yb_2SiO_5 showing the coating layer formed on the surface of the substrate.

The SiC/SiC composite material was much less reactive with the powder packs than the Si_3N_4 materials and thus required higher processing temperatures to produce a coating. The most promising coating that was formed on SiC/SiC contained both $Yb_2Si_2O_7$ and Yb_2SiO_5. This coating was produced at 1600°C in air using a Yb_2O_3 pack and is shown in the micrograph in Figure 1b.

Mechanical Properties

Selected samples of the three silicon nitride materials were tested for flexure strength with and without a coating. Test samples measuring 3×4×50 mm were placed in a 4-point bend test fixture and loaded to failure. The results of the tests are shown in Figure 2. The AS800 and the SN282 samples, which underwent pack cementation in a SrO + Al_2O_3 pack at 1500°C, show similar behavior with a strength loss of ~35% compared with the uncoated material. Because of the instability of the Sr compounds on Si_3N_4, the coating on the AS800 samples consisted of SiO_2 + $La_2Si_2O_8$, and on the SN282 samples, $Lu_2Si_2O_7$ + glass. The NT154 material, which was coated in a Yb_2O_3 + Al_2O_3 pack at 1400°C and formed $Yb_3Al_5O_{12}$, showed less strength loss (22%) and, because of the higher strength of the base ceramic, the coated sample strength was comparable to the strength of the uncoated AS800 and SN282. SEM examination of the coatings showed microcracks in the coating on AS800 (see Figure 3) and through-thickness bubbles in the coating on SN282. Both of these features can act as stress concentrators that can lower the fracture strength of ceramic materials. These types of flaws were not observed in the coating on the NT154 substrate.

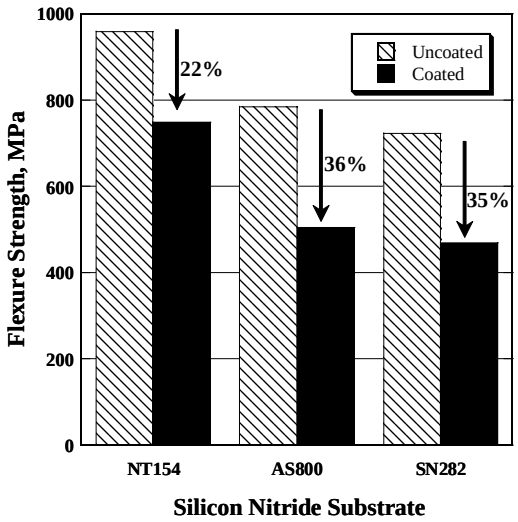

Figure 2. Comparison of the flexure strength of silicon nitride materials with and without a coating layer.

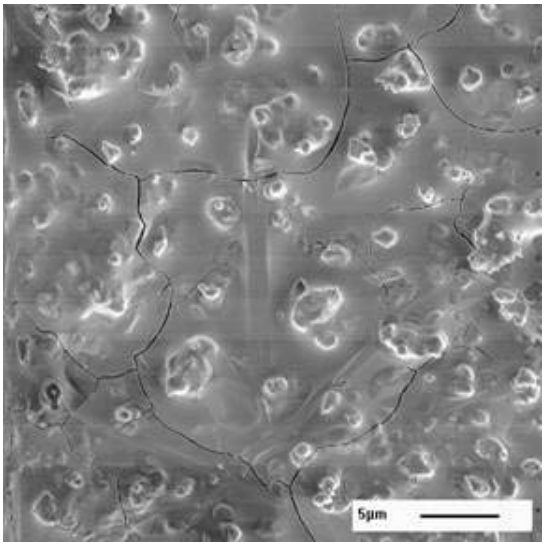

Figure 3. SEM micrograph of the coating surface of an AS800 flexure test specimen showing microcracks in the coating layer.

Exposure Testing

A new exposure testing capability was established in order to conduct screening tests of the coated materials. To determine the protective behavior of the various coating compounds, a high-temperature tube furnace was set up to allow a continuous flow of moist air to pass over samples within the heated furnace tube. Shop air under pressure was passed at 1 L/min. through a bubbler containing water at 60°C. The air then flowed into the hot zone of the furnace by passing through a port in a sealing header on one end of the furnace tube. The exposure test furnace with the bubbler is shown in Figure 4. At 60°C, the vapor pressure of water is 19.9 kPa (~0.2 atm.); thus the air flowing into the furnace contained about 20% water vapor.

Preliminary tests were conducted at 1200 and 1400°C. Early results showed the greatest improvement for samples tested at a peak temperature of

Figure 4. Tube furnace used for exposure testing of samples in a flowing stream of hot, moist air.

1400°C was with a $Yb_2Si_2O_7$ + SiO_2 coating on NT154 silicon nitride. The coated sample showed a weight gain of 0.014 mg/cm^2, while the uncoated sample gained 0.128 mg/cm^2 after 100 h of exposure.

Conclusions

Coatings of Sr- and/or Yb-based compounds were produced on Si_3N_4 and SiC/SiC substrates. Coatings on Si_3N_4 containing $SrSiO_3$ and $SrAl_2Si_2O_8$ were found to be unstable under high-temperature oxidizing conditions. Coatings of Yb-silicates were shown to be much more durable.

A limited number of samples were tested to determine the effect of a coating layer on the flexure strength of Si_3N_4. In all cases, it was found that the presence of the coating resulted in a reduction in strength, varying from 22 to 36%.

An environmental exposure testing capability for screening candidate coatings and substrates was established. Early tests show that a $Yb_2Si_2O_7$ + SiO_2 coating on NT154 Si_3N_4 may be a promising EBC system.

Environmental Protection Systems for Ceramics in Microturbines and Industrial Gas Turbine Applications—Part B: Slurry Coatings and Surface Alloying

Beth L. Armstrong
Metals and Ceramics Division
Oak Ridge National Laboratory
Oak Ridge, TN 37831-6063
(865) 241-5862; fax: (865) 574-6918; e-mail: armstrongbl@ornl.gov

DOE Technology Development Manager: Debbie Haught
(202) 586-2211;fax: (202) 586-7114; e-mail: debbie.haught@ee.doe.gov
ORNL Technical Advisor: Dave Stinton
(865) 574-5069; fax: (865) 576-4963; e-mail: stintond@ornl.gov

Objective

- Develop a low-cost, slurry-based process to apply protective coatings for silicon-based ceramic materials for use in microturbine and/or industrial gas turbine applications.
- Coordinate efforts with other relevant projects to identify the ideal coating material for steam and high-velocity resistance.

Approach

- Study and implement mechanisms of colloidal chemistry for coating systems in aqueous environments.
- Evaluate the protective capacity of coated substrates in test environments.
- Work with industrial collaborators to evaluate the feasibility of the approach and candidate materials.

Accomplishments

- Demonstrated dip coating as a viable approach for a variety of material systems, including mullite, doped aluminosilicates, and yttrium-doped silicates.
- Established strong collaborations with several industrial parties to ensure needs for environmental barrier coatings (EBCs) are being addressed.

Future Direction

- Collaborate with industrial parties to optimize and implement coating theory and technology.
- Evaluate the potential of additional candidate materials as monoliths and coatings systems.

Introduction

Monolithic silicon nitride ceramics are currently the primary ceramic material being used in combustion engine environments and are under consideration as hot-section structural materials for microturbines and other advanced combustion systems. Under oxidizing conditions, silicon nitride will typically form a surface oxidation (silicate) layer. In a combustion environment, this silicate layer can undergo rapid degradation as a result of the effects of high temperature, high pressure, and the presence of water vapor. The degradation can severely limit the useful life of the ceramic in this environment. Thus the development of an environmental protection system for the ceramic has become an essential goal for enabling the long-term use of these materials in advanced combustion engine applications. Similar to thermal barrier coatings for nickel-based super alloys that use a specialized oxide surface layer and a metallic bond coat, successful environmental protection systems for ceramics and ceramic composites will likely use multiple layers and complex combinations of materials. Most recent efforts have focused on the selection and deposition of the oxide surface layer; because of numerous factors, most of the candidates have been from the alumino-silicate family of oxide ceramics. Stable rare-earth silicate deposits have been found on component surfaces after recent engine and rig tests, indicating there may be other stable oxide compositions that have not been fully investigated.

Approach

Thin coatings of selected compositions were deposited on silicon nitride test coupons using two approaches: an aqueous-based slurry process and a reactive precursor technique. If feasible, the coated specimens were exposed to simulated high-pressure combustion environments, and the materials that demonstrated good potential were investigated further.

Slurry Coatings

Efforts have focused on the development of a slurry-based processing method to deposit thin, dense coatings of selected compositions on various silicon nitride substrates. Thin coatings of mullite were deposited on test coupons using an aqueous-based colloidal approach. The specimens were then exposed to simulated combustion environments that included water vapor to determine their viability. Work has also focused on the development and testing of new oxide materials, specifically rare-earth–doped di-silicates.

Reactive Coatings

Another approach being developed is the development of surface coatings that form in situ to produce more surface layers that either slow the growth of the silica layer or prevent it entirely. Diffusion processes for surface treatment of silicon-based ceramics will be explored to produce “volatility barrier coatings” that will enhance the performance and life of environmental protection systems. Previous efforts evaluated metallic coatings applied to silicon nitride substrates and heat-treated to create an alumina coating. In FY 2003 the feasibility of this approach was validated. In FY 2004 work was completed, and a publication was submitted fully describing this effort. No further discussion will follow in this report.

Results

Slurry Coatings: Development of Concentrated Suspensions

The ability to fabricate concentrated ceramic suspensions and optimize their rheological behavior for dip-coating is governed by interparticle forces. Long-range, attractive van der Waals forces are ubiquitous and must be balanced by one or more repulsive forces to obtain slightly shear-thinning flow behavior. Polyelectrolyte dispersants are commonly used to modify ceramic particle surfaces in order to impart repulsive electrosteric forces.[1, 2] Examples include polyethylenimine (PEI) and polyacrylic acid (PAA), which are cationic and anionic polyelectrolytes, respectively. The largest processing window for use of PEI and PAA exists when the isoelectric point of the ceramic particles is less than pH 6 and greater than pH 8, respectively. For this reason, PEI was used as the dispersant for the coating materials in this study. At low pH, amine groups along the PEI backbone become protonated. The fraction of protonated amine groups, α, is plotted as a function

of pH in Figure 1. This plot indicates that PEI is negligibly protonated at pH 11 but fully protonated at pH 5.5. In strongly protonated conditions, PEI adapts an extended conformation,

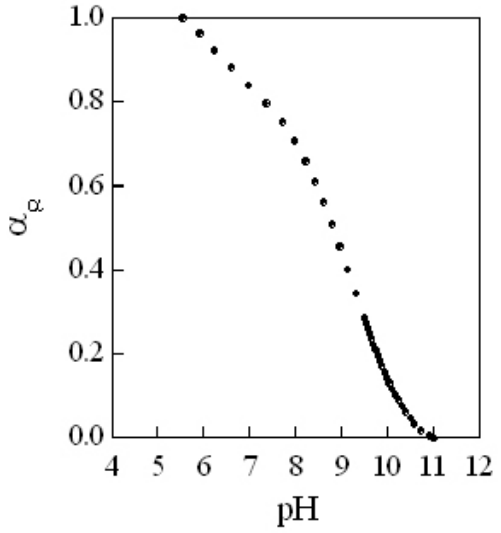

Figure 1. Fraction of protonated amine groups, α, as a function of pH in dilute PEI solutions (10^{-3} *M*). Note: $\alpha = [NH_2^+]/([NH] + [NH_2^+])$.

which is most desirable for imparting strong electrosteric forces.

Optimization of Mullite-PEI Suspension Rheology

Work continued on the optimization of mullite (MULCR®, Baikowski International Corporation, Charlotte, NC) slurry rheology for a dip-coating process. Mullite was used as a surrogate material for yttrium di-silicates in order to optimize general rheology and dipping conditions. PEI (Polysciences, Warrington, PA) with a weight average molecular weight (M_w) of 10,000 g/mole and one amine group (NH) per monomer unit was implemented as a rheological modifier for this system. Concentrated mullite suspensions (45 vol % solids) were prepared at a constant pH of 7 and varying PEI concentrations. The suspensions were ultrasonically treated for 5 min to break up weak agglomerates and mixed on a shaker table for 24 h to obtain equilibrium behavior. Rheological measurements were carried out using a controlled stress rheometer (Rheometric Scientific SR5, TA Instruments, New Castle, DE) in stress viscometry and oscillatory stress modes to measure the apparent viscosity and elastic modulus, respectively.

The apparent viscosity is plotted as a function of applied shear stress in Figure 2 for suspensions of

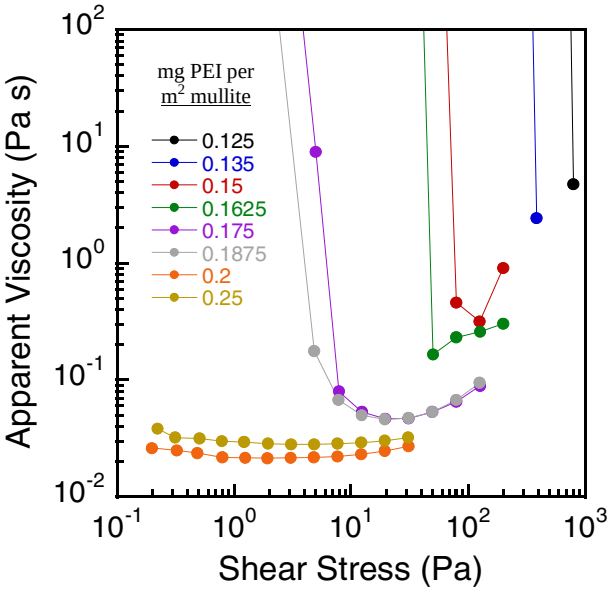

Figure 2. Apparent viscosity as a function of shear stress for concentrated mullite suspensions (45 vol% solids) of varying PEI concentration. Note, the solid lines merely guide the eye.

varying PEI concentration. The degree of shear-thinning decreased with increasing PEI concentration until nearly Newtonian flow behavior was obtained at a PEI concentration of 0.2 mg/m^2 mullite. These suspensions exhibited stable flow behavior over a 15-day time span, as shown by the data in Figure 3. The elastic modulus is plotted as a function of applied shear stress in Figure 4 for suspensions of varying PEI concentration. Solid-like behavior, indicative of colloidal gels, was observed for suspensions with PEI concentrations of less than 0.2 mg/m^2 mullite. The linear elastic modulus and yield stress decreased with increasing PEI concentration until a transition from gel- to fluid-like behavior occurred at 0.2 mg/m^2 mullite.

Substrates of varying composition—including silicon carbide (Hexaloy, Carborundum Co., Niagara Falls, NY), silicon nitride (AS800, Honeywell Ceramic Components, Torrance, CA), and metallic

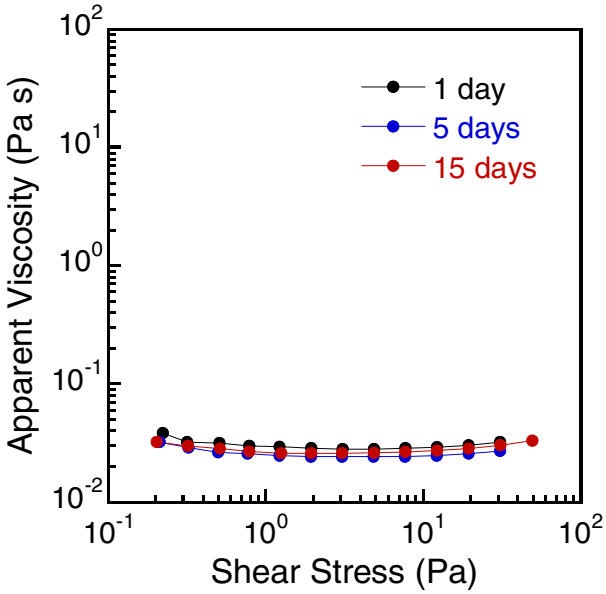

Figure 3. Apparent viscosity as a function of shear stress for concentrated mullite suspensions (45 vol % solids, 25 mg PEI/m^2 mullite) aged for varying times.

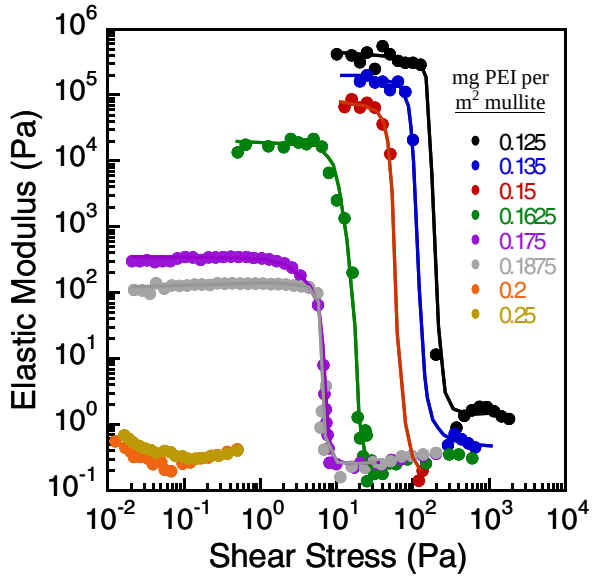

Figure 4. Elastic modulus as a function of shear stress for concentrated mullite suspensions (45 vol % solids) of varying PEI concentration. Note: the solid lines merely guide the eye.

silicon—were dipped into concentrated mullite suspensions (45 vol %) of varying PEI concentration. The substrates were dipped at a rate of 85.7 mm/min, submerged for 1 min, and withdrawn at a rate of 85.7 mm/min. Coated substrates were dried under ambient conditions and are displayed in the image gallery in Figure 5. Excellent coatings were obtained from mullite suspensions with 0.1625–0.175 mg PEI/m^2 mullite surface. Mullite suspensions with less than 0.1625 mg PEI/m^2 mullite resulted in thick, uneven coatings. The quality of the coatings decreased with decreasing PEI concentration. These features result from a particle gel network that is too strong, i.e., when the linear elastic modulus is greater than ~10^4 kPa. Mullite suspensions with 0.1875 mg PEI/m^2 mullite or more resulted in coatings with three types of defects: drying defects or "dimples," pores due to entrained air bubbles, and thickness gradients. All of these defects stem from a particle gel network that is too weak, i.e., when the linear elastic modulus is less than ~100 Pa. For example, drying defects arise from solvent wicking and particle migration from the center of each coated face to drying fronts that initiate and converge inward from the corners and edges.[3] Pores arise from air bubbles that are entrained in the low-viscosity suspensions and quickly migrate to the suspension/substrate interface during dipping. Thickness gradients result from dripping and beading of the suspensions resulting from gravity-induced flow.

Mullite Sintering Behavior

Early results suggested that the sintering atmosphere plays an important role in obtaining adherent, dense coatings. Adherent coatings have been obtained in an oxygen atmosphere but not in argon or nitrogen. It is believed that a thin, silica-rich reaction layer may form to provide a bond coat in oxygen but not in argon or nitrogen. Preliminary results show that dense coatings are achieved at 1350°C, which is significantly lower than the temperature required for densification of mullite in bulk form (1600°C). These results demonstrate the feasibility of dip-coating and sintering EBCs onto functional components.

Zeta Potential of Y_2SiO_5 and $Y_2Si_2O_7$

In order to develop an aqueous-based process for a new material system, basic surface characterization is necessary. The behavior of aqueous

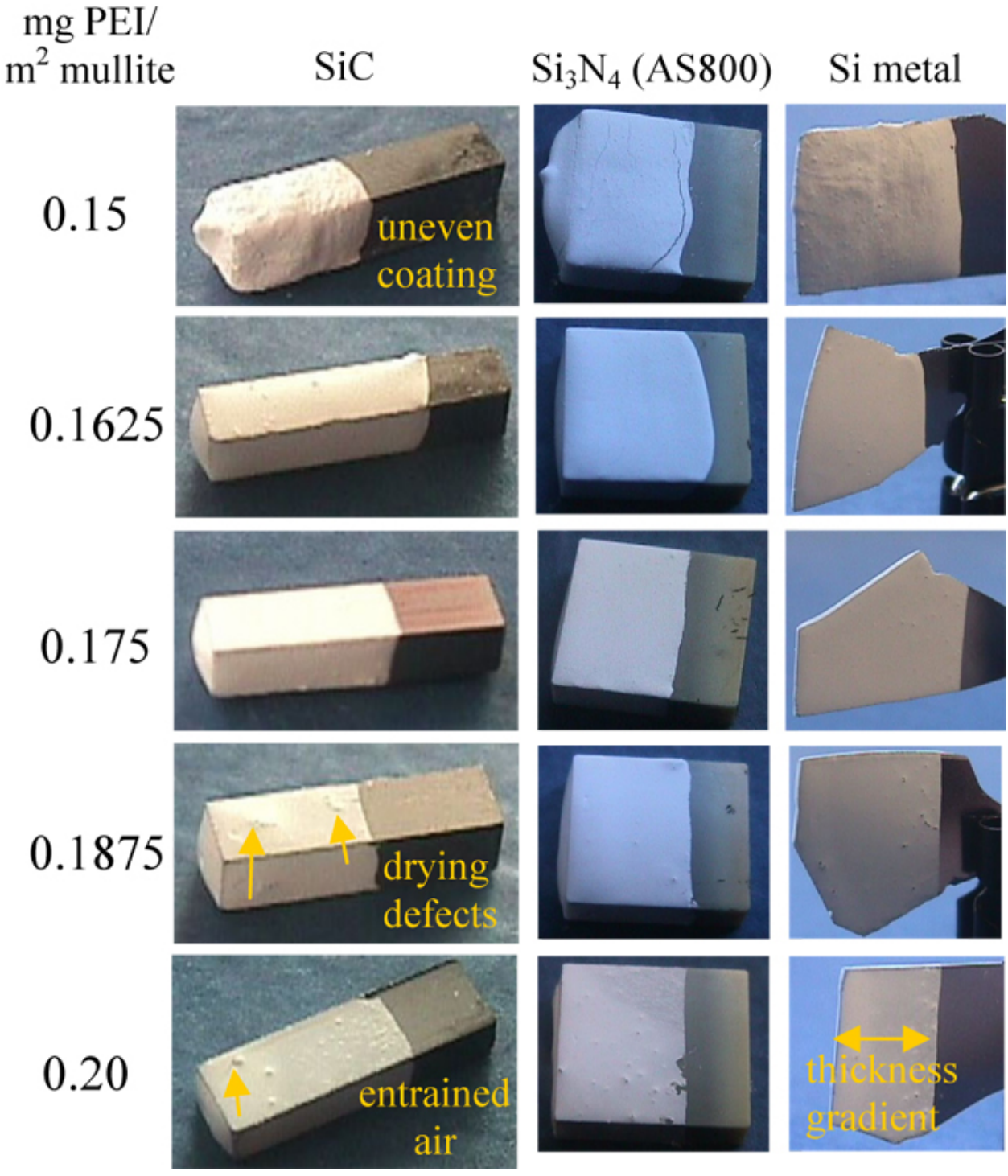

Figure 5. Mullite coatings on SiC, Si_3N_4 (AS800), and metallic silicon substrates after dipping in concentrated mullite suspensions (45 vol %) of varying PEI concentration.

suspensions composed of yttrium silicate (Y_2SiO_5) and yttrium di-silicate ($Y_2Si_2O_7$) particles was studied. Both Y_2SiO_5 and $Y_2Si_2O_7$ were obtained from Praxair Specialty Ceramics (Woodinville, WA).

Zeta-potential measurements were carried out as a function of pH for dilute Y_2SiO_5 and $Y_2Si_2O_7$ suspensions (10^{-3} vol %) using capillary electrophoresis (Zetasizer 3500HS, Malvern Instruments Ltd.). The results are shown in Figure 6. The isoelectric point (IEP) was observed at a pH of 3.5 for Y_2SiO_5, which is near the IEP reported for pure SiO_2 (pH 2–3).[4] In contrast, a higher IEP of 5.5 was observed for $Y_2Si_2O_7$. At a characteristic pH value of 9.5, a sharp decline in zeta potential occurred for both systems. The reason is that a layer of yttrium hydroxide forms on the surface of the particles at high pH.[5]

Optimization of Y_2SiO_5-PEI Suspension Rheology

Work began on the optimization of Y_2SiO_5 slurry rheology for a dip-coating process. Concentrated Y_2SiO_5 suspensions (45 vol % solids) were prepared at a constant pH of 7 and varying PEI concentration. The suspensions were ultrasonically treated for 5 min to break up weak agglomerates and mixed on a shaker table to obtain equilibrium behavior. Rheological measurements were carried out using a controlled stress rheometer in constant and oscillatory stress modes to measure the apparent viscosity and elastic modulus, respectively.

The apparent viscosity is plotted as a function of applied shear stress in Figure 7 for suspensions of varying PEI concentration. The degree of shear-thinning decreased with increasing PEI concentration until only slight shear-thinning behavior was obtained at a PEI concentration of 0.25 mg/m^2 Y_2SiO_5. The elastic modulus is plotted as a function of applied shear stress in Figure 8 for suspensions of varying PEI concentration. Solid-like behavior (i.e., a linear viscoelastic region and yield stress) was observed for all suspensions; however, the linear elastic modulus and yield stress decreased with increasing PEI concentration until minimum values of 10 Pa and 2 Pa, respectively, were observed at 0.25 mg PEI/m^2 Y_2SiO_5.

According to prior work on mullite-PEI suspensions, excellent dip coating suspensions are fabricated when the linear elastic modulus is between 300 kPa and 20 kPa and the yield stress is between 2 and 7 Pa. The appropriate linear elastic modulus range was achieved over a very narrow range of PEI concentration, i.e., 0.1625–0.17 mg PEI per m^2 Y_2SiO_5. However, the appropriate yield stress is achieved at higher PEI concentrations ranging between 0.2 and 0.25 mg PEI per m^2 of Y_2SiO_5. Clearly, it is not possible to simultaneously optimize the linear elastic modulus and yield stress with PEI additions alone. As a result, further rheological modification is required via a step such as the addition of a binder or pH modification to achieve optimal results.

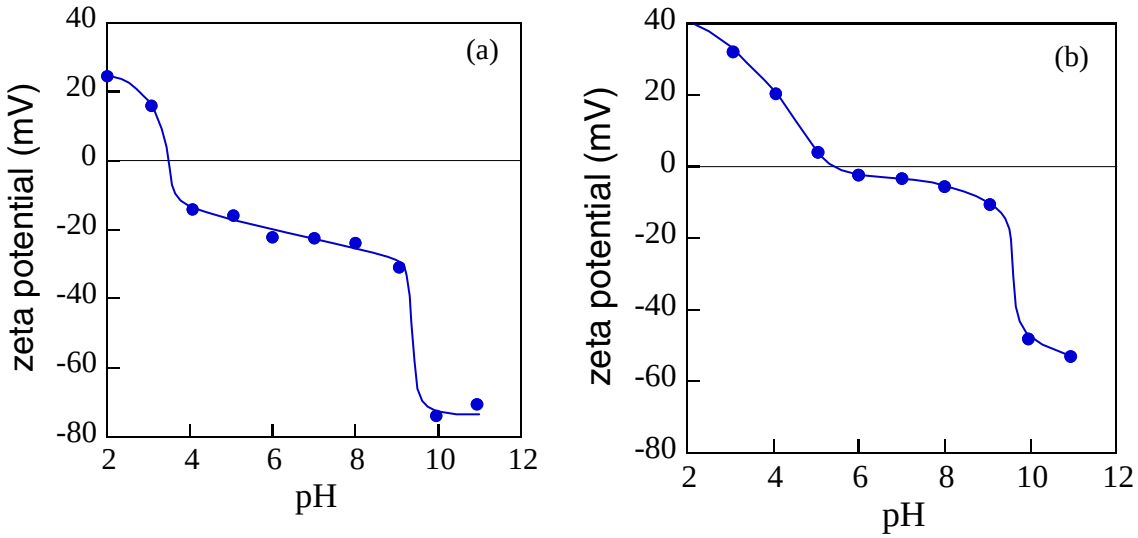

Figure 6. Zeta potential as a function of pH for (left) Y_2SiO_5 and (right) $Y_2Si_2O_7$ suspensions (10^{-3} vol%).

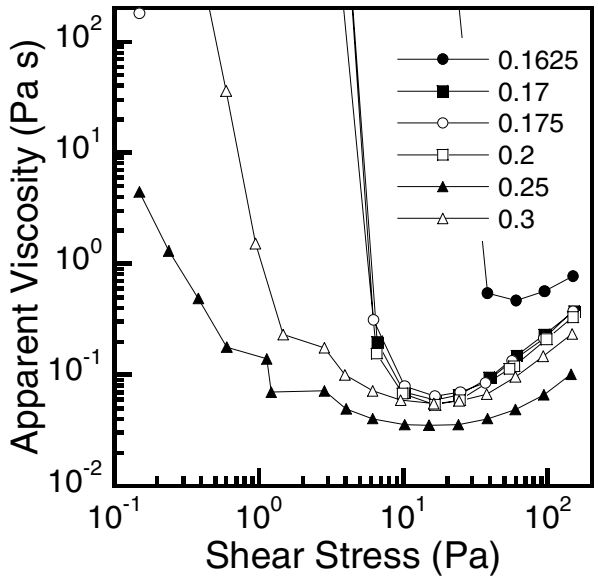

Figure 7. Apparent viscosity as a function of shear stress for concentrated Y_2SiO_5 suspensions (45 vol % solids) of varying PEI concentration. Note: the solid lines merely guide the eye.

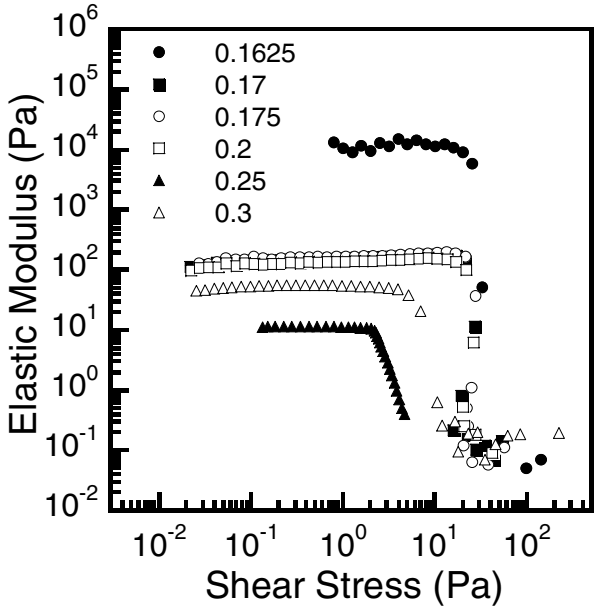

Figure 8. Elastic modulus as a function of shear stress for concentrated Y_2SiO_5 suspensions (45 vol% solids) of varying PEI concentration (in mg PEI/m^2 Y_2SiO_5).

Conclusions

Mullite coatings were formed by dipping SiC, Si_3N_4, and silicon substrates into concentrated, mullite suspensions of tailored rheological behavior. Dried coatings were crack-free and fully densified at 1350°C, which is considerably below the temperature requirement for densification of mullite in bulk form (1600°C). Mullite coatings continue to provide a baseline evaluation tool for the comparison of the efficacy of new coatings systems developed.

Concentrated Y_2SiO_5 and $Y_2Si_2O_7$ suspensions (45 vol % solids) suitable for a dip-coating process were fabricated with the use of PEI. The rheological behavior of concentrated Y_2SiO_5 suspensions ($\phi = 0.45$) was characterized to measure the apparent viscosity (η_a), linear elastic shear modulus (G'), and yield stress (τ_Y) of such suspensions in order to optimize the dip-coating process. Future work will explore how coating uniformity and thickness can be improved with additional additives.

References

1. J. Cesarano, III, and I. A. Aksay, "Processing of Highly Concentrated Aqueous α-Alumina Suspensions Stabilized with Polyelectrolyte," *J. Am. Ceram. Soc.*, 71(12) (1988).
2. J. Cesarano, III, I. A. Aksay, and A. Bleier, "Stability of Aqueous α-Al_2O_3 Suspensions with Poly(methacrylic acid) Polyelectrolyte," *J. Am. Ceram. Soc.*, 71(4) 250–55 (1988).
3. C. J. Martinez, J. A. Lewis, "Rheological, Structural, and Stress Evolution of Aqueous Al_2O_3:Latex Tape-Cast Layers," *J. Am. Ceram. Soc.*, 85(10) 2409–16 (2002).
4. J. S. Reed, Principles of Ceramic Processing, 2nd ed., John Wiley and Sons, New York, p. 658, 1995.
5. M. Pourbaix, Atlas of Electrochemical Equilibria in Aqueous Solutions, NACE International, Houston, TX, 1974.

Publications/Presentations

M. P. Brady, B. L. Armstrong, H. T. Lin, M. J. Lance, and L. R. Walker, "Feasibility Assessment of Self-Grading Metallic Bond Coat Alloys to Protect Si-Based Ceramics" presented at the Second Annual Environmental Barrier Coatings conference, November 19, 2003.

M. P. Brady, B. L. Armstrong, H. T. Lin, M. J. Lance, and L. R. Walker, "Feasibility Assessment of Self-Grading Metallic Bond Coat Alloys to Protect Si-Based Ceramics," *Scripta Mater*., submitted for publication.

Polymer-Derived EBCs for Monolithic Silicon Nitride

Rishi Raj and B. Sudhir
University of Colorado
Boulder, CO 80302
(303)492-1029; e-mail: rishi.raj@colorado.edu

DOE Technology Development Manager: Debbie Haught
(202) 586-2211; fax: (202) 586-7114; e-mail: debbie.haught@ee.doe.gov
ORNL Technical Advisor: Karren More
(865) 574-7788; fax: (865) 576-5413; e-mail: morekl@ornl.gov

Objective

- Develop a low-cost, polymer-derived environmental barrier coating (EBC) for silicon (Si) -based ceramics for use in microturbine environments.
- Optimize (polymer-derived) silicon carbo-oxynitride (SiCNO) bond coat for silicon nitride from studies on particulate composites made from transition metal oxides (hafnia/zirconia) and SiCNO.

Approach

- Study the weight change and microstructural and phase evolution in porous SiCNO–zirconia and SiCNO–hafnia composites during dry and wet oxidation at high temperatures.

Accomplishments

- The weight loss of porous SiCNO–ZrO_2 and SiCNO–HfO_2 appears to stabilize over time when they are tested in dry and humid environments at 1300°C for more than 100 h.

Future Direction

- Explore the possibility of self-healing behavior in particulate composites made from hafnia/zirconia+SiCNO in long-term tests.

Introduction

EBCs for silicon-nitride components are needed to prevent recession when they are exposed to the hot, humid combustion environment of gas turbines. Top coats of transition metal oxides, such as zirconia and hafnia, are known to resist recession. However, these oxides bond poorly to silicon nitride, and a large difference in the thermal expansion between them and silicon-nitride–based ceramics can produce spalling. The design and materials selection for the bond coat, is therefore, a key issue in the design of successful EBCs. This research program aims to study the application of polymer-derived, oxide-non-oxide silicon carbo-oxynitride SiCN(O) ceramic as a key constituent in the design of the bond coat.

Approach

A two step approach is being followed for experimental evaluation.

In step 1, particulate composites of ZrO_2/HfO_2-SiCNO are being prepared and oxidized in streaming humid environments at 1300°C. The results are characterized by change in weight, change in the surface area, and quantitative X-ray diffraction (XRD). The microstructure evolution is studied by multimode scanning electron microscopy (SEM). These experiments will provide insights into long-term stability and the bonding between SiCNO and the transition metal oxides.

In step 2, the particulate composites described will be coated with zirconia/hafnia coatings. The reactions between the coatings and the composites and their effects on weight change will be studied. These experiments also include a key question: Is it possible to deposit pore-free topcoats of ZrO_2/HfO_2 on the particulate composites.

Specimen Preparation and Testing

Porous composites of SiCNO–[yttria stabilized) zirconia (YSZ), SiCNO–hafnia, and SiCNO-Si_3N_4–zirconia] were prepared by cold-compacting the powders and sintering them in air at 1300°C for 2 h. The characteristics of the starting powders and the densities of the sintered compacts are listed in Table 1. The surface area of the sintered compacts was determined by BET analysis; this information is included in Table 1.

Coupons cut from the composites were oxidized in air at 1300°C for times of up to 100 h. The humid oxidation studies were carried out in an indigenously designed hydrothermal testing apparatus at 1300°C and in steam at a linear flow rate of 17.6 cm s^{-1}. The specimens were examined in an SEM with energy-dispersive X-ray analysis (EDAX) facility to study the microstructural evolution during oxidation. The oxidation phases were quantified by XRD using the Internal Standard Method with silicon powder (~1-μm particle size) as the internal standard.

Results

1. Microstructural and XRD Studies

Figure 1 shows the microstructures of the SiCNO–50 vol % 10YCZ and SiCNO–50 vol % hafnia that were hydrothermally oxidized at 1300°C for 100 h.

As seen in Figure 1b, the smaller hafnia particles form a ‘necklace’ structure around the bigger SiCNO particles. Further, the reaction zone around the ~6-μm zirconia particles in Figure 1a could be easily discerned, whereas the reaction zone around the hafnia particles could not be determined because of their small size (~0.6 μm). Therefore, detailed elemental profile maps were obtained for the SiCNO–zirconia composite.

Silicon mapping indicates that the reaction proceeded by the diffusion of the silicon ion into the zirconia grains. The reaction product was confirmed to be zirconium silicate (zircon) from XRD studies (Figure 2).

Figure 2 also shows the absence of silica on the surface of the oxidized sample (although there is an appreciable amount of silica within the sample bulk). This result suggests that the silica on the surface volatized, whereas as the silica inside the bulk was shielded from the streaming water vapor. The tortuous nature of the pore structure in the composite could be responsible for retaining the silica in the interior.

Figure 3 shows the XRD data from the surface of SiCNO–50 vol % HfO_2 samples that were tested in dry and humid conditions.

Table 1. Details of the starting powders and the sintered composite samples

Sample	Particle size (μm)	Density (g cm^{-3})	BET surface area (m^2 g^{-1})	Comments
Powders				
10 mol % yttria-stabilized zirconia (10YCZ)	12 ± 1	5.7		ME Inc. (cubic phase)
Hafnia	0.6 ± 0.06	9.67		American Elements (monoclinic phase)
Silicon nitride	0.6 ± 0.05	3.2		Ube Chemicals (α phase)
SiCN(O)	6 ± 0.6	2.4		Pyrolyzed from Ceraset™ (amorphous)
Particulate composites				
SiCNO–50 vol % 10YCZ	~6	3 (~7% dense) 74%	0.47 ± 0.02	Both phases have nearly 6 μm particle size after 1 h. of ball milling
SiCNO–50 vol % Hafnia	6 μm SiCNO, 0.6 μm Hafnia	3.92 (~65% dense)	3.3 ± 0.2	Hafnia was distributed around the bigger SiCNO particles. Comparatively higher surface area
SiCNO 33 vol % Si_3N_4 33 vol % 10YCZ 33 vol %	6 μm SiCNO, 0.6 μm Si_3N_4, 6 μm 10YCZ	3.05 (~82 % dense) 81%	0.8 ± 0.03	Specimens not yet tested

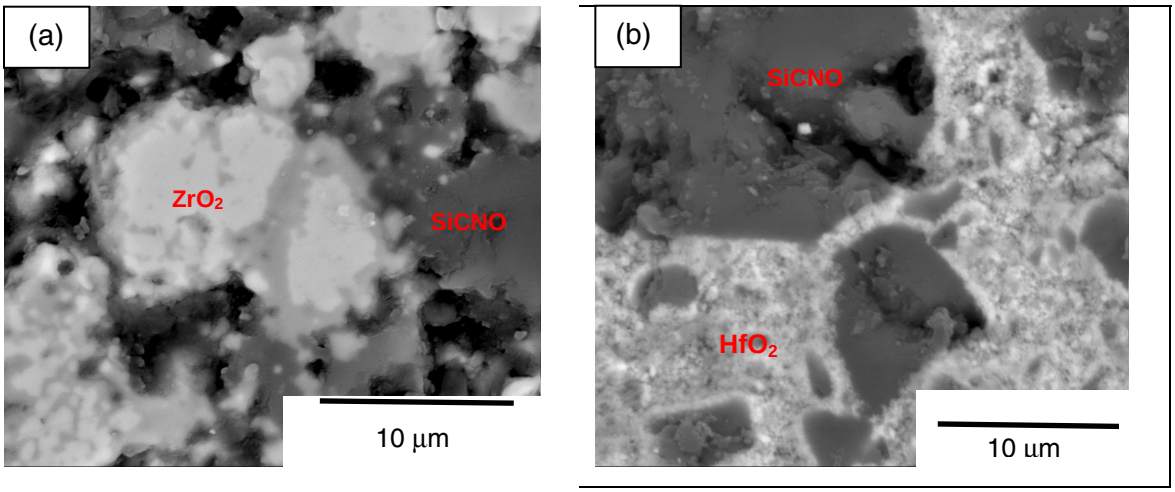

Figure 1. Micrographs of (a) SiCNO–50 vol % 10YCZ and (b) SiCNO–50 vol % hafnia composites that were hydrothermally tested at 1300°C for 100 h.

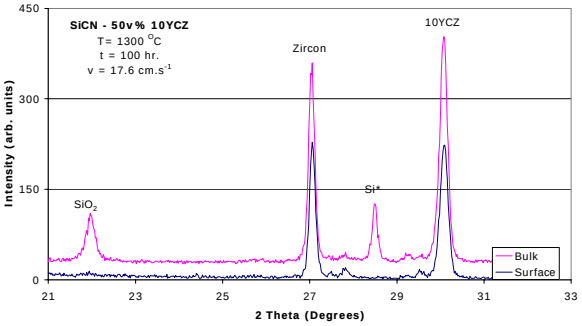

Figure 2. XRD data from the surface (solid) and bulk (powder) for the SiCNO–50 vol % 10YCZ composite. Silicon was used as an internal standard to quantitatively determine the phase evolution.

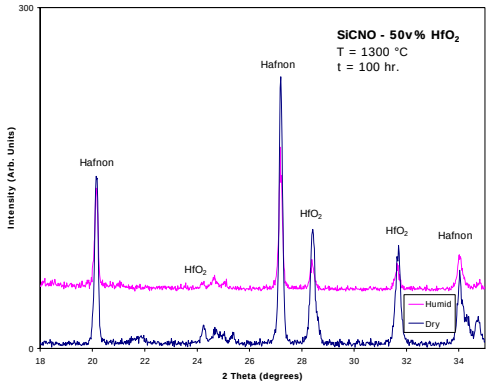

Figure 3. XRD data from the surface of SiCNO–50 vol % hafnia samples tested at 1300°C for 100 h under dry and humid conditions.

(Note that silicon powder cannot be used as an internal standard material, since its peak at 28° overlaps with that of hafnia. Therefore, other materials are being examined for quantifying the phases in this system.) In spite of the lack of quantitative information, the XRD data reveal two important features: the phase evolution is similar under dry and humid conditions, and hafnium silicate (Hafnon) is the major oxidation product. As expected, the phase evolution in this system is similar to that of the SiCNO–zirconia system, which was reported in the previous quarterly report.

In effect, the microstructural and XRD investigations show that residual oxidation products are similar under dry and humid conditions. The bonding between the transition metal oxide grains and SiCNO is due to the formation of their respective silicates. The silicate phase formation is possibly controlled by the diffusion of the silicon ion into the zirconia/hafnia grains.

2. Surface Area and Weight Change Studies

Figure 4 shows the BET surface area data for the SiCNO–50 vol % 10YCZ composite, tested in dry and wet conditions. As seen in the figure, there is no significant change in the surface area at 1300°C, although the surface area at longer times is slightly lower than those at shorter testing times.

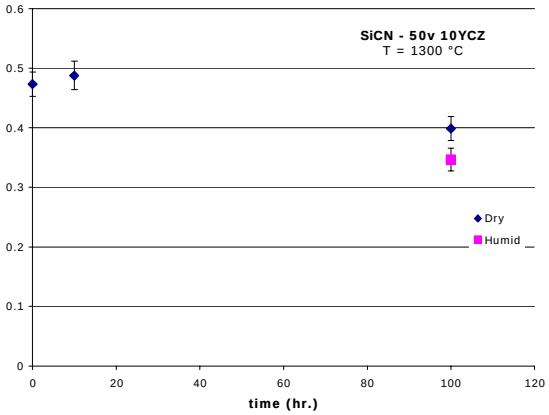

Figure 4. Evolution of the BET surface area as a function of time under dry and humid conditions.

The weight change data of the composite samples have been normalized with the initial BET surface area to obtain the specific weight change. Figure 5 shows a plot of the specific weight change vs. time for the SiCNO–50 vol % 10YCZ composite as a function of oxidation time under dry and wet oxidation conditions.

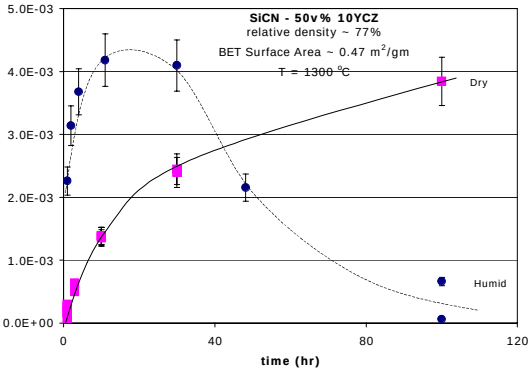

Figure 5. Time-dependent specific weight change of SiCNO–50 vol % 10YCZ composite in dry and humid conditions.

Because of the errors in the weight measurement and surface area, there is nearly a 10% error in the specific weight change. It must be noted that a positive value implies weight gain. As seen in Figure 5, there is an appreciable weight gain even in hydrothermal conditions, consistent with the formation of silica and zirconium-silicate (as determined in the XRD and microstructural analysis).

Figure 6 shows the oxidation data for SiCNO–50 vol % hafnia, again a plot of specific weight change vs. time.

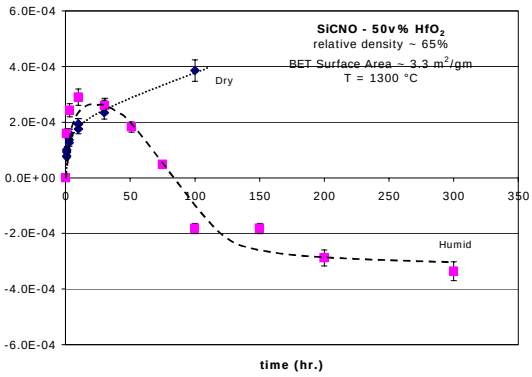

Figure 6. Evolution of specific weight in SiCNO–50 vol % hafnia composite under dry and humid conditions at 1300°C.

The change in weight for the composite that was hydrothermally oxidized for up to 300 h is also shown in Figure 5. Initial weight gain is followed by weight loss. However, at long times, the weight appears to begin to stabilize, suggesting possible self-healing behavior in the composite. A similar result is obtained for the SiCNO–HfO2 composite, as shown in Figure 6: that is, weight gain in dry oxidation, and weight gain followed by weight loss followed by an apparent trend toward apparent stable weight in wet oxidation. However, an interesting feature is that the weight increase in the SiCNO–Hafnia system is nearly an order of magnitude lower than that in the SiCNO–zirconia system under both dry and humid conditions. This point is brought out clearly in the comparative plot of the hydrothermal oxidation data of the two composites, shown in Figure 7.

It is also worth noting that the hafnia particles in the composite were nearly an order of magnitude smaller than the zirconia particles in the SiCNO-ZrO_2 composite. Normally the reaction rate is expected to increase with decreasing particle size; the result here is the opposite. Therefore, the lower weight change in the SiCNO–HfO_2 composite is significant.

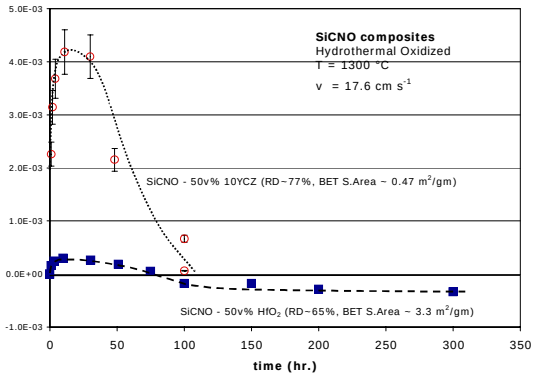

Figure 7. Comparison of the specific weight change during hydrothermal oxidation of SiCNO–zirconia and SiCNO–hafnia composites.

Conclusions

Dry and hydrothermal oxidation tests were conducted on SiCNO–50 vol% zirconia/hafnia at 1300°C for times greater than 100 h. Detailed microstructural and XRD studies were also conducted on these composites. The XRD studies revealed the presence of silica in samples tested under humid conditions even after extended times. The microstructural studies revealed zircon formation due to the diffusion of silicon ion into the zirconia grains. Further, both composites showed a weight increase, that could be related to the oxidation of SiCNO to form silica.

The weight loss during hydrothermal testing showed a tendency to stabilize at longer durations. This observation, along with the microstructural investigations, implies the presence of a passivating mechanism, such as closing of the pores due to formation of zircon. However, further studies are required to see if this mechanism can lead to a self-healing coating architecture using the composite structure alone.

Publications/Presentations

Rishi Raj, presentation at ORNL (DOE) Environmental Barrier Coatings Workshop, Nashville TN, November 2003.

Rishi Raj, “Development of Graded EBC Systems for Monolithic Silicon Nitride Ceramics,” Honeywell, Phoenix, AZ, July 15, 2004.

EBC Development for Silicon Nitride Ceramics

B. Nair, C. Lewinsohn, and Q. Zhao
Ceramatec, Inc.
Salt Lake City, UT 84092

DOE Technology Development Manager: Debbie Haught
(202) 586 2211; (202) 586-7114(fax); e-mail: debbie.haught@ee.doe.gov
ORNL Technical Advisor: Terry Tiegs
(865) 574-5173; fax: (865) 574-4357; e-mail:tiegstn@ornl.gov

Objective

- Develop a low-cost, functional environmental barrier coating (EBC) system for silicon nitride ceramics using pre-ceramic polymers.

Approach

- Apply bond-coats, derived from pyrolysis of pre-ceramic polymers, with graded thermoelastic properties to the substrate and subsequently applying low-silica activity compositions for hydrothermal corrosion resistance.

Accomplishments

- Established a collaborative relationship between Cermatec and Saint-Gobain.
- Applied multilayered EBCs on NT154 Si_3N_4 coupons received from Saint-Gobain. After application of the bond coat, the Si_3N_4 coupons retained nearly 100% of their strength.
- Coated specimens retained >75% of their flexural strength after complete EBC application.
- Recession tests at Saint-Gobain demonstrated that selected geomimetic compositions had recession resistance comparable to hot-pressed yttria.

Future Direction

- Improve hydrothermal corrosion resistance of coatings through process modification.
- Collaborate with ORNL to improve processing methods and with St. Gobain to ensure that the methodology is compatible with standard processing steps.

Technical Progress

In the Phase I project, initiated during FY 2004, a number of low-silica activity top coat compositions that are expected to be stable in turbine environments were selected using the geomimetic approach. In addition, an oxide composition with proven thermochemical resistance in the turbine environment was selected. Bond coat compositions that show good adhesion to the top coat material and the silicon nitride substrate, as well as intermediate thermal expansion between the top coat and substrate, were also selected. After the compositions were selected, a processing route was developed for the EBC system, which uses simple non-line-of-sight coating application routes such as dip-coating and painting for both the bond coat and top coat layers.

Cross-hatch, adhesive tape peel tests similar to ASTM D3359 Method A were used to demonstrate good adhesion of the bond coat to the substrate (Figure 1). Flexural testing of as-received bars compared with EBC-coated bars revealed the absence of significant degradation in strength of the substrate as a result of the coating process. It was demonstrated that both as-processed and machined NT154 Si_3N_4 bars retained nearly 100% of their strength after bond coat application. After complete EBC system application, the coated bars retained >75% of their flexural strength (Table 1).

Table 1. Testing results for coated and uncoated samples

Type	Average strength (MPa)	Standard deviation (MPa)
Uncoated (baseline)[a]	590	116
Three-layer EBC[b]	458	167

[a] Data provided by Saint-Gobain
[b] Six test bars with GeoMim-2 top coat

Note: All bars are tested at 20/40 span. AP surface will be the surface in real applications.

A strategy for collaboration between Ceramatec and Saint-Gobain was developed. The teaming strategy involves the supply of sintered Si_3N_4 tiles from Saint-Gobain to Ceramatec, coating of the samples by Ceramatec using oxide and geomimetic coatings, and post-processing and evaluation of the

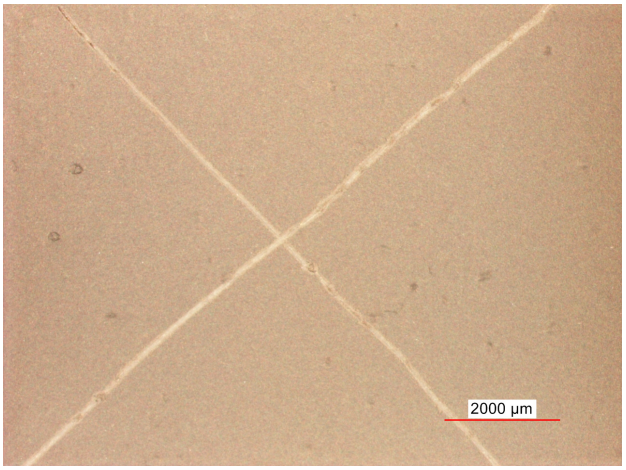

Before test

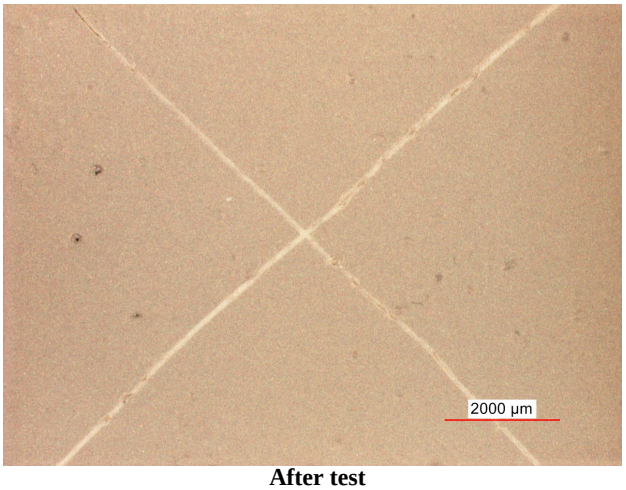

After test

Figure 1. Example of a cross-hatch, adhesive tape peel test on a NT-154 sample coated with a bond coat.

coated specimens at Saint-Gobain. Saint-Gobain also evaluated the recession resistance of sintered monolithic oxide and geomimetic coating compositions, as well as bond coat compositions.

Sintered monolithic compositions of the oxide and geomimetic compositions were sent to Saint-Gobain to evaluate the recession resistance of these materials. Tests in Saint-Gobain's recession test furnace in flowing steam containing air at 1200°C suggested that some of the geomimetic compositions had recession resistance comparable to that of hot-pressed yttria. Because these compositions also showed excellent thermal expansion match with silicon nitride and showed promise for application as thick EBC coatings on silicon nitride (Figure 2), the set of compositions were selected for further optimization in Phase II.

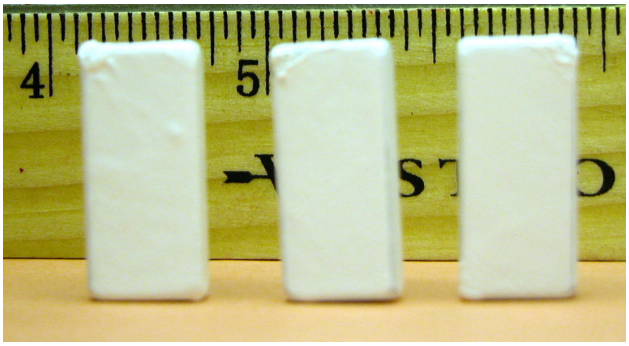

Figure 2. Example of fully coated specimens.

Saint-Gobain is also exploring secondary densification techniques for the EBCs. Therefore, experiments at Ceramatec, are under way to determine the optimum processing temperature for the select bond coat compositions.

Specimens were sent to Oak Ridge National Laboratory prior to process optimization to achieve high density and therefore were relatively porous. Initial exposure tests of these specimens in the high-temperature steam exposure reactor (the Keiser rig) indicated internal oxidation due to open porosity. Coated samples also were supplied to Argonne National Laboratory for indentation tests.

Plans

Efforts will continue to improve the hydrothermal corrosion resistance of coatings through process modification. Ceramatec will collaborate with Beth Armstrong at ORNL to improve slip rheology to reduce coating defects. Ceramatec will also coat tensile specimens provided by Matt Ferber at ORNL for evaluation. Ceramatec will continue to work with Saint-Gobain to develop compatible processing techniques.

Failure Mechanisms in Coatings

J. P. Singh, K. Sharma, and P. S. Shankar
Energy Technology Division
Argonne National Laboratory
Argonne, IL 60439
Phone: (630) 252-5123, E-mail: jpsingh@anl.gov

DOE Technology Development Manager: Debbie Haught
(202) 586-2211; (202) 586-7114 (fax); e-mail: debbie.haught@ee.doe.gov
ORNL Technical Advisor: D. P. Stinton
(865) 574-4556; fax: (865) 241-0411; e-mail:stintondp@ornl.gov

Objective

- Provide information on mechanical/microstructural behavior and resulting failure modes/mechanisms of new and emerging environmental barrier coatings (EBCs). This information is needed for EBC processing and design for improved component performance that will result in increased turbine efficiency.
- Correlate processing parameters and microstructure with performance in a service environment to optimize design of EBCs with improved performance

Approach

- Measure and model residual stresses and mechanical properties, characterize microstructure, identify failure mode(s) and mechanisms, and establish processing–microstructure–performance correlations for emerging EBCs.
- Develop appropriate test methodology and/or protocols to characterize coating integrity, provide critical property data for design purposes, and predict performance of environmental and thermal barrier coatings with greater reliability.

Accomplishments

- Completed finite element numerical modeling to estimate the effects of residual stresses at the Si_3N_4 substrate/EBC interface on the mechanical behavior of Si_3N_4 substrates coated with novel EBCs for advanced turbine applications.
- Completed mechanical and microstructural evaluation of SN282 Si_3N_4 coated with a barium-strontium-aluminosilicate (BSAS) EBC obtained from United Technology Research Center (UTRC)/Oak Ridge National Laboratory (ORNL) and AS800 Si_3N_4 coated with Ta_2O_5 –based EBCs obtained from Northwestern University/Honeywell.

Future Direction

- Characterize thermal fatigue resistance and damage evolution of Si3N4 substrates (AS800 and SN282) coated with BSAS- and Ta_2O_5-based EBCs to assess the effects of composition and microstructure. Specifically, degradation of thin EBC layers will be assessed by measuring the elastic modulus of the EBC layers as a function of thermal cycles.
- Evaluate solid-particle erosion resistance of BSAS EBC-coated SN282 and correlate the results with microscopic observations of EBC damage to provide information on EBC performance in the erosive turbine environments.

Introduction

For improved mechanical performance in elevated-temperature service environments, ceramic components are coated with EBCs. However, these coatings have been observed to degrade the mechanical properties of the underlying components as a result of undesirable thermal mismatch stresses and processing-induced critical flaws. Therefore, the composition and microstructure of EBCs are expected to have a substantial effect on mechanical properties, failure modes/mechanisms, and resulting service performance that includes oxidation, erosion, corrosion, and thermal fatigue resistance of coated components.[1,2]

Understanding the effects of EBC composition and microstructure on residual stresses and the resulting mechanical properties and failure modes is critical to developing EBC systems with improved performance. This program aims to (1) evaluate mechanical properties and coating failure modes and mechanisms, (2) identify the role of processing and microstructural parameters in coating failure, (3) develop model(s) to determine the effects of residual stresses on mechanical properties of coated components, (4) monitor damage evolution in oxidizing environments by evaluating thermal fatigue resistance, (5) identify mechanisms governing foreign object damage by evaluating erosion resistance, and (6) develop appropriate test methods/protocols for reliably predicting coating and component performance in service environments.

The goals are (1) to provide critical information needed for developing new and improved coatings with long service life and (2) to establish an appropriate test methodology to acquire properties data for improved coating design and reliable lifetime prediction for coatings and coated components to be used for distributed energy applications.

Approach

For the present study, two EBC systems (SN282 Si_3N_4 coated with BSAS, and AS800 Si_3N_4 coated with Ta_2O_5) were obtained from UTRC/ORNL and Honeywell/Northwestern University, respectively. The BSAS EBC (≈500 μm thick) consisted of a BSAS top coat, a silicon bond coat, and an intermediate BSAS+mullite layer. The Ta_2O_5 EBC (≈200 μm thick) consisted of a single Ta_2O_5 layer coated on AS800. Mechanical evaluation included flexural strength measurement of the EBC-coated substrates in a four-point bend mode. Analytical and numerical modeling was performed to estimate residual stresses and predict their effect on mechanical behavior. For numerical modeling, simulations were performed using ABAQUS standard finite element analysis (FEA) software program. The stresses were modeled on a one-fourth section of the sample in order to decrease computing time. This allowed the mesh to be tightened by four times and facilitated a denser cluster of data points to be acquired at the areas of interest. Experimentally determined elastic modulus values of the EBC layers were used in determining stresses by FEA. The results of mechanical evaluation and modeling were confirmed by microstructural characterization of critical flaws by fractography.

Results

SN282 Si_3N_4 Coated with BSAS EBC

Flexural strength characterization of the BSAS-coated SN282 Si_3N_4 specimens (with lateral dimensions of 26 × 2 mm and substrate thickness of 1.5 mm) performed in a related program indicated that the measured strength of BSAS EBC-coated specimens (357±17 MPa) was lower than the strength of the uncoated SN282 Si_3N_4 specimens (500±74 MPa). This reduction in strength was believed to be due to the presence of large tensile residual stresses in the EBC arising from thermal expansion coefficient mismatch between the substrate and the EBC. To this end, we have constructed a residual stress profile for the Si_3N_4 and BSAS EBC layers using an FEA, as shown in Figure 1. The figure clearly indicates the presence of large tensile stresses in the silicon (Si) bond coat. This was in agreement with fractographic observations, which indicated that failure initiated from preexisting flaws in the silicon bond coat. To further delineate the role of different coating layers, the four-point flexure strength of Si_3N_4 bar specimens (with lateral dimensions of 26 × 2 mm and substrate thickness of 1.5 mm), coated only with an Si layer, was evaluated with the Si top coat in tension. The measured strength of the Si-coated Si_3N_4 flexure bars was 278±11 MPa, which is ≈56% of the strength of uncoated Si_3N_4. This decrease in strength is attributed to the high tensile residual stresses developed in the silicon coating (thermal expansion coefficient,

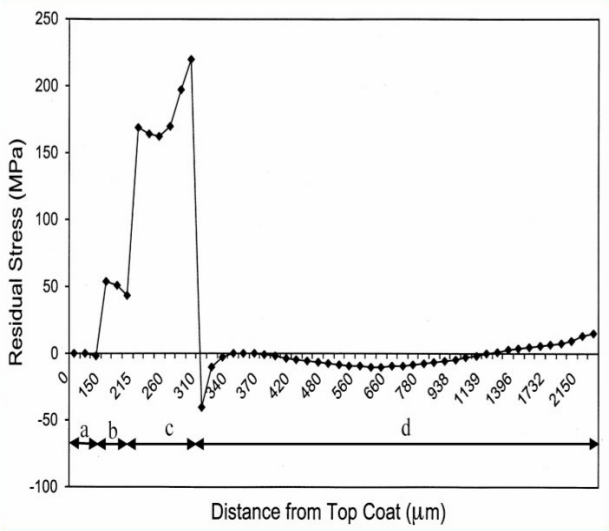

Figure 1. Residual stress distribution in the different layers of a BSAS-coated SN282 Si_3N_4 substrate as estimated by FEA. The stresses are in a direction parallel to the EBC/ Si_3N_4 interface. The letters a, b, c, and d represent the thickness of BSAS top coat, BSAS + mullite layer, silicon bond coat, and Si_3N_4 substrate, respectively.

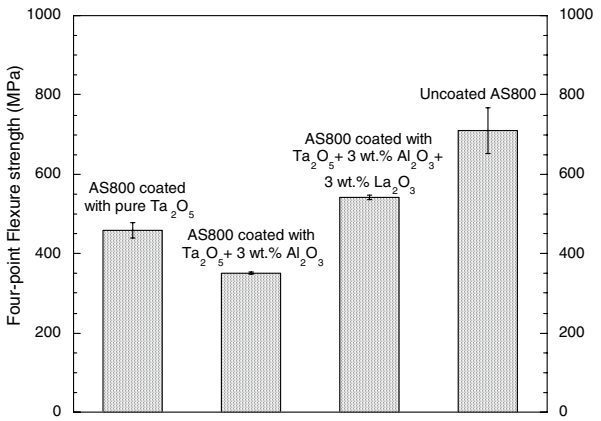

Figure 2. Effect of Ta_2O_5 based EBC composition on the flexure strength of EBC coated AS800 Si_3N_4 specimens. The flexure strength of uncoated AS800 is also shown for comparison.

α: $\alpha_{Si} = 4.9 \times 10^{-6}$/K and $\alpha_{Si3N4} = 3.3 \times 10^{-6}$/K). This was consistent with fractographic observation of the fracture surface, which clearly showed that failure initiated from the silicon coating at the Si/Si_3N_4 interface. Thus it is confirmed that tensile residual stresses in the silicon layer result in reduced strength of Si_3N_4 coated with Si, as well as that coated with BSAS EBC, and the Si layer may be the potential region for failure initiation.

AS800 Si_3N_4 Coated with Ta_2O_5 EBC

The effect of Ta_2O_5 EBC composition on the four-point flexure strength of AS800 Si_3N_4 specimens was evaluated to provide guidance on optimum EBC composition. Results are shown in Figure 2. The Ta_2O_5 EBC had been deposited using a small particle plasma spray process[3] on the substrates, which had been preheated to 450°C following a 1250°C soak. Four-point flexure bar specimens $26 \times 2 \times 1.5$ mm were machined from the coated substrates using a diamond saw. For comparison, the measured strength of uncoated AS800 specimens is also shown in the figure. It can be clearly seen in the figure that the flexure strength (543±6 MPa) of AS800 coated with Ta_2O_5 + 3 wt. % Al_2O_3 + 3 wt. % La_2O_3 EBC is the highest among the three EBC compositions. However, all the three sets of EBC-coated AS800 specimens have lower strength than the uncoated AS800 specimens.

The observed decrease in strength for the EB-coated AS800 specimens may be related to (1) the presence of residual stresses at the interface arising from thermal expansion mismatch between the AS800 substrate and the EBC and (2) the relaxation of surface stresses during coating deposition. Therefore, a 3-dimensional FEA was performed to evaluate the residual stresses arising from thermal mismatch and their effect on the stress profile during four-point flexure loading of a rectangular bar specimen of AS800 coated with pure Ta_2O_5. The simulation of the stress profile in the Si_3N_4 bar during flexure loading considered (1) the effect of residual stresses due to coefficient of thermal expansion (CTE) mismatch between the Ta_2O_5 coating and the Si_3N_4 substrate and (2) the effect of elastic mismatch between the coating and substrate during mechanical loading. Note that in addition to CTE mismatch, the residual stresses were also influenced by the elastic modulus of the thin EBC layers. Therefore, accurate evaluation of the elastic modulus of thin EBC layers is critical for reliable stress analysis and performance prediction. However, measurement of the elastic modulus of thin EBC layers by conventional techniques is difficult. To this end, we have established and standardized the protocols for elastic modulus evaluation of thin EBC layers by indentation technique and routinely use it in this program. This technique is quick and reliable.

Figure 3 shows the stress distribution in the Ta_2O_5 coating and Si_3N_4 substrate at fracture, as

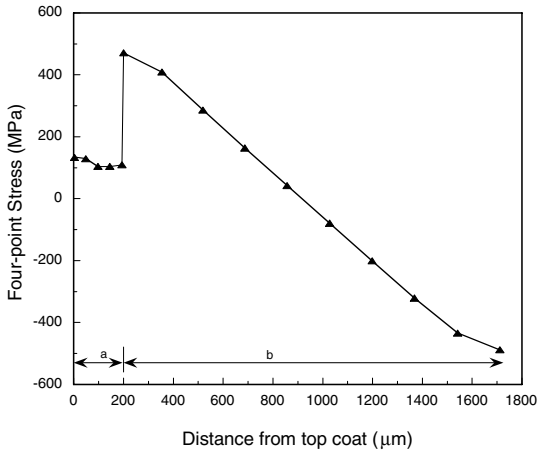

Figure 3. Stress profile (obtained by FEA) at failure in a Ta_2O_5 -coated AS800 Si_3N_4 substrate under four-point flexure loading. The letters a and b represent the thickness of the Ta_2O_5 coating and Si_3N_4 substrate, respectively.

estimated by FEA. These stresses are directed in the longitudinal direction in a plane parallel to the substrate. It is clear from the figure that the maximum tensile stress is present at the Ta_2O_5/Si_3N_4 interface. The maximum tensile stress is expected to promote the propagation of an inherent crack at the interface, leading to failure of the coated Si_3N_4 substrate. This is consistent with the observed failure of a coated Si_3N_4 substrate as shown in Figure 4, which indicates fracture initiation at the Ta_2O_5/Si_3N_4 interface.

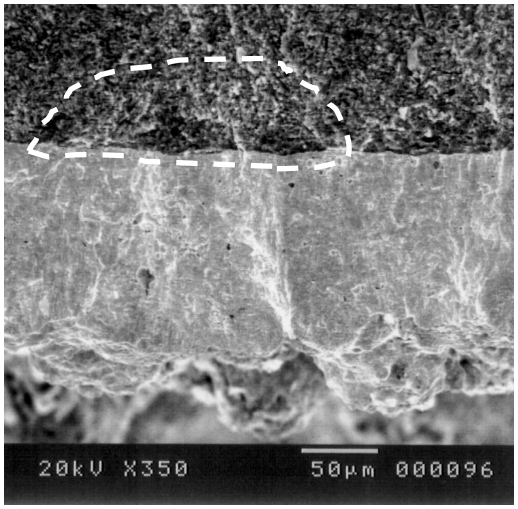

Figure 4. Fracture surface of AS800 coated with Ta_2O_5 + 3 wt. % Al_2O_3, showing the critical flaw causing fracture initiation at the EBC/substrate interface.

Conclusions

Results clearly indicate that for BSAS EBC–coated SN282 Si_3N_4, the Si layer may be the potential region of failure initiation. The strength variation in coated AS800 Si_3N_4 substrates with composition and heat treatment of Ta_2O_5 -based EBCs can be attributed to (1) a thermal expansion mismatch between the substrate and EBCs and (2) various degrees of relaxation/decrease in residual stresses present in the substrate during the deposition of EBC. It could also be partly due to the generation of undesirable flaws in EBCs. These results indicate that with appropriate coating design and processing, undesirable residual stresses can be minimized and the overall performance and lifetime of EBCs can be enhanced. Therefore, modeling studies are in progress to tailor coating design and provide guidance for processing and design optimization of EBCs with improved performance.

References

1. K. N. Lee, "Key Durability Issues with Mullite-Based Environmental Barrier Coatings for Si-Based Ceramics," *Journal of Engineering for Gas Turbines and Power*, 122 632–36 (2000).
2. S. V. Nair, Harry E. Eaton, and Ellen Y. Sun, "Mechanical Properties of an Environmental Barrier Coating on a Monolithic SiC Substrate and Its Role on Substrate Failure Behavior," *Ceramic Engr. & Sci. Proc.*, 23(4) 517–24 (2002).
3. M. Moldovan, C. M. Weyant, D. L. Johnson, and K. T. Faber, "Tantalum Oxide Coatings as Candidate Environmental Barriers," *J. Thermal Spray Technology*, 13(1) 51–56 (2004).

Awards

J. P. Singh received the 2004 James Mueller Memorial Award from the Engineering Ceramics Division of the American Ceramic Society for his scientific contributions.

Publications/Presentations

J. P. Singh, "Residual Stresses in Ceramic Composites and Coatings," James I. Mueller Award Lecture, 28th International Conference and Exposition on Advanced Ceramics and Composites, Cocoa Beach, FL, January 25–30, 2004.

K. Sharma, P. S. Shankar, and J. P. Singh, "Mechanical and Fractographic Evaluations of Si_3N_4 substrates with Environmental Barrier Coatings," poster presented at the 106th American Ceramic Society Annual Meeting and Exposition, Indianapolis, IN, April 18–21, 2004.

High-Temperature Diffusion Barriers for Ni-Base Superalloys

J. Allen Haynes and Bruce A. Pint
Metals and Ceramics Division
Oak Ridge National Laboratory
Oak Ridge, TN 37831-6156
(865) 576-2897, E-mail: pintba@ornl.gov

DOE Technology Development Manager: Debbie Haught
(202) 586-2211; (202) 586-7114 (fax); e-mail: debbie.haught@ee.doe.gov
ORNL Technical Advisor: Karren More
(865) 574-7788; fax (865) 576-5413; e-mail: morekl1@ornl.gov

Objective

- Investigate the feasibility of forming diffusion barriers between an oxidation-resistant aluminide coating and a superalloy substrate, to extend coating lifetime by reducing interdiffusion between substrate and coating.
- Evaluate the feasibility of forming a diffusion coating over an effective diffusion barrier (using model systems), since outward diffusion of Ni from the superalloy would be inhibited by an effective barrier.

Approach

- Select Engle-Brewer compounds ($HfNi_3$, $HfPt_3$, $HfIr_3$) as attractive diffusion barrier compounds and fabricate them by sputter coating followed by annealing. Subsequent aluminizing by chemical vapor deposition (CVD) at 1100°C formed an overlying aluminide coating.
- Characterize aluminized specimens and evaluate their high-temperature performance during isothermal and cyclic oxidation testing at an accelerated test temperature (1150°C).
- To assess the feasibility of forming a diffusion coating over an effective diffusion barrier, oxidize superalloys to form a thin layer of pure alumina followed by sputter coating with Ir, Ni, and Hf, annealing and CVD aluminizing.

Accomplishments

- Found that heat treatment of Pt-Hf layers resulted in a thin film of a compound with composition similar to $HfPt_3$.
- Demonstrated that a thin layer of Hf sputtered on the surface of the superalloy improved the oxidation behavior of CVD NiAl and slightly reduced Al depletion in the coating.
- Determined that CVD aluminide coatings with Hf-Pt thin films showed good oxidation resistance after 300 cycles at the accelerated test temperature of 1150°C, although the intended diffusion barrier dissolved within the coating.
- Confirmed that there are significant challenges associated with developing diffusion barriers to protect diffusion aluminide coatings.

Future Direction

- Continue thermodynamic and diffusion studies of Engle-Brewer compounds to assess their viability.
- Assess other diffusion barrier candidates.

Introduction

In order to boost the efficiency of power generation gas turbine engines, higher operating temperatures are required. Furthermore, longer lifetimes of the components are needed in order to reduce operating costs and increase system performance and safety. For the highest-temperature metallic components of a gas turbine engine, high-temperature oxidation-resistant metallic coatings are often challenged to meet higher temperatures and longer lifetimes. The majority of these protective coatings contain high Al contents to assist in the formation of a protective external alumina scale. Coatings may be degraded by loss of Al due to surface oxidation or by interdiffusion with the lower Al content substrate.[1,2] Particularly for aluminide coatings, continual reduction in the Al content eventually results in phase transformations, deformations and, ultimately, the formation of faster-growing Ni-rich oxides which quickly degrade coating performance.[3,4] While many recent studies have characterized aluminide coatings and their performance,[2–8] few have examined strategies for reducing interdiffusion.[9,10] Another detrimental effect of interdiffusion is substrate elements, such as Cr and Re, becoming incorporated into the coating and degrading oxidation resistance.[11]

Candidate diffusion barrier materials need to retard diffusion of Al (and possibly other elements) at high temperatures, possess good thermo-mechanical compatibility with the superalloy and coating, and remain relatively stable for extended periods of time at high temperatures. Engle-Brewer compounds (e.g., $ZrIr_3$, $HfIr_3$ and $HfPt_3$) are known for their high melting point and unusual phase stability,[12,13] which suggest that they may possess diffusion barrier characteristics. These compounds are an attractive option for oxidation-resistant coatings, since elements such as Hf, Ir, and Pt are known to enhance oxidation resistance.[2,8,11] The objective of this research was to assess the viability of these compounds as diffusion barriers by fabricating them in conjunction with chemical vapor deposition (CVD) aluminide coatings. A second objective was to demonstrate routes to fabricating CVD coatings over an effective diffusion barrier where Ni diffusion from the substrate will be limited.

Approach

Single-crystal superalloy (René N5 from Howmet Corp., Whitehall, MI) coupons were polished to a 1 μm finish and coated with thin bi-layer films of Hf, Pt or Ir deposited by magnetron sputter coating by Surmet Corporation (Burlington, MA) using proprietary conditions. Various combinations of Hf, Hf and Pt, and Hf and Ir were deposited. A second group of depositions on pre-oxidized substrates included Pt and Ni layers to attempt to form a diffusion coating on a surrogate diffusion barrier (the α-Al_2O_3 layer formed during pre-oxidation in low pO_2). The Pt and Ni were intended to form a β-(Ni,Pt)Al layer without Ni from the substrate.

Prior to aluminizing, various heat treatments of the as-deposited films were used to reduce residual stress, improve coating adhesion, and interdiffuse the various layers. Sputter-coated specimens were aluminized by a low-activity CVD process at 1100°C. The reactor and CVD process are described in detail elsewhere.[6] As-aluminized specimens were cyclically oxidized (1 h at temperature, 10 min cooling between cycles) at 1150°C in dry, flowing O_2. Isothermal oxidation exposures were conducted in the same environment with the mass change continuously measured by a microbalance. Selected specimens were characterized using field emission gun–scanning electron microscopy (FEG-SEM), X-ray diffraction (XRD) and electron microprobe analysis (EPMA).

Results

Pt-Hf Sputter Coatings

Initially, buckling and peeling of the coatings was a significant problem, likely due to the very smooth surface finish needed for good sputter deposition. Various annealing treatments (500–800°C) were employed to reduce residual stress and improve coating adhesion. Buckling was especially problematic for specimens with coatings >5 μm in thickness. A secondary heat treatment (800–1100°C) was used with the Hf and Pt coatings to form the $HfPt_3$ phase. Figure 1 shows examples of coatings annealed for 1 h at 500°C and 2 h at 900°C in an Ar atmosphere. With two different Pt coating thicknesses, three distinct layers were formed after annealing with the central layer close to $HfPt_3$.

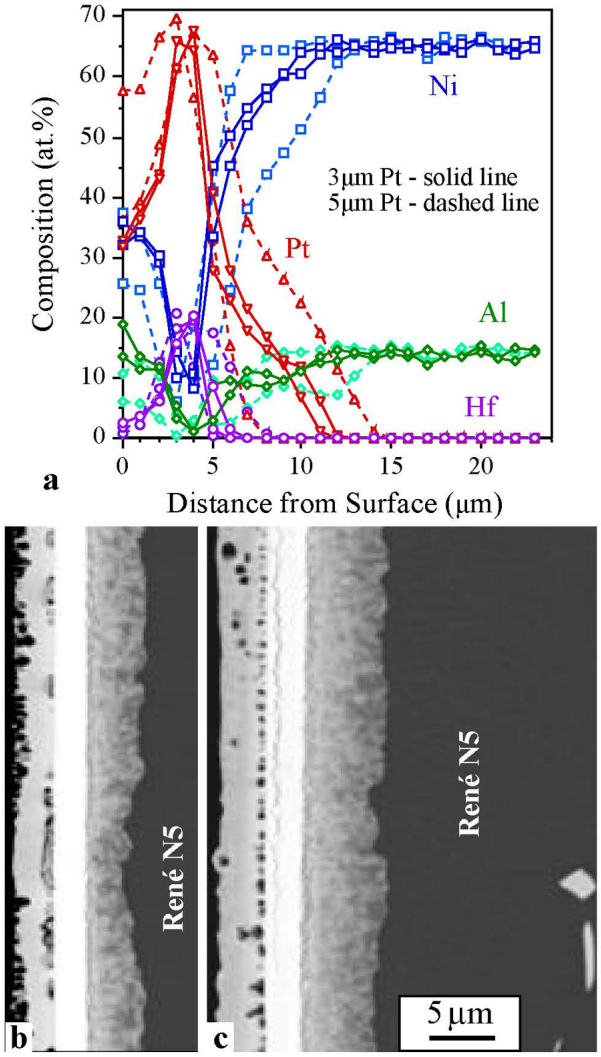

Figure 1. (a) EPMA composition profiles for the annealed but not aluminized specimens. Backscattered electron SEM images of specimens coated with (b) 1 μm Hf/3 μm Pt and (c) 1 μm Hf/5 μm Pt.

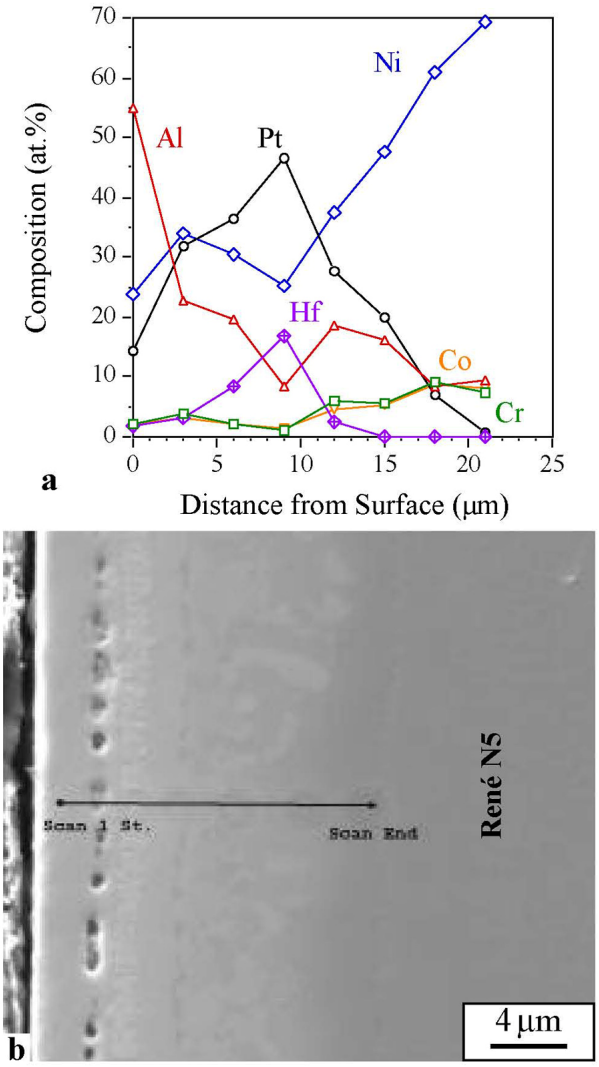

Figure 2. (a) EPMA profile of annealed specimen coated with 1μm Hf/5 μm Pt after 1h CVD aluminizing, (b) micrograph of region analyzed in (a).

However, XRD was not able to identify this subsurface phase. One promising observation was that the Hf-Pt layer had very low solubility for Al and Ni. The other two layers indicate that significant interdiffusion occurred after only 2 h at 900°C. A layer rich in Ni and Pt formed above the Hf-Pt layer, and a significant amount of Pt diffused into the superalloy.

After formation of the Hf-Pt layer, similar specimens were aluminized. Figure 2 shows a cross section after a 1-h, 1100°C CVD treatment. While a region with high Pt and Hf content is still detected (Figure 2a), the Pt and Hf contents have begun to drop compared with the as-annealed composition (Figure 1a). The surface Al content of 55% is higher than normal, suggesting that the aluminization process has been affected by the coating. However, after a 6-h CVD aluminization, the Hf and Pt were almost uniformly present in the coating, similar in composition and microstructure to a standard CVD Pt-modified aluminide coating, with little evidence of the starting Hf-Pt layer. The only remnants were some Hf-rich particles along with voids at the coating-substrate interface.

Oxidation Behavior of Pt-Hf Specimens

Two 6-h aluminized specimens with 1 µm Hf/3 µm Pt were isothermally oxidized in dry, flowing O_2 for 200 h at 1150°C. Significant buckling and heavy localized internal oxidation of the β-NiAl coating was observed after isothermal oxidation, as shown in Figure 3. There were significant amounts of Hf-rich oxide pegs in the coatings, indicating an excess of Hf.

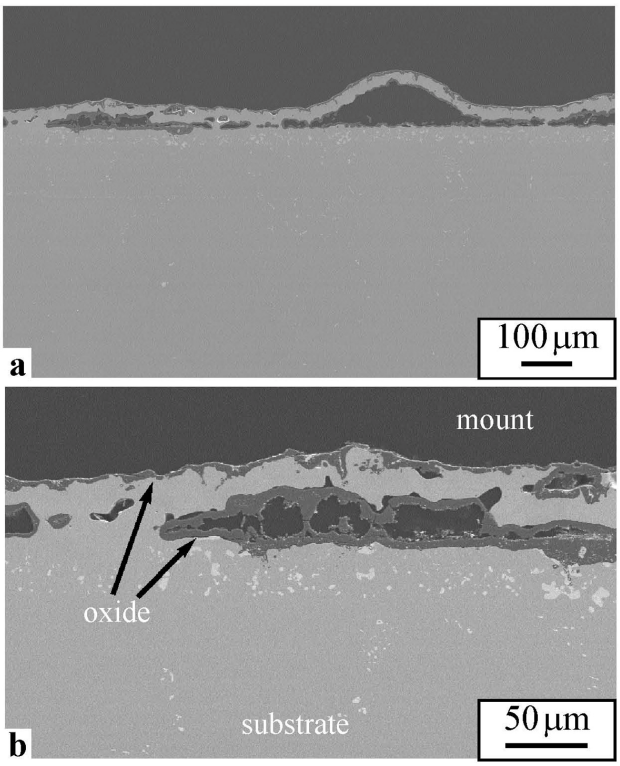

Figure 3. SEM secondary electron images of a cross section of an aluminized superalloy specimen with an initial 3 µm Pt/1 µm Hf sputter coating after isothermal oxidation for 200 h at 1150°C in dry flowing O_2. Significant coating buckling and internal oxidation was observed.

Cyclic testing at 1150°C was used to evaluate the oxidation performance of aluminized specimens. Figure 4 compares the cyclic oxidation mass change of four specimens with that of an aluminized René N5 superalloy with no sputtered Pt-Hf layer on one surface. Two different Pt coating thicknesses were evaluated 3 µm (PHA) and 5 µm (PHB). Specimen PHA-8 received an optimized heat treatment which reduced the amount of coating buckling, and as a result showed excellent oxidation behavior, with

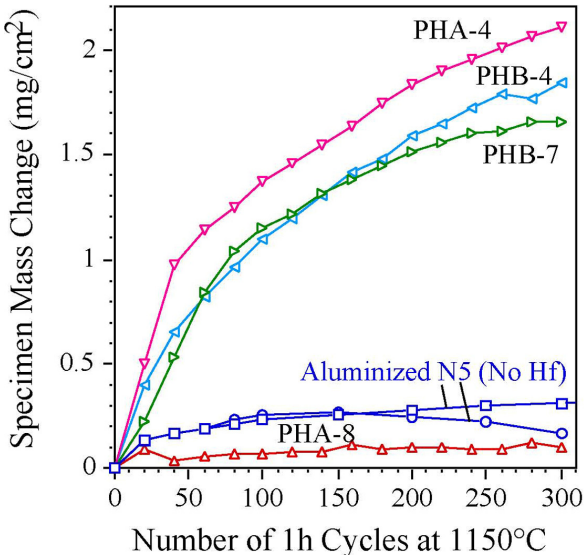

Figure 4. Mass change curves during 1150°C cyclic oxidation testing of CVD NiAl coatings with a 1µm Hf and 3 µm(PHA) or 5 µm(PHB) Pt coating and various pre-aluminizing heat treatments.

mass gains even lower than that of the CVD NiPtAl reference. The higher mass gains of the other three specimens suggest that significant internal oxidation has occurred due to buckling and delamination of the coating. Typically CVD aluminide coatings do not exhibit any macroscopic buckling (e.g., Figure 3), and buckling occurred only on the side of the specimen coated with Pt and Hf. These results suggest that if the Pt-Hf coating adhesion can be improved, an improvement in oxidation performance may be achieved.

Ir-Hf Sputter Coatings

A final batch of specimens was fabricated from Ir and Hf with the goal of forming $HfIr_3$. Delays in receiving the Ir sputter target prevented these specimens from being fully evaluated. Based on the Hf-Pt results, a different coating configuration was used. The amount of Hf was increased, and the Hf was sandwiched between two layers of Ir (3 µm Ir, 2 µm Hf, 3 µm Ir). By depositing Ir rather than Hf onto the superalloy, better coating bonding was anticipated. Some of the as-deposited tri-layer coatings showed localized spallation of the outer layer of Ir, probably due to the increased residual stress in the thick coating. However, preliminary heat treatments of the Hf-Ir coatings has shown less buckling than in the bi-layered Hf-Pt system.

Building a Coating with a Diffusion Barrier

A secondary objective of this work was to examine the scenario of "building" a diffusion coating on top of an effective diffusion barrier. In such a case, Ni diffusion from the superalloy might be limited or prevented. Two approaches to simulating such an event were examined. Both used superalloy substrates that were pre-oxidized in a low-pO_2 environment to form a thin layer of pure alumina, with the goal of using the alumina layer as a simulated diffusion barrier. In the first case, Ni was plated on the surface of the pre-oxidized superalloy specimen and was aluminized. Unfortunately, the quality of the commercial Ni plating was poor and the coatings were not successful. For example, Figure 5 shows a coating formed after 3-h CVD aluminization at 1100°C. No interdiffusion zone formed, but the NiAl layer is highly convoluted above the apparently intact alumina layer.

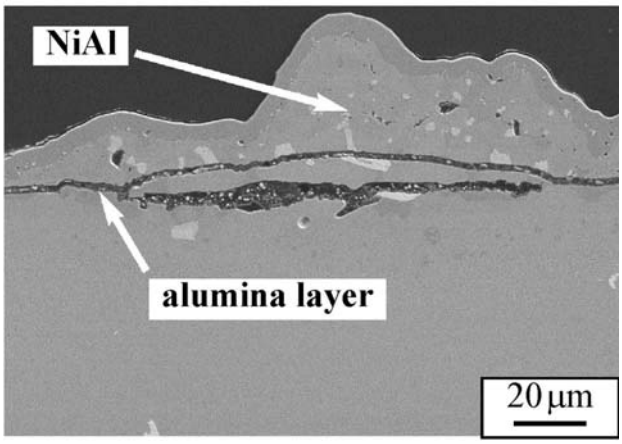

Figure 5. SEM secondary electron image of polished cross sections of CVD aluminized (3 h) pre-oxidized, Ni-plated superalloy. Because the Ni plating was not very adherent, only patches remained for aluminizing.

The second approach was to sputter first Pt and then Ni onto the surface of the alumina. The objective was to then aluminize the Pt and Ni to form a β-(Ni, Pt)Al layer on top of the alumina. It was anticipated that the Pt and alumina might form a more adherent bond, since such results have been seen previously.[14] The coatings were successfully deposited, but preliminary heat treatments have resulted in peeling of the coatings. Additional heat treatments may be successful in preventing delamination.

Conclusions

This work has shown that fabrication of Engle-Brewer compounds as thin films is possible. A Hf-Pt layer was formed with low Al and Ni content. However, during subsequent CVD aluminizing, the layer dissolved. Other similar compounds may be more successful, or a different processing method may be necessary. Future work in this area may need to include more fundamental experimental work and include new candidate materials.

References

1. A. Maricocchi, A. Bartz, and D. Wortman, *J. Thermal Spray Technol.*, **6** (2), 193 (1997).
2. Y. Zhang, J. A. Haynes, W. Y. Lee, I. G. Wright, B. A. Pint, K. M. Cooley, and P. K. Liaw, *Metall. Mater. Trans. A*, **32**, 1727 (2001).
3. J. A. Haynes, K. L. More, B. A. Pint, I. G. Wright, K. Cooley, and Y. Zhang, *Mater. Sci. Forum*, **369–372**, 679 (2001).
4. M. Gell, K. Vaidyanathan, B. Barber, J. Cheng, and E. Jordan, *Met. Trans. A*, **30**, 427 (1999).
5. Y. Zhang, W. Y. Lee, J. A. Haynes, I. G. Wright, B. A. Pint, K. M. Cooley, and P. K. Liaw, *Met. Trans. A*, **30**, 2679 (1999).
6. W. Y. Lee, Y. Zhang, I. G. Wright, B. A. Pint, and P. K. Liaw, *Met. Trans. A*, **29**, 833 (1998).
7. V. K. Tolpygo and D. R. Clarke, *Mater. High. Temp.*, **17**, 59 (2000).
8. J. A. Haynes, B. A. Pint, K. L. More, Y. Zhang, and I. G. Wright, *Oxid. Met.*, **58**, 513 (2002).
9. T. Narita, M. Shoji, Y. Hisamatsu, D. Yoshida, M. Fukumoto, and S. Hayashi, p. 351 in *Proc. Int. Symp. High-Temp. Corr. and Protection*, Hokkaido, Japan, 2000.
10. F. Wu, H. Murakami and A. Suzuki, *Surf. Coat. Tech.*, **168**, 62 (2003).
11. B. A. Pint, K. L. More, and I. G. Wright, *Oxid. Met.*, **59**, 257 (2003).
12. L. Brewer and P.R. Wengert, *Met. Trans.*, **4**, 83 (1973).
13. L. Brewer, *Acta Met.*, **15**, 553 (1967).
14. M. De Graef, B. J. Dalgleish, M. R. Turner, and A. G. Evans, *Acta Met. Mater.*, **40**, S333-44 (1992).

Awards/Patents

B. A. Pint was named to the International Advisory Board of the journal *Oxidation of Metals*.

Publications/Presentations

J. A. Haynes, Y. Zhang, K. M. Cooley, L. Walker, K. S. Reeves, and B. A. Pint, "High Temperature Diffusion Barriers for Protective Coatings," *Surface and Coatings Technology*, **188–189** (2004) 153–157, poster presented at the International Conference on Metallurgical Coatings and Thin Films, San Diego, CA, April 2004 (by Pint).

High-Temperature Heat Exchanger

Edgar Lara-Curzio
Metals and Ceramics Division
Oak Ridge National Laboratory
Oak Ridge, TN 37831-6069
(865) 574-1749; fax (865) 574-6098; e-mail: laracurzioe@ornl.gov

DOE Technology Development Manager: Debbie Haught
(202) 586-2211; (202) 586-7114 (fax); e-mail: debbie.haught@ee.doe.gov
ORNL Technical Advisor: David Stinton
(865) 574-4556; fax (865) 241-0411; e-mail:stintondp@ornl.gov

Objective

- Develop compact, low-weight, high-effectiveness thermal management system components for microturbine heat-recovery units using carbon-based materials.

Approach

- Use woven preforms of commercially available high-thermal-conductivity graphite fibers to develop compact microturbine heat recovery systems with low density, high surface area, high permeability, high thermal effectiveness, and high damage tolerance.
- Working with industrial partners, use established manufacturing processes to fabricate graphite-fiber–based microturbine heat recovery systems.

Accomplishments

- Established a collaboration with 3-Tex Inc. (of Carey, NC), to weave graphite fibers in complex 3-dimensional (3D) architectures.
- Designed a test rig to evaluate simultaneously the heat transfer and permeability characteristics of woven fiber structures.
- Fabricated 3D woven fiber structures with different levels of meso-porosity and determined their permeability.

Future Direction

- Identify optimum 3D fiber architectures that maximize heat transfer while minimizing cost and pressure drop.
- Fabricate heat exchangers using arrays of metallic tubes embedded in 3D woven fiber structures with optimum fiber architecture and evaluate their thermal efficiency using a commercial 30-kW microturbine.

Introduction

Because of the low efficiency (only about 33%) realized by traditional power generation, every year somewhere between 45 and 90 GWh of energy are lost in the United States. This would be enough to power between 45 million and 90 million households. However, by recovering waste heat, combined heat and power (CHP) systems bring energy efficiencies to upward of 70%. In the case of recuperated microturbines, the temperature of the exhaust gases is approximately 250°C. This heat can be captured to dry humid air and/or to produce hot or chilled water for use in space heating, domestic water heating, or air conditioning.

Today, most heat recovery systems for microturbines use exhaust gas–to-water heat exchangers. When heat recovery is required, a diverter flap opens, allowing the hot turbine gas to circulate through the heat exchanger. When heat recovery is not required, the diverter closes, allowing the hot gas to bypass the unit. Supply and return water temperature and gas inlet temperatures are used in the heat recovery unit to control the position of the diverter. This design enables full power to be produced at times when there may not be a need for heat.

Recently, significant efforts have been focused on the development of microturbine systems in which heat recovery is an integral part of the system. These efforts have been driven by the need to reduce the cost and the footprint of the system.

The objective of this project is to improve the efficiency (and reduce the size) of heat recovery systems for microturbines, which currently use aluminum fin heat exchangers. Because microturbine efficiency and the effectiveness of heat recovery heat exchangers are very sensitive to pressure drops, it is necessary that the design of the latter be focused on maximizing heat transfer while minimizing pressure drop.

Specifically, in this project, graphite fiber–based heat exchangers will be designed and fabricated. These systems in turn will be evaluated using a 30-kW Capstone microturbine and their performance compared against that of a Microgen Unifin® heat recovery unit.

In collaboration with researchers at the University of Western Ontario, the thermal efficiency and hydraulic characteristics of the exhaust gas–to-water heat exchanger will be modeled to identify the microstructure of the heat exchanger that optimizes heat transfer, pressure drop and cost.

Approach

This project seeks to design, fabricate, and evaluate graphite fiber–based exhaust gas-to-water heat exchangers for microturbine heat recovery systems. This concept is based on the possibility of weaving high-thermal-conductivity graphite fibers, using commercially available weaving technologies, into complex 2D and 3D architectures with high surface areas. In this concept, each fiber acts as a fin, and the large surface area provided by the fibers in contact with the microturbine exhaust gases maximizes heat transfer. In turn, the ability to control the porosity of the woven structure enables the design of heat exchangers with optimized permeability.

Weaving technologies also provide the means for weaving fibers around water-carrying tubes (Figure 1). The resulting woven structures possess a bimodal distribution of pore sizes: meso-pores, which are the pores between fiber bundles, and micro-pores, which are the pores within fiber bundles.

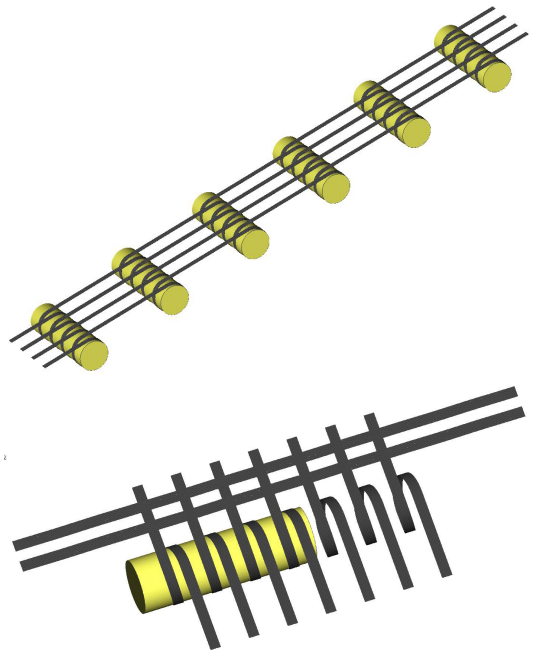

Figure 1. Schematic of woven fiber structures around tubes carrying fluids.

ORNL is collaborating with 3-Tex, a leading company in fiber weaving and braiding technolo-

gies, to manufacture woven structures with different fiber architectures.

Using a specially designed test rig, the heat transfer and hydraulic characteristics of the produced woven fiber structures will be determined. Eventually, the performance of heat exchangers fabricated with the optimum fiber architecture will be evaluated using a 30-kW Capstone microturbine and the results compared with those from a standard aluminum fin Microgen Unifin heat recovery unit.

Results

Three-D fabrics with different architectures were woven by 3-Tex at its Rutherfordton, NC, facility using its patented 3-Weave™ process. The weaves consisted of 6000-fiber tows on the X-Y plane and 3000-fiber tows in the Z direction. Fabrics were woven using Nippon Graphite (NGF) CN35 graphite fibers with intermediate elastic modulus (50 Msi) and thermal conductivity. Figure 2 depicts woven fiber structures with different values of meso-porosity between 0 and 10%.

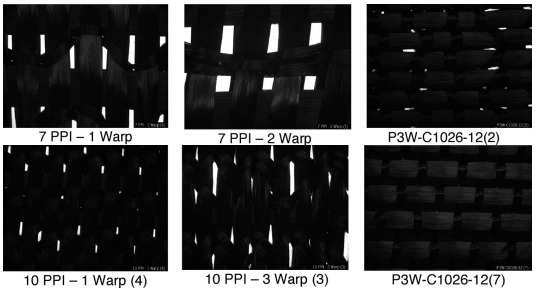

Figure 2. Three-D woven graphite fiber structures with different levels of meso-porosity.

The permeability of the 3D graphite fiber weaves was determined as a function of fiber architecture using a test rig depicted schematically in Figure 3. The results are presented in Figure 4.

It was found that the permeability of the woven graphite fiber structures increases with increasing meso-porosity. Additional work is under way to account for the effect of pore size and pore geometry on this correlation, but these results are already being used to calibrate models that will be used to optimize the heat transfer, permeability, and cost of woven graphite fiber heat exchangers.

Another aspect of this project is focused on studying the structural integrity of carbon foams. These materials are leading candidates for special

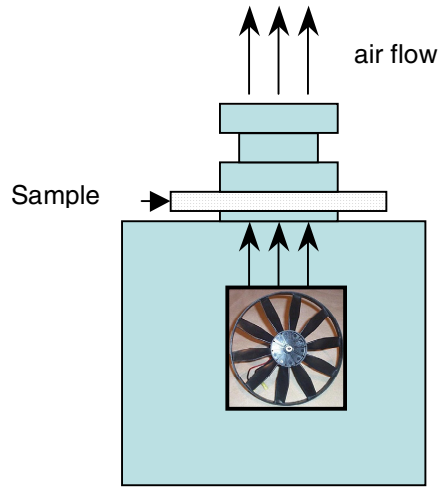

Figure 3. Schematic for the determination of permeability of woven fiber structures.

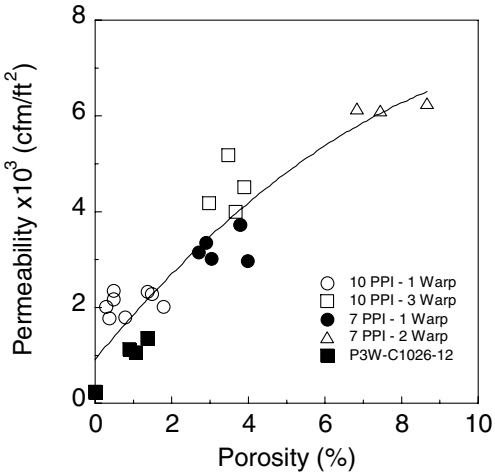

Figure 4. Effect of meso-porosity on the permeability of 3D woven graphite fiber structures.

thermal management applications, but a limiting consideration for the use of carbon foam in some of these applications is its fragile nature. The design of more robust carbon foams requires that the relationship between their microstructure and macromechanical behavior be known, but these models are lacking.

It could be argued that the macromechanical behavior of graphite foams is dictated by the collective properties of the ligaments and how these are connected. Therefore, a thorough characterization of the mechanical behavior of the ligaments could lead to an understanding of their macromechanical behavior. However, the physical dimensions of the foam

ligaments make it very difficult to perform mechanical testing on them.

To establish the relationships between the mechanical properties of individual ligaments and the macromechanical behavior of the foam, scaled versions of the foam structure, from which single ligaments could be isolated and tested, will be fabricated.

In collaboration with Argonne National Laboratory (ANL) and the Japan Fine Ceramics Center (JFCC) in Nagoya, Japan, computed tomography images of carbon foam produced at Oak Ridge National Laboratory under 500, 1000, and 1500 psig of pressure were obtained. Low-spatial-resolution (28-µm) X-ray tomography scans were performed at ANL, and higher-spatial-resolution (3-m) X-ray tomography scans were performed at JFCC. Examples of resulting digital maps are depicted in Figure 5.

These data will be used to produce enlarged digital models of the foam structure, from which physical models of the foam will be fabricated by rapid prototyping techniques.

Summary

Microturbine heat recovery systems are being developed using 3D woven graphite fiber structures. Because of the outstanding mechanical and thermal properties of graphite fibers, this approach has the potential to provide compact, durable, high-efficiency heat exchangers. Working with 3-Tex, woven structures of graphite fibers with different levels of meso-porosity have been fabricated using 3-Tex's patented 3-Weave process, and the permeability has been determined. Future work will be focused on identifying the microstructure of the woven structures that maximize heat transfer and permeability while minimizing cost. The performance of heat exchangers will be evaluated using a 30-kW Capstone microturbine and the results compared with those from commercial microturbine heat recovery units.

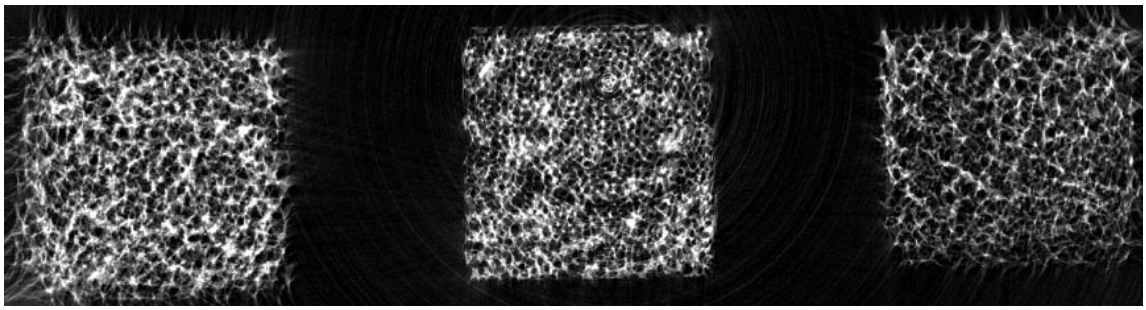

Figure 5. X-ray computed tomography scans of graphite foams of different densities.

Characterization, Modeling and Application of Porous Carbon Foam

B. E. Thompson[1] and A. G. Straatman[2]
AGS Scientific Inc., Thorndale, Ontario, Canada N0M 2P0
Phone: (519) 461-1738, e-mail: tcstraat@rogers.com
[1]Professor, University of Ottawa, Ottawa, Canada
[2]Associate Professor, University of Western Ontario, London, Canada

DOE Technology Development Manager: Debbie Haught
(202)586-2211; (202) 586-7114 (fax); e-mail: Debbie.haught@ee.doe.gov
ORNL Technical Advisor: David Stinton
(865) 574-4556; (865)241-0411 (fax); email: stintondp@ornl.gov

Objectives

- To determine the heat transfer enhancement brought about by bonding layers of porous carbon foam to a solid aluminum substrate and subjecting the surface to different heat fluxes and parallel airflow conditions.
- To determine the depth of penetration of air into the porous carbon foam for the parallel flow conditions considered.

Approach

- Bond layers of porous carbon foam to aluminum plates; machine the foam to desired thickness.
- Conduct experiments in a small-scale wind tunnel facility where the airflow and heat transfer can be accurately controlled.

Accomplishments

- The heat transfer enhancement was not a function of foam thickness for layers greater than 3mm due to a combination of the high effective conductivity and the penetration depth of air.
- The heat transfer enhancement increased by about 10% to 28% as Reynolds number decreased from about 500,000 to 150,000.
- The higher porosity specimens perform better than the lower porosity specimens due to the higher surface roughness and the more open structure of the foam.

Introduction

Porous carbon foam is a relatively new material developed at Oak Ridge National Laboratory (ORNL)[1,2] for potential application in single and multiphase heat transfer. Some of the unique features of the carbon foam are its open interconnected pore structure, which allows fluid infiltration, and its high effective (stagnant) conductivity, which enables the material to readily conduct (or entrain) heat into its internal structure. The high effective conductivity [120–160 (W/m K)] results from the high specific conductivity of the carbon material [1500–1900 (W/m K)]. In comparison, similar porosity aluminum foams have effective conductivities of [2–25 (W/m K)], resulting from a specific conductivities of 140–237 W/m K (for various aluminum alloys).[4] The high effective conductivity combined with the open, interconnected pore structure is conducive to high internal heat transfer and the potential for high convective heat transfer enhancements. The purpose of the present research is to begin to quantify the heat transfer characteristics of porous carbon foam and to develop convective heat transfer expressions that can be used in design considerations.

Porous materials have been studied for many years for application in heat transfer (see, for example[4–8]. Proper characterization of a porous material requires knowledge of the material properties, the flow and pressure drop and the internal (and external) convective heat transfer as a function of porosity and void size and shape. Knowledge of the size and shape of the voids and the surrounding ligaments is very important for understanding the heat transfer in and about the porous material and is dependent upon the process used to produce the material. While sintered-particle porous materials contain small, odd-shaped voids, a porous material produced by foaming can result in a very open, interconnected void structure. Figure 1 gives a magnified image of porous carbon foam taken at an arbitrary cross-sectional cut.[1] The image illustrates the near-spherical void shape, the interconnected structure and the relatively uniform distribution of void size inside the foam. Yu et al.[9] recently proposed a sphere-centered unit-cube geometry model for porous carbon foam, which they used in the derivation of models for the effective conductivity and permeability. The effective conductivity model was shown to yield predictions within 9% of measured results

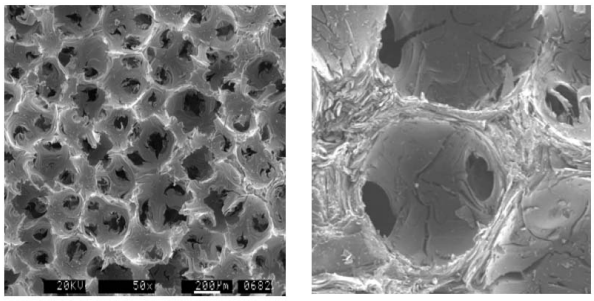

Figure 1. (a) Electron micrograph of the carbon foam surface [1]; (b) Electron micrograph of the carbon foam surface of a single pore.

for carbon foams of different porosity and void diameter. Due to a lack of experimental data, no validation could be provided specifically for the permeability. Since the geometry model[3] also provides expressions for the exposed surface area and ligament structure as a function of porosity and pore diameter, it is especially useful for providing insight into the internal and external convective heat transfer, which is of interest in the present work.

Enhancement of convective heat transfer by the use of porous materials results from the passage of fluid through the open, interconnected void structure, thereby exposing the fluid to internal surface area, which can be as large as 5,000–50,000 m^2/m^3 for porous carbon foam.[1]. The way to obtain maximum surface area exposure is to force all of the fluid through the foam, however this can result in very high pressure drops. Because of the high effective conductivity of porous carbon foam, it is also possible to obtain convective heat transfer enhancements by bonding a layer of foam to a solid substrate and allowing fluid to flow across the foam surface. The high effective conductivity ensures that the layer of foam readily entrains heat out of the solid substrate to be swept away by passing fluid. In this manner, fluid can penetrate the foam surface naturally with modest pressure drop. Convective heat transfer enhancement then occurs in two ways: first due to the roughness of the exposed surface, and second due to the additional surface area exposure to fluid that infiltrates the foam. To understand the utility of this concept, it is necessary to investigate the flow and convective heat transfer under the conditions described above.

This paper presents an experimental investigation into the flow and convective heat transfer in

porous carbon foam. The experiments described in this paper were designed to establish the enhancement of heat transfer that could be obtained by bonding a layer of carbon foam to a flat surface and then subjecting the surface to various heat fluxes and parallel airflows. The enhancement achieved under the conditions considered herein is based upon the natural infiltration of air into the carbon foam and the exposure of the infiltrated air to sub-surface area. The results of these initial tests will serve as a benchmark for all future experiments done in conditions where the surface is inclined with respect to the air flow, or cases where the airflow is impinged upon the surface.

The Carbon Foam Specimens

The carbon foam specimens tested in the present experiments were produced using the patented foaming process[10] and supplied by ORNL. Six different porous carbon foam specimens were machined from 3 different blocks of foam, i.e. two different specimens from each of the 3 different foam blocks. The specimens are characterized by number (217, 219 and 221) and by the location in the foam block (Bottom, Middle or Top) from which they were machined. To clarify the importance of the specimen location in the foam block, Fig. 2 gives Scanning Electron Microscope (SEM) images of metallographic mounted samples showing the Bottom to Top distribution of pore structure for the 3 blocks from which the specimens were obtained. It is clear from these images that the porosity and pore diameter vary considerably from Bottom to Top, the Bottom being the most dense and the Top being the most open. Properties for the six samples are summarized in Table 1. Two different pore diameters are provided in the table: the average pore diameter and the highest frequency pore diameter. It is evident by comparison of Table 1 to Fig. 2 that the average pore diameter is not always a good indicator of the openness of the carbon foam, which is very important in terms of the potential for fluid to infiltrate the foam structure. In particular, for foam 219, the average pore diameter is not seen to vary widely from middle-bottom to top according to the average pore diameter, but in terms of the highest frequency pore diameter (and Fig. 2) it is clear that the foam is more open at the Top. The final column in Table 1 shows the wide range of effective conductivities for the

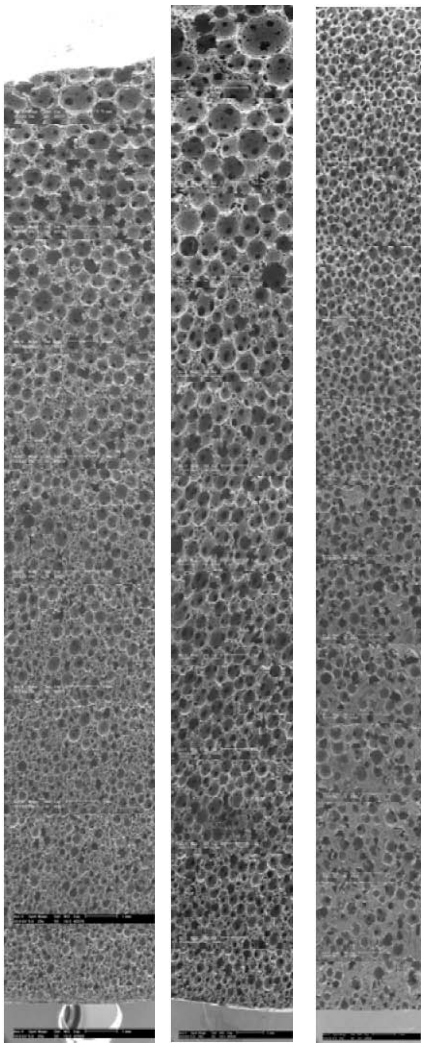

Figure 2. Electron micrograph showing cross-sections of the *Bottom* to *Top* distribution of foam structure for the 3 carbon foam blocks from which the 6 specimens were obtained.

foam specimens. The properties of the different foam specimens are used to elucidate on the convective heat transfer enhancement, which is described in detail in the Results section of the paper.

The Experiments

Experiments have been designed to investigate two important aspects of porous carbon foam subjected to an external airflow: the infiltration of air into the foam and the resulting enhancement of convective heat transfer. Though these aspects are intimately connected, it is important for application of this concept to understand them separately. The infiltration of air into the foam is examined in terms of

Table 1. Summary of properties for the carbon foam specimens tested

Specimen	Porosity [%]	Average Void Dia. [μm]	Highest frequency Void Dia.	k_{eff} [W/m K]
217 Bottom	74	310	300	108
217 Top	78	341	350	68
219 Middle-Bottom	84	643	620	64
219 Top	89	633	800	30
221 (POCO) Bottom	67	473	550	245
221 (POCO) Top	80	430	550	135

the depth of penetration and the resulting area exposure or sub-surface area recruitment, which can be estimated by the geometric model of Yu et al.[9] The depth of penetration of infiltrated air is established herein by conducting a series of experiments starting with a relatively thick layer of foam (10 mm) and then systematically machining away thin layers of foam material and repeating the experiments until the bare substrate is exposed. In all cases, the exposed surface is mounted flush with a larger surrounding surface over which the air flows. Using this technique, we estimate the depth of penetration by observing the thickness that causes an initial degradation of the heat transfer coefficient. That is, if the air naturally penetrates 5 mm into the foam and only 3 mm is available, a degradation of heat transfer can be observed. The enhancement of heat transfer is estimated by comparing the heat transfer of the exposed foam surface to that of the bare substrate once the foam has been machined away. To carry out these experiments, an experimental facility has been designed to accommodate foam samples from 0–10 mm thick. The range of heating and flow conditions were established by considering the thermophysical limits of the test fixture and the flow range of the wind tunnel. These limits correspond surface temperatures of 30 < Tp < 150ºC and airflows of 4–10 m/s. The following sections describe the theoretical basis for the experiments, the experimental facility, the test procedure and the uncertainty of the measurements.

Theoretical Basis

A schematic of the heat transfer problem under consideration is shown in figure 3. A heated (foam-coated or bare) plate of dimensions l × w is mounted flush into the surface of an unheated splitter plate a

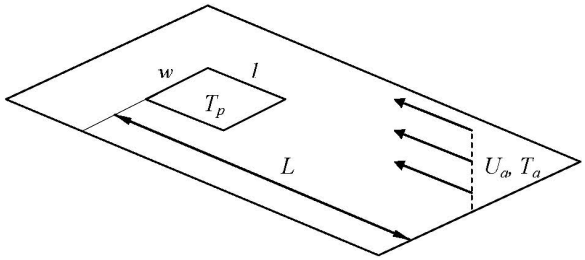

Figure 3. Schematic of geometry under consideration giving all relevant parameters.

distance L-l from its leading edge. The flow is assumed to be two-dimensional on the basis that the splitter plate is much wider than the heated plate yielding a similar profile across the entire heated section. Furthermore, the heating arrangement and control renders the plate isothermal for all conditions considered. The thermal performance of the porous carbon foam is described in terms of the dimensionless heat transfer and the dimensionless flow. The dimensionless heat transfer is characterized using the Nusselt number, NuL, which is given as:

$$Nu_L = \frac{hL}{k}, \quad (1)$$

where, h is the convective heat transfer coefficient, L is the boundary layer development length and k is the thermal conductivity of air evaluated at the film temperature (average of plate and ambient temperatures). The Reynolds number,

$$\mathrm{Re}_L = \frac{\rho U_a L}{\mu} \quad (2)$$

is used to characterize the airflow. Here Ua is the air speed measured upstream of the splitter plate, and ρ

and μ are the density and dynamic viscosity of air, respectively, evaluated at the film temperature. Convection from a heated flat plate is a classical geometry that has been studied for more than a century leading to many correlations (see, for example, Incropera and Dewitt[5]). Heat transfer correlations for the average Nusselt number for a flat plate take the form:

$$\overline{Nu_L} = C\,\mathrm{Re}_L^m\,\mathrm{Pr}^{1/3} \quad , \tag{3}$$

where C is a constant, m describes the exponential dependence of Nusselt number with Reynolds number and Pr is the Prandtl number. In the laminar regime (ReL < 500,000), the exponential dependence is m=0.5 and in the turbulent regime (ReL > 500,000) m=0.8. In cases where the thermal and hydrodynamic boundary layers do not develop from the same location, as in the present case, a modified expression of the form:

$$\overline{Nu} = \overline{Nu_L}\frac{L}{L-\xi}\left[1-\left(\frac{\xi}{L}\right)^{(2p+1)/2p+2)}\right]^{(2p/(2p+1)} \quad ,(4)$$

can be used,[6] where ξ is the unheated starting length and p=1 for laminar flow and p=4 for turbulent flow. For laminar flow, the modification to the Nusselt number is substantial, however if turbulent conditions prevail the modification is smaller since the thermal and hydrodynamic boundary layers rapidly take on the same thickness. For the present case, the roughness of the plate and foam surfaces render the flow fully turbulent even at relatively low Reynolds numbers (ReL 200,000). This is confirmed herein by considering the exponential variation of Nusselt number with ReL over the range of conditions considered.

To formulate the dimensionless heat transfer in terms of the flow and heating conditions, measurements of the heat flux into the plate, Q, the plate temperature, Tp, the air temperature, Ta, and the air velocity, Ua, are required. Once obtained, the average convective heat transfer coefficient can be formed using Newtons law of cooling:

$$\bar{h} = \frac{Q}{A(T_p - T_a)} \quad , \tag{5}$$

and the average Nusselt number is obtained as:

$$\overline{Nu_L} = \frac{QL}{kA(T_p - T_a)} \quad , \tag{6}$$

where A is the plan area of the heated plate. Since the results of importance in the present work are the enhancements obtained by bonding layers of porous carbon foam to the solid plate, all results are expressed as a ratio of the heat transfer for the foam surface with respect to the heat transfer measured for the bare (impermeable) substrate, i.e.,

$$E = \frac{\overline{Nu_{foam}}}{\overline{Nu}} = \frac{\overline{Nu_{L,foam}}}{\overline{Nu_L}} \quad , \tag{7}$$

Included in the presentation of the experimental results for heat transfer enhancement are discussions concerning the dependence of E on ReL, and on the porosity, ε, and pore diameter, Dp, of the carbon foam specimens. The remaining parts of this section describe all aspects of the experimental apparatus and procedure.

The Wind Tunnel

A small-scale, low-speed suction type wind tunnel facility was adapted to carry out the experiments on porous carbon foam. The wind tunnel is driven by a 7.5 HP blower with a variable-RPM motor capable of maximum wind speeds of 15 m/s (45 ft/sec). Figure 4 shows the test section of the wind tunnel and the orientation of the test apparatus described below. The test section of the wind tunnel is 20” H × 18” W × 54” L (0.508 × 0.457 × 1.372 m). The wind tunnel is equipped with a contraction/transition section to go from a round to a rectangular cross-section just upstream of the test section and the inlet section is equipped with a honeycomb screen to generate a good quality uniform flow with a turbulence intensity less than 1%. At the position of the test specimen, the development of boundary layers on the side walls of the wind tunnel reduces the usable width to approximately 80% of total width, i.e., two-dimensional flow exists across 80% of the wind tunnel test section, which is much larger than the width of the heated plate.

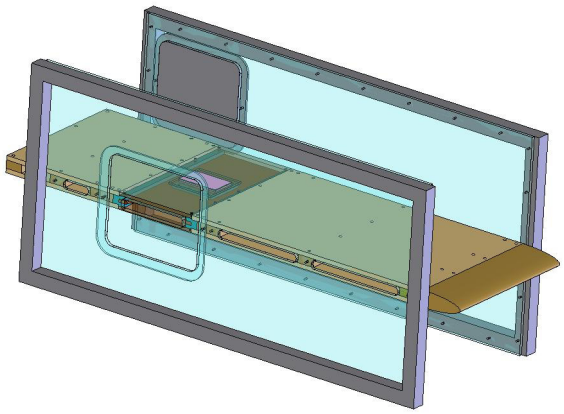

1 – Profiled nose 3 – Test fixture
2 – Splitter plate 4 – Carbon foam specimen

Figure 4. Diagram of wind tunnel test section showing the orientation of the splitter plate and test fixture.

A splitter plate, also shown in Fig. 4, was used to support the test fixture, where the foam samples were affixed. The splitter plate was instrumented with a profiled nose at the leading edge to prevent boundary layer separation. The splitter plate was used to divide the wind tunnel cross-section into two equal sections so that heat transfer could be measured on both the top and bottom of the test fixture. In this manner, energy losses from the test fixture to the surroundings were minimized; the only actual energy losses were due to heat transfer from the test fixture to the splitter plate, which were also minimized by mechanical isolation. The profiled nose and the surface of the splitter plate were rough enough to render the boundary layers fully turbulent over the entire range of conditions considered. This was made evident by the Nusselt number dependence on ReL, as will be shown in the forthcoming results.

The Test Fixture

The test fixture, shown as a cross-sectional view in Fig. 5, was located 0.895 m from the leading edge of the splitter plate. In this location, a two-dimensional developing boundary layer flow was achieved, as discussed previously. The test fixture was designed to slide in and out of the splitter plate so that specimens could be easily removed and

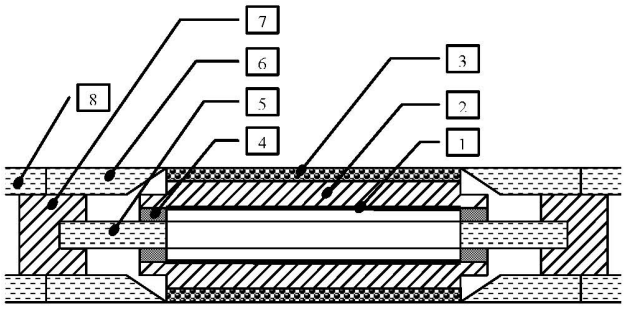

1 – Kapton heating element 5 – Phenolic support board
2 – Aluminum plate 6 – Phenolic board
3 – Carbon foam specimen 7 – Aluminum guide rail
4 – Brass spacer 8 – Upper surface of splitter plate

Figure 5. Cross-sectional view of the test fixture (not to scale) to illustrate the orientation of all of the major components.

modified. The fixture itself was constructed from 3 sheets of 12mm-thick phenolic board held together using hardwood spacers. The center board was supported by aluminum guides, which were fastened to the splitter plate using cap screws. Once in place, the upper and lower phenolic boards were flush with the upper and lower surfaces of the splitter plate to ensure that no boundary layer interruptions would occur. A rectangular opening 0.0762 w × 0.1207 l m was cut into the center of the upper and lower phenolic boards to expose the surfaces of the carbon foam test specimens.

The foam samples were bonded to the upper surfaces of aluminum plates by a brazing operation in which the entire plate was heated to obtain a uniform layer of molten brazing material and the foam was pressed onto the surface allowing the braze material to solidify. While brazing was used to minimize the contact resistance at the aluminum/carbon foam interface, braze material was found to penetrate approximately the first millimeter of foam, thereby not allowing infiltrated air to flow near the interface. The foam was machined to the desired thickness using a high-speed fly cutter. To ensure that the material removed during machining did not penetrate the foam structure, the foam was machined vertically and carbon shavings were vacuumed away from the cutter as material was removed. This eliminated any visible signs of carbon-shaving penetration into the foam.

The plates were heated using rated 150 W Kapton flexible heaters. The heaters were 0.0762 m wide and 0.127 m long, with a total watt density of 15,500 W/m^2. The heaters were bonded to the underside of the top and bottom aluminum plates using a manufacturer-supplied adhesive material. A 1 mm thick metal plate with locking screws was then used to compress the heaters to the plates to prevent the heaters from coming loose through repeated use.

The plates and heaters were assembled using spacers of different thickness, depending upon the foam thickness, such that the upper and lower surfaces of the carbon foam were flush with the surfaces of the phenolic boards and the splitter plate. As the foam was machined away from the plate surfaces, thicker and thicker spacers were used to ensure that the carbon foam surfaces were always flush with the surfaces of the splitter plate

Instrumentation

Instrumentation was required to monitor the velocity and temperature of the inlet air, the temperature of the aluminum plates and the heat flux into the plates. A Pitot-tube was mounted on the tunnel wall and was centered to record the free stream air velocity at the inlet of the wind tunnel test section. A variety of air speeds ranging from 3–10 m/s were used in the experiments. Inlet air temperature measurements were performed using quick-disconnect copper/constantan precision thermocouples (T-type) with miniature connectors and resistant-temperature-detector probes (RTD). The RTDs had a 100-ohm rating with a sensor length of 114 mm and 3.18 mm in diameter. One RTD was mounted on the wall near the contraction of the tunnel to measure the inlet temperature of the air, another was positioned outside to record the room temperature and another set of four were positioned downstream of the heated plate to record the air temperature after heating. The thermocouples were 152 mm long with a sheath diameter of 1.6 mm.

To monitor the aluminum plate temperature (and to ensure uniformity of the plate temperature), nine thermocouples were installed near the upper surface of the top aluminum plate, and two were positioned in the bottom plate. The drawing shown in Fig. 6 shows the location of the temperature measurement points in the upper aluminum plate. Holes were drilled from the sides of the aluminum plates to ensure that the upper surface remained smooth once all of the foam was machined away. The holes were drilled such that the tips of the thermocouples were 1mm from the exposed surface. The thermocouples were all pressed into the holes using a conductive paste to ensure a good thermal contact.

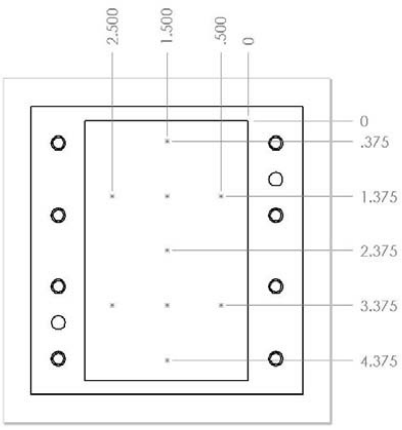

Figure 6. Plan view of the upper aluminum plate showing the locations of the temperature measurement points.

The plate heaters were powered using an AC variable power supply. The heat input was continuously monitored using voltage and current measurement transducers attached to the output of the heat source.

Data acquisition was done using a NI PCI-6014 basic multifunction I/O & NI-DAQ, AMUX-64T Analog Multiplexer with reference Temperature sensor and the 8-channel SC-2042-RTD. All programming was done using the Matlab data acquisition pack.[12] Signals from the thermocouples were converted to temperatures using a polynomial correlation on the recorded voltages referenced to an ambient air temperature on the data acquisition board.

Test Procedure

As described in the previous section, samples were inserted into the fixture, adjusted to be flush with the upper and lower surfaces of the splitter surface and then tested for several air speeds and heat fluxes.

To establish the appropriate test conditions, the first set of carbon foam specimens was tested for 3 air speeds (in the range 3–10 m/s) and 3 heat fluxes (in the range 20–70W) per foam thickness. To en-

sure that an adequate number of foam layers were considered to characterize the heat transfer performance, the first set of samples was tested for thicknesses of 10, 8, 7, 6, 5, 4, 3, 2, and 1 mm of porous carbon foam. An examination of the data showed that the heat transfer was insensitive to the foam thickness when the foam was relatively thick; enhancements that were observed at 10mm were also observed for 8, 7, 6 and 5mm; below 5mm more significant changes were observed. Thus, all subsequent tests were conducted for 10, 5, 3, and 1 mm layers of carbon foam. As such, the total number of experiments per specimen set was reduced to 24; i.e., 4 foam-layers × 3 air speeds × 2 heat fluxes. While the exact conditions for each specimen varied somewhat, the results cover approximately the same range of flow and heat transfer conditions, as will be seen in the results described below.

For a given test condition, temperature readings from the thermocouples and RTDs were obtained for different wind speeds as measured by the Pitot-tube. Over the range of conditions considered, the maximum variation in the temperature of the aluminum plate was less than 1%, indicating that the specimens were effectively isothermal. On the basis of its high effective conductivity, the carbon foam layer was assumed to be at the temperature of the aluminum substrate. Measurements of the carbon foam surface using a portable temperature measurement device confirmed this assumption. Once a complete set of tests was done for a particular carbon-foam thickness, the test fixture was removed, the specimen was machined to the next desired thickness, and the same tests were repeated. This procedure was continued until all of the carbon foam was machined away and the surface of the aluminum plate was exposed.

Measurement Uncertainty

An uncertainty analysis was carried out to establish the error in the velocity, heat flux and temperature measurements.

Velocity measurements were taken at the entrance of the wind tunnel test section using a Pitot tube. The Pitot tube was connected to a barocell pressure transducer and also to a voltmeter. The wind tunnel control was adjusted until the barocell indicated a pressure value corresponding to the target air speed. Apart from instrument error in the tunnel controls, the only error here was due to the barocell zero setting estimated to be less than 2%. This error was accounted for in every reading.

The plates were heated using a power unit connected to flexible heaters, which were glued to each of the plates. The heat input was read from the power unit and also from a digital voltmeter/ammeter, which was connected between the power unit and the heaters. The Uncertainty of the heat input readings is estimated to be less than 1%, which is insignificant compared to the heat losses inside the test fixture. Since only the enhancement of heat transfer is of interest in this study, any uncertainty in the heat input is essentially cancelled out in the calculation of E.

Each of the 11 thermocouples used to monitor the plate temperature was calibrated using boiling water. Mean voltages were registered as detected by each thermocouple. Several readings were taken at the beginning (for different times – 30, 45, 60, 80, 90mins) at the steady heat supply rate. The precision error in the mean voltages was then evaluated based on a t-distribution and a 95% confidence interval and repeated for 3 representative thermocouples. On this basis, the uncertainty in the temperature measurements on the upper plate for all 96 data sets was approximately 4.5%. It was also observed that the temperature measurement between the top and bottom plates varied by up to a maximum of 11%. The most noticeable differences occurring for thick foam layers (7–10mm). It is expected that this was due to slight differences in the air flow patterns of the upper and lower portions of the test section.

It is important to note here that the test facility was designed to minimize potential errors in the results. The test section was divided into two equal sections so that a symmetric heat transfer experiment could be conducted, thereby minimizing extraneous heat losses. To further reduce the uncertainty, all reported results are presented as a ratio with respect to the heat transfer of the bare aluminum plate, which was measured using the same procedure as the foam specimens. In this manner, any uncertainty in the input heat flux and heat losses in the test fixture are essentially cancelled out, or at least rendered small relative to other factors. In fact, it is felt that the scatter in the heat transfer enhancement data is mainly due to irregularities in the carbon foam specimens and surface irregularities due to machining. Further discussion of this is offered in the next section.

Results and Discussion

To verify the flow regime under which the present measurements have been conducted and to establish the present benchmark flat-plate results, experiments were carried out to obtain the heat transfer for the bare aluminum plates over the full range of heating and flow conditions considered. Figure 7 shows the results of these experiments and illustrates that the average Nusselt number varies with Reynolds number according to the dependence established for fully turbulent conditions (m= 0.8). As stated earlier, this was anticipated due to the roughness of the profiled nose and the splitter plate surfaces over which hydrodynamic boundary layers develop. The results for heat transfer enhancement from carbon foam surfaces are now shown using the results from Fig. 7 as a baseline.

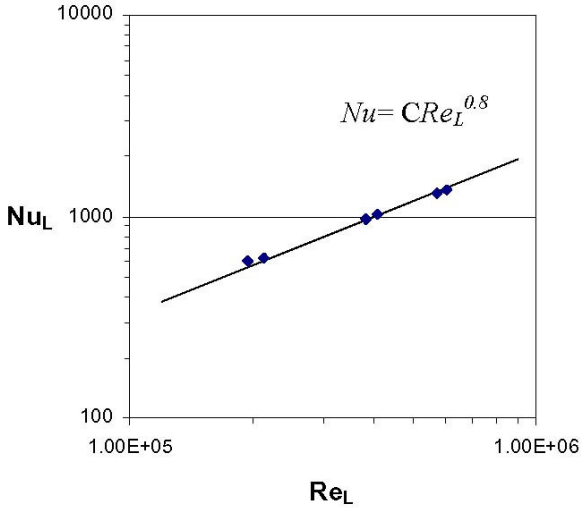

Figure 7. Plot showing the present results for the Nusselt number variation with Reynolds number for the bare aluminum plate. The solid symbols indicate the data points from 6 different experiments.

Figure 8 shows the convective heat transfer enhancement for the carbon foam samples described in Table 1. The plots in Fig. 8 contain complete data for 5, 3 and 1mm of foam and for clarity, only selected data for 8 and 10mm since the results are similar to that for thinner foam layers. All of the plots indicate some enhancement of convective heat transfer, although there is significant scatter on any given plot. Despite the scatter, there appear to be trends in all cases with respect to foam thickness and ReL. The results for different foam thickness are very important. At the outset, the purpose of testing different foam thicknesses was to attempt to establish the depth of penetration of air into the foam.

The present experiments show that the heat transfer is not a strong function of the foam thick ness; heat transfer enhancements that were obtained with 10mm of foam were also obtained, on average, for 5 and 3mm of foam, as shown in Fig. 8a–d. At 1mm foam thickness, the results are seen, on average, to degrade somewhat (and be more highly scattered), probably due to the presence of braze material in the pores. The observations of heat transfer with respect to foam thickness suggest two things: that the foam temperature is the same as the temperature of the aluminum substrate independent of foam thickness due to its low conductive resistance, and that the depth of penetration of air into the foam is relatively small for parallel flow conditions. When comparing the plots in Fig. 8, it is evident that, on average, there is no decisive advantage for using more than 3 mm of foam. This means that the depth of penetration of air into the foam is as little as 3–5 pore-diameters (assuming that the first 1 mm of foam is filled with metallic braze material). Though the penetration depth of air is certainly dependent upon the pore diameter and porosity of the foam, it is difficult to resolve this influence due the non-uniformity of pore diameter and the difficulty of machining the foam thickness to within small fractions of a millimeter. Thus 3 mm serves as a first approximation for the desired thickness of porous carbon foam for parallel flow conditions. It is important to note that the depth of penetration of air into the foam is expected to be a strong function of the incidence of the foam surface with respect to the air flow, i.e. in the limit of an impinging airflow, the air would penetrate the foam surface much more deeply leading to much higher enhancements in convective heat transfer.

Concerning the dependence on ReL, the enhancements shown in Fig. 8 are seen to be higher for low air speeds (about 1.28 on average) and lower for high air speeds (about 1.10 on average), with an approximately monotonic variation. This trend can be explained in terms of the near-surface fluid activity and the relative air flows in and across the porous carbon foam. In a parallel flow, the air is not driven into the foam, but the roughness of the foam surface

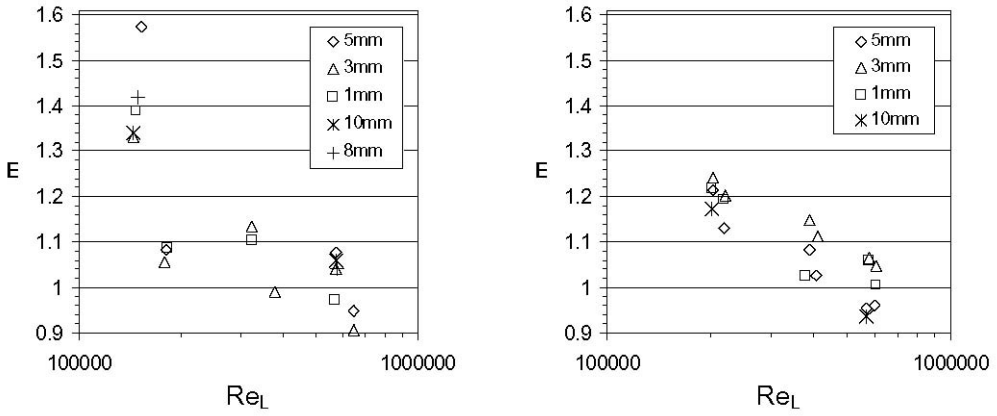

(a) 217-Bottom (b) 217-Top

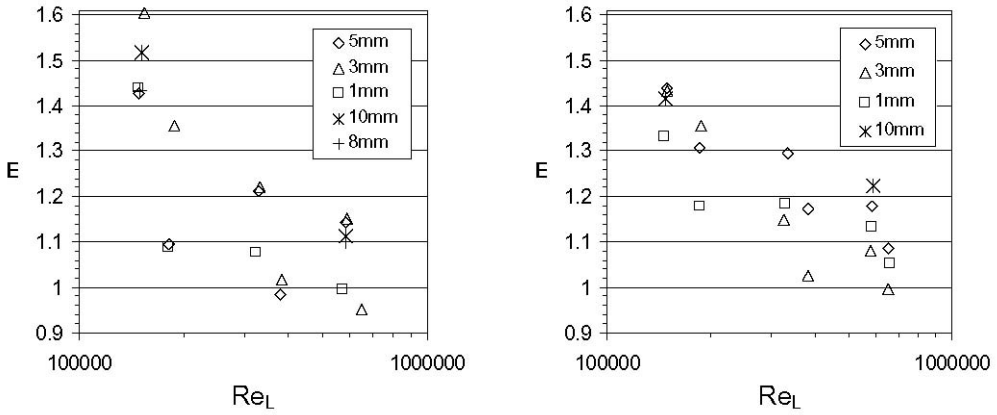

(c) 219-Middle-Bottom (d) 219-Top

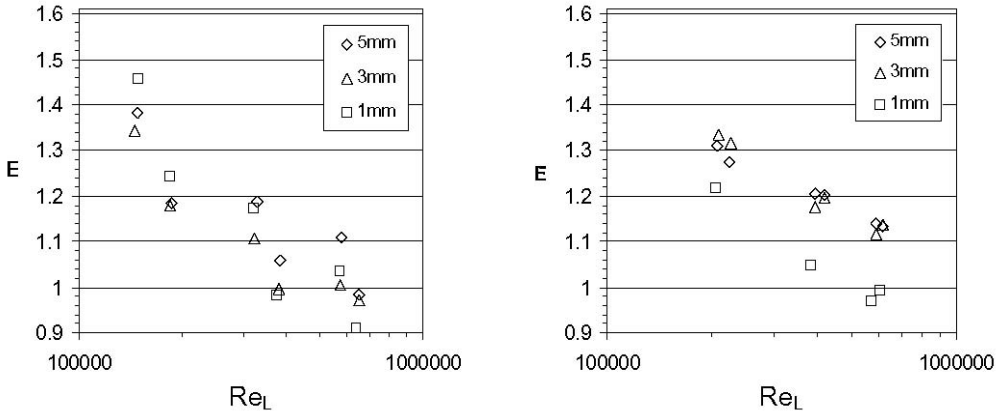

(e) 221-Bottom (f) 221-Top

Figure 8. Results of heat transfer enhancement as a function of Re_L for all of the foam specimens described in Table 1.

produces disturbances of the sublayer resulting in the production of near-surface eddies. The eddies actively penetrate the foam setting up (weak) pressure gradients near the foam surface, thereby causing air to pass through the interconnected pore structure before returning to the free stream. The air that passes through the foam is exposed to the vast internal surface area thereby enhancing the net con-

vective heat transfer of the specimen. At low air speeds (i.e. low ReL), the momentum of the near-surface eddies is low, but the relative amount of air passing through the foam is "significant" with respect to the air flow across the exposed surface of the foam. At high air speeds, the near-surface eddies are very energetic, but the amount of air passing through the foam is "small" with respect to the external flow. As such, the enhancement of convective heat transfer is higher at low air speeds and lower at high air speeds. It is likely that at very high air speeds, the enhancement in heat transfer performance would be due only to the increased roughness and exposed surface area.

Figure 9 compares the Bottom and Top specimens of each of the numbered blocks for foam layers of thickness 5mm and 3mm. From these plots, even more insight is gained concerning differences in heat transfer enhancement due to changes in the effective conductivity and the openness of the foam. As discussed above, the influence of the effective conductivity appears to be minimal for the specimens considered. It is expected that specimens with a very low effective conductivity would degrade the heat transfer from the substrate since there would be minimal means for conducting heat into the foam to be convected away; in this case the foam would serve more to insulate the substrate from the passing airflow.

For the specimens considered in the present experiments, the high effective conductivity renders the foam virtually isothermal at the substrate temperature. In other words, the thermal resistance due to the conductivity of the porous carbon foam is small compared to the convective resistance. While this is expected to be a function of the flow incidence and flow condition, the observation concerning the insensitivity of the heat transfer enhancement to effective conductivity is significant since the cost to produce the foam is a function of the desired specific conductivity.

In terms of the openness of the foam, Fig. 9 show that in general, the higher porosity, larger pore diameter foam layers produce the greatest enhancements in heat transfer. This was an anticipated result since a more open foam structure has a rougher exposed surface (higher friction coefficient) and fosters the infiltration of air and the subsequent exposure to internal surface area. The roughness of the exposed surface influences the activity of the near-wall flow: the more rough and irregular the exposed surface, the more energetic the fluid motions and the higher the infiltration into the foam. It is important to understand, however, that continuously increasing the openness of the foam will not lead to continuous enhancements in the convective heat transfer. There does exist a theoretical limit beyond which further increases in the openness of the foam will cause decreases in the heat transfer enhancement. In the limit of zero-porosity, no air passes through the foam and no enhancement in convective heat transfer occurs. At the other extreme where the porosity is near 100%, the air can pass freely through the foam, but there is insufficient solid material to conduct heat through the foam and insufficient internal surface area to exchange heat with the infiltrated air. Thus, enhancements in the convective heat transfer would be minimal. A balance must be struck between the amount of material for conducting heat into and throughout the foam, and the openness of the foam to allow airflow with minimal pressure drop. In the present experiments, the convective heat transfer (on average) increased in the more open pore structure indicating that the foam structure may not yet be at the theoretical optimum described above.

Figure 10 compares the results of the different foam specimens for foam layers of thickness 5mm and 3mm. Figure 10a compares the results of the three specimens characterized as "bottom" and Fig. 10b compares the results of the three "top" specimens. These comparisons provide similar insight to the comparisons given in Fig. 9, i.e. that the effective conductivity has a minimal influence compared to the openness of the foam. This result is even more clear in Fig. 10 since the effective conductivity and the porosity and pore diameter cover a much wider range of values. In three of the four plots, Foam 219, which is most open but has the lowest effective conductivity, provides nearly the highest heat transfer enhancements.

Summary of Results

An experimental study was conducted to quantify the convective heat transfer enhancements that can be obtained by bonding a layer of porous carbon foam to a solid metal substrate. The following main points are made to summarize the present experimental results:

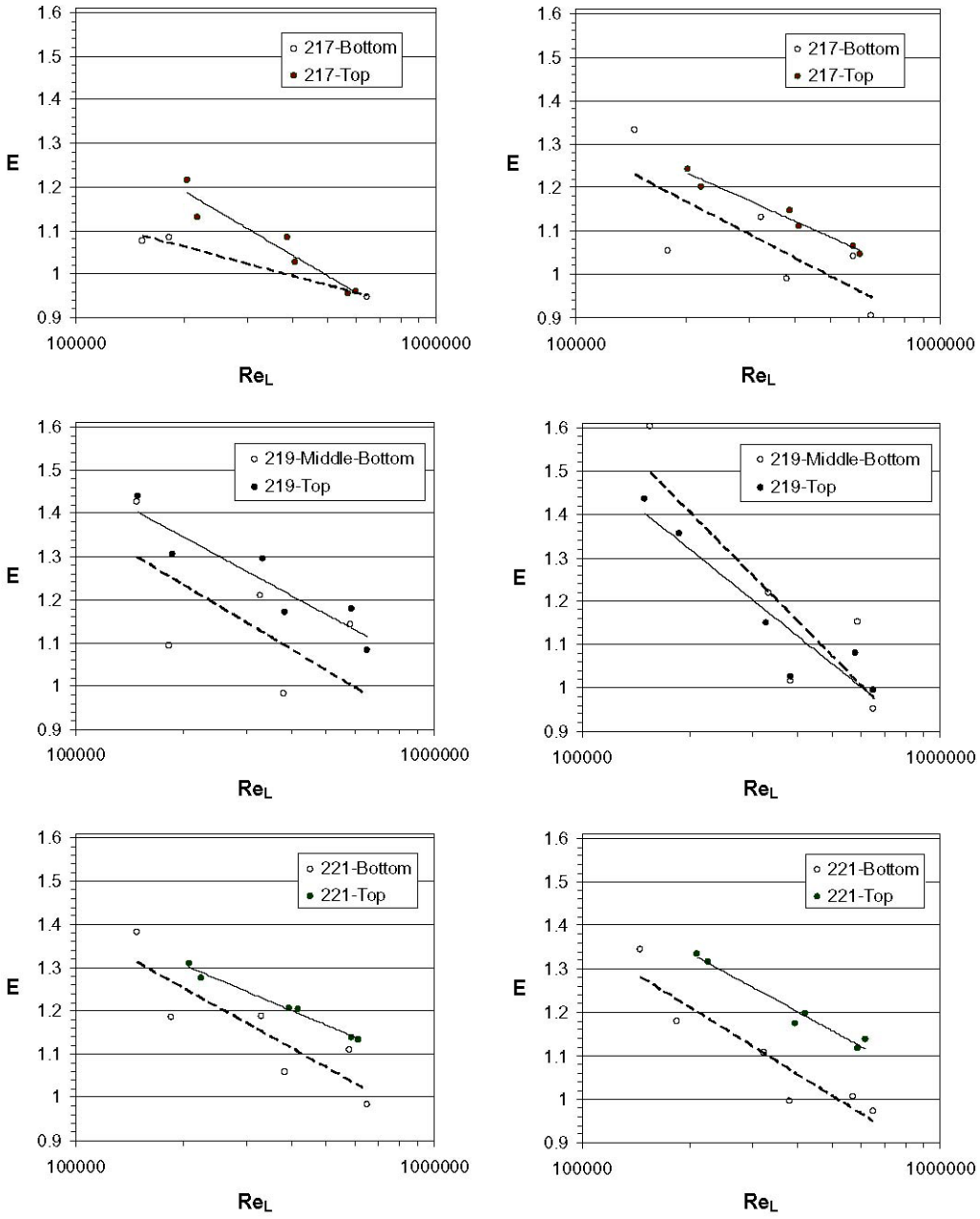

Figure 9. Comparison of convective heat transfer enhancement for the Bottom and Top specimens of Foams 217, 219 and 221, respectively. The plots on the left correspond to 5mm layers and the plots on the right correspond to 3mm-thick layers of carbon foam. The dashed line in each plot gives the approximate trend for "Bottom", while the solid line is for "Top"

1. The heat transfer enhancement was not a strong function of the foam thickness; enhancements observed for 10mm of foam were also observed (on average) for 5 and 3mm of foam. Due to the high effective conductivities of the foam specimens considered, the conductive resistance of the foam was insignificant and the foam layers were essentially isothermal at the temperature of the aluminum substrate. Thus, the depth of foam required to obtain the best heat transfer

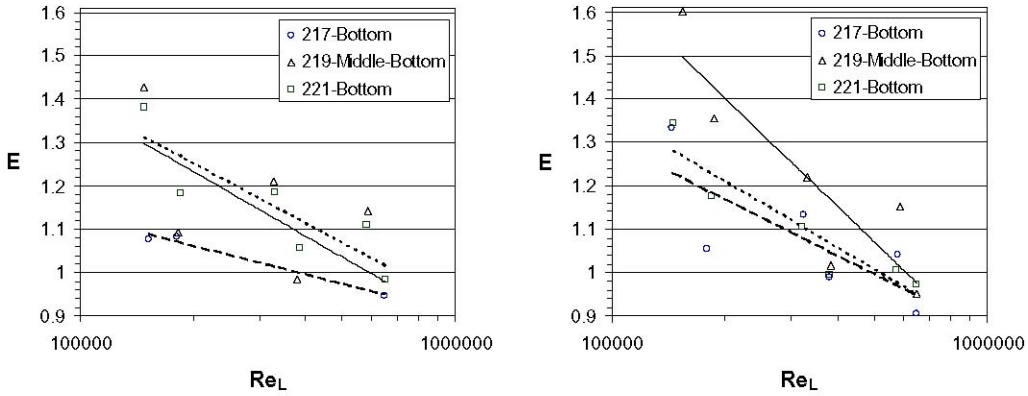

(a) 5mm and 3mm comparisons, respectively

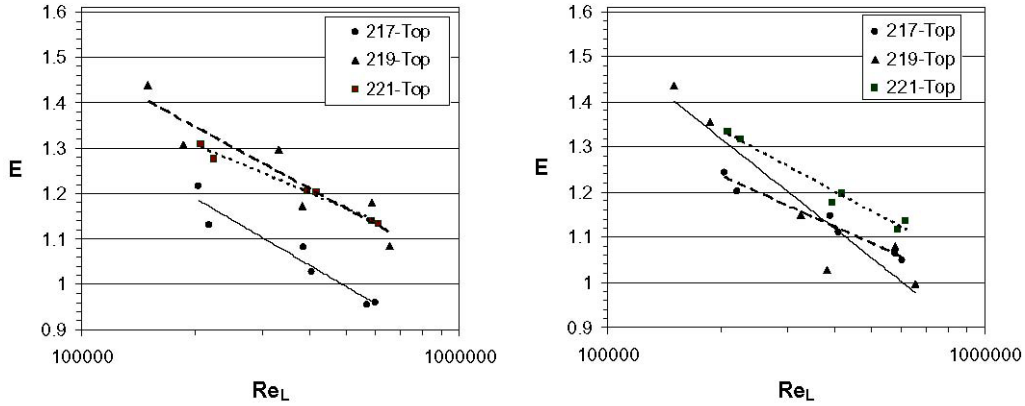

(b) 5mm and 3mm comparisons, respectively

Figure 10. Comparison of the convective heat transfer enhancement for all of the foam samples obtained near the bottom (a) and top (b) of the foam blocks. Results are shown for 5mm-thick (left) and 3mm-thick (right) foam layers. The long dashed line is an approximate trend line for 217, while the solid line is for 219 and the short dashed line corresponds to 221.

enhancement is selected based upon the depth of penetration of air, which for parallel flow applications was deduced to be approximately 3mm.

2. At the lowest ReL considered, the average enhancement of convective heat transfer was approximately 28%; at the highest ReL considered, the average enhancement of convective heat transfer was approximately 10%. The trend from low to high ReL was approximately monotonic. While the activity generated near the rough foam surface is a function of ReL, the heat transfer was observed to be a stronger function of the relative airflow inside the foam and passing across the foam.
3. The comparisons indicate that on average the higher porosity specimens perform better than the lower porosity specimens due to the higher surface roughness and the more open structure of the foam. The higher surface roughness fostered the production of energetic near wall activity, which penetrated the foam surface thereby taking advantage of the subsurface area for convective heat transfer.

The results of the present study will serve as a benchmark for all subsequent experiments at different airflow incidence angles and for different flow conditions.

References

1. Klett, W.J., Hardy, R., Romine, E., Walls, C., Burchell, T., 2000, "High-thermal conductivity, mesophase-pitch-derived carbon foam: effect of precursor on structure and properties," Carbon, 38, pp.953–973.
2. Gallego, C.N. and Klett, W.J., 2003, "Carbon foams for thermal management," Carbon, 41, pp.1461–1466.
3. Paek, W.J., Kang, H.B., Kim Y.S. and Hyum, M.J., 2000, "Effective Thermal Conductivity and Permeability of Aluminum Foam Materials," Int. J. of Thermophysics, 21(2), 453–464.
4. Luikov, A.V., Shashkov, A.G., Vasiliev, L.L. and Fraiman, Y.E., 1968, "Thermal Conductivity of porous system," Int. J. Heat and Mass Transfer, 11, pp.117–140.
5. Kar, K.K. and Dybbs, A., 1982, "Internal heat transfer coefficients of porous metals, " in Heat Transfer in Porous Media, Beck JV, Yao LS, edited, HTD-22, ASME.
6. Kaviany, M., 1995, "Principles of heat transfer in porous media," 2nd edition, Springer-Verlag, New York.
7. Vafai, K. and Hadim, A.H., 2000, " Handbook of porous media," edited by Kambiz Vafai and Haimd A. Hadim, Marcel Dekker, New York.
8. Bhattacharya, A, Calmidi, V.V., Mahajan, R.L., 2002, "Thermophysical properties of high porosity metal foams," Int. J. Heat and Mass Transfer, 45, pp. 1017–1031.
9. Yu, Q., Thompson, B. E., Straatman, A. G., "A unit-cube based model for heat transfer and pressure drop in porous carbon foam," Submitted for publication to ASME J. Heat Transfer, 2004.
10. Klett, W.J., 2000, "Process for making carbon foam," United States Patent, Patent number: 6,033,506.
11. Incropera, M., Dewitt, F., 2003, Fundamentals of heat and mass transfer, Wiley publishing.
12. Ameel, T. A., 1997, "Average effects of forced convection over a flat plate with an unheated starting length," Int. Comm. Heat and Mass Transfer, 24(8), pp. 1113–1120.
13. MATlab, The Mathworks Incorporated, 2002.

Spark Plug Erosion and Failure

M. P. Brady and H. T. Lin
Metals and Ceramics Division
Oak Ridge National Laboratory, Oak Ridge, TN 37831-6068
(865) 576-8857; fax: (865) 574-6098; e-mail: linh@ornl.gov
(865) 574-5153; fax: (865) 241-0215; e-mail: bradymp@ornl.gov

DOE Technology Program Manager: Debbie Haught
(202) 586-2211; fax: (202) 586-7114; e-mail: Debbie.haught@ee.doe.gov
ORNL Technical Advisors: David Stinton and Tom King, Jr.
(865) 574-4556; fax: (865) 241-0411; e-mail: stintondp@ornl.gov
(865) 241-5756; fax: (865) 241-0411; e-mail: kingtjjr@ornl.gov

Objective

- Provide a critical insight into the corrosion/erosion mechanisms of spark plug electrodes as a function of field exposure time and engine conditions.
- Increase the erosion resistance of spark plug electrode materials for advanced natural gas (NG) reciprocating engines to enable engine emission and efficiency goals.

Approach

- Characterize engine-tested spark plugs to identify key erosion mechanisms/limitations of currently used materials.
- Develop and optimize new electrode materials for improved erosion resistance based on understanding gained from the characterization effort

Accomplishments

- Identified key materials-related phenomena impacting the electrode wear of NG spark plugs. Established a framework with end users to study spark plug wear mechanisms as a function of engine conditions at multiple field sites.
- Developed a benchtop test rig protocol to screen developmental electrode materials.
- Established a partnership with Federal Mogul (Champion) for improving the performance and durability of spark plugs for NG engines. This work includes optimizing precious metal electrode inserts, investigating alternative non-precious insert materials, and improving the compatibility and manufacturability of base electrode materials.

Future Direction

- Characterize erosion of currently used spark plugs as a function of time, ignition system, and engine exposure conditions to firmly establish the dominant degradation phenomenon.
- Manufacture new developmental alloys and deliver to Federal Mogul for assembly into spark plugs for engine testing.

Introduction

NG reciprocating engine manufacturers have identified ignition systems as one of the key technologies to achieve cost/performance/emission characteristics goals for lean and stoichiometric engines. Spark plug erosion and subsequent failure have been identified as a major issue in long-term durability of NG ignition systems. Current spark plug lifetimes are on the order of only 1000–4000 h, which results in loss of performance and necessitates frequent, costly downtime maintenance for plug replacement. Desired spark plug lifetimes for NG engine end users are on the order of at least 8000 h (~1 year). It has been recognized that as cylinder pressures, compression ratios, and ignition voltages increase, and conditions move further to lean burn to reduce emissions, spark plug reliability and lifetime performance will become even more critical and could limit further advances in engine development.

This effort was initiated in FY 2004 to characterize used spark plugs after field service to gain insight into the electrode corrosion/erosion processes that limit the spark plug lifetime. It is being pursued in collaboration with the DOE Advanced Reciprocating Engine Systems (ARES) program. The long-term goal is to design new electrode materials based on the fundamental understanding gained from the characterization work to improve the lifetime and reliability of NG spark plugs to meet a 1-year lifetime goal.

Approach

The spark plugs used in this study were acquired from Caterpillar Inc., part number 194-8518, in sets of 16. These are J-type spark plugs with electrodes consisting of a nickel (Ni)-base alloy (~ nominal 90–95 wt. % Ni) and tip inserts of the center and ground electrodes of iridium (Ir) and platinum-tungsten (Pt-W) base alloy, respectively. The spark plugs were used in several Caterpillar 770 e-KW NG engines until significant wear was observed, which required that they be replaced. Two sets of these worn spark plugs, with operating service times of 2020 and 4386 h, were characterized in the present study. A similar set of new (unused) spark plugs was also acquired for comparison.

The electrode tip surfaces of new and worn plugs were examined by optical microscopy and scanning electron microscopy (SEM), combined with qualitative compositional analysis by energy dispersive X-ray techniques. Select spark plugs were also ground and prepared for SEM examination by standard metallographic techniques. Quantitative compositional analysis was performed on the polished cross-sections by electron probe microanalysis (EPMA) using pure element standards. Spectroscopic analysis of sparks from new plugs and used plugs was also performed by R. Richards in collaboration with the ARES program.

Results

SEM analysis of the electrode side surfaces (Ni-base alloy) and Ir and Pt-W tip inserts of the spark plug after 4386 h of field service is shown in Figures 1 and 2. The side surfaces of the Ni-base alloy ground electrode (Figures 2a and 2b) were covered with a glassy phase enriched with calcium (Ca), zinc (Zn), phosphorous (P), and sulfur (S). An oxide phase containing Pt and Ni was also observed with a significant quantity of Ca. In addition, the center electrode showed a similar oxidation product, again containing significant quantities of Ca (Figures 3a and 3b). Note that manganese, chromium, and silicon, alloying elements of the Ni-base alloy electrode, were also detected in various regions.

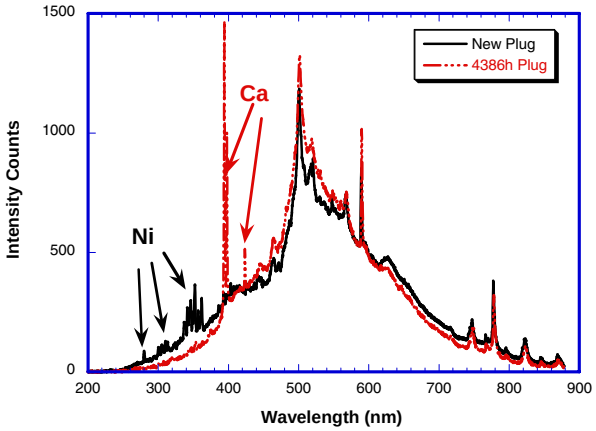

Figure 1. Comparison of emission spectra from a new and used spark plug indicates the presence of Ca in the used plug that is not shown in the new plug.

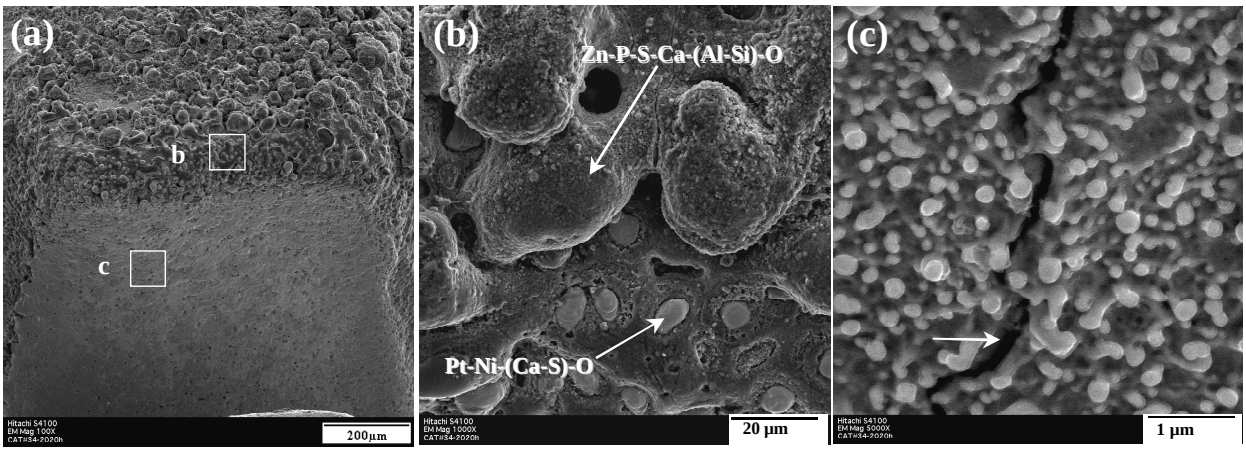

Figure 2. SEM micrographs of Pt-W alloy ground electrode showing substantial formation of glassy phase enriched with Ca on electrode side surface (b) and crack generation and localized melting on Pt-W alloy tip insert surface (c).

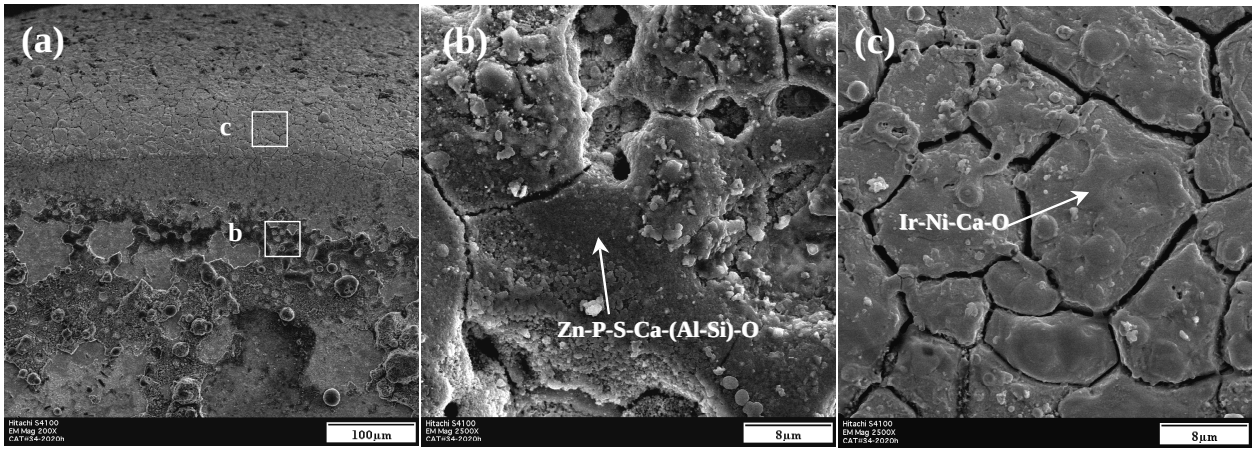

Figure 3. SEM micrographs of Ir central electrode showing substantial formation of glassy phase enriched with Ca on electrode side surface (b) and intergranular cracking and Ir-Ni glassy phase formation on Ir tip insert surface (c).

Examination of the Pt-W tip insert surface showed features of extensive cracking and local melting (droplet morphology) but no apparent formation of surface oxide layer, as shown in Figure 2c. The absence of oxide formation on the Pt-W tip insert surface indicated that the oxide phase could be sputtered off during the sparking process, and thus significant material loss could occur during sparking at the Pt-W ground electrode tip insert.

In contrast, at the Ir tip insert (Figure 3c), the surface was fully covered by a glassy phase containing Ir, Ni, and Ca (substantial intergranular cracking was also observed). The presence of Ca, Zn, P, and S, commonly used as additives, could come from the lubricant used for NG engines.[1,2] Note that introduction of Ca (known as a glass modifier) could significantly decrease the softening temperature and viscosity of any amorphous phase(s), thus possibly enhancing the surface erosion of the Ni-base electrode and Pt-W/Ir tip inserts during spark at elevated temperatures. The observation of Ca in the electrode surfaces was consistent with spectroscopic studies performed under the ARES program, which detected significant quantities of Ca in the spark from the used plugs.

SEM cross-sections of the used plug after 4386 h of field service are shown in Figure 4. Significant wear of the Ni-base electrode was observed at the corners of both the Pt-W ground and the Ir central electrode (Figure 1). (Spectroscopic studies of new spark plugs also indicated significant Ni emissions, suggesting that wear initiates at the corner regions with the Ni electrode alloy). Comparison of the surface areas of both the Pt-W alloy and the Ir

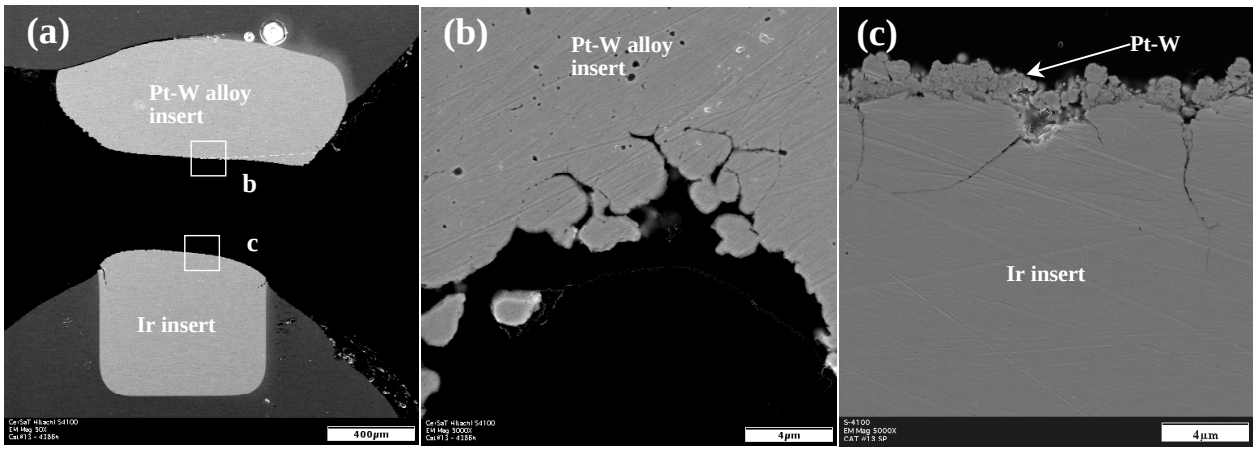

Figure 4. SEM micrographs of polished cross section of 4386 h used spark plug showing significant generation of intergranular cracking in Pt-W alloy (b) and Ir insert (c).

tip inserts between new and used spark plugs showed significant area reduction, ranging from 30 to 40% for Pt-W and 10–15% for the Ir insert. The reduction indicates that the Pt-W insert wore at a much faster rate than the Ir insert. Substantial intergranular cracking was evident in both the Pt-W and Ir electrode inserts. Some surface regions of the Ir insert were coated with Pt-W alloy, presumably as a result of flaking off of the Pt-W insert material after crack coalescence (Figure 3c). In addition to typical surface erosion processes/material loss phenomena resulting from sputtering, melting, ablation, particle erosion, and related effects during sparking,[3,4] the generation, growth, and coalescence of intergranular cracks could lead to significant material loss and could accelerate erosion during field service.

Literature studies have reported that precious metals, particularly Pt, can be susceptible to intergranular cracking when exposed to hydrocarbon environments at elevated temperatures.[5] Also, the observed cracking in the Ir could be the result of brittleness due to ductile-brittle-transition temperature issues, possibly associated with the segregation of impurities at Ir grain boundaries.[6,7] Characterization of partially worn spark plugs after controlled short-term time intervals is needed in order to determine the relative contribution of this intergranular cracking to the loss of electrode tip material. (Such efforts will be pursued in FY 2005).

Figure 5 shows SEM images of the interface between the Ni-base alloy and the Pt-W alloy insert. An oxidized crack was found to extend along much of the interface, ranging from 30 to 75% of the interface length and nearly completely separating the Pt-W tip from the ground electrode. Pt-Ni oxide and significant intergranular cracking in the Pt-W alloy insert were observed in front of the crack tip (Figures 5b and 5c). Such cracking, plus oxide formation, has been observed consistently in many end-of-life used plugs and is suspected to be the life-limiting final step in the wear/erosion process.

Susceptibility to oxidation and crack initiation and growth at this location could result from the interdiffusion between the Pt-W tip and the Ni alloy during manufacturing by the welding process. EPMA of new (unused) spark plugs showed significant interdiffusion of the precious metal tips with the Ni electrode alloy, particularly with the Pt-W alloy tip insert (Figure 6). The Ni-base electrode/Pt-W alloy interdiffusion zone varied from 300 to 500 µm, whereas the interdiffusion zone with the Ir insert was only about ~150 µm.

Conclusions

The analysis of new and near-end-of-life spark plugs tested in an NG engine suggests that oxidation/corrosion and materials compatibility issues contribute significantly to electrode erosion. From an alloy design standpoint, of particular utility to improve electrode erosion resistance were the findings of

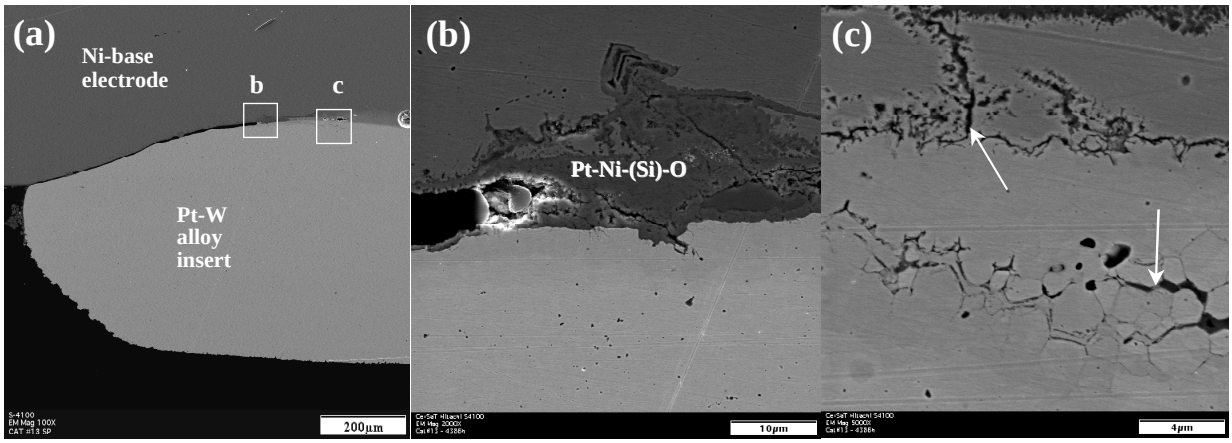

Figure 5. SEM micrographs of Pt-W alloy insert showing crack extended 50% along the Pt-W insert and Ni-base electrode interface (a), crack and Pt-Ni oxide phase at the crack tip (b), and substantial generation of intergranular cracking in Pt-W insert in front of the crack tip (c).

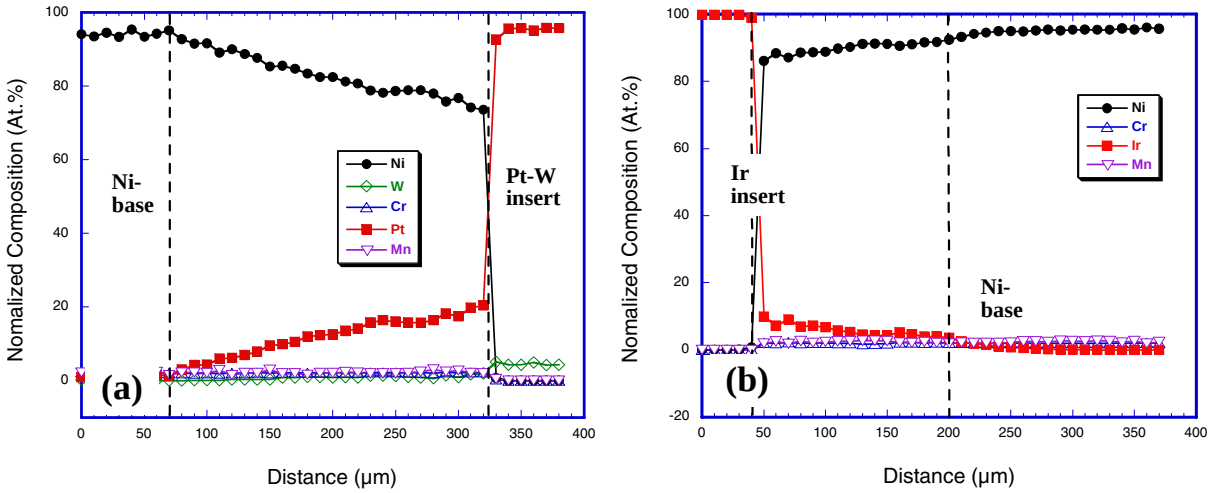

Figure 6. Electron probe microanalysis of (a) Pt-W insert and Ni-base interface and (b) Ir insert and Ni-base electrode.

- materials incompatibility and oxidation/cracking at the Pt alloy insert/Ni electrode alloy interface and
- oxidation and intergranular attack of the Pt and Ir inserts.

Alloy development efforts in FY 2005 will address these issues by (1) identifying and evaluating existing commercial alloys for improved compatibility between the electrode and the Pt/Ir inserts, (2) evaluating microalloyed insert materials for improved oxidation/cracking resistance, and (3) studying model Al_2O_3, Cr_2O_3, NiO, and SiO_2 forming alloys to identify the optimum method for electrode oxidation protection/wear reduction in NG spark plug applications. A partnership was initiated with Federal Mogul to provide a route to manufacture spark plugs for benchtop and engine testing incorporating new materials and to provide a mechanism to translate findings under this program into practice.

References

1. L. (Tex) Leugner, "Natural Gas Engine Lubrication and Oil Analysis—A Primer in Predictive Maintenance and Condition Monitoring," *Practicing Oil Analysis*, September 2003.

2. H. M. Abi-Akar, “A Test Method to Evaluate High Temperature Corrosion,” paper 00530, presented at Corrosion 2000, NACE International Annual Meeting, Houston, 2000.
3. K. Nishio, T. Oshima, and H. Ogura, “A Study on Spark Plug Electrode Shape,” *Int. J. of Vehicle Design*, **15**, 119–130 (1994).
4. A. Lasagni, F. Soldera, and F. Mucklich, “FEM Simulation of Local Heating and Melting During Electrical Discharge Plasma Impact,” *Z. Metallkd*, **95** , 1–7 (2004).
5. W. Kock, D. Lupton, J. Merker, and J. Meinhardt, “PGM-Alloys as Corrosion-Resistant High-Temperature Materials,” *Ber. Bunsenges. Phys. Chem.*, **102(**9), 1284–1290 (1998).
6. S. S. Hecker, D. L. Rohr, and D. F. Stein, “Brittle Fracture in Iridium,” *Metall. Trans. A*, **9A,** 481 (1978).
7. L. Heatherly and E. P. George, “Grain-boundary Segregation of Impurities in Iridium and Effects on Mechanical Properties,” *Acta Materilia* **49**(2), 289–298 (2001).

Awards/Patents

M. P. Brady was named to the International Advisory Board of the journal *Oxidation of Metals.*

M. P. Brady and H. T Lin, “Erosion Resistant Materials for Spark Plug Electrodes,” internal ORNL invention disclosure, September 2004.

Advanced Materials for Exhaust Components of Reciprocating Engines

P. J. Maziasz, N. D. Evans, J. J Truhan, and K. L. More
Metals and Ceramics Division
Oak Ridge National Laboratory
P.O. Box 2008, MS-6115
Oak Ridge, TN 37831-6115
(865) 574-5082; fax: (865) 754-7659; e-mail: maziaszpj@ornl.gov

DOE Technology Development Manager: Debbie Haught
(202) 586-2211; fax: (202) 586-7114; e-mail: debbie.haught@ee.doe.gov
ORNL Technical Advisor: Thomas J. King, Jr.
(865) 241-5756; fax: (865) 576-5413; e-mail: kingtjjr@ornl.gov

Objectives

- Determine natural gas reciprocating engine limitations imposed by various in-cylinder and exhaust system components, employing a systems approach.
- Identify material performance issues and provide better materials for improved performance, higher efficiency, and lower costs.

Approach

- Establish relationships with advanced reciprocating engine systems (ARES) original equipment manufacturers (OEMs) and engine component suppliers.
- Begin a comprehensive analysis of intake and exhaust valves and seats.
- Characterize and compare new and engine-tested in-cylinder components to establish mechanisms and progression of degradation.
- Extend the commercialization of new CF8C-Plus cast austenitic stainless steel to ARES exhaust component upgrade applications

Accomplishments

- Exchanged site visits between ARES OEMs and Oak Ridge National Laboratory (ORNL) to define, begin, and assess progress of an initial in-cylinder component characterization project.
- Established relationships with ARES OEMs and component suppliers to address and enable engine component upgrade solutions.
- Completed characterization of a new exhaust valve to provide a baseline for material selection of advanced reciprocating engines.

Future Direction

- Complete characterization of an initial set of current intake and exhaust valves and seats to define performance limits and failure mechanisms
- Define component upgrade solutions and begin characterizing processing or alternate alloys in collaboration with component suppliers.
- Establish relationships with ARES OEM suppliers of cast exhaust manifolds to enable a side-by-side engine test of current alloys and CF8C-Plus steel components.
- As an outcome of discussions with ARES OEMs and of the results of work completed in FY 2004, explore formation of a partnership among OEMs, lubricant and additive suppliers, and ORNL to develop lubricating oils for natural-gas–fired engines that provide effective lubrication for extended service intervals, prevent or minimize the formation of in-cylinder oil deposits, and avoid the poisoning of exhaust catalysts.

Introduction

Achieving higher efficiency and lower emissions in natural-gas–fueled ARES will require increased pressures and temperatures for in-cylinder and exhaust components. In FY 2004, this ORNL project concluded an initial phase of exhaust valve characterization and was expanded to define a much broader program to characterize the behavior and address the limitations of various critical in-cylinder and exhaust system components due to performance, temperature capability, and tribological capabilities. ORNL has developed partnerships with ARES OEMs and expanded the project scope to include intake and exhaust valves and their respective seats, as well as other exhaust components. The first phase of this project is analyzing new and aged components and characterizing bulk physical metallurgical changes, as well as surface and tribological behavior related to lubrication, wear, and oxidation.

Approach

The approach used for the characterization of in-cylinder components has been to compare as-manufactured (new) and engine-tested components to establish the effects of engine aging on component wear and oxidation. This approach was expanded from receiving individual, cleaned components to receiving complete engine head assemblies so that surfaces, as well as component interactions (valves and seats) and orientations, were preserved. Phase I of this new project began with components exposed to ~2000 hours of engine service and continued with components having significantly longer engine exposures. The analysis of engine-exposed valve system components has been divided into two parallel paths, the microstructural stability of the materials of construction and surface effects, which include oxidation, wear/erosion, and deposit formation due to lubricant break-down.

The approach for exhaust components is to compare high-temperature properties of current exhaust manifold alloys, such as SiMo or nickel-resist cast irons, with advanced alloys like the new CF8C-Plus cast austenitic stainless steel. If the properties advantages are sufficient, then making prototype components with the advanced alloy will be addressed with component suppliers.

Technical Progress

Nickel-based super alloys such as Nimonic, Pyromet, and Waspaloy are used to make exhaust valves for a variety of advanced diesel and ARES engines. These valves are complex systems with weld overlays on the valve seats and coatings on the combustion faces. It is possible for the filet region of the exhaust valve to experience temperatures close to 700°C, and temperatures in the valves of advanced ARES engines may be even higher. High-temperature engine exposure changes the base-metal microstructure and mechanical properties, as well as the structure at the coating and base-metal interface.

Microcharacterization of exhaust valves of a typical Ni-Cr-Fe super alloy (γ' precipitation hardened) was completed in FY 2004. Microcharacterization of the valves in the middle of the combustion face, comparing fresh and engine tested valves, is shown in Figure 1.

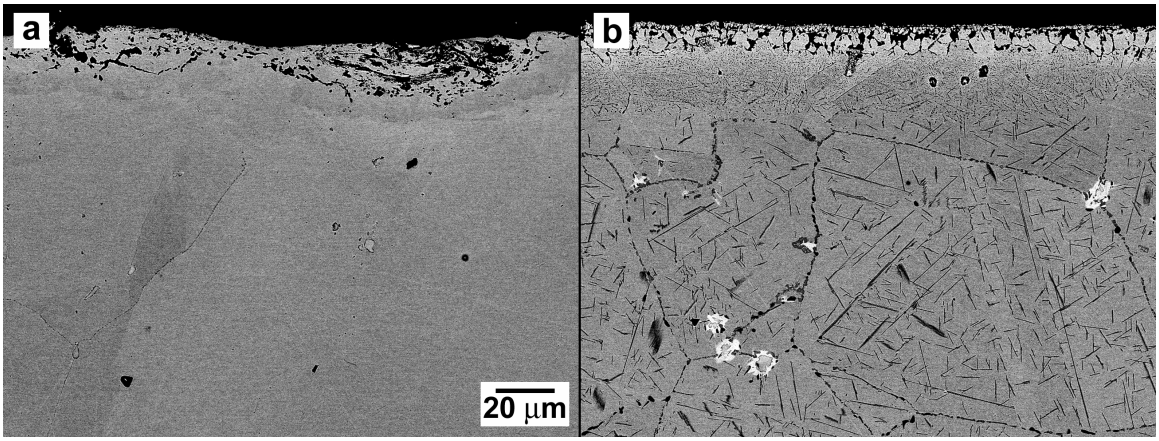

Figure 1. Microcharacterization of the middle of the combustion face region of a typical Ni-Cr-Fe super alloy exhaust valve when new (a) and with several thousand hours of ARES engine service (b).

Aging during engine service produces significant changes in microstructure, causing additional precipitation in the matrix and along grain boundaries (Figure 1). There are large TiO_2 and Al_2O_3 particles beneath the surface of the combustion face of the fresh valve resulting from prior processing or heat treatments. Some of these become entrained in the chromia scale that develops at the surface during service, and more oxide particles (mainly the Ti oxides) develop underneath the scale during service. Higher magnification of the bulk microstructure in the center of the valve and farther up in the filet is shown in Figure 2. The uniform dispersion of needles that precipitate in the matrix of the valve body are pure α-chromium particles (confirmed by electron diffraction).

Exposure to engine service also produces Cr-rich $M_{23}C_6$ carbide precipitation [identified by X-ray energy-dispersive spectroscopy microcompositional and analytical electron microscopy (AEM) electron diffraction data] along the grain boundaries of the exhaust valve (Figure 1). Finally, the Ni-Cr-Fe super alloy exhaust valve is heat-treated prior to service to produce a fine dispersion of $(Ni,Ti)_3Al$ γ' precipitation within the grains for high-temperature strength (Figure 3). Aging during several thousands of hours of engine service significantly coarsens the intragranular γ' precipitation (Figure 3). Analysis of the initial ARES exhaust valve was completed, and these data set the stage for the development in Phase I of a more comprehensive in-cylinder and exhaust component program, which began in FY 2004.

After the initial phase was completed, a more comprehensive in-cylinder and exhaust component assessment and improvement program was started. This included a systems approach to the analysis rather than analyzing isolated components and single effects. ORNL received aged cylinder heads that included intake and exhaust valves, valve seats, valve guides, and the oils and surface deposits accumulated during ~2000 hours of engine service. ORNL also received a complete set of new, unused baseline components to better define aging/service effects by comparison. In the initial characterization of the engine components exposed for ~2000 hours, several bulk cross-sections were cut from representative areas of intake valves and their corresponding valve seats and guides for microstructural evaluation. Particular attention was paid to analyses of

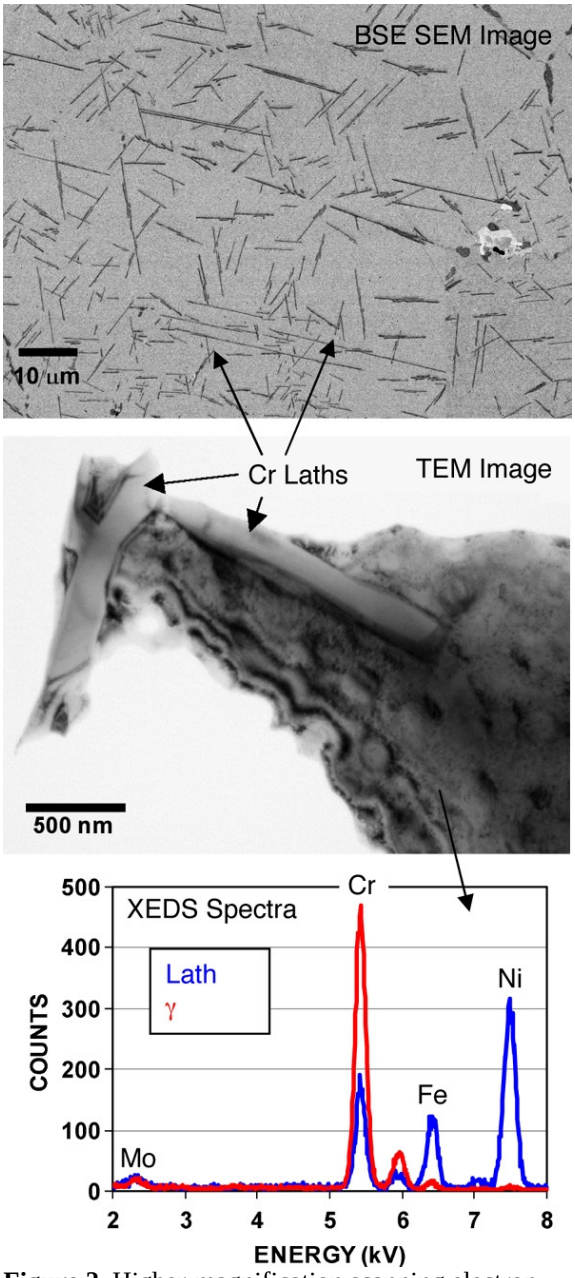

Figure 2. Higher-magnification scanning electron microscopy and transmission electron microscopy (TEM) of typical matrix microstructure in a Ni-Cr-Fe super alloy exhaust valve after engine service, including X-ray energy-dispersive spectroscopy from particles near the edge of the TEM foils.

deposits formed on the different component surfaces, evaluating evidence for tribology/wear on various contact surfaces and quantifying surface oxidation effects. Am image of a section cut from an intake valve head showing the surface deposits on the air side is shown in Figure 4.

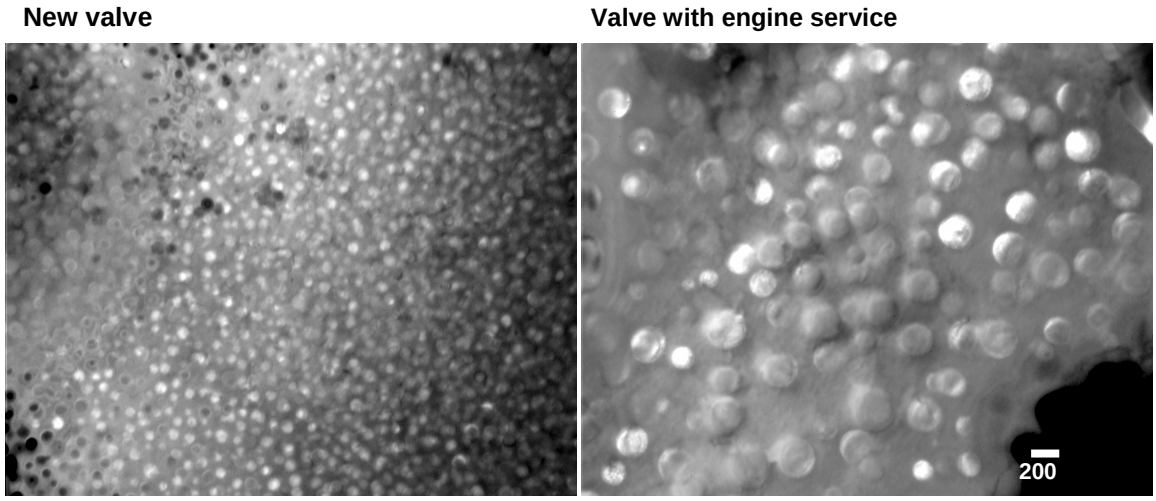

Figure 3. AEM microcharacterization of the middle of the filet region of a typical Ni-Cr-Fe super alloy exhaust valve, using dark-field imaging of γ' precipitation with an ordered superlattice reflection, for a fresh valve and a valve with several thousand hours of ARES engine service. Service aging produces significant coarsening of the intragranular (Ni,Ti)3Al γ' precipitation that strengthens the alloy at high temperatures.

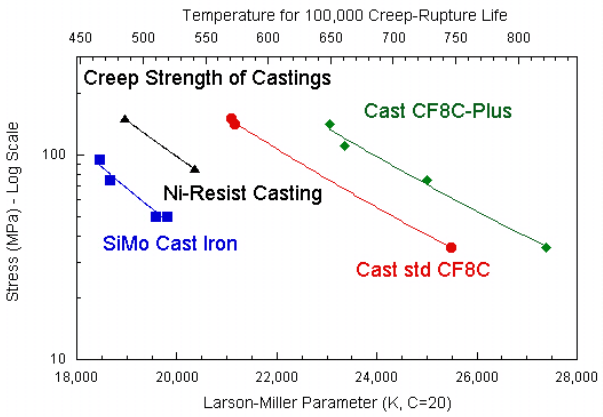

Figure 4. Larson Miller parameter plot of creep rupture stress for high SiMo and nickel-resist cast irons and standard CF8C and the new CF8C-Plus cast stainless steels tested in air at various temperatures.

After 2000 h, the deposits on the valve tulip were significant. Some discoloration and spallation on the valve-seating surface was also observed. A cross-section scanning electron microscope (SEM) image of the deposit formed during 2000 h of engine use on the intake valve tulip surface is shown in Figure 5. The tenacious surface deposit was identified as a calcium zinc phosphate and was >300 µm thick in many areas. The calcium, zinc, and phosphorous originated in the oil (as the oil additive

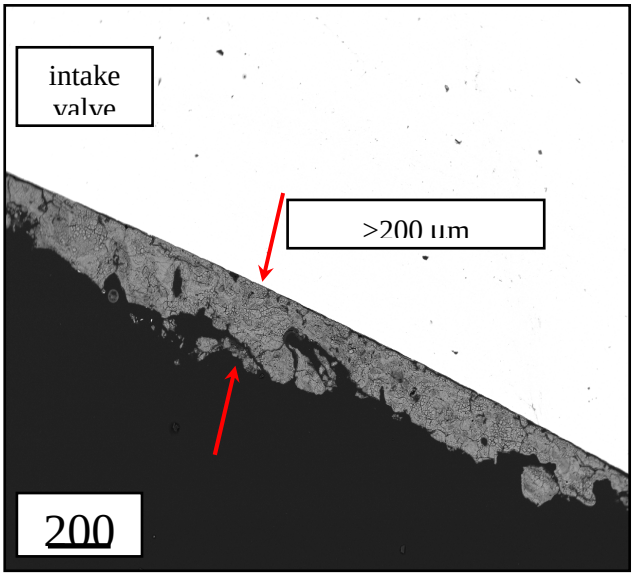

Figure 5. SEM cross-section image of (Ca,Zn) phosphate deposit formed on surface of intake valve tulip after ~2000 h.

ZDDP). The thickness of the phosphate deposit that formed during a relatively short engine run indicates some excess oil coming from the stem/guide into contact with the tulip surface and burning/oxidizing on the valve surface. In addition to the stable deposit formation on the tulip surface, a similar (albeit thinner) calcium-zinc -phosphate oxide deposit was

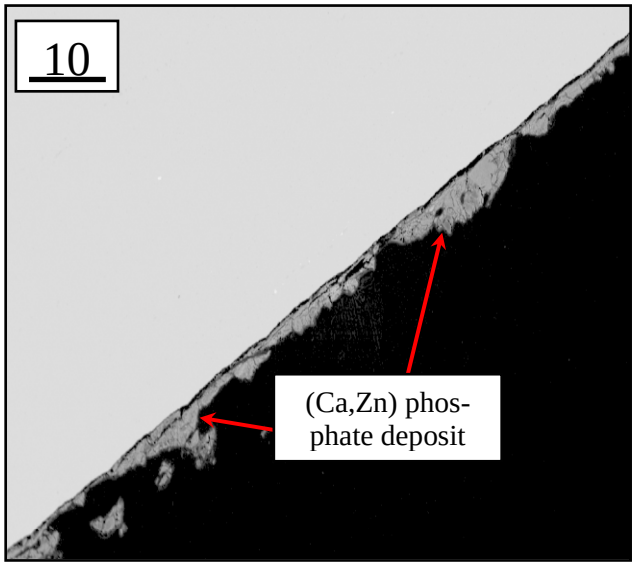

Figure 6. SEM cross-section image of (Ca,Zn) phosphate deposit formed on intake valve sealing face after ~2000 h.

identified across the entire valve seating (contact) face (Figure 6).

In addition to the initial characterization of engine-exposed valve components after ~2000 h, ORNL is currently generating the characterization data for components after exposure to longer (~7000-h and ~24,000-h) engine tests, including bulk metallurgical changes caused by aging and stress within each component, as well as analysis of the surface deposits and oxidation/corrosion changes to assess environmental or tribological effects on the components. This effort will continue and will be concluded in FY 2005.

A two-pronged approach is being taken to address the issue of loss of valve function as a result of oil deposit formation. The first effort will be to identify materials or surface treatments that better resist the hot gas oxidation and erosion leading to material loss. This approach needs to be taken in concert with identifying alloys with sufficient microstructural stability for extended high-temperature exposure. The second is to develop a strategy to prevent or minimize oil deposit formation in the first place. An effort was initiated in 2004 to track oil degradation during engine operation, and to relate the degradation to the additive package in the new oil and the efficiency of contaminant removal during engine operation through more advanced filtration. Comparison engine tests are currently being defined that will determine the relative contributions of oil composition and contaminant control to oil deposit formation. These tests will enlist the efforts of an engine OEM, a major heavy-duty filter manufacturer, and ORNL. An advanced oil test is currently being developed to measure the content of the heavy organic contaminant known as "sludge," which is thought to act as a precursor to oil deposit formation.

Future work in the area of lubricant effects is employing thermal stability tests to determine the tendency of oils to form deposits as a function of composition and aging. The formation of a consortium of OEMs, lubricant and additive suppliers and ORNL will be explored to develop better lubricating oils for natural gas–fired engines that provide effective lubrication for extended service intervals, prevent or minimize the formation of in-cylinder oil deposits, and avoid the poisoning of exhaust catalysts.

Finally, in FY 2003, ORNL and Caterpillar developed a new cast austenitic stainless steel, CF8C-Plus, that has the potential for use in exhaust component applications in advanced heavy-duty diesel engines. Typical exhaust manifolds and turbocharger housings are made from SiMo cast iron, which has poor strength above 550–600°C and can be susceptible to thermal fatigue cracking during severe cycling after prolonged use. Some applications use nickel-resist cast iron for better heat resistance. Standard CF8C steel (Fe-19Cr-9Ni-0.7Nb-0.07C), which has good castability and sufficient strength up to about 600–625°C, is not strong enough at higher temperatures. Moreover, it contains large amounts (20–25 vol. %) of δ-ferrite, which transforms into σ-phase during aging at 600°C and above, severely reducing ductility. CF8C-Plus steel was developed to be stronger and much more resistant to fatigue and thermal fatigue so that it could be used in severe thermal cycling conditions. CF8C-Plus was developed in about 1 year, with a special "engineered microstructure" that contains no δ-ferrite in the as-cast microstructure and hence forms no σ-phase forms during aging. The creep-rupture resistance of a new commercial heat of CF8C-Plus at 750–850°C is far better than that of SiMo or nickel-resist cast irons, and better by almost a factor of two in rupture strength than the standard CF8C steel (Figure 4). CF8C-Plus was commercially scaled up in 2003–2004, and commercialization for several different component applications will continue and expand in

FY 2005. ORNL began discussions with a commercial stainless steel foundry that can make trial CF8C-Plus stainless steel exhaust manifolds for ARES engines at the end of FY 2004, and efforts to produce prototype components will continue in FY 2005.

Conclusions

ORNL completed detailed microcharacterization of Ni-Cr-Fe super alloy exhaust valves. The Ni-Cr-Fe super alloy valve contains a mixture of titanium and aluminum oxides beneath the surface of the combustion face of fresh valves, and more titanium oxide particles form during service aging. Service aging produces large lath precipitates of α-chromium in the γ' hardened matrix, increases the precipitation of Cr-rich $M_{23}C_6$ along the grain boundaries, and significantly coarsens the intragranular γ' precipitation.

ORNL began Phase I of a more comprehensive and systematic effort to characterize the effects of ARES service on in-cylinder and exhaust component materials. Characterization includes observation of surface deposits, tribological and oxidation effects, and bulk metallurgical aging effects on the various components. The interaction of engine lubricants with metal surfaces is being studied to optimize lubricant performance in the natural gas operating environment. This work will be reported separately beginning in FY 2005.

ORNL began interaction with a commercial foundry to produce ARES engine exhaust manifolds of CF8C-Plus cast stainless steel for testing and evaluation.

Publications/Presentations

P. J. Maziasz and M. J. Pollard, "High-Temperature Cast Stainless Steel," *Advanced Materials & Processes* (ASM-International), **161**, 57–59 (October 2003).

N. D. Evans, P. J. Maziasz and L. R. Walker, "Microstructure and Microanalysis of Ni-based Superalloy Exhaust Valves," *Microscopy and Microanalysis*, **10** (Suppl. 2) 645–655 (2004)

P. J. Maziasz, "Highlights of ORNL Efforts to Improve High-Temperature Performance of Austenitic Stainless Steels," invited presentation made during visit to General Electric Power Systems, Schenectady, NY, March 18, 2004.

P. J. Maziasz, "Development of CF8C-Plus: A New Cast Austenitic Stainless Steel With Improved Heat-Resistance and Performance Above 650°C," invited presentation made at the ASM Peoria Chapter Meeting, April 5, 2004.

P. J. Maziasz, J. P. Shingledecker, N. D. Evans and M. J. Pollard, "Advanced Cast Austenitic Stainless Steels for Diesel Engine and Gas Turbine Components," presentation at DOE FreedomCAR and Vehicle Technologies Program Review at ORNL, June 15, 2004.

P. J. Maziasz, K. L. More, and J. J. Truhan "ORNL Characterization of In-Cylinder Materials for NG-Fired Reciprocating Engines," invited talk given during a visit to Waukesha Engine Division, Dresser Inc., August 25, 2004, Waukesha, WI.

Recognitions and Awards

ORNL and Caterpillar received a 2003 R&D 100 Award for the development of CF8C-Plus cast stainless steel. The award was presented at the annual R&D 100 Award banquet in October 2003.

Phil Maziasz was appointed vice-chair of the ASM Technical Programming Board and vice-chair for the ASM 2004 Materials Solutions Conference and Exposition.

Phil Maziasz served as chair of the ASM and TMS Joint Commission on Metallurgical and Materials Transactions Journal through December 2003.

Phil Maziasz was appointed to the ASM William Hunt Eisenman Award Committee in 2004; he also continued to serve as the chair of the Honor and Awards Committee of the ASM Oak Ridge Chapter in 2004 and is a member of the executive committee.

Appendix A:
Acronyms and Abbreviations

3D	three-dimensional
AA	accelerated attack
AL	Allegheny-Ludlum
ANL	Argonne National Laboratory
AP	as-processed
APDL	ANSYS parametric design language
Ar	argon
BAS	barium aluminosilicate
BPF	brazed plate and fin
BPFR	brazed plate and fin recuperator
BSAS	barium-strontium-alumino-silicate
CFCC	continuous fiber ceramic composite
CHP	combined heat and power
CLP	closed-loop processing
CMM	coordinate measuring machine
CT	computed tomography
CTE	coefficient of thermal expansion
DBC	diffusion barrier coating
DE	distributed energy
DG	distributed generation
DOE	U.S. Department of Energy
EBC	environmental barrier coating
EPMA	electron probe microanalyzer
HIP	hot isostatic pressing
HEEPS	HIP Engineered Environmental Protection Surface
IBR	integrally bladed rotor
IEP	isoelectric point
LAN	local area network
MPI	message passing interface
NASA	National Aeronautics and Space Administration
NDC	nondestructive characterization
NO_x	nitrogen oxides
ODS	oxygen-dispersion strengthened
OEM	original equipment manufacturer
ORNL	Oak Ridge National Laboratory

PAA	polyacrylic acid
PE	polyethylenimine
PS	primary surface
PSR	primary surface recuperator
SA	solution annealing
SAS	strontium aluminosilicate
SEM	scanning electron microscope/microscopy
Sr	strontium
TBC	thermal barrier coating
TTBC	thick thermal barrier coating
TET	turbine exit temperature
TSN	toughened silicon nitride
UTS	ultimate tensile strength
XRD	X-ray diffraction
Yb	ytterbium
YSZ	yttria-stabilized zirconium